Hybrid Integrated opto-electronic oscillators

Peppino Primiani

UNIVERSITÉ DE RENNES 1

THESE DE DOCTORAT DE

L'UNIVERSITE DE RENNES 1

ECOLE DOCTORALE N° 596
Matière Molécules et Matériaux
Spécialité : Photonique

Par **Peppino Primiani**

Hybrid Integrated Opto-Electronic Oscillators

Thèse présentée et soutenue le 17 mai 2021
Unité de recherche : Institut FOTON – Equipe DOP
Entreprise : III-V Lab
Thèse N° : (10)

Rapporteurs avant soutenance : (11)

Olivier LLOPIS	Directeur de recherche CNRS, LAAS (Toulouse)
Laurent VIVIEN	Directeur de recherche CNRS, C2N (Marcoussis)

Composition du Jury :

Olivier LLOPIS **Rapporteur**
Directeur de recherche CNRS, LAAS (Toulouse)

Laurent VIVIEN **Rapporteur**
Directeur de recherche CNRS, C2N (Marcoussis)

Mehdi ALOUINI **Directeur de thèse**
Professeur des Universités, Université de Rennes 1 (Rennes)

Marc BRUNEL **Examinateur**
Professeur des Universités, Université de Rennes 1 (Rennes)

Cécilia DUPRÉ **Examinateur**
Ingénieur de recherche, CEA-Leti (Grenoble)

Frédéric van DIJK **Encadrant industriel**
Ingénieur de recherche, III-V Lab (Palaiseau)

UNIVERSITÉ DE RENNES 1

Titre : Oscillateurs Opto-Electroniques Integrés Hybrides

Mots clés : Oscillateur Opto-Electroniques, Photonique micro-ondes, Circuits Photoniques Integrés Hybrides

Résumé : Les Oscillateurs Opto-Electroniques (OEO) permettent la génération par voie optique de signaux ultra-pures dans le domaine des micro-ondes, et commencent à être déployés dans différents systèmes, y compris les systèmes de guerre électronique (RADAR, échantillonnage optique).
Toutefois la taille des OEOs empêche leur intégration dans des systèmes exigeants en termes de SWaP (size, weight and power consumption).

A ce propos, les technologies d'intégration des Circuits Intégrés Photoniques (PICs) offrent la possibilité de fabriquer des composants avec différentes fonctions optiques sur la même puce, avec des avantages significatifs pour la compacité.

L'objectif de la thèse est l'étude des performances d'un OEO intégré, dont nous proposons une architecture avec un PIC hybride InP/SiN.

Le Phosphure d'Indium (InP) est le substrat choisi pour la fabrication des composants actifs, notamment diodes laser (DFB), amplificateurs optiques (SOA), modulateurs à électro-absorption (EAM) et photodiodes (PD). Ces composants sont fabriqués dans une plateforme de fabrication bien maîtrisée par le III-V Lab.

Le PIC passif est fabriqué sur une plateforme Silicium avec des guides en Nitrure de Silicium (SiN) enterrés dans de la sílice pour atteindre des faibles pertes de propagation, développée dans le cadre de cette thèse avec le CEA-Leti de Grenoble. Ces PICs incluent des lignes à retard, pour remplacer la fibre optique, mais aussi des résonateurs en anneau pour la fonction de filtrage électrique.

Une étude expérimentale a permis de valider les différentes briques de l'architecture proposée.

Title : Hybrid Integrated Opto-Electronic Oscillators

Keywords : Opto-electronic Oscillators, Microwave Photonics, Hybrid Photonic Integrated Circuits

Abstract : Optoelectronic Oscillators (OEOs) allow the generation of electrical signals with high spectral purity in the microwave domain. OEOs start to be deployed in several systems for applications such as electronic warfare.
However, OEOs are still limited in deployment for which SWaP (size, weight and power consumption) is a key factor.

Photonic Integrated Circuits (PICs) allow for the fabrication of devices with different functions on the same substrate, with a sensitive reduction of the total footprint.

This thesis has the objective to study the performances of integrated OEOs, for which an architecture with an hybrid InP/SiN PIC is proposed.

Indium Phosphide (InP) is the platform of choice for the fabrication of active components, namely lasers (DFB), optical amplifiers (SOA), electro-absorption modulators (EAM) and photodiodes (PD). The fabrication platform has been consolidated through the years at III-V Lab.

The passive PIC is fabricated on a Silicon platform with Silicon Nitride (SiN) waveguides buried in sílica to reach low propagation losses performances, developed with the CEA-Leti in Grenoble. These PICs try to replace the optical fiber with on-chip delay lines, but also integrate ring resonators as electrical filters.

Experimental data are used to validate the different building blocks of the proposed architecture.

A mio padre

TABLE OF CONTENTS

TERMS AND ABBREVIATIONS

ADC	Analog to Digital Converter
CW	Continuous Wave
DFB	Distributed Feedback Laser
DSP	Digital Signal Processing
EAM	Electro-Absorption Modulator
EDFA	Erbium-Doped Fiber Amplifier
EML	Externally Modulated Laser
ESA	Electrical Spectrum Analyzer
HNLF	Highly Non-Linear Fiber
HPA	High Power Amplifier
LNA	Low Noise Amplifier
LO	Local Oscillator
OEO	Opto-Electronic Oscillator
OSA	Optical Spectrum Analyzer
PC	Polarization Control
PD	Photodiode
PIC	Photonic Integrated Circuit
PPLN	Periodically Poled Lithium Niobate
RoF	Radio over Fiber
SOA	Semiconductor Optical Amplifier
SMSR	Side-Mode Suppression Ratio
SWaP	Size, Weight and Power consumption

General Introduction

Low noise frequency references are used in all electronic systems such as Radar systems, wireless telecommunication, both on Earth and on satellites, and generically in all analog applications.

These references, often referred to as Local Oscillators (LO), serve several purposes among others the synchronization and the up- and down-conversion of the signals.

In high-end applications, as Radars, the phase noise of the Local Oscillator signal directly affects the sensitivity of the receiver system. Other applications can be even more demanding: in satellite telecommunications the parameters of Size, Weight and Power consumption (SWaP) pose a real challenge to be tackled.

Among all technologies, Opto-Electronic Oscillators (OEO) have proven to be a good source of optically generated microwave signals. The advantage of optical generation of microwave signals is that long spools of low losses optical fiber can be used as a delay element, enhancing the phase noise response of the system. The upper limit of the generation frequency is manly given by the electrical bandwidth of the opto-electronic components, such as directly modulated lasers, modulators, and photodiodes, which could potentially reach 70 GHz. On the other hand, the whole system is quite bulky and subject to the environmental conditions such as temperature variations and mechanical vibrations.

Photonic Integration Technologies can offer a way to improve an OEO in terms of Size, Weight and Power consumption. Photonic Integrated Circuits (PICs) can be fabricated on a variety of semiconductor or dielectric substrates. In a span of around twenty years PICs have grown in complexity from one or few to several thousands of opto-electronic components integrated on the same chip, similarly to what happened to electronic circuits after the first transistors were fabricated. The telecommunication market is leading the path in this rapid expansion phase, trying to cope with a widespread growth of bandwidth demand with the 5G network, where photonics plays a key role in all parts of the network architecture. As of 2020, PICs are in the ramp-up phase of the mass production, also taking advantage of semiconductor processing technologies borrowed from electronic manufacturing.

Mass production capabilities and decades of research in the field of photonics allowed an overall reduction in the final cost of production for PICs. The photonic ecosystem grew all over the world with services ranging from fabrication foundries, design and packaging for the several available platforms. Silicon Photonics is taking the lead for the natural integration with CMOS electronics, but integration platforms such as Indium Phosphide (InP) and Gallium Arsenide (GaAs) are still the choice for active components fabrication.

Besides the telecommunication and mainly digital market, the analog applications as well can take advantage of the developments in photonic integration technologies: Integrated Microwave Photonics became a new area of interest for research and development.

Among the ways Integrated Microwave Photonics can assist in building better systems, there are for sure two functional blocks in which it can truly make a difference: the generation of microwave signals and photonic-assisted signal processing.

The generation of microwave signals with PICs can be declined in different fashions, such as Opto-Electronic Oscillators or optical frequency comb generators.

Few attempts at integrating an Opto-Electronic Oscillators were made by research groups around the world. However, to date, there is no definite "golden unit" to compare with when it comes to PIC-based Integrated OEOs, with each demonstrator having strengths and weaknesses. It was natural for the Microwave Photonics team of III-V Lab to tackle this challenge back in 2014, when this thesis started. Given the proven expertise in Microwave Photonics of the lab, it was clear that integrated photonics could try to replicate the performances of the standalone systems, but the strength of integrated microwave photonics was somewhere else: the integration of the optical components opens the possibility to make use of photonic architectures and scale down bulky setups in a small footprint. Two of them will be discussed during this thesis, namely heterodyne generation of microwave signals through optical components, increasing the frequency generation capabilities potentially to the mmW band, and optical injection locking of the two lasers, which drastically improves the stability of the electrical signal.

Optical combs, which earned T. Hänsch and J. Hall a Nobel prize in Physics in 2005, can be used as precise frequency synthesizers; the integration of self-referenced optical combs on PICs was demonstrated by U.S. researchers as early as 2017. Optical combs, especially for their pulsed operation as Mode-Locked Lasers, are of particular interest for microwave applications; a mode-locked laser built with some processes developed within this thesis was demonstrated this year by III-V Lab.

Photonic signal processing applications, on the other hand, have reached good maturity. Among the demonstrators shown in the last years we can name photonic-assisted Radars, True-Time Delays for Phased Array Antennas, and photonic-assisted Analog-to-Digital Converters.

The concept of filtering is one of the basic building blocks for photonic signal processing. In the specific case of an OEO, an electrical filter is needed to select the oscillation frequency of the system. In the Integrated OEO architecture proposed in this thesis the RF filtering function is performed with an integrated ring resonator. One of the key functions demonstrated in this manuscript is the possibility to use ring resonators as microwave band-pass filters for OEO applications.

More generally, photonic filtering has seen the growth in the field of programmable photonic filters in the last few years, which act as the optical counterpart of electrical FPGAs, with high reconfigurability capabilities. These structures can allow further flexibility in the design of a complex PIC with software-defined filtering functions.

This manuscript has the purpose to discuss the research on Photonic Integrated Circuits performed at III-V Lab during my thesis. The main objective is to fabricate an integrated OEO, however each of the four chapter represents a milestone in the development of such a subsystem.

The starting point, and the topic of Chapter 1, is to understand what an Opto-Electronic Oscillator (OEO) is. A quantitative treatment of the oscillation condition is presented. Moreover, the noise performances of the OEO are described in terms of phase noise and its components. The impact of

noise on radar and other communication systems is introduced.
Several OEO architecture are shown throughout the chapter since many of them are of interest as integrated photonic frequency reference generators; a state of the art of such PICs is presented.
The final paragraph of Chapter 1 presents the proposed architecture for an application-specific hybrid PIC working as an Opto-Electronic Oscillator.

Chapter 2 is devoted to the discussion of the passive integration platform included in the proposed architecture. The choice of material system for the passive platform will strongly influence the performances of the system, thus an extensive state of the art of the different photonic integration technologies is presented. The key parameters for the choice are propagation losses and chip footprint. The choice to use Silicon Nitride (SiN) on Silica (SiO_2) waveguides on a Silicon wafer was made, due to the potential of this material system. The second half of the chapter presents the several elements designed on the platform developed with CEA-LETI in Grenoble, starting from the waveguide design, up to more complex structures such as ring resonators, which are key components for the electrical filtering function in the optical domain. The chapter ends with the measurements on the produced wafers, such as propagation losses and ring filtering properties. From the very beginning the passive platform was meant to accommodate building blocks that were not directly related for Opto-Electronic Oscillators. Besides the optical frequency comb, a low linewidth laser with SiN Bragg gratings was demonstrated as well. This topic will be better discussed in the Ph.D. thesis of Sylvain Boust.

The topic of Chapter 3 is the active integration platform on Indium Phosphide (InP), where devices such as lasers, modulators, optical amplifier, and photodiodes are fabricated. The design of such building blocks is presented after a brief review of the physical theory of photon generation and absorption.
The chosen integration technique is the butt-joint, which allows the epitaxial growth of different semiconductor layer stacks in different locations of the wafer and thus the chip. Details of the fabrication steps are given throughout the chapter.
A design was proposed and fabricated within an internal Multi-Project Wafer run, allowing the integration of DFB lasers, electro-absorption modulators (EAM), semiconductor optical amplifiers (SOA) and photodiodes. The PIC layout is co-designed with the proposed passive PIC designs described in Chapter 2, allowing testing and packaging of the Hybrid PIC through butt-coupling. The results from testing the standalone components on the PIC are shown in the last paragraph and conclude this section.

The last part of this thesis is Chapter 4, presenting the experimental results of the Photonic Integrated Circuits characterized during the three years, and is divided in 4 sections, one for each class of experiments.
The first section attempts to validate two key functions of the active integration platform for microwave photonic applications: the use of EAM modulators on InP as analog amplitude modulators, and the possibility to fabricate photodiodes with the same layer stack as the one of the EAM. Stable oscillations at 10 GHz were observed with a simple lab setup involving two Externally modulated lasers (EML), and EDFA, and an electrical amplifier.
The second section presents the measurements performed on the PIC discussed in Chapter 3, which integrates the 2 EML functions of emitter and receiver together. Oscillations could not be obtained due to lack of optical power and a strong RF crosstalk effect on the chip alumina submount.
The third section discusses the techniques of optical heterodyne frequency generation and optical injection locking. A PIC with two DFB lasers was used to generate a beatnote on a fast photodiode.

The output electrical frequency was tuned between 15 and 20 GHz. Stable oscillations were obtained thanks to the on-chip cross-injection locking of the two lasers. Two similar experiments were carried on previously in the lab, both on the same PIC, both for frequency multiplication of an external frequency synthesizer, one with a fiber-based, the other with an on-chip reinjection path.
The fourth and last section of this manuscript is devoted to the demonstration of electrical filtering with ring resonators. The resonator is tested in an add-drop configuration in which it acts as a bandpass filter at the desired oscillation frequency, in our case 10 GHz. The bandwidth of the filter was measured to be 600 MHz, which corresponds to the filter bandwidth in the optical domain.

1 OPTOELECTRONIC OSCILLATOR

This chapter is dedicated to the general description of an Optoelectronic oscillator (OEO), its working principle and the figures of merit of such a system. A brief digression is also presented on how the performances of the OEO affect the system in which it is integrated, especially for radar applications.

An optoelectronic oscillator is a system capable of delivering a pure electrical signal in the radiofrequency range by using optical components [1] and in particular long optical delays. When such signal is used as a reference, it is called "Local Oscillator" (LO).

The function of local oscillator is deployed in many systems involving signals transmissions such as radars, Radio over Fibre (RoF), analog links and satellite and wireless telecommunication systems. The local oscillator may be the signal of interest to be distributed (clock distribution) or work as an electrical carrier for data (RoF), or it can be used as one input of an electrical mixer to perform up or down conversion of electrical frequencies.

The idea of building an oscillator out of photonic components came out early [2] in the history of photonic devices, as soon as such devices (especially directly modulated lasers and photodetectors) reached a sufficient level of maturity. The Local Oscillator (LO) technologies used up to that moment were quartz oscillators or magnetrons. Quartz oscillators have natural frequencies ranging from 10 to 100 MHz (Figure 1), and need electrical multiplication stages to reach higher frequencies. The problem with frequency multiplication is that it adds at least a constant noise of 20*log(N) (where ***N*** is the multiplication factor) to the phase noise spectrum, if an ideal frequency multiplication process is considered. In the real case the multiplication chain noise figure will be higher than the ideal case, which is a strong limitation in reaching high frequency operation.

The main advantage of an optoelectronic oscillator over quartz oscillators is the possibility of direct synthesis of the frequency of interest. Optoelectronic oscillators have now reached phase noises levels as low as an ideally multiplied quartz oscillator [3].

The second main advantage of electrical signal generation by optical means is the use of optical fibre for the propagation of the signal. Propagation losses on optical fibres reached values of 0.2 dB/km, allowing the creation of long cavities with high quality factors. For example, a fibre of 2 km (which is a relatively short cavity for an OEO) gives a delay τ of 10 μs, with a corresponding quality factor that can be found with

$$Q_{RF} = \pi f_{osc} \tau \tag{1}$$

where f_{osc} is the oscillation frequency. The above equation also shows that the RF quality factor scales linearly with the oscillation frequency.

An optoelectronic oscillator can be analysed in terms of properties starting from a very basic oscillator scheme of a gain element and a frequency-selective filter, as shown in Figure 2. In the case of an opto-

electronic oscillator, the gain is given by the microwave optical link and RF frontend; the filtering is made with a long spool of optical fibre in addition to electrical bandpass filters.

The following paragraphs will describe the figures of merit of a generic oscillator and the working principle of an optoelectronic oscillator.

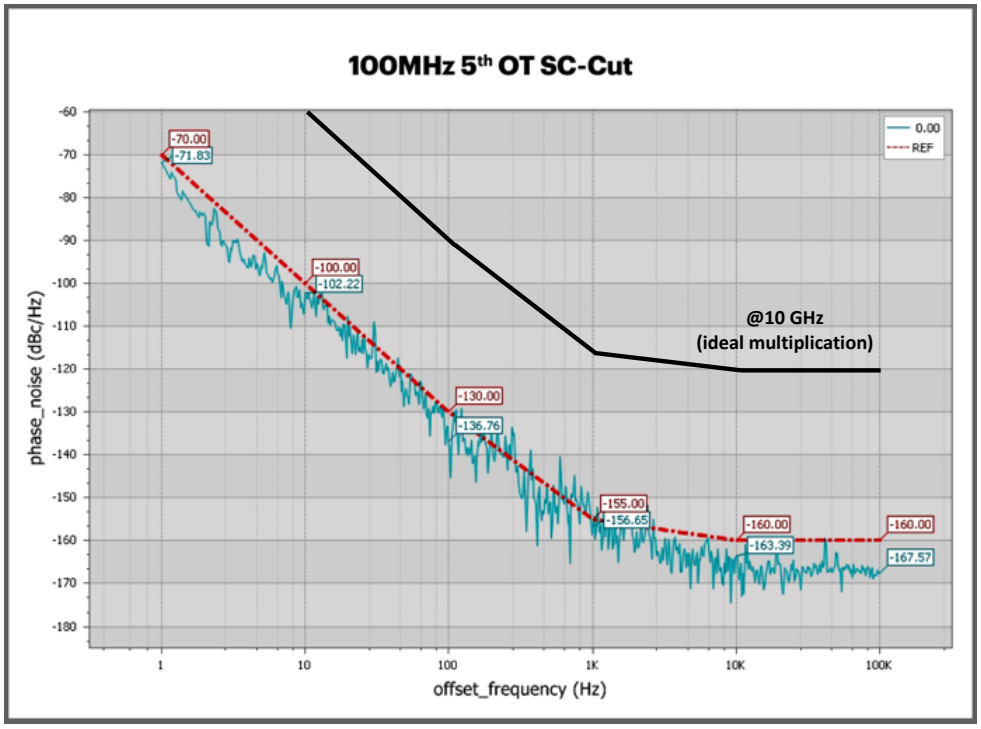

Figure 1. Commercial Quartz Oscillator Phase noise elaborated from [4]. Black curve: noise of the ideally multiplied oscillator from 100 MHz to 10 GHz. Blue curve: serial number measurement. Red: Specification mask of the product.

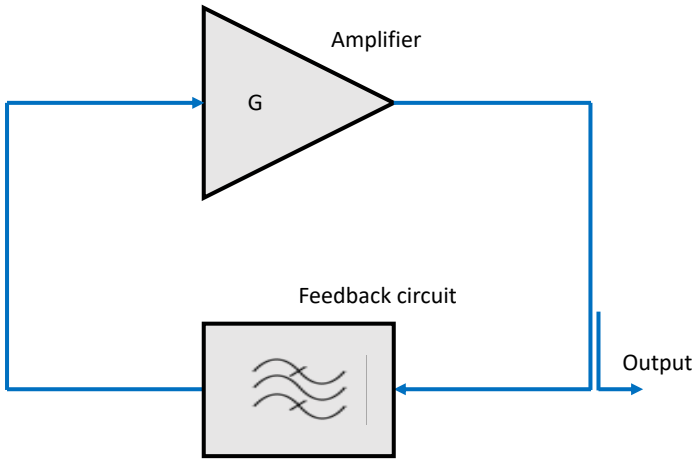

Figure 2. Principle of a feedback oscillator, where an amplifier of gain ***G*** and a frequency selective filter are shown in the feedback loop.

1.1 OPTOELECTRONIC OSCILLATOR WORKING PRINCIPLE

In this paragraph, the working principle of an Optoelectronic Oscillator is presented in a qualitative way, to describe how the resonant cavity is created by a mixed optical and electrical circuit.

The simplest OEO architecture is the one depicted in Figure 3. It contains a Continuous Wave (CW) laser, an amplitude modulator, a fibre delay line, a photodiode, an electronic passband filter and an electronic amplifier.

- The principle of operation is the following:
- The CW laser is injected in the amplitude modulator, which is biased conveniently.
- This CW signal travels through the fibre spool of length L, being delayed of a time $\tau=L/c$.
- The optical signal is detected on the photodiode, which converts the delayed signal and noise in the electrical domain.
- The output of the photodiode is fed to an RF amplifier.
- The output is filtered through a passband electrical filter. A portion of the filtered signal is fed to the amplitude modulator's RF input.
- The amplitude modulator has now an input RF signal, after the first signal round trip, which is the noise signal coming from the photodiode (from the photodiode itself but also from the photodetected light), filtered and amplified.

For those electrical frequencies where the gain is higher than losses, a stable microwave signal builds up. The system can thus be seen as a resonant cavity in the electrical domain, in which the signal is propagated on an optical carrier for a major fraction of the cavity length. The amplitude modulator performs the electrical-to-optical conversion, while the photodiode performs the inverse transformation.

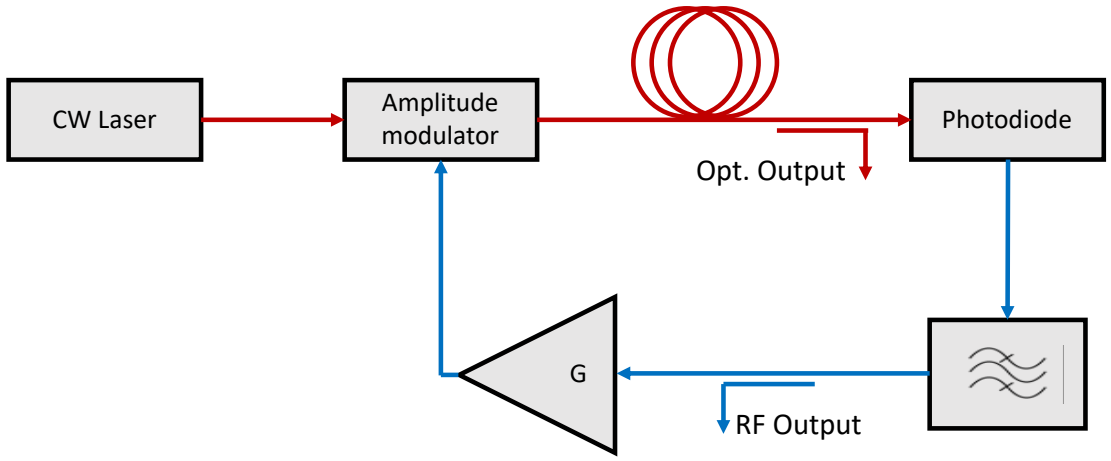

Figure 3. Standard OEO architecture, with optical (red) and electrical (blue) paths. The electrical part contains an RF amplifier and a bandpass filter

The two filtering elements in the cavity are the fibre delay and the electrical filter, and each of them has a different effect on the cavity itself. The long fibre coil sets the total delay of the cavity, since the propagation distance in the optical domain is much greater than the one in the electrical domain, so that the length of the fibre roughly corresponds to the length of the total cavity.

Since the OEO is equivalent to a ring cavity, the response of the fibre delay is a comb of evenly and closely spaced peaks; the fibre delay governs the finesse of the total cavity and the spacing of the natural cavity modes.

If this kind of system is left in free-running mode, it can oscillate at the natural frequency of the cavity (FSR) and each of its harmonics, provided that the RF gain is positive at those electrical frequencies. An electric filter is added to select one oscillation frequency in the electrical domain (figure 4). The filter's bandwidth should ideally contain only one harmonic of the cavity to ensure stable oscillation and avoid mode hopping [5].

It must be noticed that a fibre loop of 2 km gives an ***FSR*** of 100 kHz, calculated with $FSR = c/(n * L)$. Thus, a narrow electrical bandpass filter should be used.

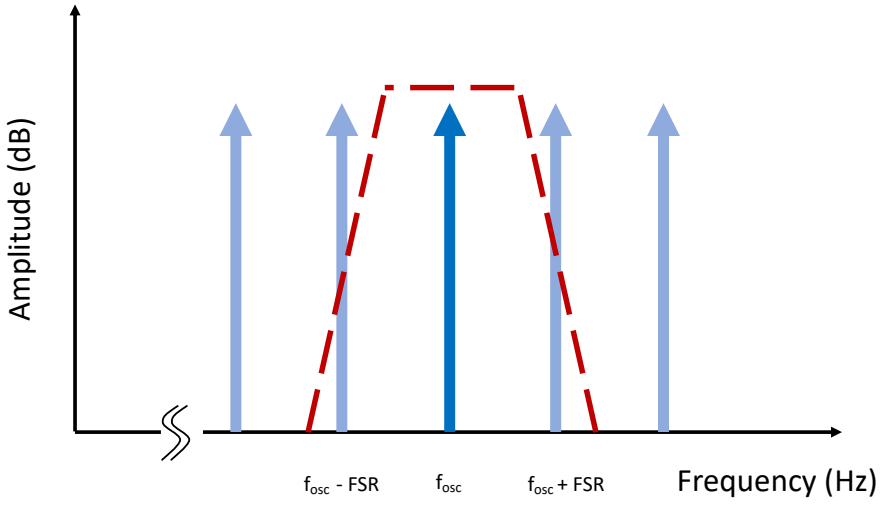

Figure 4. Filtering mechanism of an OEO. The blue arrows represent the natural cavity modes. The red dashes represent the frequency response of the bandpass filter in the OEO loop.

1.2 REQUIREMENTS FOR OPTOELECTRONIC OSCILLATORS

An (electronic) oscillator is a device capable of generating a reference signal in the electrical domain at one precise frequency. In this paragraph, the figures of merit of an oscillator will be briefly reviewed.

1.2.1 OSCILLATOR PHASE NOISE

Ideally, an oscillator delivers a stable and monochromatic signal, which can be described as a perfect sinusoid in the time domain ***t*** [5]:

$$V(t) = V_0 \cos(2\pi f_{osc} t + \phi) \tag{2}$$

where V_0 is the signal amplitude, f_{osc} is the oscillation frequency, and ϕ is the phase of the signal.

Real oscillators signals are affected by two types of noise: amplitude noise and phase noise. The real signal can be written as

$$V(t) = V_0\big(1 + \mathrm{a(t)}\big)\cos(2\pi f_{osc} t + \phi(t)) \tag{3}$$

in which the amplitude is modulated by a varying, random amplitude ***a(t)*** and the fixed phase ϕ is replaced by a random phase $\phi(t)$. We can expect the noise to be small with respect to the signal, so we can set $a(t) \ll 1$ and $\phi(t) \ll 1$.

The effect of the noise is to enlarge the spectrum of the signal in the frequency domain (Figure 5). A noiseless signal like the one in equation 2 has a Fourier transform corresponding to a Dirac delta function centred at the oscillation frequency. A noisy signal (equation 3) has a spectral footprint that depends on the level of noise of the carrier.

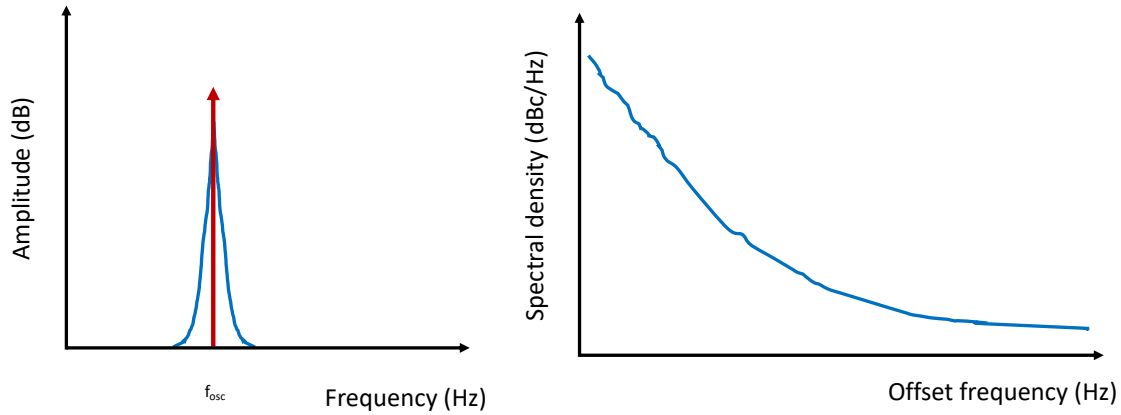

Figure 5. Left: Spectral footprint of ideal and real periodical signals; red: ideal signal (eqn 2); blue: real signal (eqn 3). Right: power spectral density of the noisy signal presented on the left side.

In long term measurements the random phase $\phi(t)$ drift is not necessarily found in one period of the signal but can exceed the $[-\pi; \pi]$ interval, gaining or losing one or more periods. Thus, the random phase generates a frequency fluctuation that can be described by the functional

$$(\Delta\omega)(t) = \frac{d}{dt}\phi(t) \tag{4}$$

which is the instantaneous frequency fluctuation.

The random phase and frequency fluctuation can be normalised with respect to the oscillation frequency, in order to be expressed in time units (seconds):

$$x(t) = \phi(t)/\omega_0 \tag{5}$$

$$y(t) = \frac{d}{dt}x(t) = (\Delta\omega)(t)/\omega_0 \tag{6}$$

which are respectively the phase time fluctuation and the fractional frequency fluctuation.

It must be noticed that $x(t)$ is not ambiguous as $\phi(t)$ since it allows the accumulation of phase cycles.

It is clear now that the random phase fluctuation causes an instantaneous frequency instability, which broadens the spectrum of the signal (Figure 5, right). Another way to understand this is to consider the Barkhausen stability condition for phase, stating that the phase shift of the oscillating loop must be zero at the oscillation frequency. If the phase in the loop can be modelled as a random process (as stated in the discussion above), then the phase condition is met for frequencies following the phase fluctuations, provided that gain is equal to 1 in the bandwidth of interest.

From the random phase $\phi(t)$ one can extract the one-sided power spectral density $S_\phi(f)$, defined as the Fourier transform of the autocorrelation function of $\phi(t)$:

$$S_\phi(f) = \int \mathbb{E}\{\phi(\tau)\phi(\tau + t)\}e^{-j2\pi ft}dt \tag{7}$$

In practice, the quantity that is measured reads:

$$10\log_{10}[\mathcal{L}(f)] = 10\log_{10}\left[\frac{1}{2}S_\phi(f)\right] \tag{8}$$

and is expressed in dBc/Hz, which means “dB with respect to the carrier in 1 Hz bandwidth”. The frequency scale (abscissae) is a frequency scale relative to the carrier frequency. This single sideband (SSB) phase noise spectrum is one of the most important figures of merit of an oscillator device.

The phase noise spectrum can be modelled by a power law:

$$S_\phi(f) = \sum_{i=-4}^{0} b_i f^i \tag{9}$$

where b_i are experimental coefficients and f is the frequency. Since phase noise spectra are plotted in log-log scale, the i-th power of the above formula is a straight line with a slope of $i*10$ dB/decade (Figure 6). Each power law corresponds to a specific noise process, so each of them can be isolated and recognized in the phase noise spectrum. These noise processes are shown in the following table.

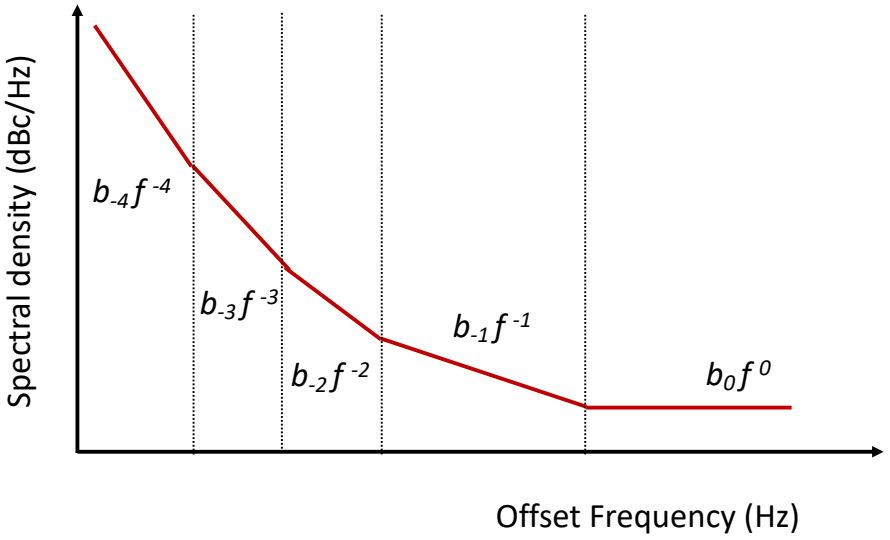

Figure 6. Representation of the power law in the phase noise spectrum. showing five different slopes from different physical processes. The coefficients are described in Table 1.

Coefficient	*Slope (10dB/decade)*	*Noise process*
b_0	0	White phase noise
b_{-1}	-1	Flicker phase noise
b_{-2}	-2	White frequency noise
b_{-3}	-3	Flicker frequency noise
b_{-4}	-4	Random walk frequency noise

Table 1. Description of noise processes in an oscillator noise power law, with their respective coefficient and slope

1.2.2 Impact of Local Oscillator phase noise on RADAR system performances

Radars are among the most demanding systems in terms of purity of the local oscillator, as it impacts directly the sensitivity of the system. A Pulsed Wave Doppler Radar will serve as an example.

In a standard radar architectures, the local oscillator intervenes both on the transmitter and receiver sides. The LO signal is amplified towards the antenna to generate the transmitted signal. At the reception, it is used as one input of a frequency mixer to perform signal downconversion to baseband,

where the low frequency signal can be digitized (Figure 7). Usually, the same LO is used as a clock reference for the analog-to-digital conversion. In this case, a frequency division may be needed.

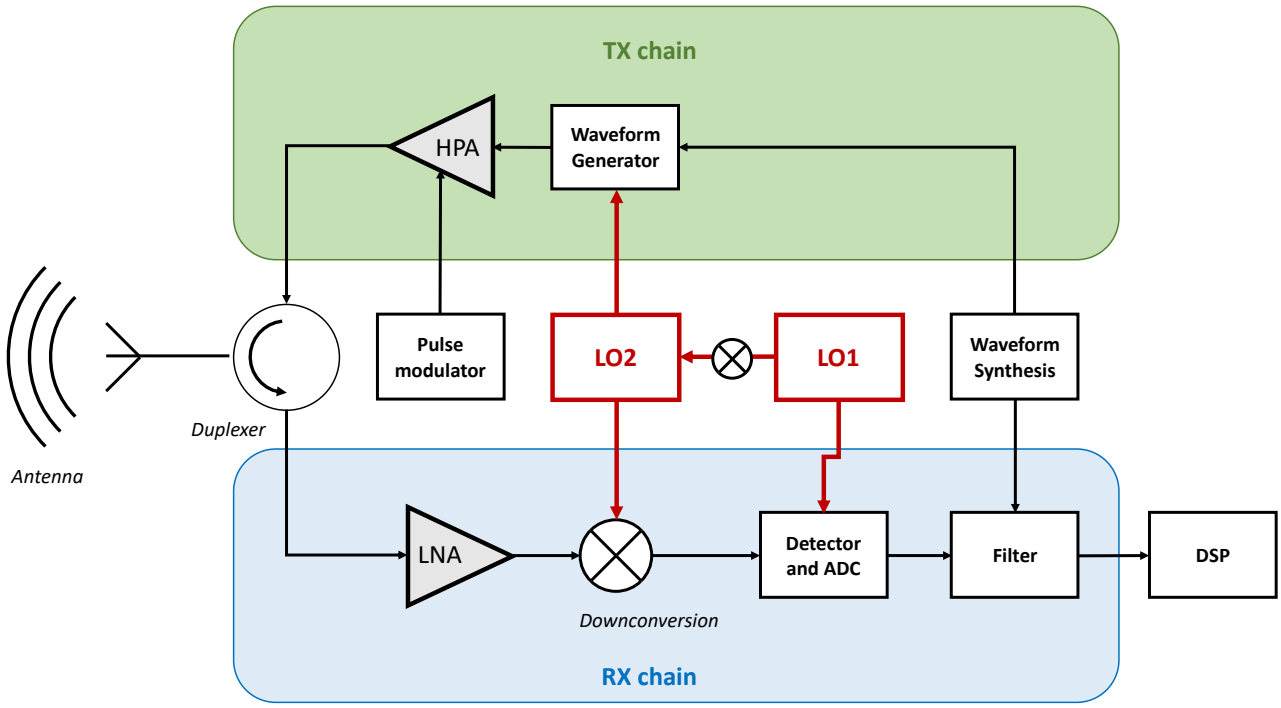

Figure 7. Pulsed Radar block diagram [6]. The local oscillator intervenes in signal generation, detection, and digitization. LNA: Low noise Amplifier. HPA: High Power Amplifier. DSP: Digital Signal Processing. LO1: Low Frequency Local Oscillator. LO2: Local Oscillator obtained from LO1 by multiplication.

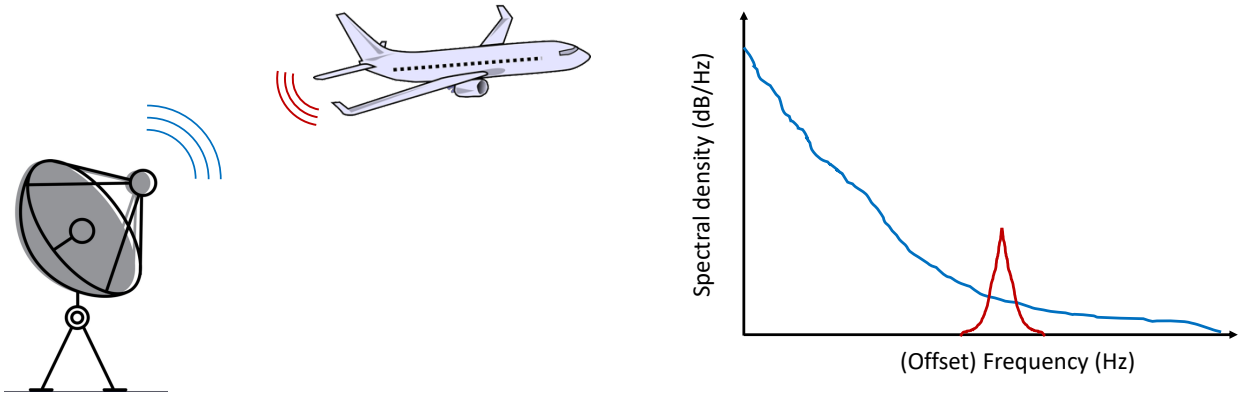

Figure 8. Left: Doppler Radar working principle. A moving target generates an echo signal, shifted in frequency with respect to the carrier from the emitter. Right: Detection scheme principle. The echo signal (red) is detected at an offset frequency from the carrier due to the down-conversion. The blue curve is the carrier phase noise, that will be the noise floor of the detection system.

As depicted in Figure 8, a radar system detects the Doppler frequency shift caused by a moving target. The Doppler frequency shift of a moving target is

$$f_d = \frac{2v_r f_0}{c} \tag{10}$$

where v_r is the relative velocity (in m/s), f_0 the emitted radar frequency and c is the speed of light. The radar emitted frequency depends on the application, but we can restrict to the case of X and Ku-band radars: the reason behind this is that those are the preferred frequency bands for medium range detection radars for space, airborne and maritime military and civil navigation and imaging systems. An X-band radar mounted on a plane can play the role of interceptor or perform ground target imaging. Table 2 shows the magnitude of the Doppler shift for two speed ranges: the frequency shift range is between 1 kHz (slow target) and 1 MHz (very fast target). In order to faithfully decode the received echo signal the phase noise of the local oscillator must be as low as possible, in order not to cover the signal with the noise; a received signal which lies 3 dB above the noise level is called Minimum Detectable Signal (MDS) and in practical cases has values ranging from -100 to -110 dBm.

Figure 8 is a simplified picture of the working principle of a radar. More sophisticated emission techniques and signal processing are needed in order to faithfully detect objects, especially when one is interested in position and vectorial velocity. However, the impact of the local oscillator noise will have an impact on the MDS even if more sophisticated architectures and detection techniques are used.

Radar frequency (GHz)	***Doppler shift at relative speed of***	
	100 m/s (kHz)	***3000 m/s (kHz)***
3	2	60
10	6.7	200
30	20	600

Table 2. Doppler shift of a moving object for different speeds and radar frequencies. For reference, the average speed of a multirole combat aircraft is 670 m/s.

1.3 MODELLING OF AN OEO

This section describes the mathematical treatment of the oscillation conditions for the microwave cavity which has been previously described in a qualitative way. The conditions for oscillation involve both amplitude and phase conditions [7]**.**

1.3.1 (SMALL SIGNAL) OPEN LOOP GAIN

We can consider the simplest OEO configuration with a laser, a modulator, a fiber delay, a photodetector and an electrical amplifier.

The CW power emitted by the laser (P_L) is injected in the amplitude modulator (here a Mach-Zehnder modulator), which has fiber-to-fiber fractionary coupling losses (including propagation losses inside the device) of T_{FF}. The optical power leaving the modulator is:

$$P_{out} = P_L \frac{T_{FF}}{2}\left\{1 - \eta \sin \pi \left(\frac{V_{in}(t)}{V_\pi} + \frac{V_B}{V_\pi}\right)\right\} \tag{11}$$

where η depends on the extinction ratio of the modulator, V_π is the half wave voltage, V_B is the DC bias and $V_{in}(t)$ is the (AC) signal fed into the modulator.

A photodetector converts the optical power to electrical current. This signal passes through an amplifier of gain G_A, so the total output electrical signal is:

$$V_{out}(t) = V_{ph}\left\{1 - \eta \sin \pi \left(\frac{V_{in}(t)}{V_\pi} + \frac{V_B}{V_\pi}\right)\right\}. \tag{12}$$

The photovoltage V_{ph} defined as:

$$V_{ph} = \frac{1}{2} P_L T_{FF} \rho R G_A\,, \tag{13}$$

where ρ is the photodiode responsivity and R the photodiode electrical resistance.

We can find the open-loop small signal gain as the derivative of the output with respect to the input signal [1]:

$$G_S = \left.\frac{dV_{out}}{dV_{in}}\right|_{V_{in}=0} = -\frac{\eta\pi V_{ph}}{V_\pi}\cos\left(\frac{\pi V_B}{V_\pi}\right). \tag{14}$$

The maximum gain is obtained when the modulator is biased in quadrature (at V_B=V_π), and the photocurrent is strong enough to drive the modulator, setting the threshold condition for V_{ph}:

$$V_{ph} = \frac{V_\pi}{\eta\pi} \tag{15}$$

These equations set the basis for the self-sustained oscillation and give a hint on the choice of components for building an oscillator.

Equation 15 describes how self-sustained oscillations are possible if the photodiode signal can directly drive a modulator even when the electrical amplifier gain is set to 1. It is clear then that an all-optical gain OEO can be built provided that the modulator has a small RF driving voltage and the detected optical power in the loop is sufficient [8]. Optical amplification can be used as well.

1.3.2 PHASE CONDITION

The Free Spectral Range is the spacing of resonant modes of a cavity. For a ring cavity of length ***L*** it is given by:

$$\mathrm{FSR} = \Delta f = \frac{c}{nL} \tag{16}$$

where ***c*** is the speed of light and ***n*** is the refractive index of the medium (in the case of optical fibres, ***n=1.5*** can be assumed). This response is a comb of evenly spaced peaks, for which the frequency is an integer multiple of the cavity length. The peaks appear when, after a round trip in the loop, the signal is in phase (Barkhausen condition):

$$\Delta\phi = 2\pi m \tag{17}$$

where ***m*** is a natural number.

For an ideal cavity, the result of this condition would be a train of Dirac delta functions (infinite finesse). Due to optical and electrical losses causing a finite finesse, the linewidth of the cavity modes is enlarged (Figure 9).

The dispersion of the optical fibre can be neglected since at the electrical frequencies of interest (3-30 GHz) the spacing in wavelength for an OEO working at 1.5μm is small (0.03 – 0.3 nm).

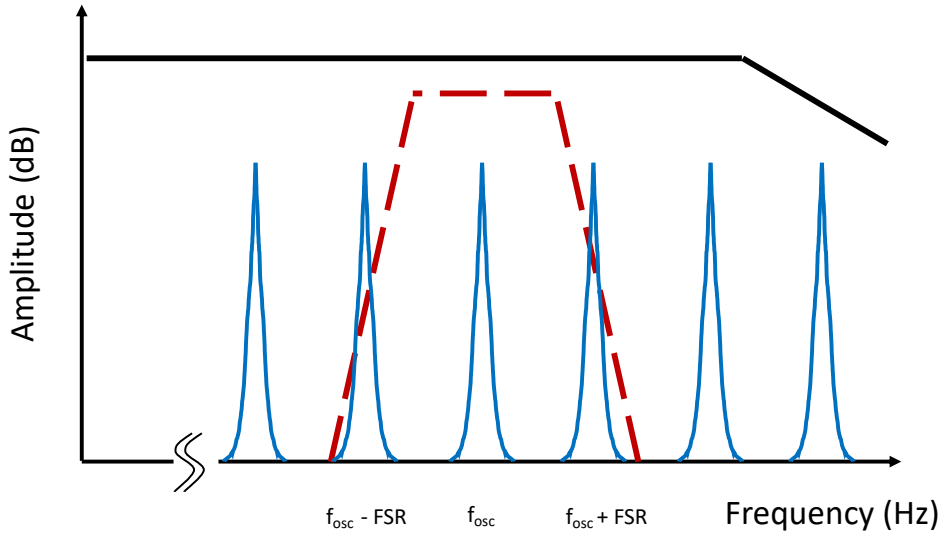

Figure 9. Frequency selection mechanism in an OEO. The blue peaks correspond to the phase-matching condition. The black line is the frequency-dependent microwave link gain. The red dashed line is the passband filter response.

1.4 OPTOELECTRONIC OSCILLATOR ARCHITECTURES

The simplest configuration of an optoelectronic oscillator was described earlier. In order to overcome some intrinsic limitations of the system, other configurations were proposed in the

literature. This section serves as a non-exhaustive list of these configurations, being limited to those who are of direct interest for this manuscript.

1.4.1 DOUBLE DELAY LINE (DUAL LOOP) OEO

Long fibre delays are better suited for higher spectral purity oscillators. The drawback of a such cavities is that the modes of the cavity itself are close to each other. The excess noise coming from the presence of these cavity modes can be seen in the phase noise spectrum as spurious peaks appearing at few tens of kHz away from the carrier, at the corresponding cavity's free spectral range. Since a radar's target causes a Doppler frequency shift of few kHz as well, noise in that range must be kept as low as possible.

The solution to reduce the spurious contribution on the phase noise is to use two parallel fibre delays [3], [9]. A simple way to figure out the effect of the two fibre delays is to think of an imbalanced Mach-Zehnder interferometer: the first, long fibre delay is used to create a high finesse cavity; the second one, much shorter, is needed to filter out the harmonics of the longer cavity. The optical signals are detected on two separate photodiodes, then recombined in the electrical domain. The effect of such a discriminator on the phase noise is to preserve the close-to-carrier phase noise, which is governed by the long cavity modes and finesse, and to reduce the peaks of the spurious modes in the high frequency region.

The power combination after the photodiodes must be done with the two signals in phase, to obtain the maximum amount of electrical power.

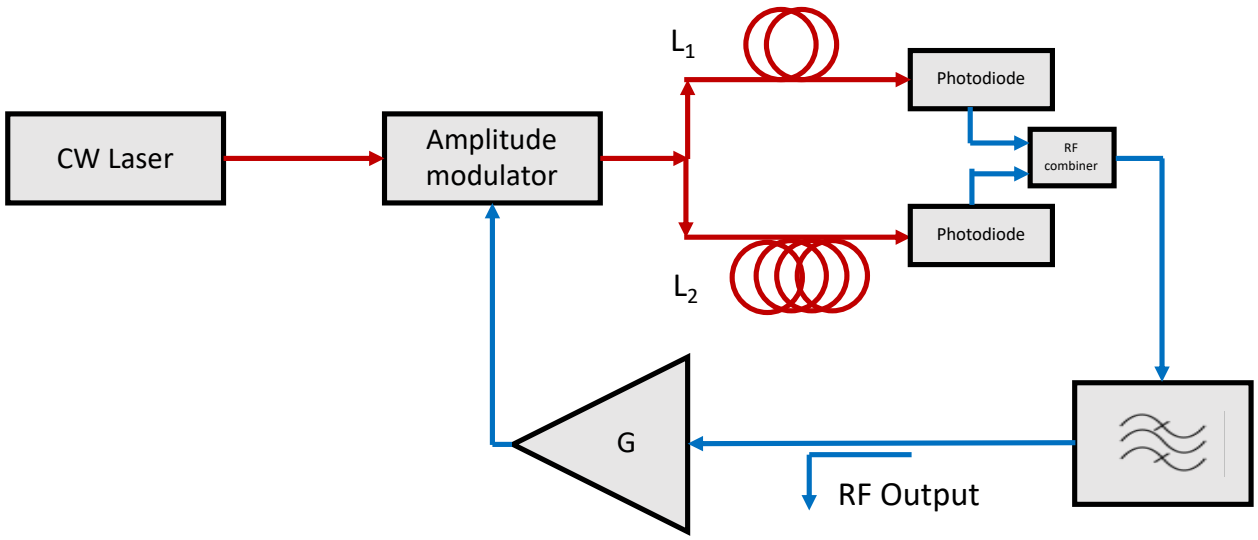

Figure 10. Architecture of a Dual Loop OEO. Two different optical delay lines are converted in the electrical domain and combined. This architecture reduces spurious modes in the phase noise.

1.4.2 COUPLED OPTO-ELECTRONIC OSCILLATOR

A Coupled Opto-Electronic Oscillator (COEO) is a system in which the continuous wave laser is replaced by a mode locked laser. Mode locked lasers are optical systems emitting several wavelengths that have the property of being in phase with each other. The beating of those optical modes on a photodiode produces a narrow linewidth electrical signal. In the optical domain those modes, when they are in phase, give rise to short optical pulses with a certain repetition rate f_{rep}.

In terms of mode filtering, the COEO works exactly like a dual loop oscillator, but one of the loop is purely optical (the ring laser).

In terms of working principle, a COEO uses the microwave signal generated on the photodiode to perform a self-phase lock loop on the ring laser [10].

Such configuration is not restricted to fibre ring lasers but can also be built with a semiconductor mode-locked laser [11].

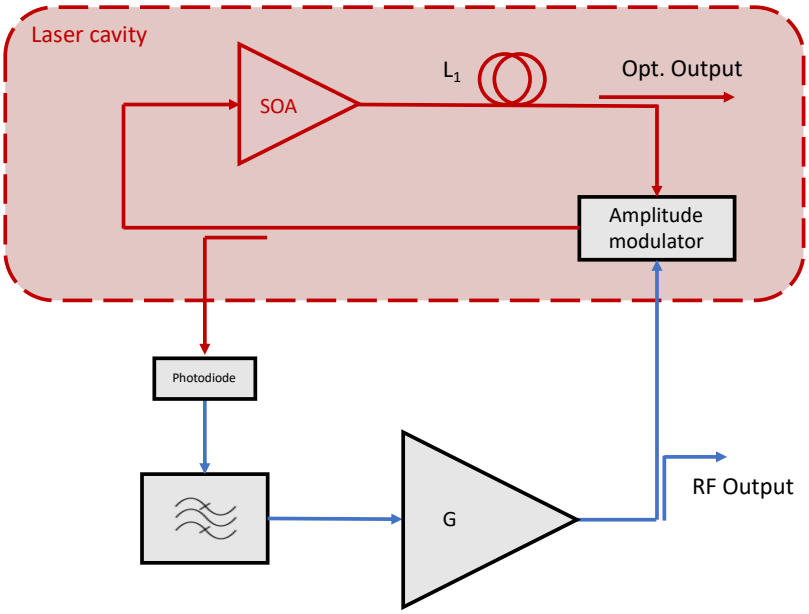

Figure 11. Architecture of a Coupled Optoelectronic Oscillator (COEO). The shaded red area is the ring laser cavity for the generation of optical pulses.

1.4.3 DUAL WAVELENGTH TUNEABLE OEO

The objective of an OEO is to create the purest and most stable RF signal as possible. On the other hand, the tunability of the output frequency is very low (few MHz) and is usually achieved by fibre stretching or phase shifters in the electrical domain. In order to overcome this limitation, two optical tones can be used to generate an RF signal by heterodyne mixing on a photodiode. The two optical tones can be independently generated by two lasers [12], or can share the same optical cavity [13].

The photodiode will detect the two continuous wave signals and their difference in the GHz range. Furthermore, a semiconductor laser's emitting wavelength can be easily tuned by current injection or heating, and even a small change in wavelength corresponds to a substantial frequency shift in the microwave domain.

It must be noticed that if the two laser sources have independent cavities, which is usually the case, their phase is uncorrelated, leading to an electrical beat signal linewidth that is roughly the sum of the optical linewidth of the lasers, depending on their nature. One way to reduce the electrical linewidth is to perform a phase correlation between the lasers by optical reinjection [14].

1.5 Opto-electronic oscillator architecture using photonic integrated circuits: state of the art

In the latest few years, the number of publications on integrated optoelectronic oscillator has seen an increase. Photonic integration technologies reached a sufficient maturity for demonstrators to be built.

A first attempt of generation of RF signals with integrated optics has been made by UCSB [15] where an integrated (Silicon Photonic) Mode-locked laser is used. The optical signal is converted to electrical domain by a commercial photodiode, filtered, amplified, and reinjected on the integrated saturable absorber.
The phase noise performances were not good enough (-3 dB linewidth of the tone of 14 kHz) for practical applications. Moreover, a narrower electrical filtering is needed to decrease the number of competing oscillations modes in the optical ring cavity. The limitations of this architecture were mainly coming from the losses in the silicon optical waveguides that limits the length of the ring optical cavity and, by means of consequence, the Q factor.

However, this proof of concept demonstrated that silicon photonics was a promising platform for photonic and electronic integration and volume production.

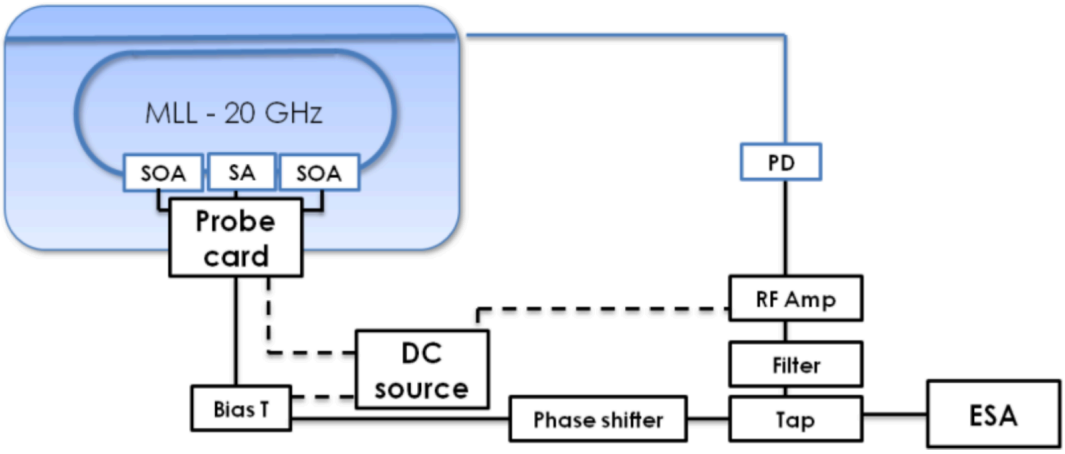

Figure 12. Block diagram of the integrated OEO in Ref [15, 16]. The ring laser in blue is integrated on a silicon-on-insulator with hybrid gain section integration.

Gunn et al. [17] used a different approach where the optical gain chip is external, while the photodiode, the modulator, and the RF front-end are integrated in a small footprint device. They obtained -112 dBc/Hz phase noise at 10 kHz offset for an OEO working at 10 GHz that is insufficient to be practically used, but they significantly improved the system compactness.

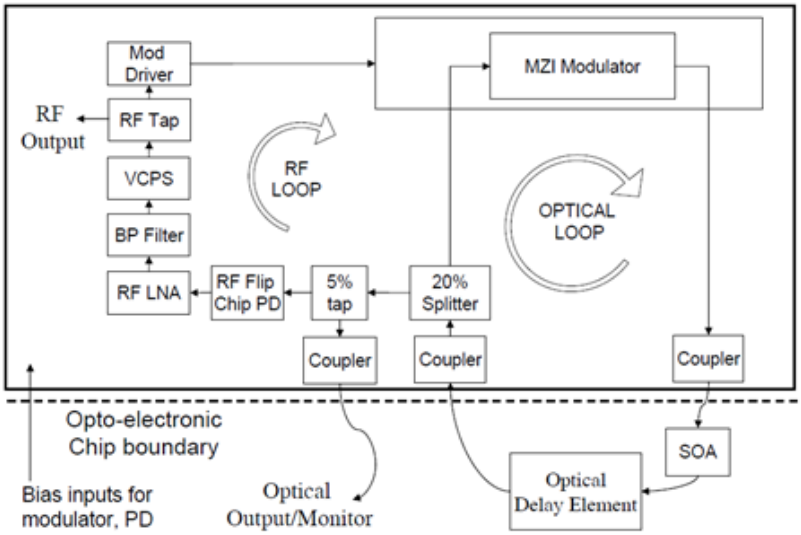

Figure 13. Block diagram of Ref [17]. Optical and electrical functions are integrated on a CMOS electro-optical platform.

Zhang et al. [18] integrated a phase modulator and a photodiode on a silicon photonic chip to be used in their OEO. The pump laser is external, but hybrid integration could be possible. The main interest of this technique is that it uses the combination of phase modulation and the filtering capability of a ring resonator in order to make the OEO tunable by changing the laser wavelength without the need of an external RF filter. But the phase noise is still high, higher than -90 dBc/Hz at 10 kHz offset for a 5 GHz signal generation.

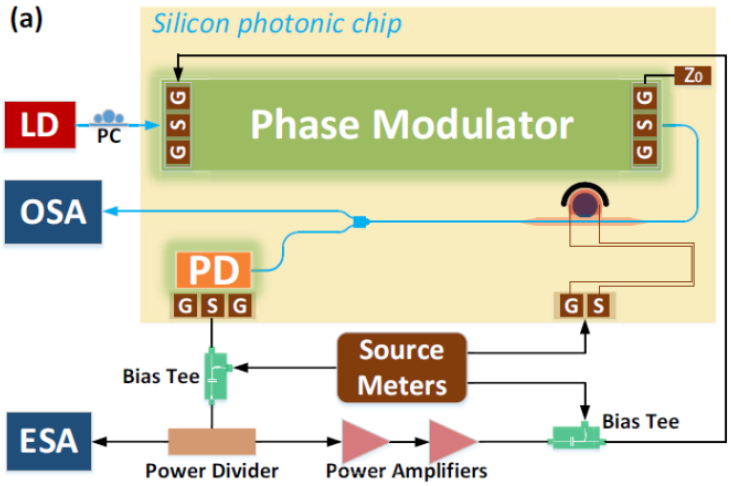

Figure 14. Working principle of the device described in [18]. LD: laser diode; PC: polarization controller; Z_0: matching impedance; PD: photodiode; OSA: Optical Spectrum Analyzer

An interesting example of photonic integration for frequency synthesis is demonstrated by Spencer et al. [19] in 2017. The frequency comb is generated with Silicon Nitride or silica ring resonators. The big advantage of this architecture is that it could result in very low phase noise using self-referencing techniques using optical frequency combs and comparing octave spaced tones. But this demonstration is far from a compact as it needs to fiber-interconnect chips made on different fabrication platforms.

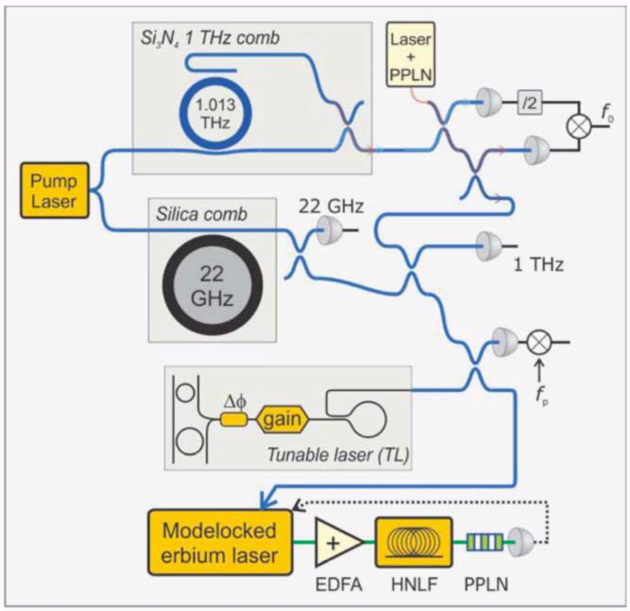

Figure 15. Chip Layout from Ref [19]. The system is a self-referenced frequency comb.

Ilchenko et al. demonstrated how powerful resonators can be for microwave filtering [20]. The work carried on at JPL on opto-electronic oscillators and Wispering Gallery Mode (WGM) silica resonators gave birth to the first commercially available miniaturized OEO from OEWaves [21].

It has to be noticed that the phase noise from datasheet is very low. The frequency of the measurements should be between 28 and 36 GHz. But this solution is using prism coupled high Q disk resonators that require and expensive packaging operation that is far from what could be done with a photonic integration.

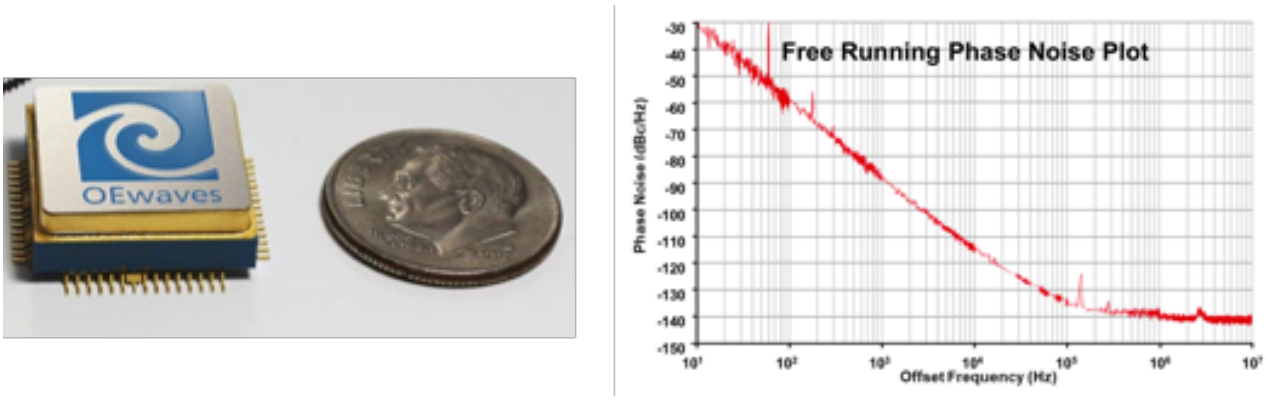

Figure 16. Left: OEwaves' NANO-OEO [20]. Right: phase noise measurement from the datasheet.

1.6 Compact Hybrid III-V/SiN OEO: architecture proposition

In this section I describe the approach of Hybrid Photonic Integrated Circuits for Microwave Photonic applications we intended to develop.

In this thesis the approach that will be followed for the integration of an Optoelectronic Oscillator is based on a hybrid Photonic Integrated circuit approach, where the active optical elements are integrated on a photonic platform on InP, whereas the microwave filtering is performed by resonator-based photonic circuit with SiN waveguides. The chosen reference architecture can be seen in Figure 17. The Indium Phosphide active chip contains a CW laser, an electro-absorption modulator (EAM), two optical amplifiers (SOAs) and a high-speed photodiode. Two optical ports allow the output and input coupling in the passive photonic chip.

The InP chips are fabricated using III-V Lab's integration platform for high speed devices, described in Chapter 3. The work in this thesis uses this integration technology as a generic platform, in which a first-generation demonstrator of such active chip can be built from basic building blocks. The measurements on those PICs are presented in Chapter 4. However, some limitations arose in such platform in terms of optical and electrical power handling. This led us to propose an improvement of such platform for Microwave Photonic-specific applications, where optical power and low noise are key parameters.

The passive PIC has the purpose of delaying and filter the optical signal by means of ring resonator-based architectures. Those two functions have a common requirement of low propagation losses, to allow meter-class on-chip delays and narrow filtering in the microwave domain. For this purpose, a low propagation losses platform has been developed in collaboration with CEA-LETI, part of III-V Lab. Silicon Nitride on Silica PICs have been fabricated on 200mm Silicon substrates in Grenoble, then diced, processed and measured in Palaiseau. Such platform will be the subject of Chapter 2. A state of the art of photonic integration platform is presented as well, in order to explain the choice of the SiN waveguides among others, and the subsequent waveguide and building blocks design.

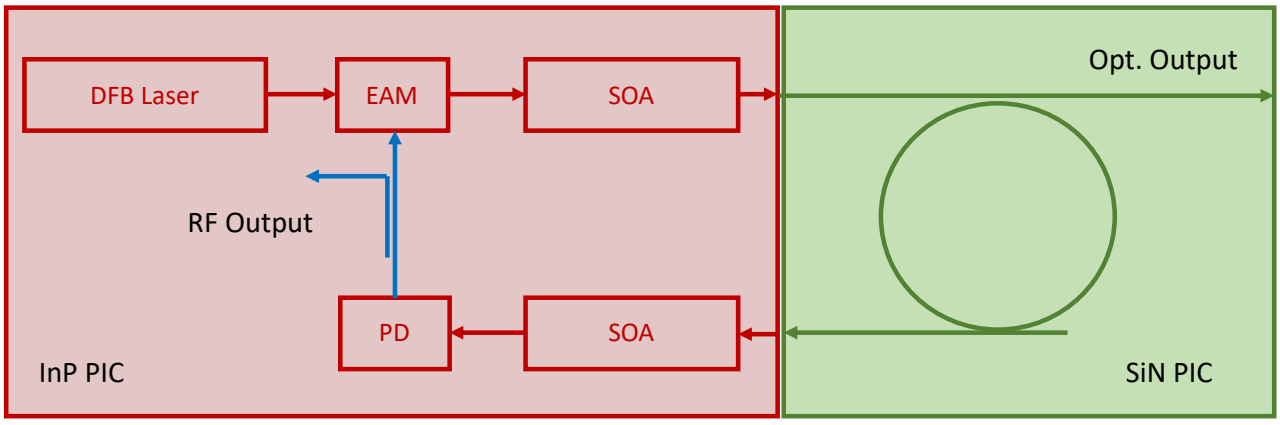

Figure 17. Proposed architecture of the Hybrid PIC for Optoelectronic Oscillator integration

2 LOW PROPAGATION LOSSES PLATFORM FOR MICROWAVE PHOTONIC APPLICATIONS

Integrated microwave photonics is the key technology for compact generation, processing and transport of high speed analog signals [22]***. This chapter reviews the available platforms for passive devices and their respective advantages and drawbacks. The design of a passive photonic integration platform with SiN/SiO_2 waveguides is presented; a strong emphasis is put on the ease of hybrid integration of these passive platforms with the InP active PIC.***

Optical fiber delays are one of the key elements of a microwave photonic system, especially for what concerns signal processing and transport. Optical fibres have extremely low propagation losses (0.2 dB/km at 1.5 μm, as seen in Figure 18) and a bandwidth of tens of terahertz for optically carried RF signals. The low loss parameter of fibres is what enables the creation of a long, high finesse optical cavity in classical optoelectronic oscillators experiments [1]. However, the typical cavity length for an OEO goes from 1 to several km of fibre. For classical, bulky OEO architectures such fibre length is not an issue. However, when all the active functions are integrated on a mm-size InP chip, the fibre coil is suddenly too encumbering to fit into a smaller package.

The primary objective of the passive photonic components studied in this thesis is to transpose low loss optical fibre capabilities into an integrated platform for microwave photonics applications. Propagation losses have a strong impact on the system performances for microwave photonics applications.

For example, the filtering properties of a ring resonator depend on the propagation losses of the waveguide the filter is built with. The finesse of a resonator measures the ratio between the width of the resonance peak and the resonator's free spectral range:

$$F = \frac{\mathrm{FWHM}}{\mathrm{FSR}}. \tag{18}$$

The filter needed for an optoelectronic oscillator is as narrow band as possible, to mimic both the response of a long fibre delay and of an RF filter at the desired oscillation frequency. A finesse of 50 for a 10 GHz ring resonator filter corresponds to a 200 MHz full width half maximum. By modelling the ring response, one finds that such finesse is reached with losses lower than 2 dB/m, as seen in Figure 19. The calculation was made with a custom MATLAB script, considering a 3mm radius SiN ring resonator, with a 10% coupling strength [23].

Values in Figure 19 set a target in terms of propagation losses for the passive platform to be chosen.

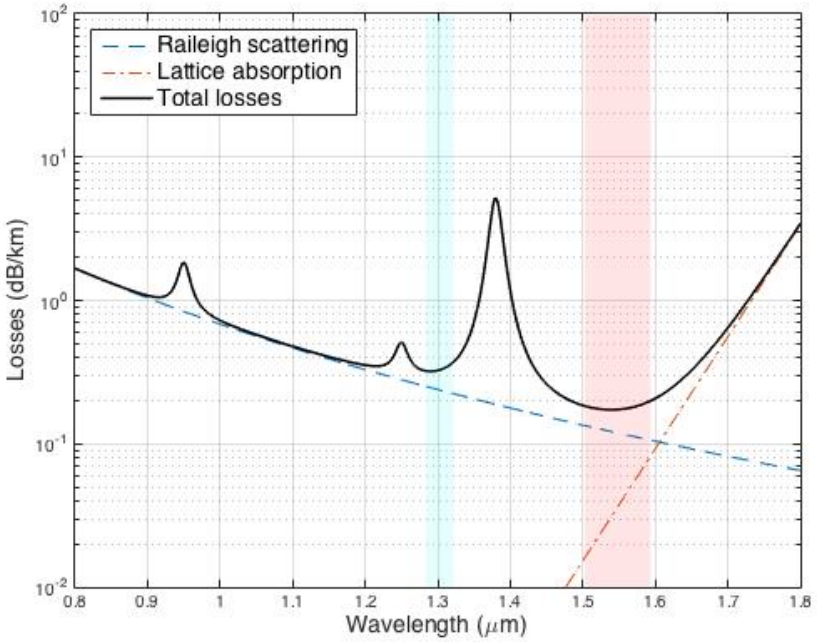

Figure 18. Simulated optical fiber losses depending on wavelength. O-band (1310nm) and C-band (1550 nm) are shaded in blue and red, respectively.

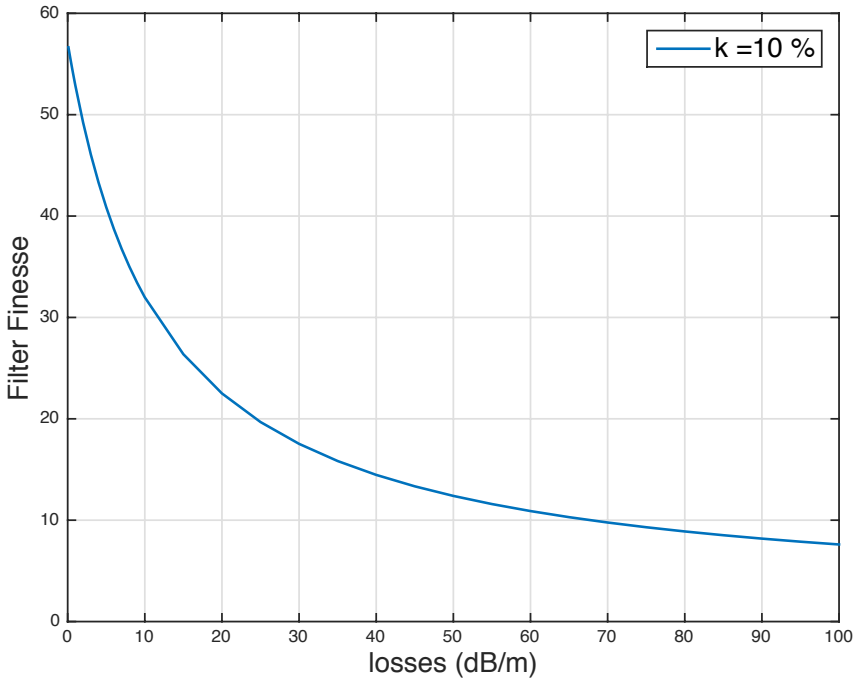

Figure 19. Filter finesse for a 3mm radius (10 GHz) Silicon nitride (n_{eff} = 1.47) ring resonator. Coupling factor is 10%. Propagation losses have a strong impact on the filtering properties of ring resonators.

2.1 LOSS PROCESSES IN OPTICAL WAVEGUIDES

This paragraph provides a brief description of loss mechanisms in optical waveguides, which provides useful pieces of information and a theoretical basis for the choice of the material system itself.

An optical signal propagating in a medium along an axis (z) undergoes an exponential decay in power described by the equation:

$$P(z) = P_0 e^{-\alpha z} \tag{19}$$

where P_0 is the reference power of the signal (for example, the power injected in a waveguide or optical fibre), and α is the attenuation factor of the material. In the above equation the attenuation factor is expressed in units inverse of a length [m^{-1}]. Throughout this chapter the losses will be expressed in units of [dB/m]. The unit conversion for this parameter is then defined as:

$$\alpha\ [dB/m] = a\ [m^{-1}] * 10 \log_{10} e \cong 4.34 * a\ [m^{-1}]. \tag{20}$$

The range of values this parameter covers is extremely large. Optical fibres have extremely low losses per unit length (0.2 dB/km, or 0.0002 dB/m), while integrated waveguides can range from around 1 dB/m to 100s of dB/m.

Among the causes of optical losses there are random defects of the material, physical properties of the material itself, and the optical mode – waveguide interaction.

2.1.1 RANDOM MATERIAL DEFECTS

The first source of optical losses can be identified in the point-wise defects of the crystalline structure of the material in which light is propagating: this process is known as Rayleigh scattering [24]. This process is found on both dielectric and semiconductor materials. The main feature of this process is its dependence on wavelength: Rayleigh scattering, shown in Figure 18, is proportional to λ^{-4}.

This scattering process is the least interesting in this dissertation since it is significant only at low wavelengths, namely the 0.8 to 1.1 μm region. Moreover, defects are randomly distributed in the material, so their reduction can only be addressed within the material deposition or growth process. High optical quality materials have the least possible defect concentration per unit volume.

Variations in quality between the core and cladding materials can make this process impactful, but only if a significant amount of optical power density interacts with the defect, which can happen in the two extreme cases:

- High material defect density in the near proximity of the waveguide: the number of defects is high enough to induce diffusion of low or medium optical power density signals propagating in the waveguide;

- Presence of few defects, but high optical power: this is the case for high Q silica microspheres, in which the optical power recirculates in the resonant structure yielding very high optical power concentrations; in this case, Rayleigh scattering and absorption are the ultimate limiting factors of such structures [25].

2.1.2 PHOTON-ASSISTED ELECTRONIC TRANSITIONS

The second source of absorption is the proper material absorption, linked to the physical properties of the material the waveguide is made of. A photon can be absorbed with two different processes: interband transitions and free carrier (intraband) absorption. At the wavelengths of interest, they are mainly found on semiconductor materials. The semiconductor case is the one we will consider mainly for our system.

In interband transition process the particles involved are a photon and an electron in the valence band. The photon is absorbed and the electron is promoted to a state in the conduction band; the energy and momentum must be conserved in the process, so the photon provides the energy difference between the starting and ending electron state; the photon itself, however, carries a very low momentum thus the transition is said to be "vertical" (no change in the electron wavenumber $\boldsymbol{k}$). This is the absorption mechanism that is typical of crystalline materials for photon energies close or above the the bandgap energy ($\boldsymbol{E_\gamma > E_g}$).

Two additional cases of interband absorption are worth mentioning:

- Two-photon absorption (TPA) process: in this process two photons are needed to provide the energy for the electronic transition from the valence to the conduction band ($\boldsymbol{2E_\gamma > E_g}$). This is a key process in silicon that has strong TPA in the 1550 nm band, limiting the power handling of silicon-based photonic circuits.
- Inter-valence band absorption (IVBA) process: in this process an electron from the spin-orbit (SO) valence band is excited and reaches a free state in the heavy holes (HH) or light holes (LH) valence bands, which are the ones usually considered in the study of direct bandgap semiconductor absorption processes. The IVBA, as every other electronic transition, needs the final electronic state to be free, thus this is the predominant loss mechanism in p-doped InP and related materials [26], reaching losses up to 20 cm^{-1}.

The free carrier absorption process involves an electron, a photon and one phonon. In a crystalline material, the electron must be already in an excited state, so it must move along the band (or scattered to a different conduction band). As before, the photon provides energy without momentum change; the phonon, on the other side, provides the momentum but carries very low energy. It must be noticed that the photon energies involved are much lower than those in the previous case [27].

In non-crystalline materials a similar process is observed: the absorption of a photon excites a vibrational mode of a molecular bond, in which two electrons are shared. It has to be noticed that nonstoichiometric impurities, such as residual hydrogen atoms incorporated during the deposition process of silica-based materials, can create dangling bonds which absorb light through an analogous physical process. Those absorption peak can have energies corresponding to photon wavelengths in

the energy range of interest [28]; high temperature annealing can partially solve this issue through diffusion and desorption of the excess hydrogen atoms.

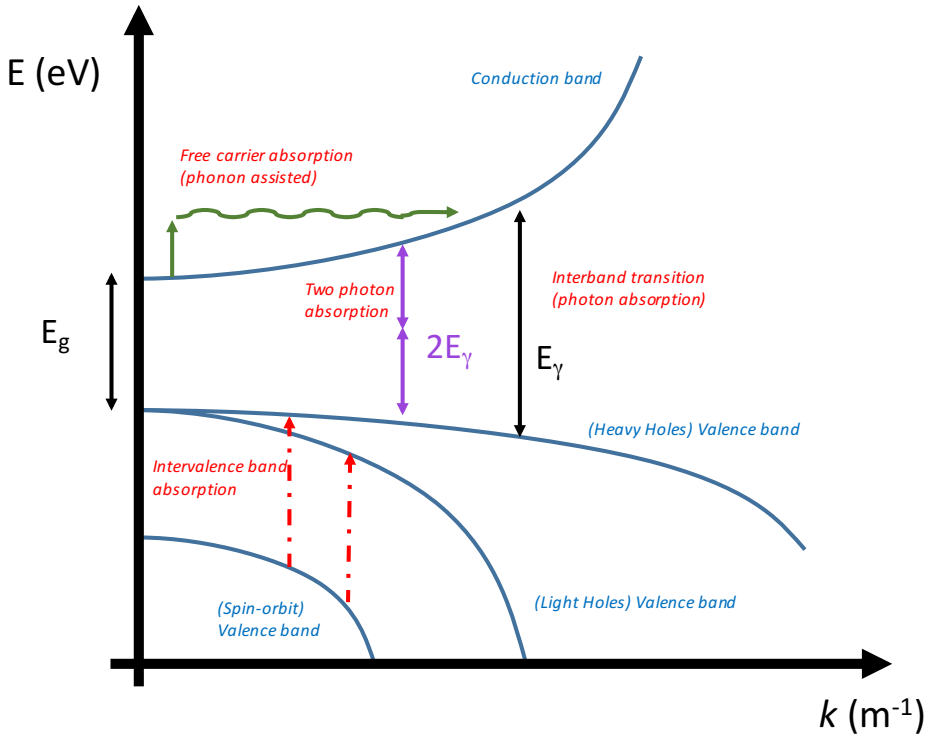

Figure 20. Band transition processes in a direct-gap semiconductor. Energy band names and transitions described throughout the chapter are specified in the figure.

2.1.3 SIDEWALL ROUGHNESS SCATTERING

The development of this paragraph is based on the model studied by Barwicz and Haus [29]***, describing how the coupling to the radiation modes is assisted by waveguide sidewall roughness.***

The problem of light loss in waveguide was studied in the literature to analyse the physical processes behind material absorption and point-wise defect scattering. One can imagine having a perfectly grown, defectless material to work with, and that the said material has been chosen wisely in order to have a negligible absorption at the wavelength range of interest.

At this point the design and material system choice of the waveguide start to have a meaningful impact and will determine the ultimate losses performances of said waveguide geometry and material system combination.

The model introduced by Barwicz and Haus [29] links the radiation efficiency of the leading-order mode of a waveguide towards the radiation modes in the environment.

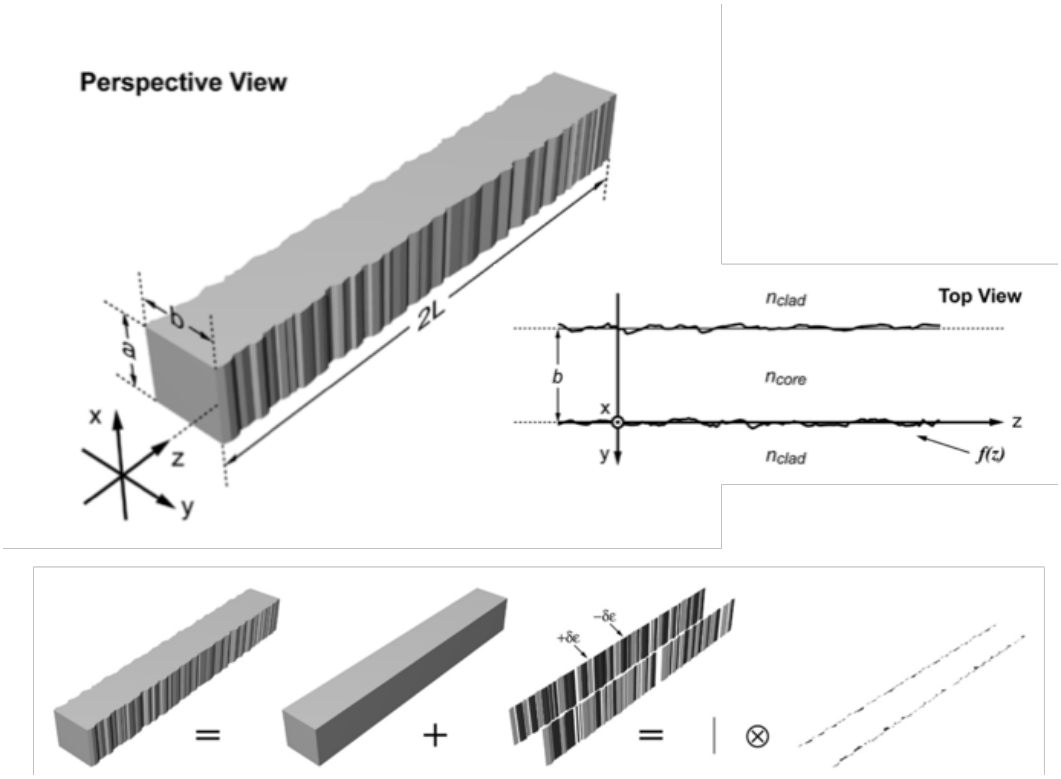

Figure 21. Top: Perspective and top view of a real waveguide with an arbitrary roughness profile. Bottom: decomposition of the same waveguide into a perfect waveguide and the corresponding roughness profile, that can be further reduced to a 1D profile. Elaborated from [29].

The channel waveguide is divided in a straight, perfect waveguide, and a superimposed roughness profile with zero mean value on the sidewalls (Figure 21). The autocorrelation function ***R(u)*** of the roughness profile ***f(z)*** of the waveguide is assumed to have a Gaussian profile:

$$R(u) = \langle f(z)f(z+u)\rangle \approx \sigma^2 \exp\left(-\frac{|u|}{L_c}\right). \tag{21}$$

where σ^2 is the roughness variance and $\boldsymbol{L_c}$ the correlation length. The spectral density of such profile is the Fourier transform of the autocorrelation function, transforming the spatial coordinate $\boldsymbol{u}$ into special frequencies ξ:

$$\tilde{R}(\xi) = \int_{-\infty}^{+\infty} R(u)\exp(i\xi u) = \frac{2\sigma^2 L_c}{1+L_c^2\xi^2}. \tag{22}$$

Only the roughness profile will generate a radiation pattern, since the eigenmode of the perfect waveguide has no coupling with the radiation modes.

The roughness profile is decomposed again into a roughness infinitesimal element and a roughness profile array. An important result of the mathematical treatment is that the (ensemble average) power spectral density <***F***> of the roughness array per unit length is:

$$< F > \propto \tilde{R}(\beta - n_{clad}k_0\cos\theta). \tag{23}$$

This is important in the measure that it shows that only modes with spatial frequencies that satisfy the inequality:

$$\beta - n_{clad}k_0 < \xi < \beta + n_{clad}k_0 \tag{24}$$

participate to the radiation losses. The difference $\beta - n_{clad}k_0 = (n_{eff} - n_{clad})k_0$ is larger for higher contrast waveguides, thus a large number of spatial modes participates to the radiation. Moreover, when calculating the complete radiation pattern, the polarization current density also depends on the refractive index difference between core and cladding, with a factor $n_{core}^2 - n_{clad}^2$ appearing in the equation for the total losses per unit length.

Figure 22 shows how the scattering losses increases when 3 different refractive index differences are considered (reprinted from [29]). The material system used in the simulation is silicon-based: the three materials used (Si, SiO_2, Si_3N_4) are standard materials used in CMOS-compatible fabrication processes.

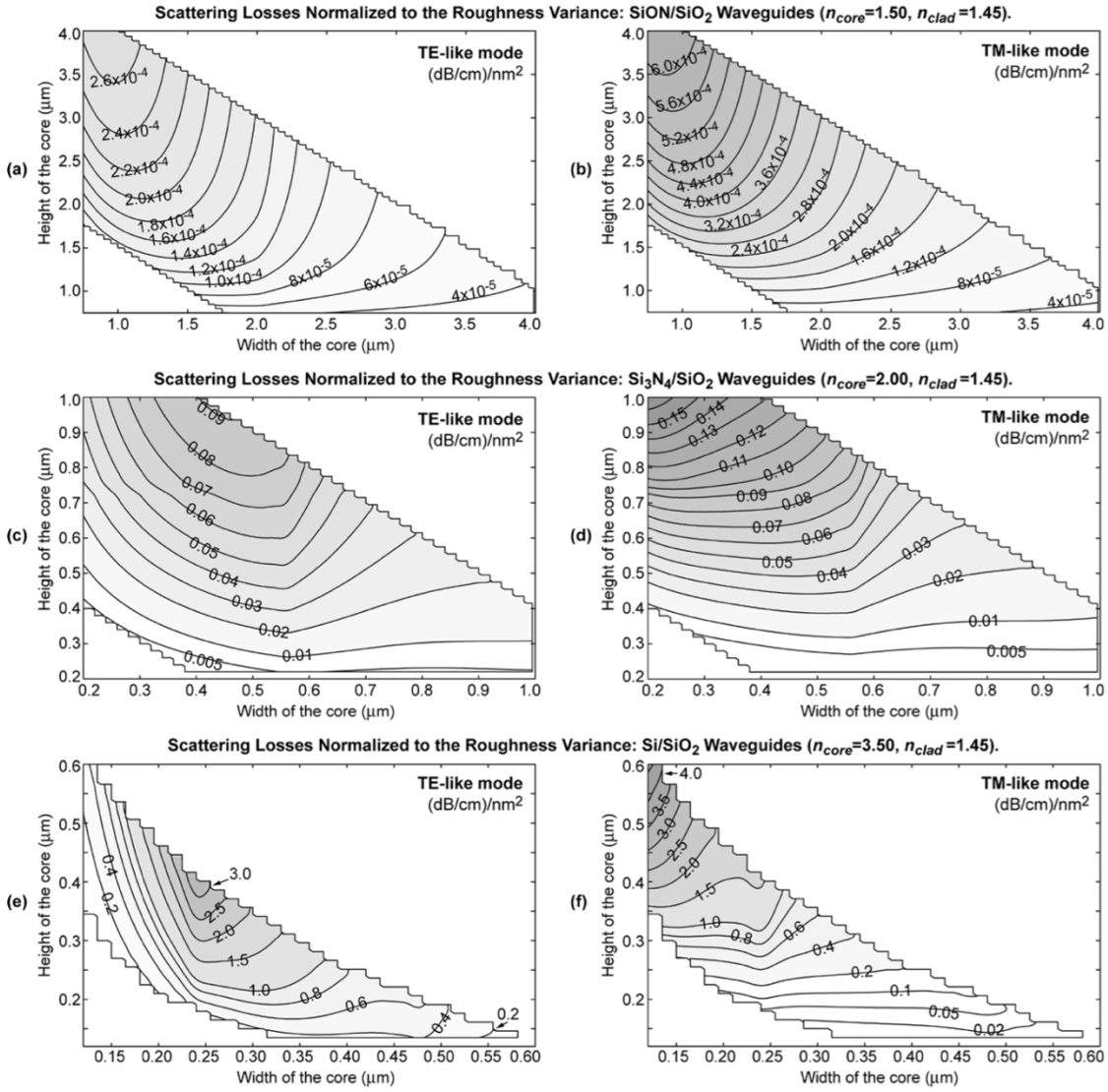

Figure 22. Simulated scattering losses for TE (a, c, e) and TM (b, d, f) modes for low contrast (a, b), moderate contrast (c, d) and high contrast (e, f) waveguides. The curves represent waveguide geometries with the same simulated losses (width and height of the core); the values are normalized to the roughness variance of the waveguide. Reprinted from [29].

The above mathematical treatment shows how the lower the index contrast between core and cladding in waveguides, the lower the losses coming from surface scattering. This justifies that, when one wants to fabricate low losses waveguides, low index contrast waveguides seem more suitable for the purpose.

2.2 COMPARISON OF MATERIAL SYSTEMS

In this section the different Photonic integration technologies will be reviewed, along with some other solutions that are not directly linked to integration but showed state-of-the-art performances in chip-scale microwave photonics, and will serve as a comparison for the performances of the integrated devices.

There exists a wide variety of platforms and material systems for photonic integration, as could be already seen in the previous paragraph. However, the choice of the Photonic integration platform is a key parameter in the design of the system, as different platform have of course strengths and weaknesses. The trade-off is made starting from the target system performances and extracting each building block's parameters from well-established physical models.

The figure of merit of losses is obviously the starting point for the choice of the material systems for the low losses platform. The second important desirable feature for such a platform is the easiness of integration with the active devices platform, for which we already chose an Indium Phosphide (InP) substrate, or with additional functionalities other than delay and filtering, such as nonlinear (harmonic) effects for comb generation or the integration of phase shifting sections. The different available options for the photonic passive circuits platform are listed below, and the integration aspect with InP is discussed for each one of them.

2.2.1 INDIUM PHOSPHIDE (INP)

The Indium Phosphide platform is the one of choice for the majority of the optoelectronic devices in near and mid-infrared applications, with two quaternary alloys (InGaAsP and InAlGaAs) with bandgap energies for direct emission between 1.2 μm and 1.7 μm and material refractive indices between 3.16 (InP) and 3.55 (InGaAs).

This material system enables monolithic integration of active and passive optoelectronic components. III-V Lab has already demonstrated a mm-wave tunable electrical signal generator, where lasers, amplifiers, modulators and high-speed UTC photodiodes were integrated along with passive MMIs couplers and waveguides [30].

Devices such as ring-based mode-locked lasers were built on the COBRA integration platform. An active section (two amplifiers and a saturable absorber) is integrated in the ring path; this device acts as an optical comb generator [16].

InP-based technologies can provide both high and low index contrast waveguides, depending on the material choice and the waveguide geometry. The biggest limitation for InP-based devices, at the wavelengths of interest, is the material absorption, coming from the physical processes described in 2.1.

The use of InP substrate as low loss platform is highly desirable due to the integration on the same substrate of all other devices. However, a 10 GHz ring on InP has a corresponding length of 1 cm; propagation losses of 30 dB/m would limit the finesse to around 10, as calculated by a custom MATLAB script [23]. The corresponding quality factor is 200000 for a coupling of 10%. Despite being useful for ring lasers, optical filtering and comb generation, ring resonators on InP are not yet capable of delivering the desired quality factor needed for RF filtering for integrated OEO applications.

The side view of the available passive waveguides in the InP integration platform are shown in Figure 23. Table 3 shows the waveguide properties of the selected references. The material of the waveguide core is often indicated with the corresponding photoluminescence (PL) emission wavelength, roughly corresponding to the energy bandgap.

Reference	***Guide type***	***Guide material (PL wavelength)***	***Guiding waveguide dimensions (μm²)***	***Losses (dB/m)***	***Notes***
D'Agostino [31]	Shallow ridge	InGaAsP (1.2μm) / InP	2*0.6 μm²	40	TE, Zn doping
	Deep ridge	InGaAsP (1.2μm) / InP	2*0.6 μm²	140 ± 20	TE, undoped
Lysevych [32]	Shallow ridge	InGaAsP (1.1μm) / InP	3*1 μm²	39	
Van Dijk [30]	Shallow ridge	InGaAsP (1.17μm) / InP	2.5 * 0.5 μm²	-	
Angenent [33]	Rib	InGaAsP (1.3μm) / InP	4.5*0.32 μm²	18	multimode

Table 3. References for InP-based waveguides and relevant waveguide parameters

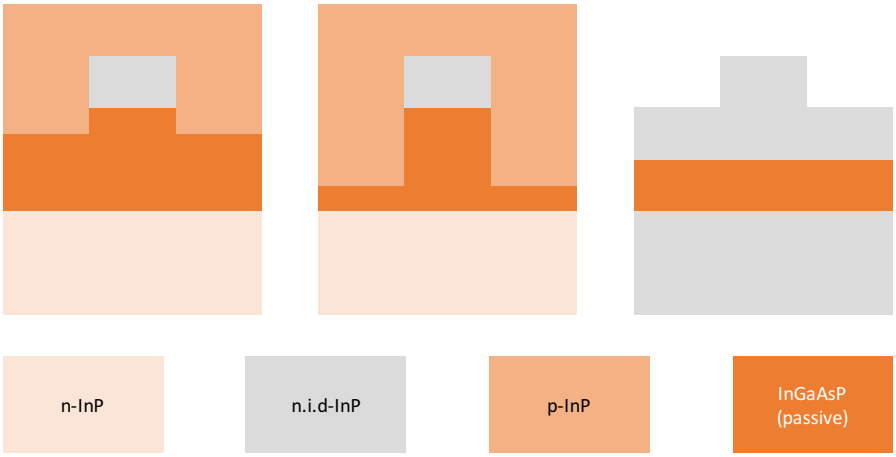

Figure 23. InP-based waveguides describer in the references from Table 3. Left and center: deep ridge waveguide. Right: shallow ridge waveguide. Bottom: color code for the different materials

2.2.2 Silicon on Insulator (SOI)

Research in silicon photonic rapidly increased in the last decade, since the first III-V on SOI laser were demonstrated [34, 35], [36]. This platform has a high potential in the telecommunications and on-chip interconnect areas. The main advantage of silicon photonics is the capability to merge on a single chip both electronic and photonic devices through CMOS-compatible optoelectronic fabrication. Many integration techniques are available, depending on the user's need and application [37].

Silicon-on-Insulator waveguide technology belongs to the high index contrast waveguide class. The core of the waveguide is made of silicon ($n_{Si} = 3.48$) and the geometry of the waveguide can be engineered to reach lower losses operation. Waveguides with rib geometry [38] have lower losses than rectangular [39] or ridge waveguides [40], similarly to InP-based waveguides, due to the lower effective index contrast and lower overlap with the edges of waveguides. The high index contrast allows compacity and high integration density capabilities.

This platform is however limited by the intrinsic properties of Silicon. First of all, the presence of two photons absorption processes described in 2.1 limit the power handling capabilities of the waveguides. Due to the high index contrast between the core and cladding materials the optical power is highly confined in the silicon layers, thus the power density is significant, and the nonlinear effects increase in magnitude with increasing optical power density.

The properties of the waveguides for a selection of reference papers are given in Table 4. A cut view of the different Silicon waveguide geometries is shown in Figure 24.

Reference	*Guide type*	*Guiding waveguide dimensions (μm²)*	*Losses (dB/m)*	*Notes (minimum bending radius when available)*
Biberman [38]	rib	2.05*(0.22 + 1)	2.7	2.45 mm radius ring resonator
Gardes [41]	rib-like	1.5 *(0.17+0.6)	21	
Vlasov [42]	strip	0.5*0.2	36	5 μm bending radius

Table 4. References for Silicon-On-Insulator waveguides and relevant waveguide properties.

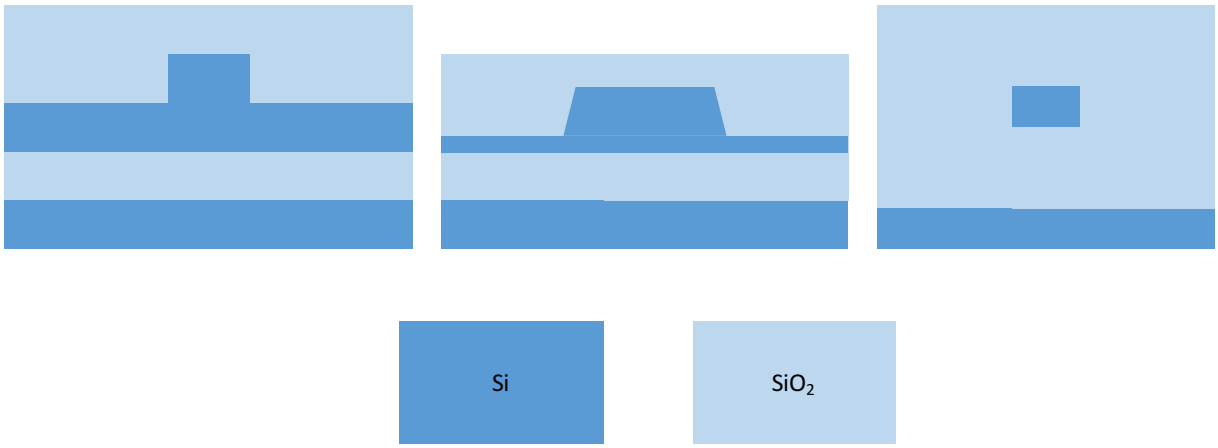

Figure 24. Representation of silicon-On-Insulator waveguides of the references discussed throughout the paragraph. Left: rib waveguide. Center: rib-like waveguide. Right: strip waveguide. Bottom: color code for the different materials

2.2.3 SILICA-BASED TECHNOLOGIES

Silica is one of the most widely used materials in optics. Optical fibres, planar lightwave circuits and other devices like microspheres can be built on silica.

Silica-on-silica platforms, also called Planar Lightwave Circuits (PLC) were among the first to be fabricated and studied. The waveguide is usually made of doped silica, which gives a varying index contrast from 0.75% to 4%, depending on doping level. Higher index contrast reduces the footprint of devices but increases propagation losses and fibre to chip coupling losses due to the smaller core size and the smaller mode diameter. Adar et al. [35] reported losses of 2.6 dB/m in phosphorus doped silica waveguides.

More recently, Lee et al. [43] reported losses of 0.08 dB/m in suspended SiO_2 waveguides, for on-chip delay lines. Due to the waveguide geometry, however, this technology is difficult to use for photonic integrated circuits, as it is not easy to define a set of building blocks (e.g. couplers and splitters) to build complex circuits.

The last technology presented in this paragraph is whispering gallery modes resonators. It cannot be considered as a photonic integration solution but enables performances that are worth mentioning. Ilchenko et al. reported silica microspheres with quality factors higher than 10^9 [44] [25] for compact optical microwave filtering. Optical coupling with these resonators was too complex to get compact integration but this research gave birth to the first chip-size OEO based on polished edge disk cavities [20]. It has to be noticed that, besides silica, other materials have been used to build similar resonant structures: toroids and disks have been fabricated on CaF and MgF [45].

The relevant reference works and their waveguide properties are summarized in Table 5. A cut view of the waveguide geometries is shown in Figure 25.

Reference	***Guide type***	***Dimensions***	***Losses (dB/m)***	***Notes***
Adar [35]	Channel waveguide	5*5 µm²	2.6	Index contrast 2%; 3cm radius ring resonators
Lee [43]	Suspended waveguide	8*10 µm²	0.08	SiO_2/air
Ilchenko [25]	Silica microsphere	100-500 µm (radius)		$Q > 10^9$
Sedlmeir [45]	MgF_2 microdisk	1.19 mm (radius)		$Q > 7*10^8$

Table 5. References for Silica-based technologies and waveguides.

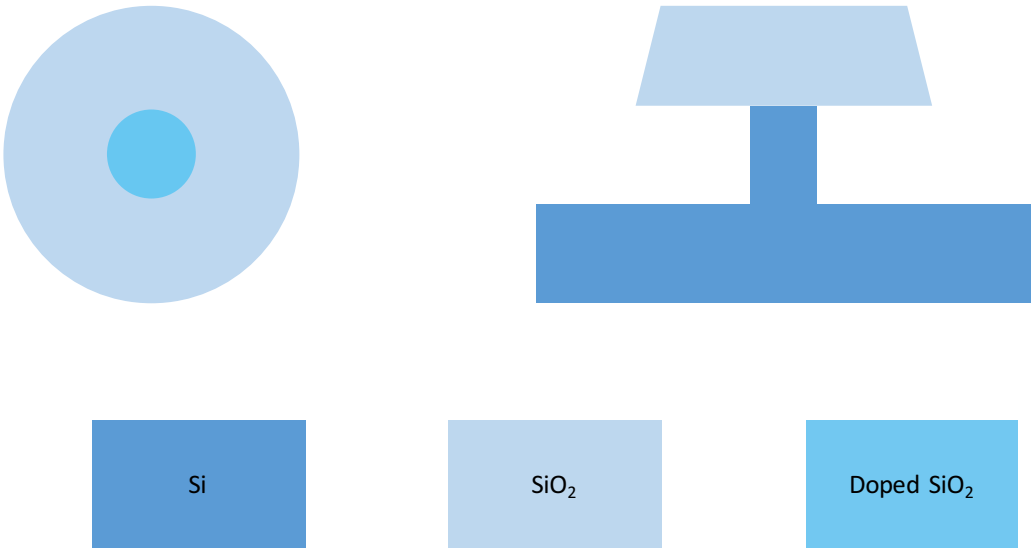

Figure 25. Silica-based waveguides described throughout the paragraph. Left: channel waveguide. Right: suspended silica waveguide on silicon pillar. Bottom: color code for the different materials

2.2.4 SILICON NITRIDE (SIN)

Silicon Nitride waveguides, using stoichiometric Si_3N_4 or not stoichiometric Si_xN_y, have a lot of potential due to their large transparency region, going from visible to mid-infrared wavelengths (< 1 μm to 5 μm) [46] and a refractive index that is significantly higher than silica, so the latter can be used as a waveguide cladding material.

Silicon Nitride-based technologies gained popularity due to the versatility of the material, providing either low losses or highly nonlinear waveguides. The difference between the two technologies lies in the geometry of the waveguides and the overlap of the resulting optical mode with the silicon nitride core.

Waveguides for nonlinear applications need a relatively thick silicon nitride layer in order to increase the optical confinement within the material, enhancing the nonlinear effects of the ensemble through the high density of optical power in the core. Many defects can be created during the growth of such thick layers due to the high tensile strain induced by the silicon nitride on silicon substrates. Growth and annealing cycles increase the quality of the material and avoid cracking on the surface when the thickness is greater than 400 nm [47].

Just for comparison, silicon nitride has a nonlinear Kerr coefficient n_2 of $2.6*10^{-19}$ m^2/W while crystalline silicon has a Kerr coefficient of $4*10^{-18}$ m^2/W. In the telecom wavelength region, however, silicon has a high two-photon absorption coefficient, while SiN has no TPA due to the higher bandgap energy.

Silicon nitride waveguides needs a bit of engineering to achieve anomalous group velocity dispersion (GVD) at the wavelength of interest, namely thick layers (>400 nm), and usually multi-mode waveguides.

When the waveguide is made thin (of the order of 100 nm), the overlap of the optical mode with the waveguide sidewalls is greatly reduced, as the size of optical mode is increased. This will in turn reduce the optical losses due to scattering on the sidewalls. The result is a high aspect ratio (HAR) waveguide.

Reference	***Guide type***	***Guiding waveguide dimensions (μm²)***	***Losses (dB/m)***	***Notes (bending radius)***
Mao [48]	channel	700x400 nm	210	
Bauters [49]	HAR	40 nm thick	0.1	
Luke [50]	channel	910x1800nm	4.2	

Table 6. References for SiN-based waveguides.

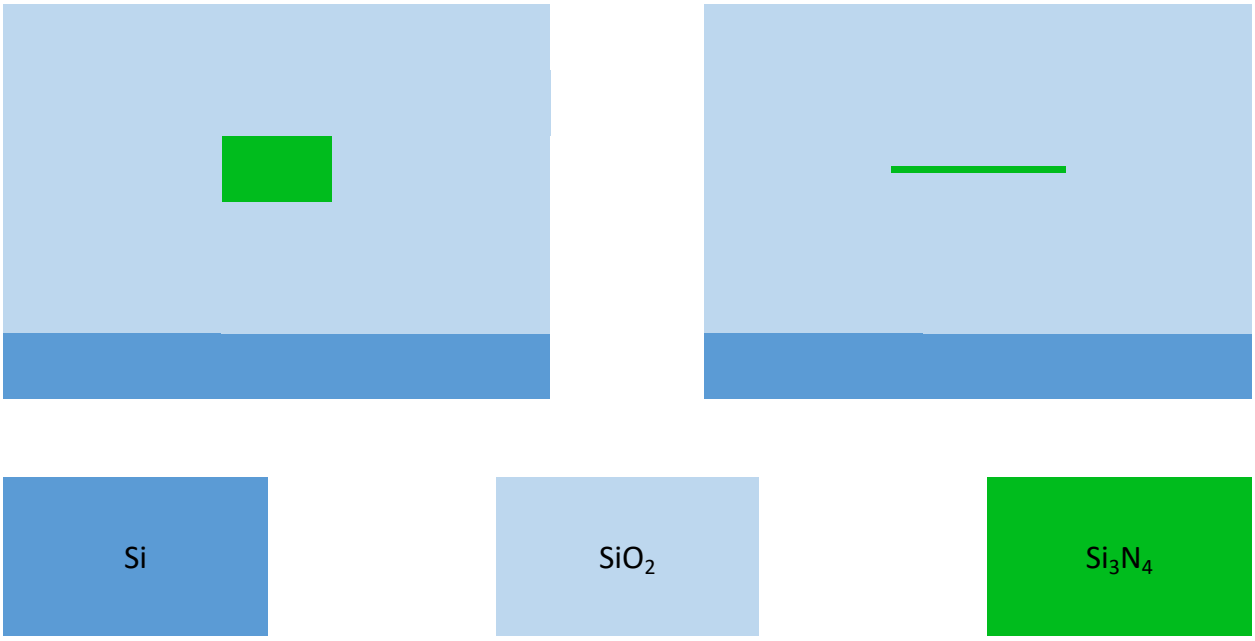

Figure 26. Silicon nitride waveguides. Left: channel waveguide. Right: high aspect ratio waveguide.

2.2.5 CHOICE OF THE WAVEGUIDE

After the review of the available technologies at the time of the beginning of my research, the choice of the waveguide material is a matter of compromise among the various parameters that must be considered. These parameters are listed in Table 7 to compare the advantages and drawbacks of each technology.

Propagation losses remain the key parameter to be addressed in order to have good filtering properties. Silica and SiN are the best platforms to work with in this scenario. The idea behind integration, however, is also to decrease the chip size in order to increase the density of devices per unit area. The footprint of the circuit strongly depends on the refractive index difference, thus an intermediate material like SiN looks more promising than silica technology.

Following the thought process throughout all section 2.2, we chose to work with stoichiometric, high aspect ratio silicon nitride waveguides.

Parameter	***InP***	***Silica PLC***	***SiN/SiO2***	***SOI***	***MgF_2/CaF_2***
Propagation losses	– –	+++	++	+	+++
Footprint	++	–	+	+++	–
Integration techniques with InP	***Monolithic***	***Edge coupling (hybrid)***	***Edge coupling (hybrid)***	***Edge coupling (hybrid) III-V on Si (heterogeneous)***	***Angled facets fibers; PIC interposers***

Table 7. Comparison between photonic integration technologies and their compatibility with InP material system

2.3 LOW LOSS SiN PLATFORM

This section is the description of the waveguide design process to achieve low propagation losses operation.

The development of a low loss passive platform is one of the two main objectives of this thesis, the other being the evaluation of InP PICs for microwave photonics applications.

The previous paragraph gave details of waveguide losses processes and a review of the state of the art of available waveguide technologies. We chose to work with SiN waveguides to meet the target propagation losses.

The refractive index of silicon nitride is intermediate between the one of silicon (3.48) and silica (1.45). The refractive index of stoichiometric SiN was measured by ellipsometry at Leti in Grenoble, where the wafers are produced, and is shown in Figure 27. A value of 1.9804 at 1550 nm was considered for the simulation and design purposes.

The imaginary part of the refractive index ***k*** was also measured at the same time. However, the value was well below the sensitivity of the instrument, so the measurement reading was identically zero for all wavelength values.

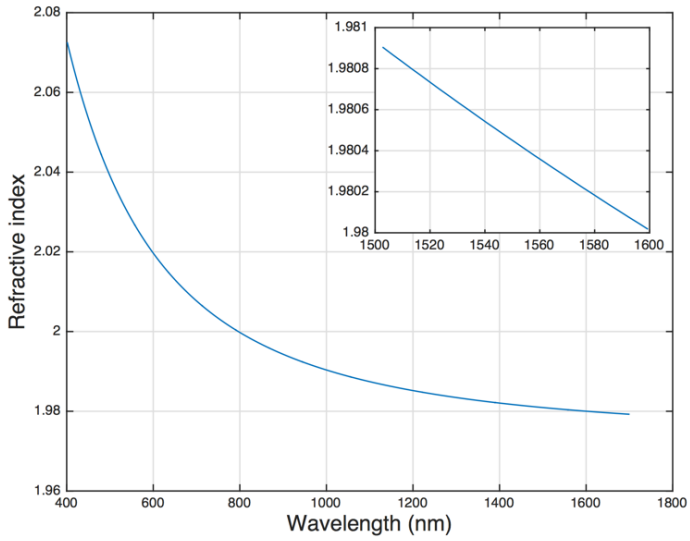

Figure 27. Refractive index of stoechiometric SiN measured at CEA-Leti on a calibration wafer. The inset shows the detail around 1550 nm

Following the development of [49], the geometry is restricted to rectangular waveguides with high aspect ratio between width and the thickness. Despite being simple, this geometry allows us to tailor the two parameters we are interested in, propagation losses and chip size, by simply changing the thickness of the core layer.

Since the propagation losses depend on the overlap of the optical mode with the edges of the waveguide (Figure 28), losses will increase with waveguide thickness, and surface and sidewall roughness. The parameters to be optimised, being losses and bending radius, change in opposite ways when the waveguide thickness is changed, so a compromise is needed.

The thickness of the waveguide layer can be controlled by the deposition method or by polishing (chemically, mechanically or both) the wafer. The variation in thickness should be limited to few nanometers throughout the whole surface of the wafer.

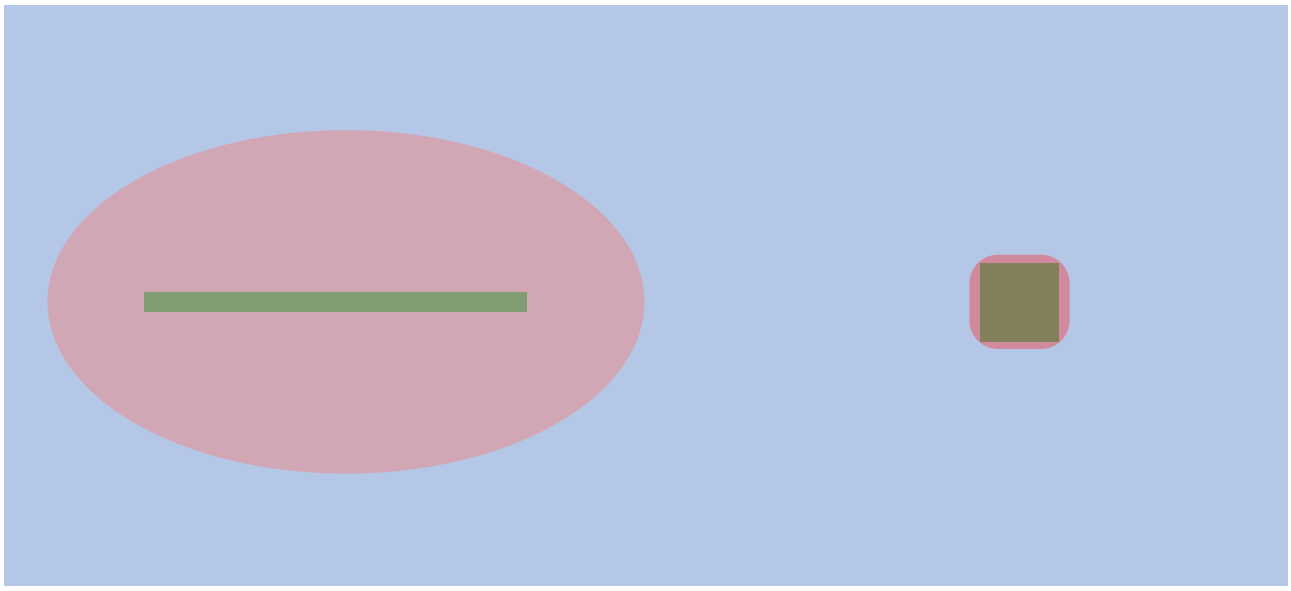

Figure 28. Comparison between low confinement (left) and high confinement (right) SiN waveguides and the respective optical mode overlap.

2.3.1 IMPACT OF WAVEGUIDE DESIGN ON PROPAGATION LOSSES

This paragraph shows the design process of the Silicon Nitride waveguides, needed to build the building blocks and integrated circuits described in the following one.

Section 1 of this chapter described the general mathematical treatment of losses in optical waveguides, where the main parameter was the index contrast of core and cladding.

The study is now restricted to a material system (SiN on SiO_2) and a waveguide with rectangular geometry. Barwicz [29] showed how losses decrease when the core height is reduced. The numerical values in Figure 29, where only the SiN/SiO2 waveguide computation is shown, are normalised to the variance of the roughness σ. With a hypothetical σ of 10 nm, one can see that losses of 0.5 dB/cm (50 dB/m) are expected when the core of the waveguide has a thickness around 200 nm, thus the core thickness must be further reduced to follow the clear trend of reduced losses with reduced core height.

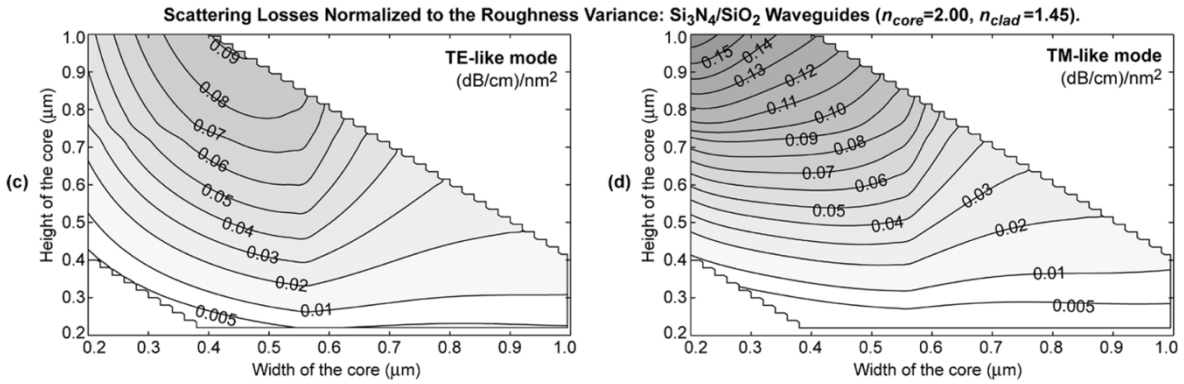

Figure 29. Numerical computation of losses of SiN on SiO2 waveguides for the estimation of the propagation losses. Reprinted from [29].

The roughness in the horizontal plane is set by the deposition technique and the initial flatness of the lower cladding layer, thus great care must be taken when considering the initial wafer flatness and the deposition technique uniformity. The roughness variance of sidewalls and top/bottom walls, however, are governed by different processes: the sidewalls are defined by an etching process and strongly depend on how the process is performed.

It is convenient to separate the scattering losses contributions for surface and sidewalls, each with their corresponding mean square roughness [51], in order to evaluate the total scattering losses:

$$\alpha = \sigma^2_{\text{sidewall}} \Pi_{sidewall} + \sigma^2_{\text{surface}} \Pi_{surface} \qquad (25)$$

where α is the scattering losses, Π are the scattering losses for a given interface in units of dB/m/(nm^2) and σ are the roughness variances for a given surface. Values for different core thicknesses and width have been simulated by Bauters [49]. Figure 30 (reprinted from [49]) shows that the impact of the two surface scattering contributions differs by order of magnitudes, so thickness homogeneity on the wafer should have the foremost attention during the waveguide fabrication process. Techniques such as chemical-mechanical polishing (CMP) increase the surface uniformity and improve the overall losses performances.

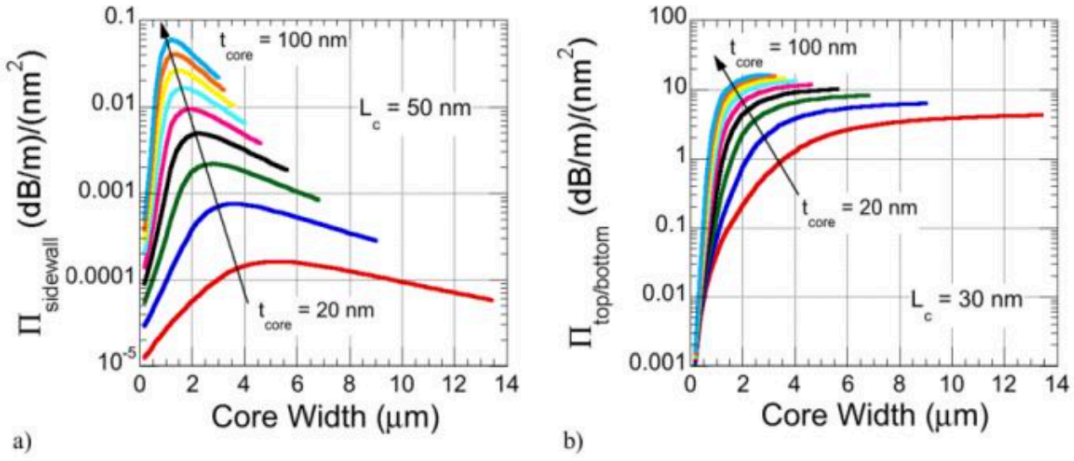

Figure 30. Simulated sidewall scattering parameters for core thicknesses ranging from 20 to 100 nm. Left: sidewall scattering parameter (with $\boldsymbol{L_C}$ = 50 nm) Right: surface scattering parameter (with $\boldsymbol{L_C}$ = 30 nm). Reprinted from [49].

From the parameters extracted from [49], a best-case and a worst-case scenario are estimated. The best-case scenario is supposed to have 0.5 nm of surface and 10 nm of sidewall roughness, whereas the values are increased to 2 nm and 20 nm, respectively, for the worst case. The expected range for scattering losses is shown in Figure 31, for core thickness from 70 to 100 nm.

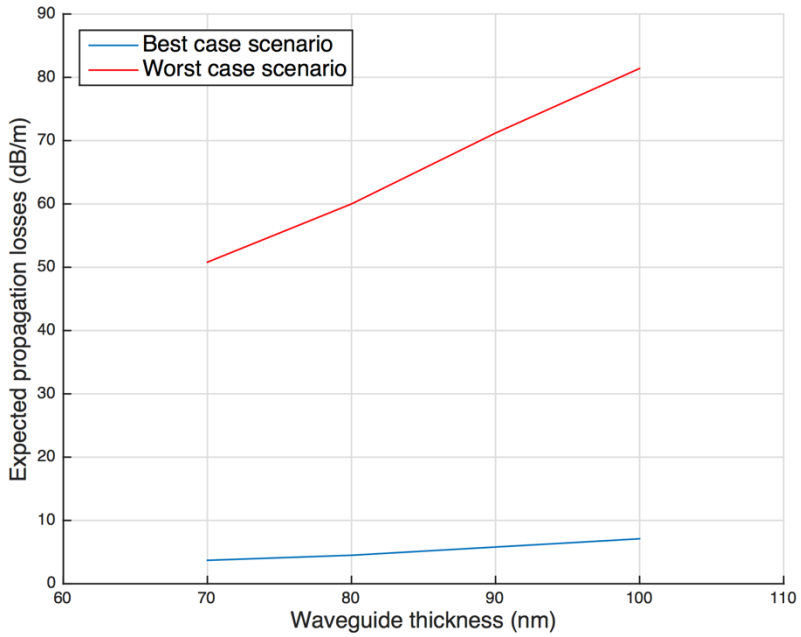

Figure 31. Computed simulation losses for a best-case and worst-case scenario based on technological process capabilities in our foundry.

The core thicknesses considered in this graph are voluntarily higher when compared to the 50 nm thick cores [52] which resulted in losses of 0.7 dB/m. The reason is that a thin core would lead to a higher critical bend radius due to the reduced confinement and that would be impractical to build the circuits needed for this thesis with a reasonable footprint.

Up to now, all parameters were considered to be wavelength-independent, and the interaction between different atomic species has been neglected. In optical fibres the involuntary introduction of hydrogen atoms during fabrication leads to formation of OH- ions which have absorption peaks in the near infrared. Those absorption peaks can be clearly seen in Figure 18 and led to the standardisation of the optical communication technologies to circumvent these absorptions regions, hence the 1300 nm (O) and 1550 nm (C) bands.

A phenomenon analogous to the previous one is found in SiN-based waveguides: the involuntary introduction of hydrogen atoms leads to N-H bonds that have transition energies inside the O and C bands. This is the reason why silicon nitride waveguides show higher losses between 1520 and 1580 nm [28], as shown in Figure 32.

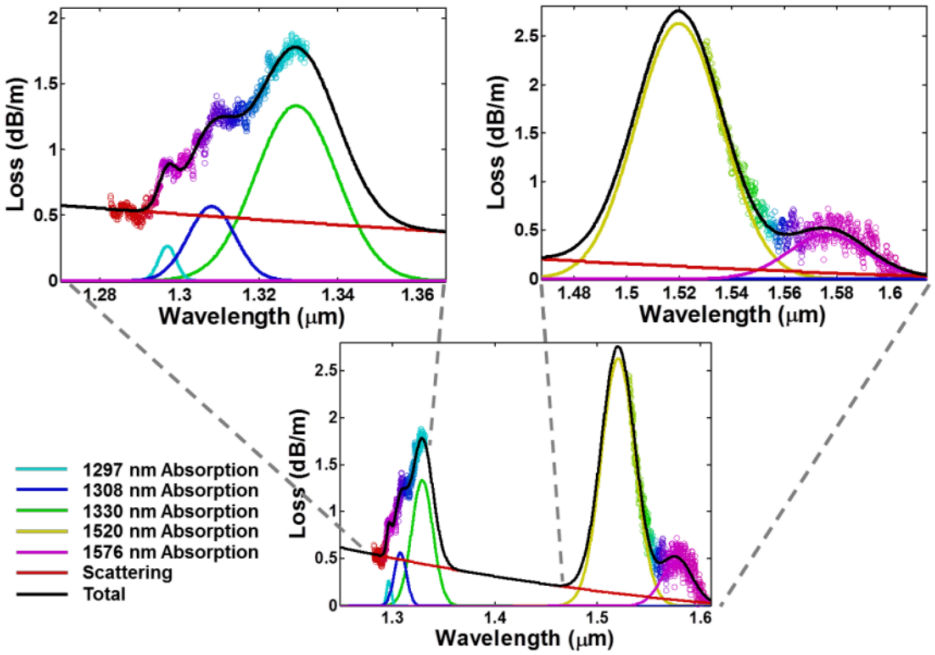

Figure 32. Measurements of the N-H parasitic absorption peaks in O and C band, a primary loss factor for SiN waveguides. Reprinted from [28].

2.3.2 SINGLE-MODE WAVEGUIDE DESIGN

The first action to be performed is the study of the eigenmodes of the waveguide. A waveguide supporting only one mode is often preferable, since the coupling between eigenmodes can lead to losses during propagation in a PIC. Indeed, in this case part of the light is not available as it is coupled to an unwanted optical mode.

The objective of this paragraph is to go into the details of the waveguide design process, analysing the available parameters and their impact on the waveguide behaviour. The tolerance of this behaviour to a variation of the cladding refractive index and to waveguide bending is also taken into account.

Important parameters in the waveguide design process are the refractive indices of the materials and the geometry and dimensions of the waveguide. The refractive index is an intrinsic property of the material (although it may vary slightly following the fabrication technique). The waveguide geometry and dimensions, on the other hand, can be chosen to engineer the waveguide properties, such as single-mode behaviour, polarisation-dependent effective refractive indices and losses, specific dispersion, minimum bending losses, etc.

When considering the case of a rectangular waveguide, with core index n_{core}, surrounded by a cladding with index n_{clad}, a pratical condition for single mode operation is that there is one and only one mode with an effective refractive index higher than n_{clad}. Since the only parameter that can be changed on the waveguide is the width, once that the thickness of the material has been chosen, a simulation of the effective refractive index of several modes in function of the width is performed on FIMMWAVE.

In practice, only the first two TE modes (TE_{00} and TE_{01}) and the first TM mode (TM_{00}) are needed for the simulation.

Figure 33 shows such simulation for a 90 nm thick waveguide. The TE_{01} mode can be excited from width larger than 3 μm. The TM_{00} mode is not excited if the gain medium output mode is quasi-exclusively TE, as in the active devices we are using.

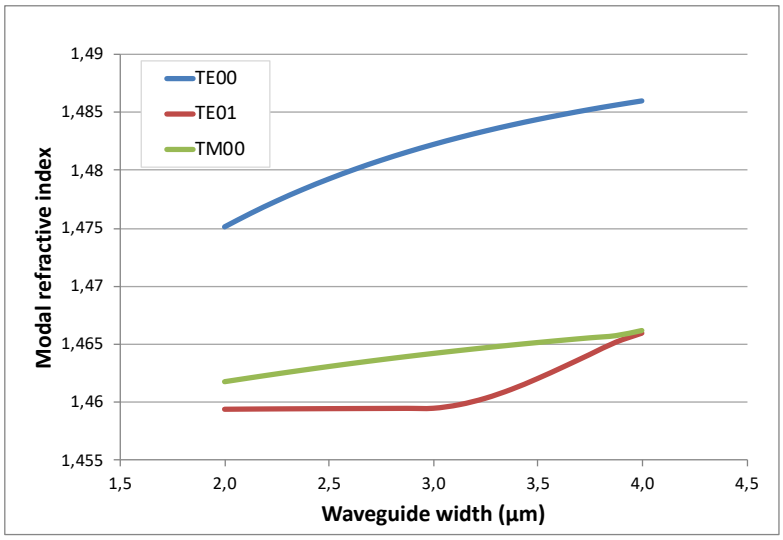

Figure 33. Simulation of effective refractive indices of the two first TE (TE_{00}, TE_{01}) modes and the first TM (TM_{00}) mode of a 90nm thick waveguide. The single mode cut-off width is below 3 μm. Silica index is 1.46.

The cut-off width for the single-mode operation region depends on the n_{clad} value as well. As stated previously, the refractive index of a material may vary with respect to deposition or growth conditions. The refractive index of silica is well known, but the nature of the silica used as cladding material was not known at the time of these simulations. For example, thermally grown silicon oxide is denser than CVD-deposited oxide, resulting in a higher refractive index. Both materials were good candidates for cladding material, the former due to the extremely high material quality due to the CMOS-like thermal oxidation process, the latter due to the simplicity and versatility of the growth process. The design needs to be robust with respect to the cladding refractive index parameter, in order to allow flexibility on the choice of the cladding material.

Figure 34 shows how for a range from 1.44 to 1.46 of the refractive index of the Silica cladding the design must take into account for 200 nm of variation of the single mode cut-off width.

For each SiN thickness in the range of interest, the single-mode cut-off found with the bent waveguide simulation is plotted in Figure 35. A conservative approach is used: the nominal width of the waveguide for design will be chosen a couple of hundreds nanometers below the presented values. This also takes into account the contribution of bent waveguide propagation, which will be presented in the next paragraph.

Figure 36 shows the simulated SiN on SiO_2 waveguide. This waveguide has a thickness of 90 nm and a width of 3 μm.

It can be seen that the optical mode is strongly asymmetrical in the two directions (note the two different space scales in the mode profiles). This result comes from the very weak confinement in the vertical direction due to the thin core. The thin core also results in a non-gaussian mode profile, in which the mode exponentially decays into the cladding. It must be noticed that thick oxides claddings are needed in order to avoid coupling to the substrate.

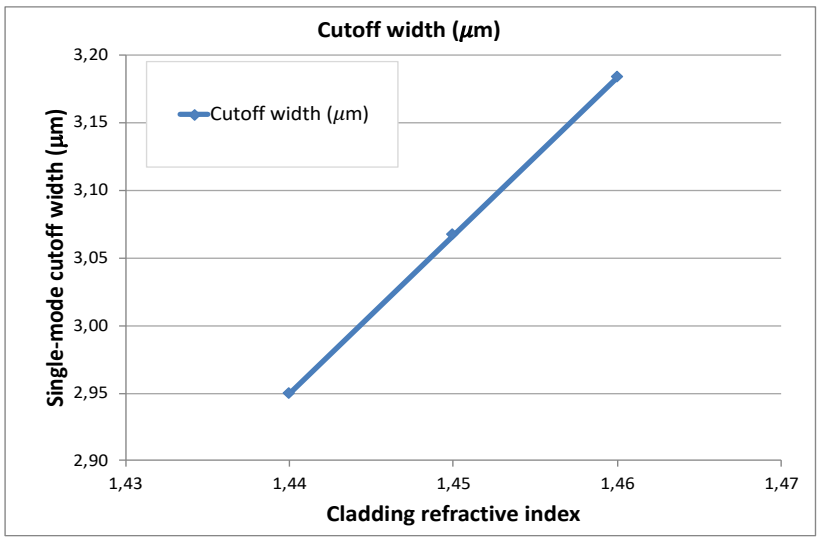

Figure 34. Single mode waveguide cut-off width for 90 nm thick waveguide for different values of the cladding refractive index

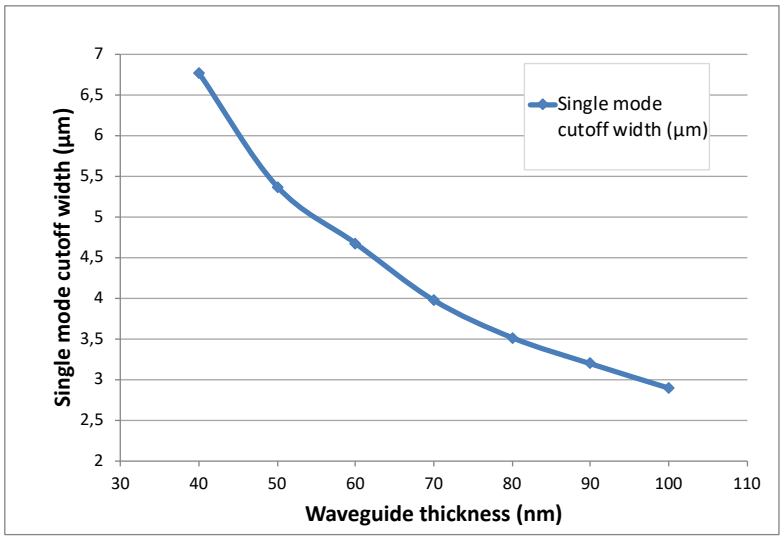

Figure 35. Single mode cut-off width for various core thicknesses, with a conservative cladding index n_{clad}=1.46.

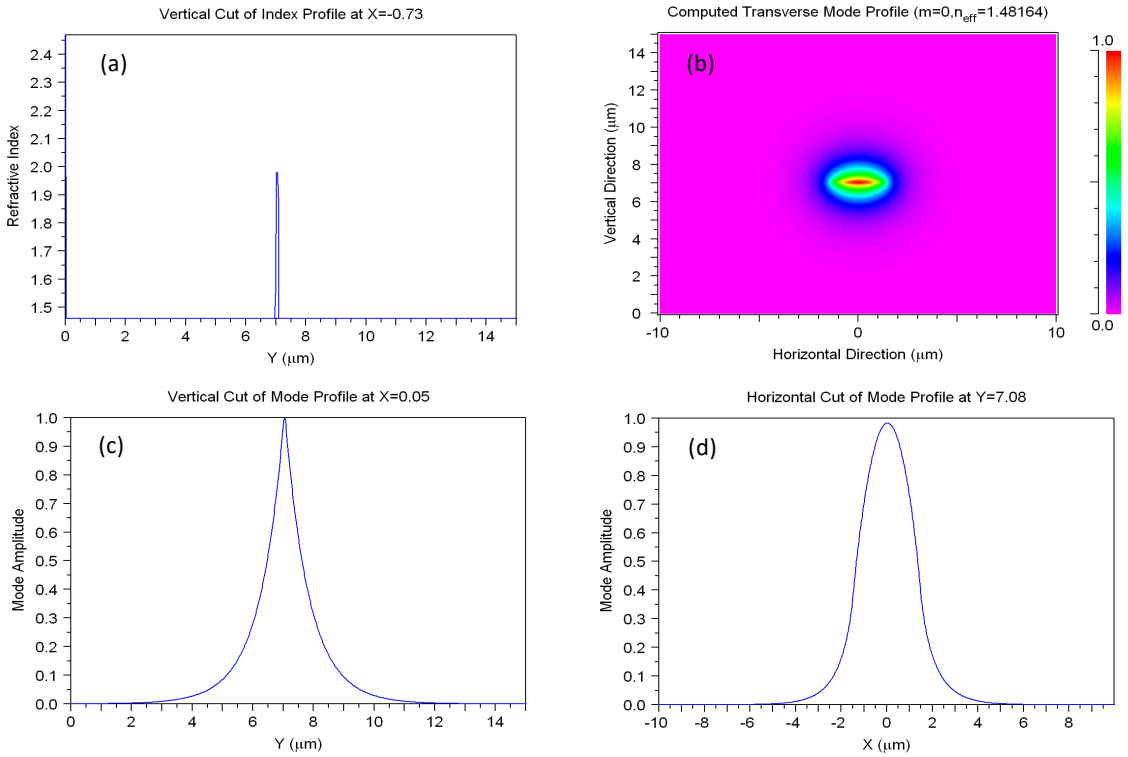

Figure 36. BEAMPROP simulation of the computed TE_{00} mode profile for the 90 nm *3 μm waveguide. Refractive index profile (vertical cut) (a); intensity plot (b); vertical cut (c); horizontal cut (d).

2.3.3 Bend Design

The study of bends is of primary importance in PIC design: propagation in bent waveguides is a lossy process, and setting the level of acceptable losses, and in turn the lower limit for the bending radius, has a direct impact on the footprint of the circuit itself.

When light propagates in a bent waveguide with constant radius of curvature $\boldsymbol{R_C}$, as an arc of circle, the phase front in the external region has a higher tangential velocity in order to keep the wavefront plane. This effect is equivalent to light propagating through a straight waveguide with an equivalent non-uniform refractive index profile. The index profile of such an equivalent waveguide can be written in first order approximation as [53]:

$$n_{eq}^2(x) = n^2(x)\left(1 + \frac{2x}{R_c}\right) \quad with \quad x \ll R_c \tag{26}$$

and Maxwell's equations can be solved in this framework to find the mode profile in the bent waveguide.

The caustic line in Figure 37 sets the region where the tangential velocity of the phase front would exceed the speed of light, in order to keep the phase fronts plane. Beyond the caustic line the wavefront is bent and radiation of light occurs.

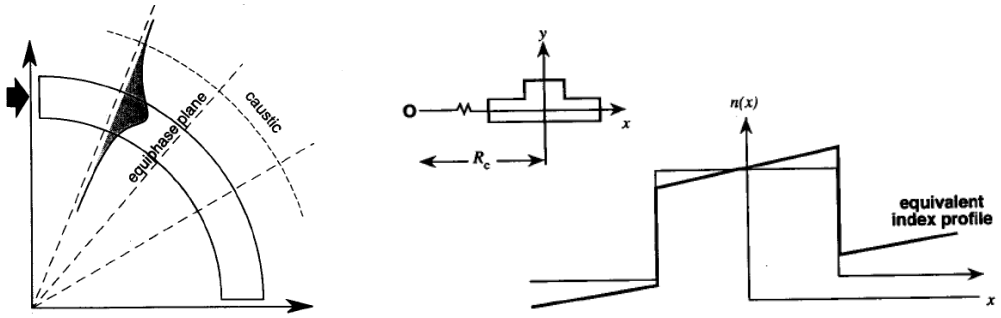

Figure 37. Straight to bent waveguide conformal mapping. Left: wavefront propagation in a bent waveguide. Right: equivalent refractive index profile of the bent waveguide.

Simulation of waveguide losses were performed on FIMMWAVE, using a complex solver. The simulation is performed for the most conservative value of n_{clad}, which is in this case n_{SiO2}=1.46. The reason is that a higher cladding refractive index increases the optical confinement in the cladding, enhancing the tangential losses effect as the guiding is weaker.

The complex solver has the capability to find a complex propagation constant β, including propagation velocity and losses. Since no material absorption is considered, the only possible losses coming from this simulation are bending losses. Perfect Matching Layers (PML) are used on the sides of the simulation region to mimic the behaviour of radiated light beyond the caustic. Simulations were performed for different thicknesses and radius of curvature. A limit of 10 dB/m of additional losses is set, and a corresponding critical radius is directly found on Figure 38.

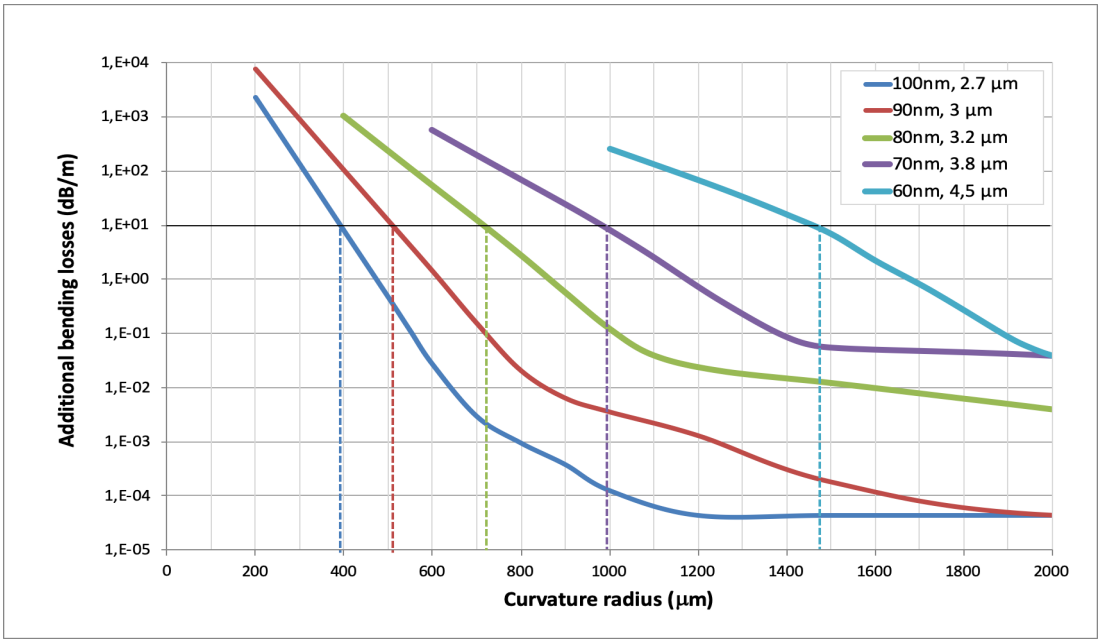

Figure 38. FIMMWAVE simulation of single-mode waveguides additional losses due to bending. We obtain the critical bending radius for each waveguide when considering additional bending lossed of 10 dB/m.

For the PIC design, however, using arcs with fixed curvature radii is not optimal due to the mode profile and effective index mismatch between a straight and a bent waveguide. Bends with continuously varying radius of curvature were used in order to remove transition losses; the design of the adiabatic bends were performed by P. Labeye at CEA, following the Lagrangian optimisation procedure discussed in his paper [53]. In Figure 39 the radius of curvature of the optimised bend is shown.

The optimised bend profile follows a parametric approach in which propagation losses due to the bent profile are calculated and the radius of curvature throughout the bend is modified to minimize said losses. It has to be noticed that this calculation is strongly dependent on the input waveguide curvature. For example, in the simplest case of a straight waveguide injecting an optical mode into a bent waveguide, the curvature of the bend must start from zero and adiabatically increase to ensure as much mode profile matching at each infinitesimal section of the bent waveguide.

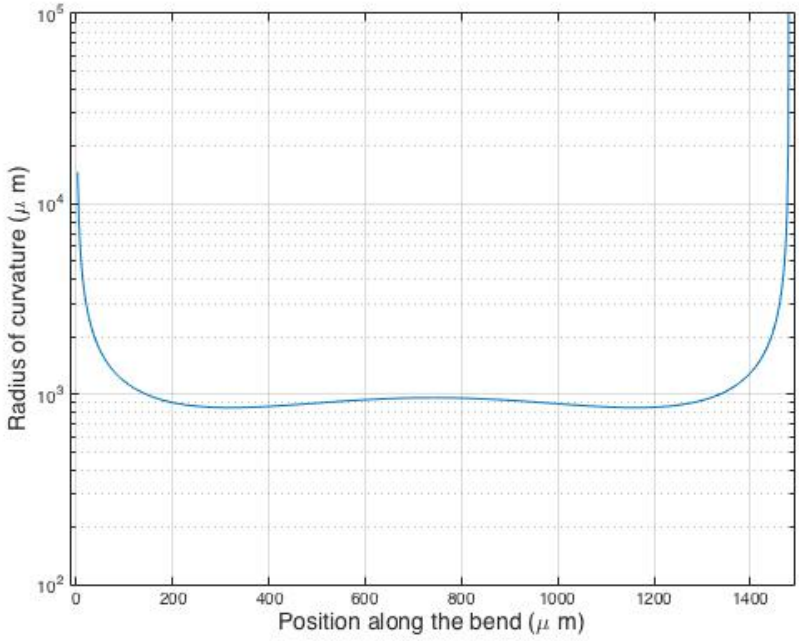

Figure 39. Radius of curvature of an adiabatic bend of equivalent bending radius of 1mm. Waveguide structure designed by P. Labeye (CEA-LETI).

2.3.4 CHIP OUTPUT MODE ADAPTER

This section describes the adaptation of optical modes between the active and passive PICs, which is a fundamental building block for hybrid integration. The adaptation is obtained by changing the width in a tapered waveguide.

Optical power needs to be transferred between the active and passive photonic circuits. In order to decrease coupling losses, the size and divergence of optical modes from to two respective chips should be as similar as possible. At III-V Lab the technological process and the design for high power devices were well established; mode adaptation was thus performed on the passive platform. To give an idea of the mode size that are of interest, the mode field diameter of a standard 1.55 μm optical fibre

(SMF28) is of 10 µm. The mode field diameter of high-power semiconductor optical amplifiers (SOA) is of about 4.1 µm *3.3 µm.

Rules of thumb for mode adaptation are the correspondence of the mode size for the two devices that must be coupled. However, the passive platform has a higher index contrast than InP-based waveguides and the passive platform has, in our case, a larger difference between x and y direction guiding compared with the InP platform. The optical mode profile in the ***x*** and ***y*** axes directions is not perfectly Gaussian, especially in the vertical (***y***) direction where the thin layer of nitride weakly confines the optical field, as seen in Figure 36.

The mode shape and size is changed by tapering the width of the waveguide, in order to reduce the effective refractive index and enlarge the optical mode, thus reducing the divergence.

Simulations of the output optical mode dimension as a function of the silicon nitride waveguide width at the end of the taper are shown in Figure 40. Waveguide widths below 1 µm are needed in order to enlarge the mode diameter for the two axes. Figure 41 shows the mode simulation from a spot size adapter adapting the optical mode from an 800 nm wide waveguide, for a SiN thickness of 90 nm and the corresponding mode divergence.

The design of the output mode adapter is tailored to be coupled with high power structures fabricated at III-V Lab.

Alignment tolerance between active and passive components was evaluated as well, as shown in Figure 42. Butt-coupling has few micrometers tolerance, which is compatible with both active alignment and flip-chip techniques and are well within the sensitivity of modern alignment machines, going down to 200 nm.

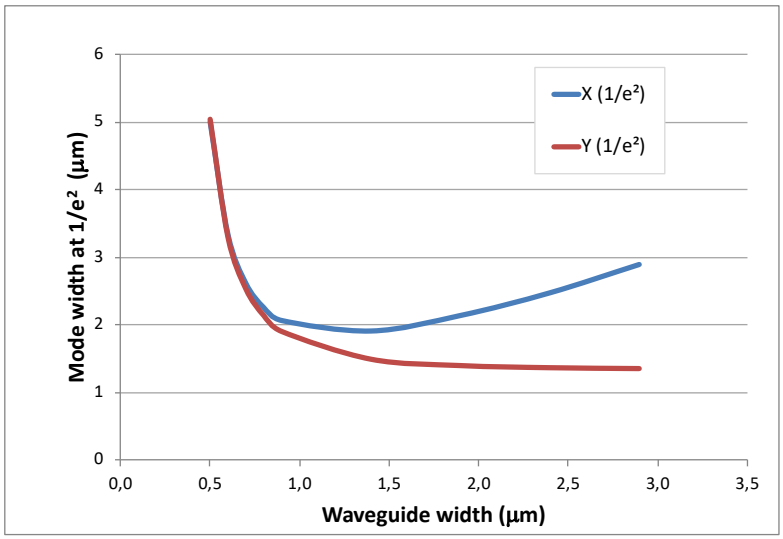

Figure 40. FIMMWAVE simulation of the optical mode dimension in the vertical and horizontal directions as a function of the waveguide width. The thickness of the waveguide is 90 nm.

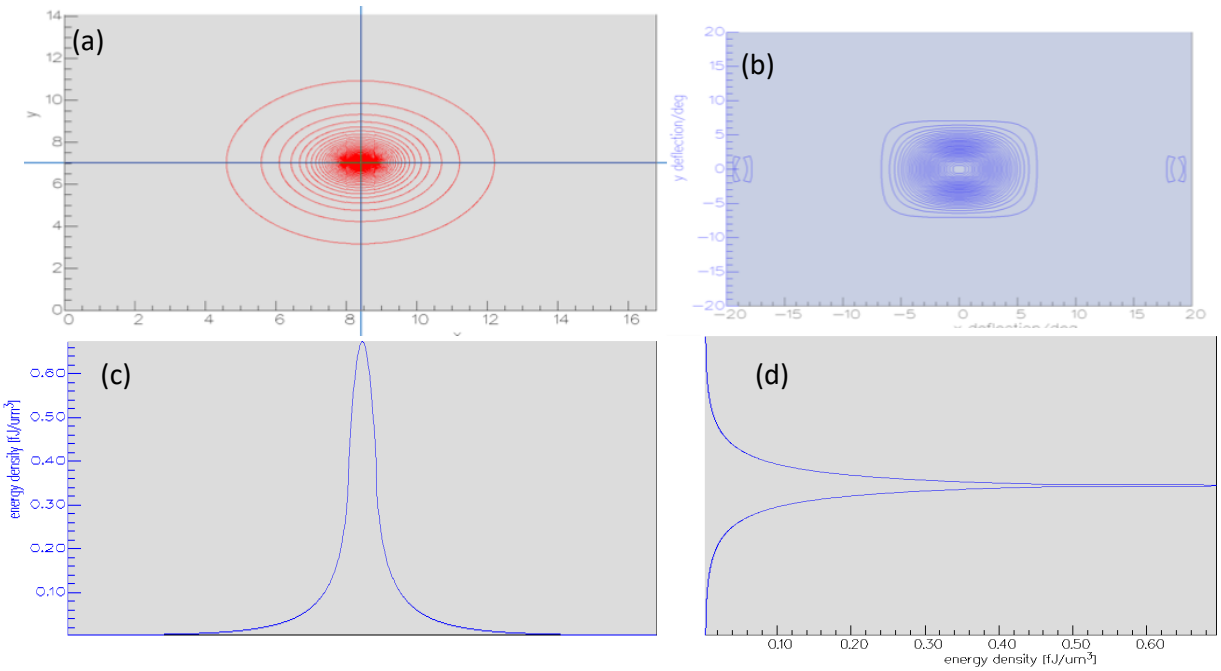

Figure 41. FIMMWAVE simulation of the computed optical mode (a) and mode divergence (b) for a 90 nm *800 nm waveguide. Figures (c) and (d) show the horizontal and vertical cut of the modal intensity profile.

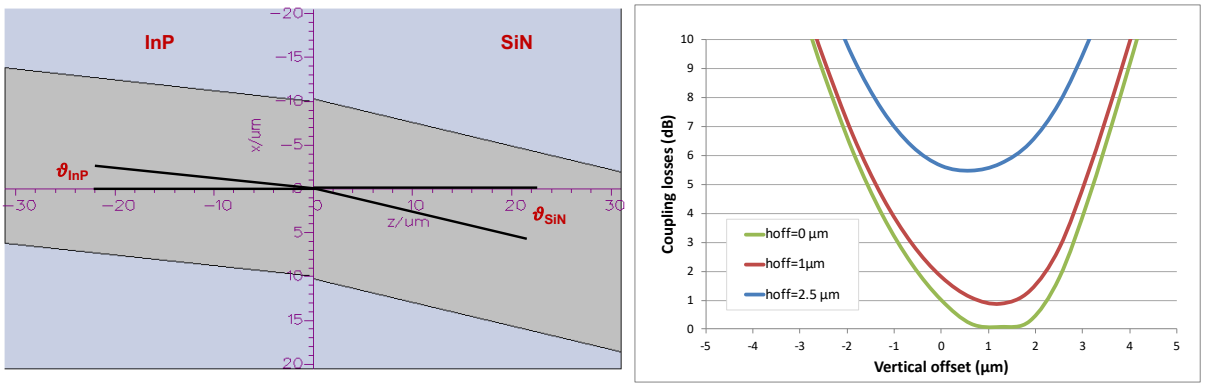

Figure 42. Left: Simulated structure of the butt-coupling between active and passive PICs. Right: Coupling losses tolerances with vertical and horizontal (h_{off}) misalignments. The computed angles for optimal angular alignment are $\theta_{InP} = 7°$, $\theta_{SiN} = 15.5$ °.

It must be noticed that in order to have low losses on the tapered waveguide, the tapering must be smooth, and the transition region must be long enough to avoid coupling to the radiation modes.

Figure 43 shows the computed losses for three different final taper widths as a function of the taper length. The starting point is the 90 nm *3 µm waveguide waveguide. Very short tapers (100 nm) are possible at a price of 1 dB optical loss.

A further degree of flexibility in taper design is the taper shape. Figure 44 shows a comparison of the refractive index change along the propagation axis z for a linear and an exponential taper shape, and

the relative power of the 0-th order mode along the taper position. When using an exponential taper shape, the effective refractive index changes rapidly in the initial region, where the impact on the losses is lower, and in a much slower way in the final part, where the mode adaptation process is critical. Thus, an exponential profile allows lower losses tapers or shorter tapers with the same losses of a corresponding linear one.

As a first iteration of the design, the choice of working with long (500 μm), linear tapers. The difference in losses between a linear and exponential taper did not justify an increased complexity of the layout design. The output taper shape can still be changed in future iterations, as an optimization of the parameters of this building block.

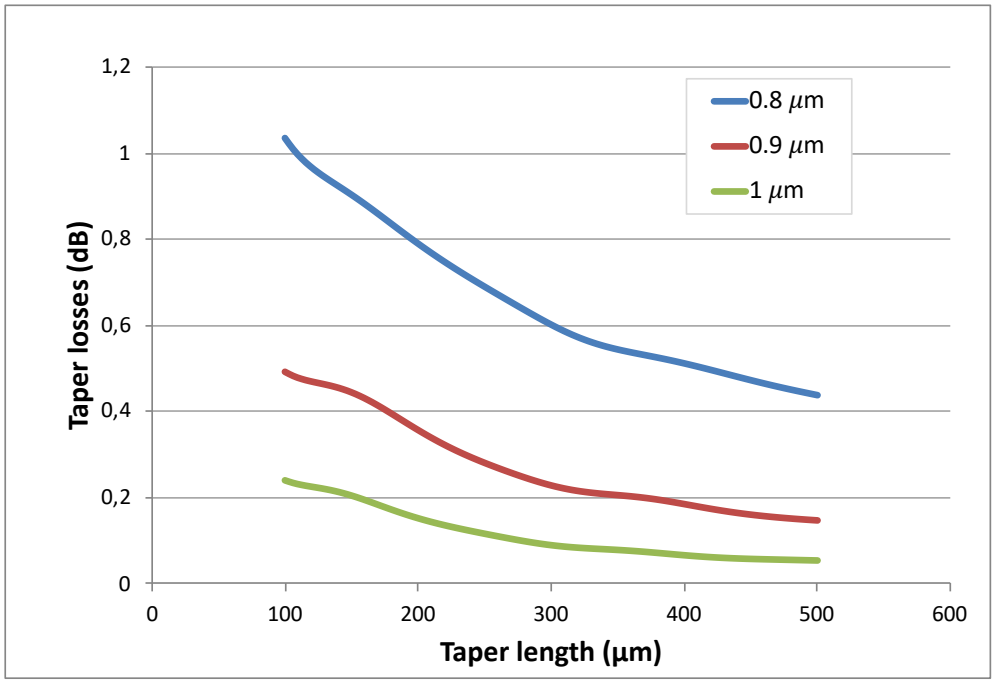

Figure 43. Simulated additional losses of a linear waveguide taper. The taper length design is strongly affected by the low loss requirement.

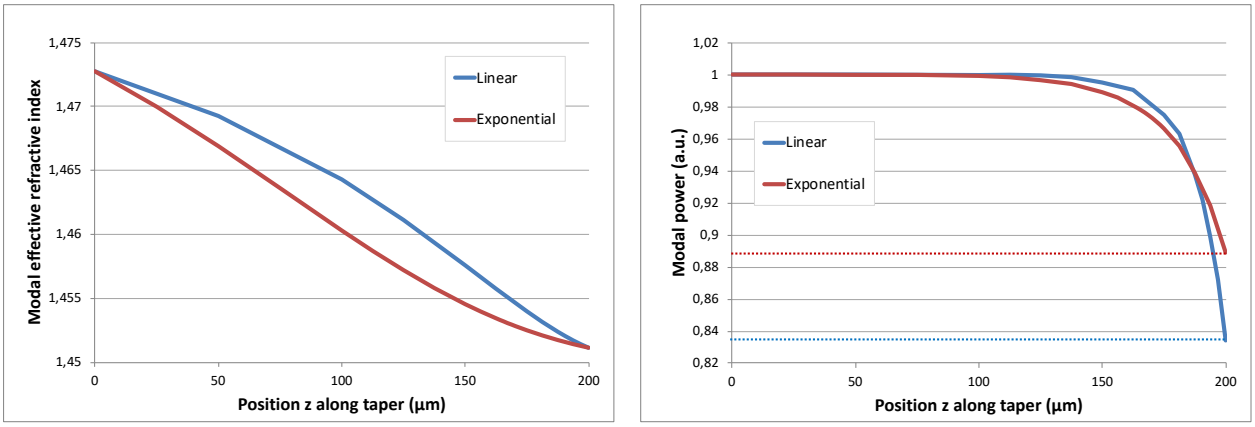

Figure 44. Modal effective refractive index profile (left) and modal power (right) of the TE_{00} mode along the taper for linear and exponential taper shapes.

2.4 DEVICES DESIGN AND SIMULATIONS

This section presents the simulation methods and results for the different building blocks of passive devices, such as directional couplers, ring resonators, optical delays and Bragg gratings.

2.4.1 BRAGG GRATINGS

Bragg gratings are not directly linked to optoelectronic oscillators for the architecture presented in Chapter 1, but allow the fabrication of on-chip reflectors for hybrid low linewidth lasers or mode-locked lasers. It is a rather simple but yet versatile class of reflectors for planar lightwave circuits. The Bragg gratings designed in this paragraph and measured in 2.7.3 were designed as a basic building block of the passive SiN platform in collaboration with CEA-LETI, in order to extend the applications of the platform itself to hybrid III-V/SiN low linewidth lasers for LIDAR applications, which has become the subject of the Ph.D. thesis of Sylvain Boust, who pursued the research in this field at III-V Lab based on this same integration platform.

The principle of a Bragg grating is to use a periodic change of the refractive index in order to increase the reflection associated to interfaces between medium having different refractive indices. On our platform we implemented it with a periodic variation of the waveguide width so that the refractive index difference generates multiple reflections all along the grating. The reflections will add up in phase for a specific wavelength, called Bragg wavelength, which is defined as:

$$\lambda_B = \frac{2n_{eff}\Lambda}{\mathrm{m}}, \tag{27}$$

where Λ is the period of the waveguide corrugation and n_{eff} is the average effective index of the mode, m is the order of the grating.

A second parameter to characterise Bragg gratings is the grating strength κ, which gives a measure of the coupling strength between the forward and the backward propagating signals, and has the units of inverse length. For practical purposes the value κL is used, which is the coupling strength multiplied by the length of the grating itself. This quantity also gives the peak value of reflectivity of the grating:

$$R_{max} = \tanh^2 \kappa L. \tag{28}$$

Values between 1 and 1.5 give a good compromise between grating length, strength and reflection bandwidth.

Bragg gratings were simulated on MATLAB by implementing a transfer matrix method (TMM) algorithm. The input parameters are: the central wavelength of the designed Bragg grating, the effective refractive indices for the two waveguide widths and the number of periods.

The following simulations were performed on 70 nm thick, 3.8 μm wide SiN waveguides, to design Bragg gratings for the first generation of devices. The effective refractive index of the optical mode is 1.47403, found with FIMMWAVE's eigenmodes solver.

FIMMWAVE allows the calculation of several parameters of a structure, as can be a waveguide, to find parameter-dependent quantities. A fine sweep on the width of the waveguide allows us to find the effective refractive index as a function of the width (Figure 45) and try different width differences to tailor the strength of the grating.

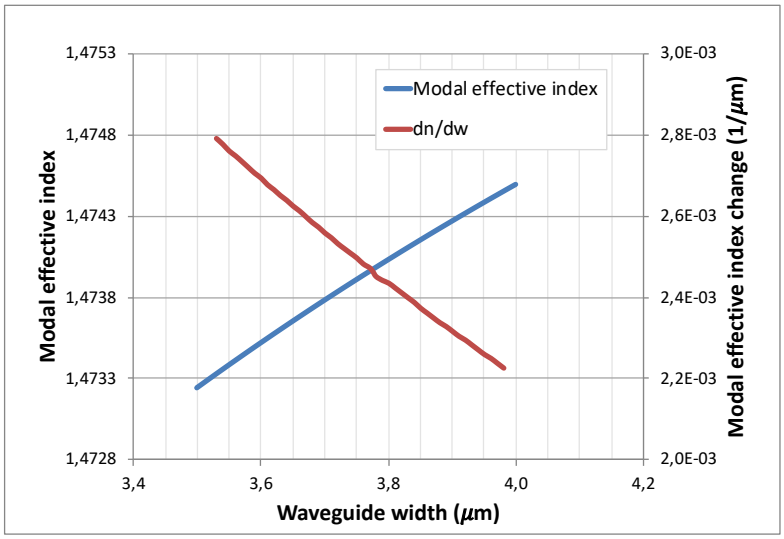

Figure 45. Simulated modal effective index with waveguide width for Bragg grating design.

The first simulation is performed with a 30 nm width difference in the grating, with a n_2 value of 1.47396; the corresponding grating period is 526 nm, for a first order grating. Reflection spectra are shown in Figure 46 and simulation results for the main parameters of the grating are shown in the corresponding table. It must be noticed that since the refractive index contrast is extremely low ($7*10^{-5}$), the obtained reflection is very low, with a maximum of 70% for a 13.46 mm long grating, which is roughly the longest path we could accommodate on the chip for the reflector.

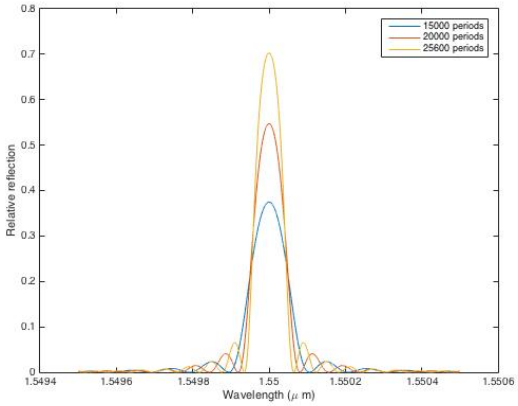

Periods	*Length (mm)*	*κL*	*FWHM (nm)*	*Max R (%)*
15000	7.89	0.712	0.108	37.5
20000	10.52	0.950	0.089	54.7
25600	13.46	1.216	0.079	70.3

Figure 46. Left: reflectivity of the Bragg grating with 30 nm width difference (15000, 20000 and 25000 grating periods). Right: property table of the Bragg gratings

When the width difference is increased to 90 nm, the corresponding refractive index difference goes up to $2.2*10^{-4}$, which is high for the reflector lengths we are addressing. The length of the grating is basically not influencing the maximum reflection value past the 20000 periods, as it already saturates to almost 100% of reflection. The results of such simulation are presented in Figure 47.

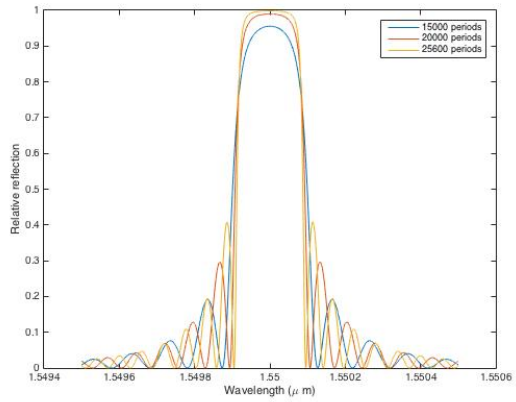

Periods	*Length (mm)*	*κL*	*FWHM (nm)*	*Max R (%)*
15000	7.89	2.239	0.200	95.5%
20000	10.52	2.285	0.186	99.0%
25600	13.46	3.821	0.175	99.8%

Figure 47. Left: reflectivity of the Bragg grating with 90 nm width difference (15000, 20000 and 25000 grating periods). Right: property table of the Bragg gratings

An intermediate value of indentation of 50 nm was also considered, for optimization and fabrication process validation. The strength of the grating and the width of the reflective window are the two main parameters used to design a reflector for an external cavity laser. The amount of reflection is chosen considering gain threshold calculations, facet coupling losses and the possibility to have a backside monitoring of power and wavelength when integrating such devices in real systems.

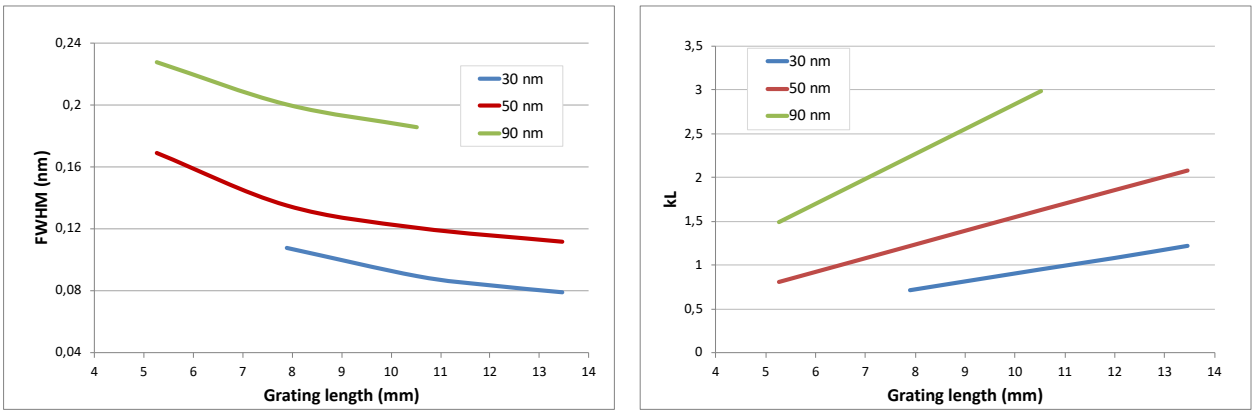

Figure 48. Simulations of Bragg grating properties. Left: Full Width Half Maximum. Right: grating strength ***κL.***

2.4.2 DIRECTIONAL COUPLERS

Directional couplers are devices made of two adjacent waveguides that enable the transfer of optical power between those two waveguides. Efficient coupling is needed for high quality factor ring resonators, since the coupler losses add up to the propagation losses and can have a strong impact on the response of the device.

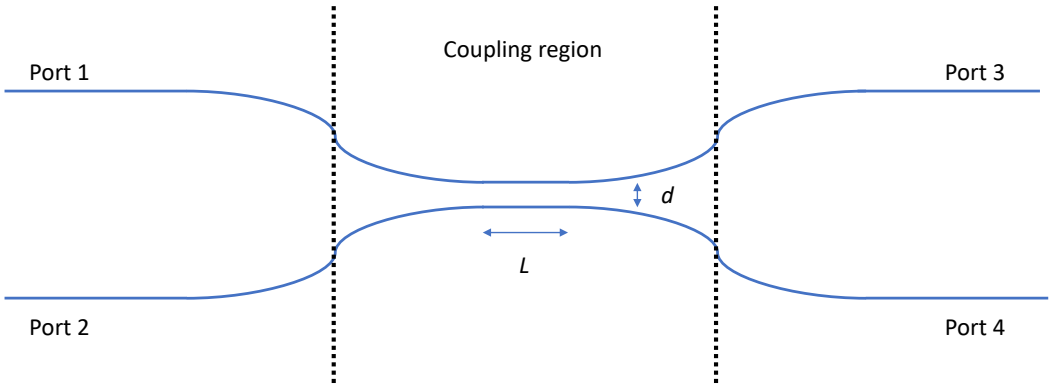

Figure 49. Layout of a generic directional coupler, with its main parameters: distance ***d*** between waveguides and straight coupling section ***L***. The coupling region between the dotted lines is the interaction region of the two waveguides.

A directional coupler has four ports, as shown in Figure 49, and the electric fields in the waveguides are governed by the following equation:

$$\begin{pmatrix} E_3 \\ E_4 \end{pmatrix} = \begin{pmatrix} t & k \\ -k^* & t^* \end{pmatrix} \begin{pmatrix} E_1 \\ E_2 \end{pmatrix} \tag{29}$$

where ***t*** and ***k*** are the matrix elements for the coupler. For an ideal, lossless coupler conservation of energy occurs and $t^2 + k^2 = 1$. The squares of ***t*** and ***k*** have the physical meaning of portion of optical power passing through (***t***) or crossing (***k***) the coupler with respect to the input port.

The objective is to design directional couplers with excess losses as low as possible. In the case of coupling in a ring resonator, the simplest layout is to couple a straight bus waveguide to a circular ring. Even if the ring has a radius of some millimetres, the bent and the straight waveguide have different propagation constants so there is a phase front mismatch between the two waves. A more efficient solution could be to have a bent bus waveguide following the curvature of the ring [54].

The solution proposed here is to use the soft bends as connectors to create symmetrical directional couplers, provided that also the ring is made with the same bent shapes. The advantage of this configuration is that one has a better localised coupling region, in which the coupler is perfectly symmetrical but the distance between the two waveguides is weakly tapered to avoid coupling to radiation modes [55]. A second advantage of using adiabatic bends is that the coupling strength can be increased by adding a straight section in the coupler without suffering mode mismatch. The rationale of this choice lies in the fact that excess coupler losses increase with decreasing waveguide spacing [54].

The simulation of the coupler structure was performed on FIMMWAVE. In order to speed up the simulation process, a 1D+Z structure was used, applying the effective index method [56] through a routine written in Python which finds the equivalent refractive index profile of the coupler. The computing time went from around 1 hour per point to less than ten seconds for the whole simulation sweep.

The first simulation is performed to extract the fraction of power (k^2) coupled from port 1 to port 4 at zero coupling length, for different waveguide separations. As expected, the coupling increases when the two waveguides are brought closer together, as can be seen in Figure 51. The residual coupling can be quite high for very close waveguides. Gaps of around 1 μm are quite tricky to control precisely during the fabrication phase, and those small gap couplers also increase the coupler's excess losses.

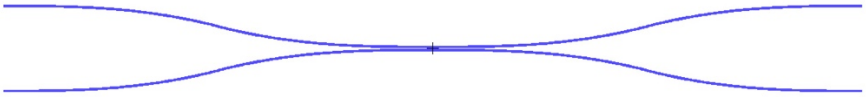

Figure 50. Mask layout of the designed directional coupler with adiabatic bends.

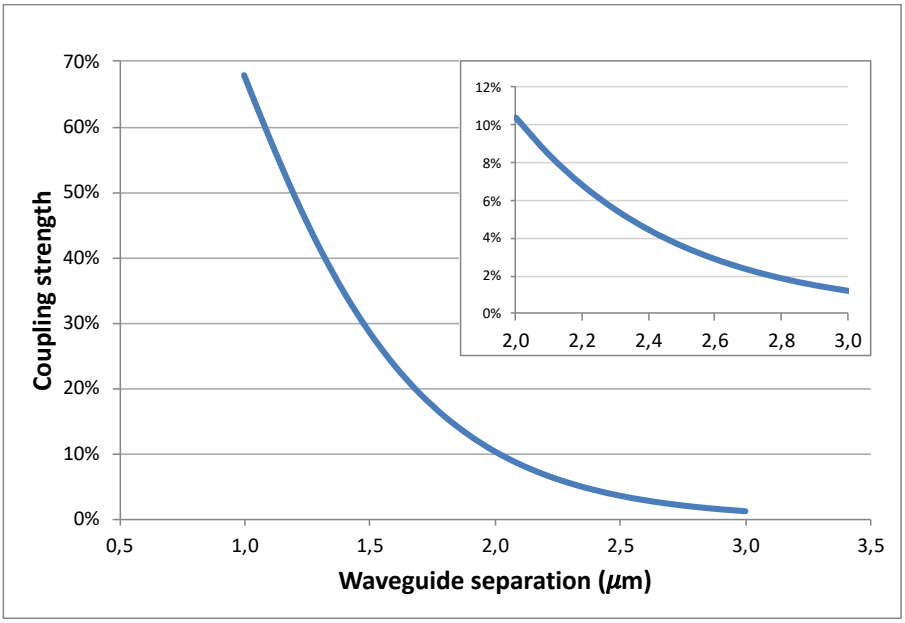

Figure 51. Simulated coupling factor k^2 of the designed optical coupler when the waveguide distance d is changed. The inset shows coupling values lower than 10%, which is the design area for high-Q ring resonators.

Again, the sweep function of FIMMWAVE can be used to track the variation of selected parameters. Figure 52 shows a map of the coupling value when the length of the straight section of the coupler is changed. The simulation was performed for several values of the coupler waveguide distance, in order to have a further degree of flexibility for coupler design.

From Figure 52 one can extract the values of waveguide distance ***d*** and coupling length ***L*** in order to design a coupler with a certain coupling strength. These values can be used for coupling to ring resonators or as directional couplers, beam splitters and combiners within the optical circuit. This building block was extensively used in the design of the lithography mask of OHY4 where complex passive circuits combining ring resonators, delay lines and Bragg gratings were integrated.

The excess coupler losses, however, can't be simulated on FIMMWAVE since they come from the coupling of light to high order and radiation modes.

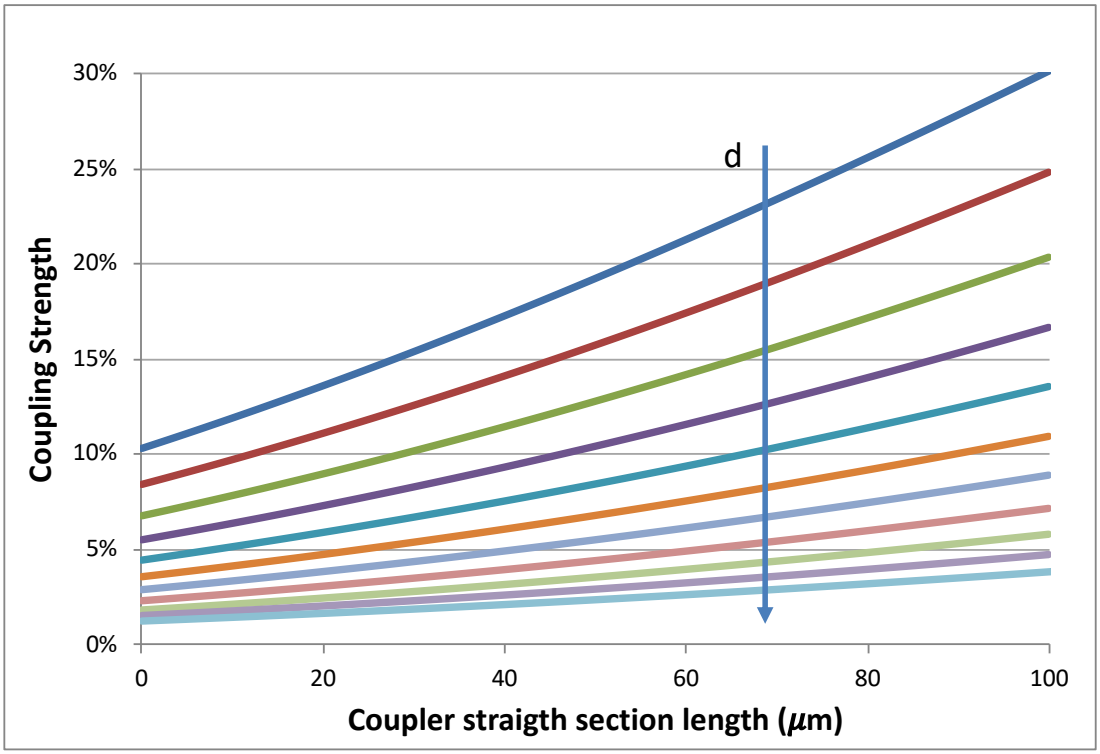

Figure 52. Simulated coupler strength with respect to two parameters: waveguide distance ***d*** and straight section length ***L***. The distance is swept from 2 to 3 μm with 0.1 μm steps.

2.4.3 RING RESONATORS

Ring resonators emerged as a key component for integrated optics. They can be used alone or in combination with other rings and building blocks to create complex on-chip optical cavities and filters [57].

The basic configuration of a ring resonator is a ring cavity coupled to a bus waveguide through a directional coupler (two ports ring resonator). A portion of the light coming from the bus waveguide is injected in the ring, it is delayed and injected in the second input port of the directional coupler. Due to the phase shift of the ring, the input and delayed signals will be in phase at specific wavelengths; the response of this cavity is periodic with the period corresponding to the ring's Free Spectral Range (***FSR***), which is defined as [23]:

$$FSR = \frac{c}{n_g L_{res}} \ [Hz] \tag{30}$$

In order to compute the transfer function of the ring resonator, we need to compute the relations between the electric fields at the input and output of the directional couplers. The interaction between those fields are described by the directional coupler matrix relation:

$$\begin{pmatrix} E_{t1} \\ E_{t2} \end{pmatrix} = \begin{pmatrix} t & k \\ -k^* & t^* \end{pmatrix} \begin{pmatrix} E_{i1} \\ E_{i2} \end{pmatrix}, \tag{31}$$

where $\boldsymbol{t}$ is the transmission factor, $\boldsymbol{k}$ is the coupling factor, and $t^2 + k^2 = 1$.

The following assumptions were made:

- Directional couplers are reciprocal and lossless, implying that the transfer matrices of the couplers are unitary;
- Only one polarisation is considered and there are no elements in the system able to couple optical modes with different polarisations;
- All losses encountered by an optical mode are incorporated in the attenuation factor $\boldsymbol{a}$;
- The complex amplitudes $\boldsymbol{E}$ are normalised so that the squared magnitude of each field gives the modal power;
- Only passive rings are considered; this implies that $\boldsymbol{a_r}$ (the round-trip fractional losses parameter) takes values between 0 (infinite losses) and 1 (lossless ring).

Two ports ring resonators

The simplest case that can be considered is that of a ring resonator coupled to one bus waveguide.

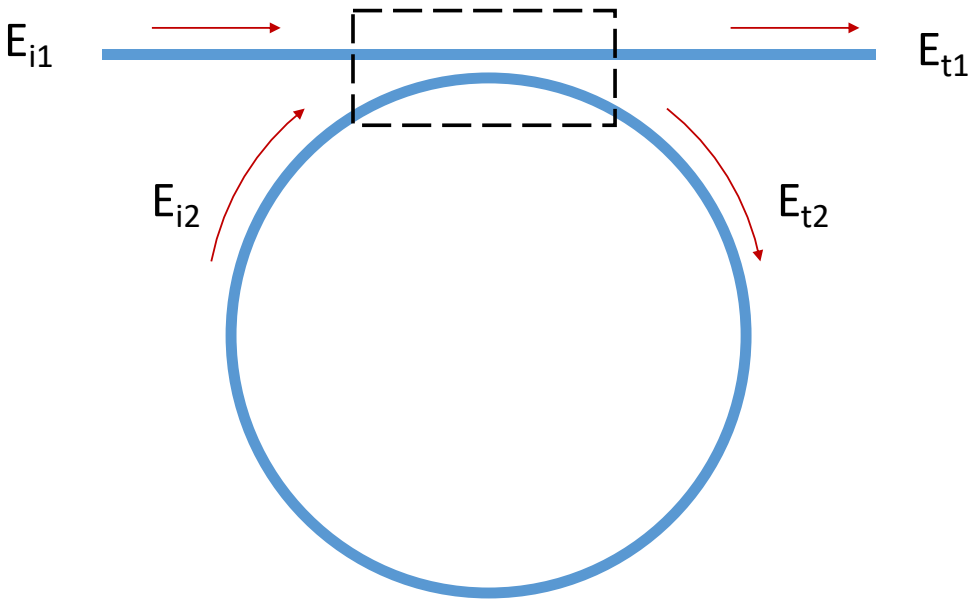

Figure 53. All-pass ring resonator structure and electric fields used for the response computation. The dashed area is the coupling region.

We can establish further relations between the optical fields. The field E_{i2} corresponds to the delayed signal E_{t2} of our round trip in the ring, so we can write

$$E_{i2} = \alpha_r e^{j2\pi n_{eff} L/\lambda} E_{t2} \tag{32}$$

where the exponential term is the phase shift of the signal (and the whole exponential argument can be rewritten as $j\theta$), and α_r is the fractional ring losses.

We proceed by rewriting E_{i2} in function of the input E_{i1}:

$$E_{i2} = \frac{\alpha_r k^* e^{j\theta}}{\alpha_r t^* e^{j\theta} - 1} E_{i1} \tag{33}$$

We can now directly obtain the output response E_{t1} from the coupler matrix relation; E_{i1} is supposed identically equal to 1 for all wavelengths, so the transfer function can be found:

$$E_{t1} = \frac{t - \alpha_r e^{j\theta}}{1 - \alpha_r t^* e^{j\theta}} \tag{34}$$

This response is a periodical arrangement of notch shapes, shown in Figure 54. The on-resonance condition $\theta = 2\pi m$, with m integer, gives the minima of the transmission, so the measured intensity at such wavelengths is:

$$P_{t1,res} = \frac{(\alpha_r - t)^2}{(1 - \alpha_r t)^2} \tag{35}$$

while the off-resonance intensity ($\theta = (2m + 1)\pi$) can be written as:

$$P_{t1,offres} = \frac{(\alpha_r + t)^2}{(1 + \alpha_r t)^2} \tag{36}$$

It can be noticed that the intensity pattern is symmetrical with respect to the exchange of α_r and t parameters. This can raise some ambiguities when trying to extract propagation losses from ring resonators; the only way to distinguish the two parameters is through their known dependence on the wavelength [58].

The response of the ring can be minimized in resonance condition by adjusting the coupling transmission with respect to the (expected) loss value:

$$t_{cr} = \frac{1}{\alpha_r}. \tag{37}$$

This condition is called critical coupling and gives the highest ring rejection.

Some more parameters are needed to fully characterize a filter. The bandwidth of the filter is the wavelength region for which the filter losses are lower than 3dB (half of the power). This quantity can be found from the previous equations when setting this condition:

$$\Delta\lambda = \frac{\lambda^2}{\pi L_{res} n_g} \frac{1 - \alpha_r t^2}{\sqrt{\alpha_r t^2}}. \tag{38}$$

From the previous definition we can find the finesse of the ring:

$$F = \frac{FSR}{\Delta\lambda} = \frac{\pi\sqrt{\alpha_r t^2}}{1-\alpha_r t^2}. \tag{39}$$

The finesse is related to the quality factor, which is a common parameter in the electrical domain to measure a filter's performances. The finesse and quality factor are linked by the equation:

$$Q = \frac{\lambda}{\Delta\lambda} = \frac{n_g L}{\lambda} F. \tag{40}$$

The quality factor is high at optical frequencies due to micrometer size of the wavelength. The finesse, however, can be used to compare ring resonators when they are used as electrical filters for optically carried microwave signals.

There is one last parameter, called the build-up factor, that measures the (relative) electrical field density inside the resonator. It is defined, at resonance, as

$$B = \frac{1+\mathrm{t}}{1-\mathrm{t}} \tag{41}$$

which, for high quality factor resonators (***1-t*** << ***1***) justifies the use of such resonators in non-linear devices in order to generate optical combs.

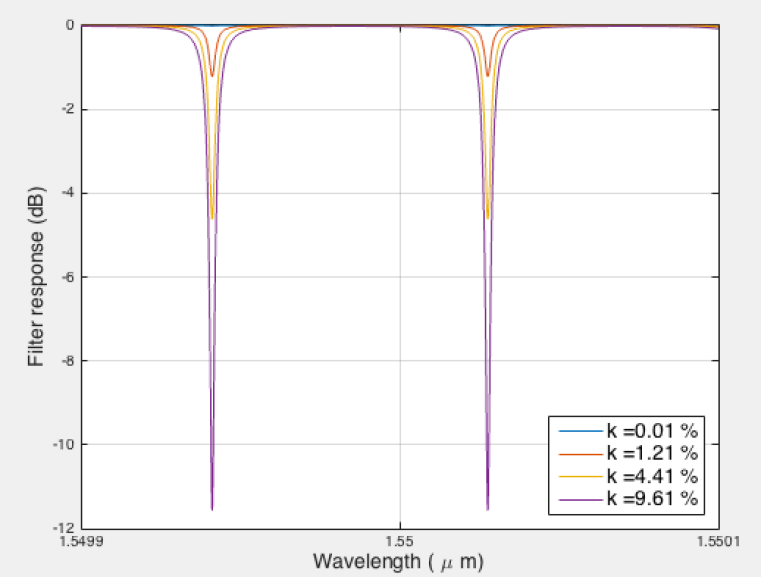

Figure 54. Simulated response of a two ports ring resonator, with the coupling factor as a parameter. The losses considered in the simulation are 1 dB/m.

Four ports ring resonators

Four ports ring resonators have a second bus waveguide to couple light in or out the ring resonator, as shown in Figure 55. Those two additional ports are commonly called "add" and "drop" since this configuration was first used in WDM systems for wavelength (de)multiplexing purposes. In our case, the "add" port ($\boldsymbol{E_5}$) is unused, and the "drop" port is the band-pass filter output ($\boldsymbol{E_d}$).

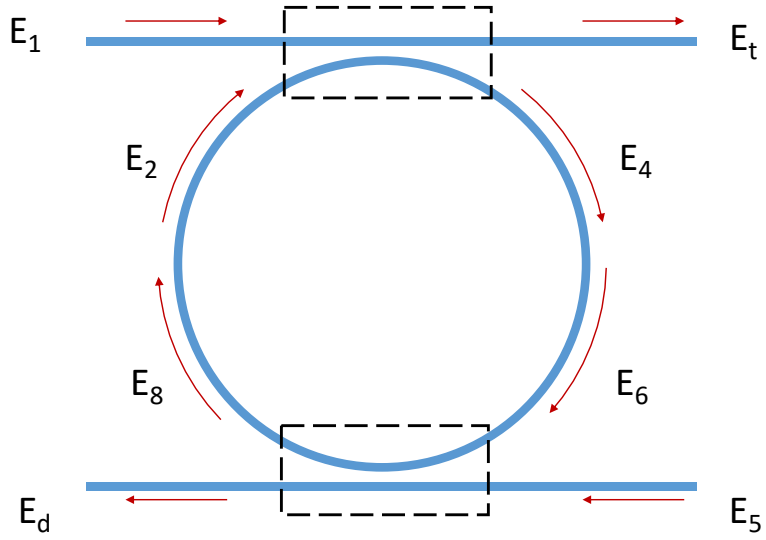

Figure 55. Four ports ring resonator structure and electric fields used for the response computation. E_t and E_d indicate the through port and the drop port, respectively.

The mathematical treatment to find the device's transfer function has the same starting point of the two ports case. This time, eight electrical fields are involved. The founding relations of the fields inside the ring are:

$$\begin{cases} E_6 = \sqrt{\alpha_r}\, e^{j\theta/2} E_4 \\ E_2 = \sqrt{\alpha_r}\, e^{j\theta/2} E_8 \end{cases} \tag{42}$$

and by taking into account the case in which the two directional couplers are different from each other, we can write the two output fields as:

$$E_t = \frac{t_1 - t_2^* \alpha_r e^{j\theta}}{1 - t_1^* t_2^* \alpha_r e^{j\theta}} \tag{43}$$

$$E_d = \frac{-k_1^* k_2 \sqrt{\alpha_r} e^{j\theta/2}}{1 - t_1^* t_2^* \alpha_r e^{j\theta}} \tag{44}$$

The feature of the ring resonator that is seen during measurement is the intensity response, which is the square of the absolute value of the electric fields computed above. In resonance conditions they can be written as:

$$P_{t,res} = \frac{(t_1 - t_2 \alpha_r)^2}{(1 - t_1 t_2 \alpha_r)^2} \tag{45}$$

$$P_{d,res} = \frac{k_1^2 k_2^2 \alpha_r}{(1 - t_1 t_2 \alpha_r)^2} \tag{46}$$

The resulting response of the filter is again a periodical arrangement of stop-band and pass-band filters for the through port and the drop port, respectively. Figure 56 shows the response for both ports for a 10 GHz ring resonator.

An interesting feature of ring resonators is the increase of the group delay at resonance due to light recirculating in the structure. This property is useful for integrated OEO since the effective length (delay) of the passive OEO cavity can be increased using ring resonators. Figure 57 shows the group delay of the signal and the response of the drop port simulated as described in [23]. The group delay is expressed in units of the intrinsic group delay for the same propagation length as the resonator length.

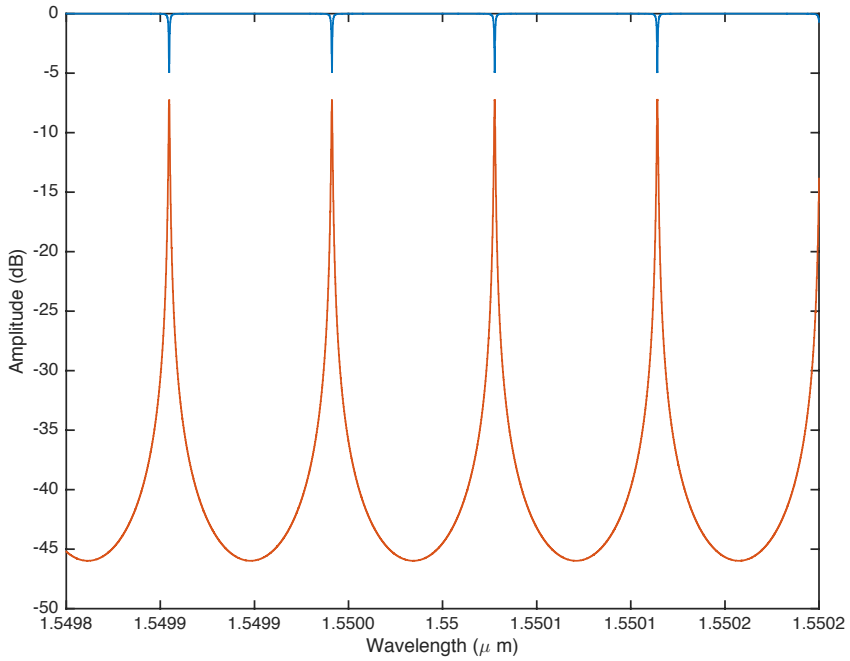

Figure 56. Four-port ring resonator response simulation. Blue curve: through port. Red curve: drop port.

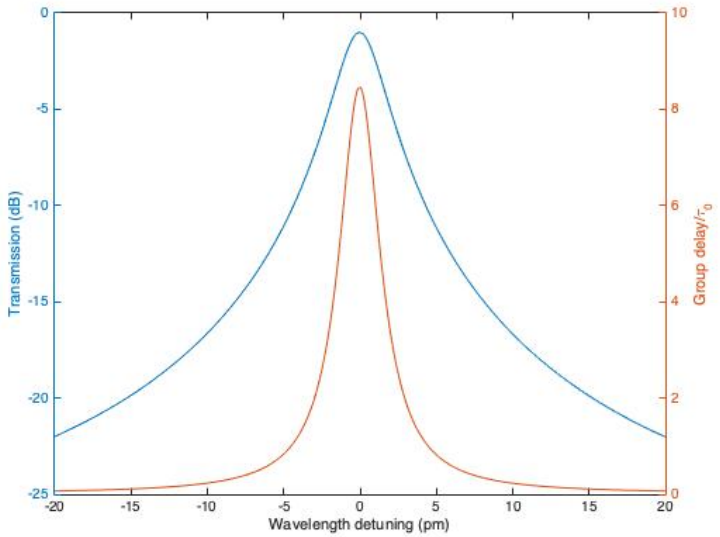

Figure 57. Simulated intensity response and group delay of the drop port of a four ports ring resonator.

Lossy directional couplers

Generally speaking, directional couplers have a certain amount of excess losses, meaning that the total power coupled in the output waveguide is lower that at the input of the coupler itself, as described in 2.4.2. This changes the device's transfer matrix to:

$$\begin{pmatrix} E_{t1} \\ E_{t2} \end{pmatrix} = a_c \begin{pmatrix} t & k \\ -k^* & t^* \end{pmatrix} \begin{pmatrix} E_{i1} \\ E_{i2} \end{pmatrix}, \tag{47}$$

in which the factor a_c is the fractional coupler loss factor, having a value of 1 for lossless couplers.

The response of a two ports ring resonator is modified as follows:

$$E_{t1} = a_c \frac{t - \alpha_r a_c e^{j\theta}}{1 - \alpha_r a_c t^* e^{j\theta}}. \tag{48}$$

It is important to notice that those two sources of losses are of different nature, and happen in a distributed (ring propagation losses) or point wise (coupler losses) fashion, but the contribution of each factor can't be distinguished for a two ports resonator when only the optical spectra are observed.

For the four ports case the starting point equation is exactly the same as the two ports resonator. The response of the through and drop ports are modified as follows:

$$E_t = a_c^2 \frac{t_1 - t_2^* a_c^2 \alpha_r e^{j\theta}}{1 - t_1^* t_2^* a_c^2 \alpha_r e^{j\theta}}, \tag{49}$$

$$E_d = a_c^2 \frac{-k_1^* k_2 \sqrt{\alpha_r} e^{j\theta/2}}{1 - t_1^* t_2^* a_c^2 \alpha_r e^{j\theta}}, \tag{50}$$

from which we can see that the coupling losses act as a scaling factor both for propagation losses and for the response of the ring itself.

Figure 58 shows the degradation of the ring filter response due to coupler excess losses.

The impact of the coupler excess losses can be high: excess coupler losses of 0.1 dB correspond to 5.5 dB/m additional propagation losses for a 3 mm (10 GHz) ring resonator, not to mention they appear with a factor 4 in the power spectral response of the resonator itself.

Following the design of low loss couplers in 2.4.2, we propose a novel layout for a ring resonator, shown in Figure 59. The ring itself is designed connecting four adiabatic 90° bends described in 2.3.3.

As the bend is adiabatic and symmetrical inside the coupling region, there is no difference between coupling two S-bends or between an S-bend and a complete 90° arc. Propagating losses of less than 1 dB/m have been already demonstrated; thus, excess coupler losses could become the ultimate limiting factor for ring resonator quality factor performances. Moreover, the bends can be directly connected to straight waveguides, thus the whole parameter set of coupling length, coupling distance and ring FSR can be chosen by design.

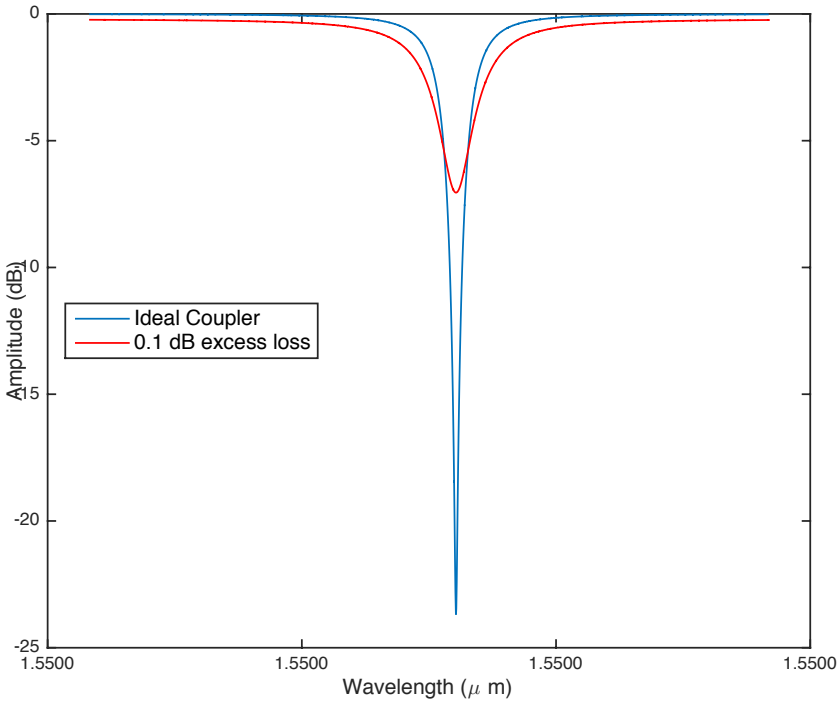

Figure 58. Comparison of the through port response of an ideal (blue) and lossy (red) directional coupler.

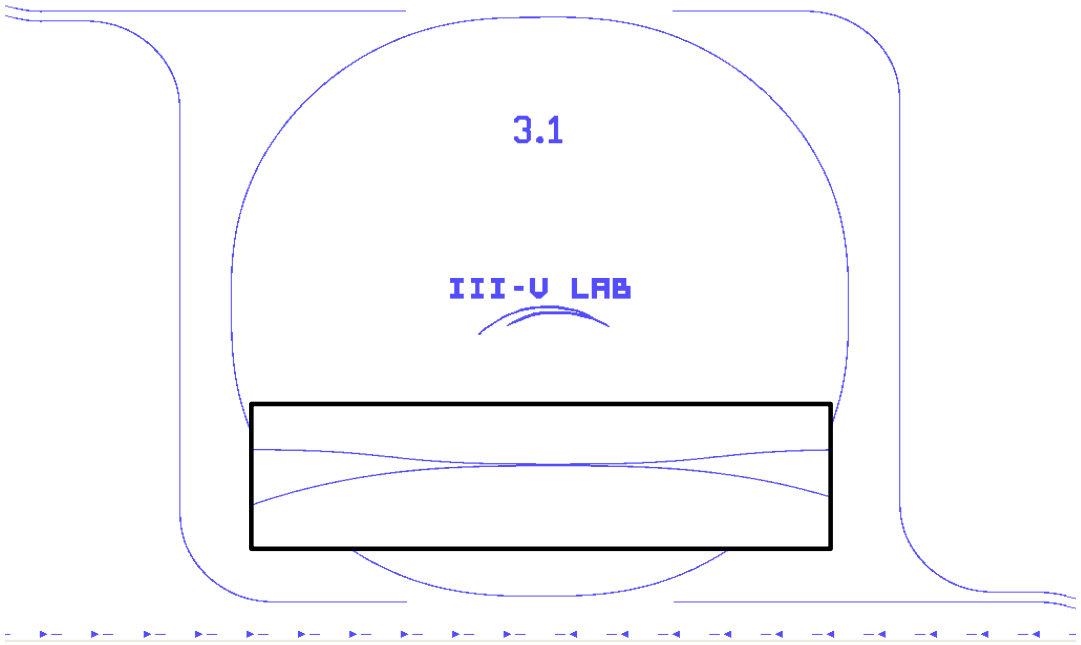

Figure 59. Non-circular ring resonator layout. The inset shows the detail of the coupling region.

2.5 PASSIVE DEVICES FABRICATION PROCESS

This section describes the fabrication process flow of passive devices. The fabrication was performed in CEA-LETI in Grenoble, with the coordination of Jean-Marc Fedeli.

The fabrication process is shown in Figure 60. It starts with an 8 inches silicon wafer, which has undergone thermal oxidation (a). The thickness of the silicon dioxide varies between 6 and 13 μm, depending on the thickness of the waveguide, to avoid light coupling to the silicon substrate. The thickness of the wafer is of 725 μm, to withstand the tensile strain produced by the relatively thick layer of SiO_2. Thermal oxide is very dense and has excellent optical properties, with low defects concentration, low impurity concentration and thus low optical losses; this oxide will act as the lower cladding of the waveguide.

A layer of stoichiometric silicon nitride (Si_3N_4) is deposited with the desired thickness (less than 100 nm), with a thin oxide protection layer (b). A 20 nm layer of Titanium is deposited for e-beam lithography to allow charge evacuation and to be used as a hard mask. E-beam lithography allows high design freedom for the design phase, but the writing process can be time consuming.

A faster approach for waveguide definition is Deep UV (DUV) lithography, (c,d) which is a classical lithographic process with a 192 nm exposition wavelength, allowing high resolution lithography. Both waveguide definition processes were used during the thesis. It must be noticed that both lithographic techniques have a sufficient resolution to allow the fabrication of Bragg gratings. A layer of High Temperature Oxyde (HTO) is then deposited (e) and treated with chemical-mechanical polishing (CMP) to have a flat surface. Finally, a second wafer with thermal oxide is bonded on top (f) and the substrate is removed (g). At this point Ti/TiN heaters are integrated through deposition (h) and lithography (i).

Once the wafer is ready, we proceed to the separation of devices. For the first batch of wafers the devices were diced and then polished on the optical accesses. The polishing was performed using an abrasive paste with Al_2O_3 nanoparticles with average size of 4 μm. This procedure is expensive and time consuming.

For the second batch the facets are directly etched on the wafer. For this procedure a thick resin mask is deposited and patterned (j); the oxide is then etched selectively to obtain a flat vertical surface (k). The remaining oxide is used as a hard mask to perform a silicon-selective Deep Reactive Ion Etching (DRIE) of around 100 μm depth (l). The DRIE process can be made highly anisotropic so that the high aspect ratio etching is feasible. The same deep etching process can be used to create on-chip suspended heaters for thermal phase adjustment (Figure 63). Only an additional step of etching is needed with respect to the facet definition: an isotropic Si etching is performed right after the anisotropic DRIE to underetch the waveguide. The devices are then separated by dicing the wafer from the rear side, as can be seen from the final cut view of the wafer (m).

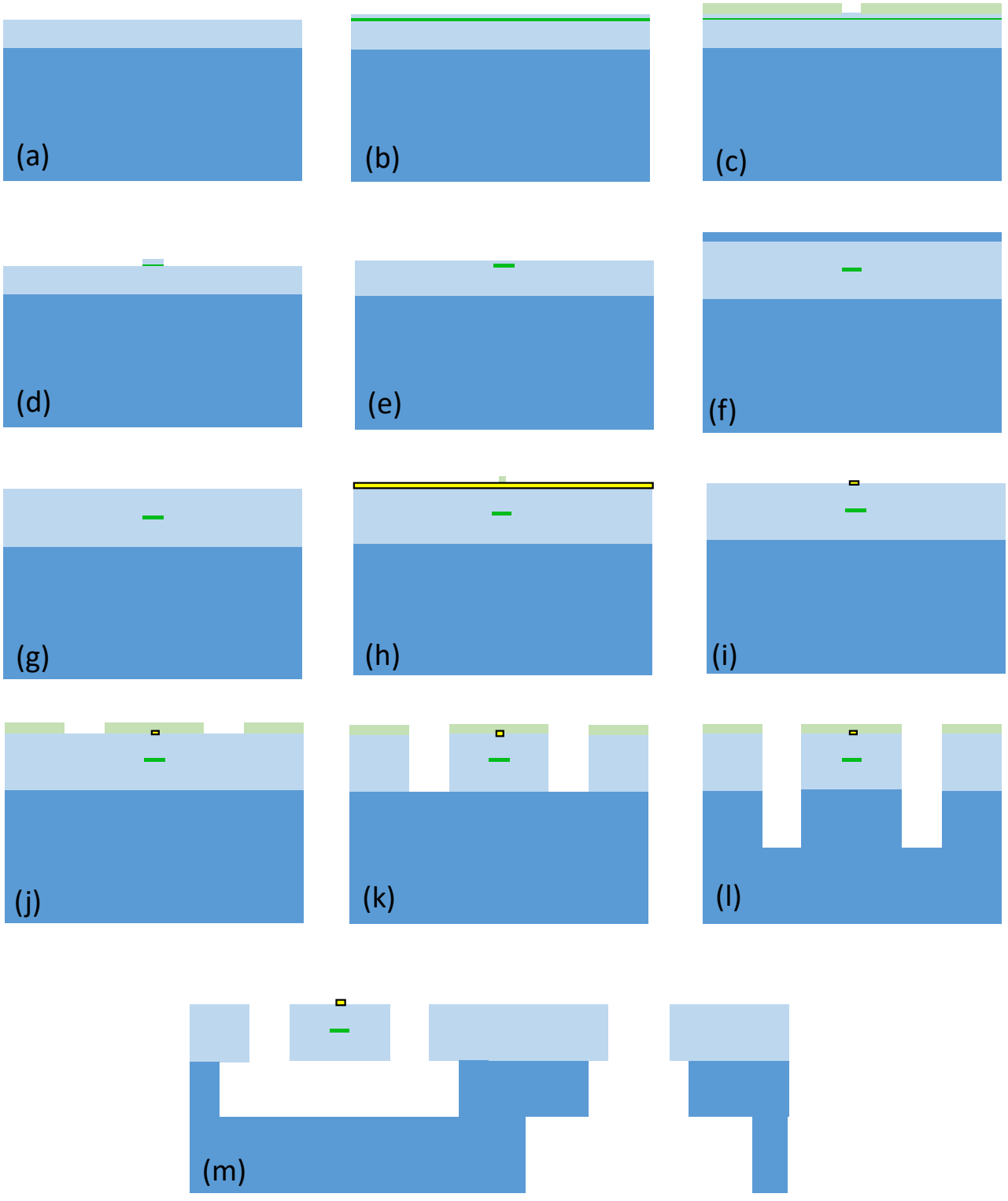

Figure 60. Complete SiN platform fabrication process flow, including suspended heater sections and etched facets definition.

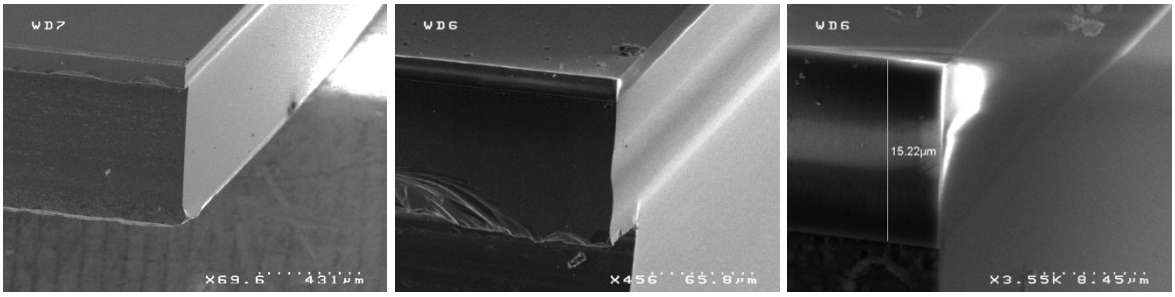

Figure 61. Wafer-level facet etching. From left to right, on can see the entire wafer, the 100 µm DRIE etching, and a view of the etched silica facet. Courtesy of J.M. Fedeli.

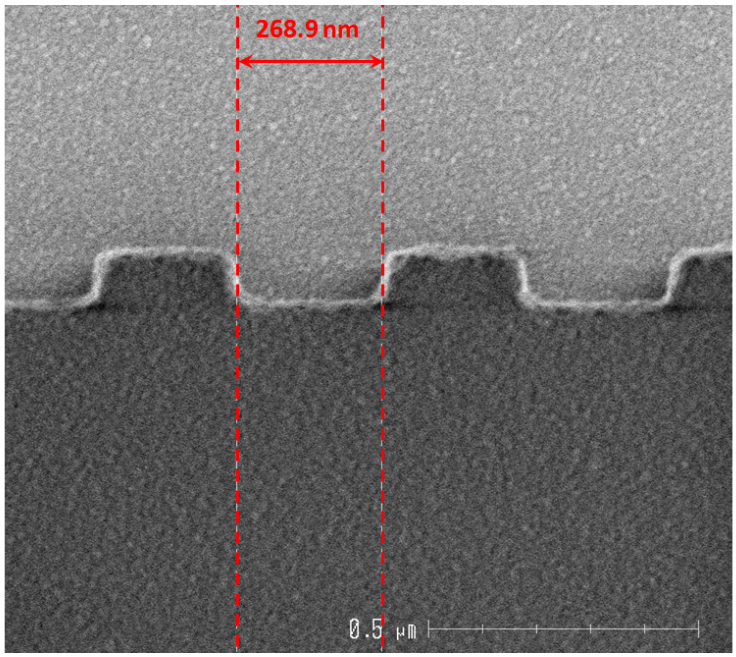

Figure 62. Scanning Electron Microscope image of a fabricated first order Bragg grating with DUV lithography. Courtesy of J.M. Fedeli.

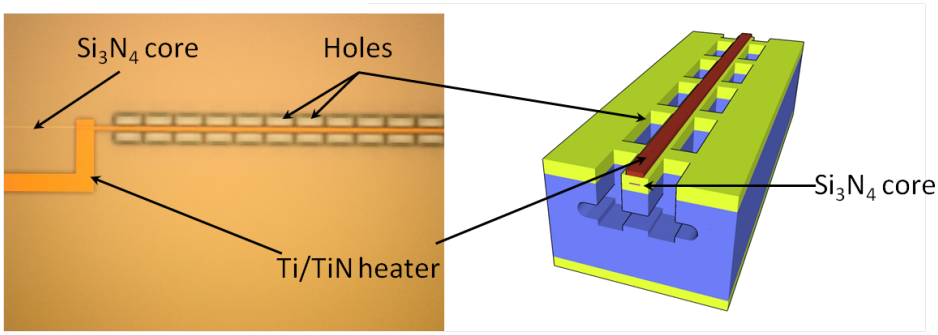

Figure 63. Microscope image and 3D view of suspended Ti/TiN heated integration on the SiN platform. Courtesy of J.M. Fedeli and S. Boust.

2.6 FABRICATED PASSIVE DEVICES

This paragraph describes the two generation of devices fabricated at CEA-Leti during the thesis. At the end of the paragraph a resumé of mask layouts is given in form of a table.

2.6.1 FIRST GENERATION

In the first generation a nitride thickness of 70 nm was used. This choice was made with a target loss of the class 1 to 10 dB/m. Four layouts for DUV lithography were designed. The dimension of the physical mask for DUV lithography is 22x22 mm. Layout masks are shown from Figure 64 to Figure 68. The main objective of the DUV batch is to have a wide number of identical samples in order to assess process reproducibility. However, as in the first generation the dicing of the wafer and polishing of facets was done manually, only few samples were processed and tested. The four layouts consist mainly in test structures or targeted devices.

Figure 64 shows a layout in which test structures were fabricated for some of the building blocks, namely the Bragg reflectors described earlier, MMI 3 dB splitters with various lengths and widths, small ring resonators to measure bending radius losses. A test structure with weak directional couplers were integrated as well. This structure has the purpose of assessing coupling strength for the first generation of ring resonators, consisting in a circular ring and a straight bus waveguide.

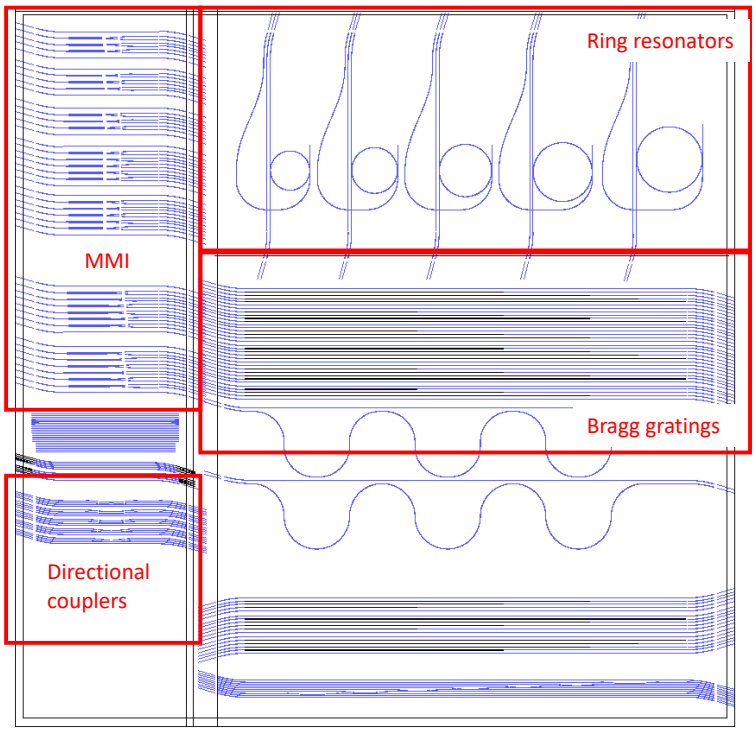

Figure 64. Test cell layout "MMICOUP" with several test structures. An entire wafer was processed with DUV lithography.

Figure 65 shows the layout of a test structure for propagation losses measurement. It consists of four delay lines with different lengths ranging from 70 to 95 cm. It has to be noticed that the integrated delay line of 95 cm has a footprint of around 1mm^2.

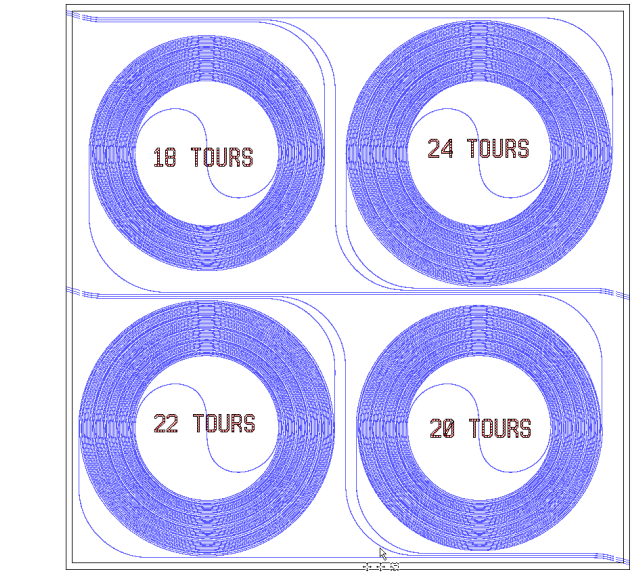

Figure 65. Test cell layout "LIGNPERT" with spirals of different lengths (up to 95 cm) for losses measurement. An entire wafer was processed with DUV lithography.

Figure 66 shows the layout for a four ports 8 mm radius ring resonator, corresponding to an FSR of 3.9 GHz. The drop port output is on the same side as the input port: these chips were designed to be directly butt-coupled to the InP OEO PIC.

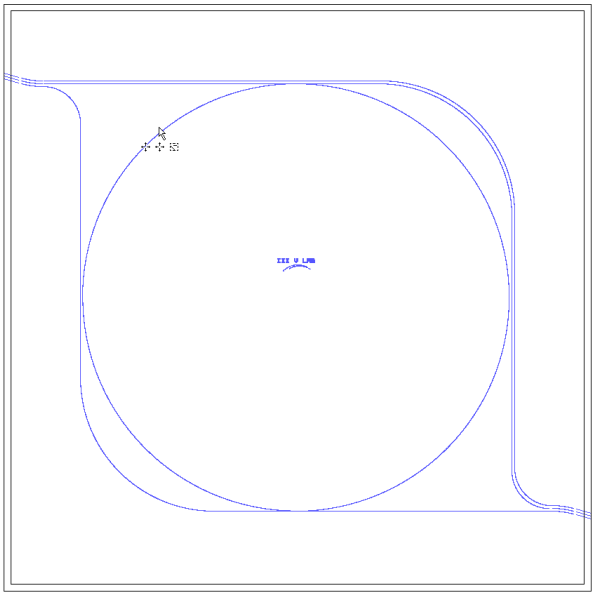

Figure 66. Test cell layout "ANN8" for ring resonators properties measurement. An entire wafer was processed with DUV lithography.

Figure 67 shows another design for the integrated OEO passive cavity. In this design a 78 cm long delay line precedes a 4 mm (7.8 GHz) ring resonator. The delay line and the ring resonator are connected "in series", meaning that the output of the delay line feeds the resonator. The two designs on the DUV mask in figure are identical in their main parameters; the circuit on top is designed to be coupled to the InP OEO PIC, while the circuit on bottom is for standalone measurements.

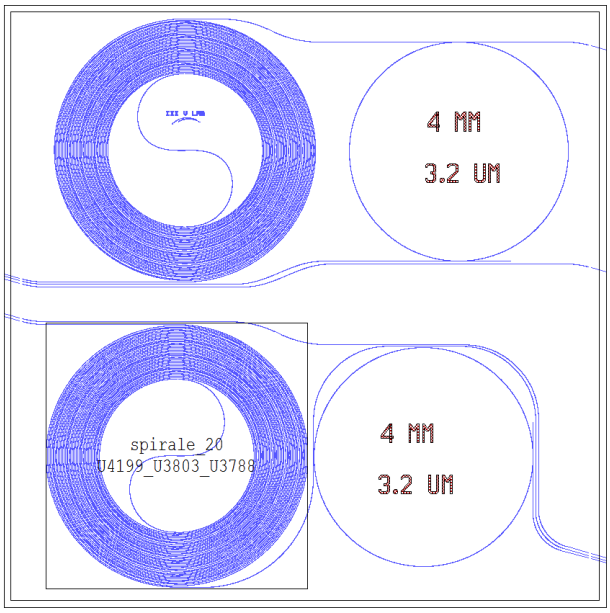

Figure 67. Test cell layout "ANN4" with a delay line and a ring resonator. Top PIC is for butt-coupling with the InP PIC, bot PIC is for fiber-assisted configurations. An entire wafer was processed with DUV lithography.

All previous designs were integrated with few more in the ebeam wafer layout, shown in Figure 68.

The other designs integrated on the mask are:

- Ring resonators of radii 3, 4, 6 and 8 mm, corresponding to 10.5, 7.8, 5.2 and 3.9 GHz, respectively;
- Ring-based reflectors for low linewidth lasers, with different design parameters;
- Passive OEO cavities similar to the one in Figure 67, with rings of 3 and 4 mm radius, with parallel or series coupling with the delay line.
- Ring reflectors for high purity Mode-locked Lasers (MLL)
- A device consisting of 9 rings of 3 mm radius, with different coupling strength.

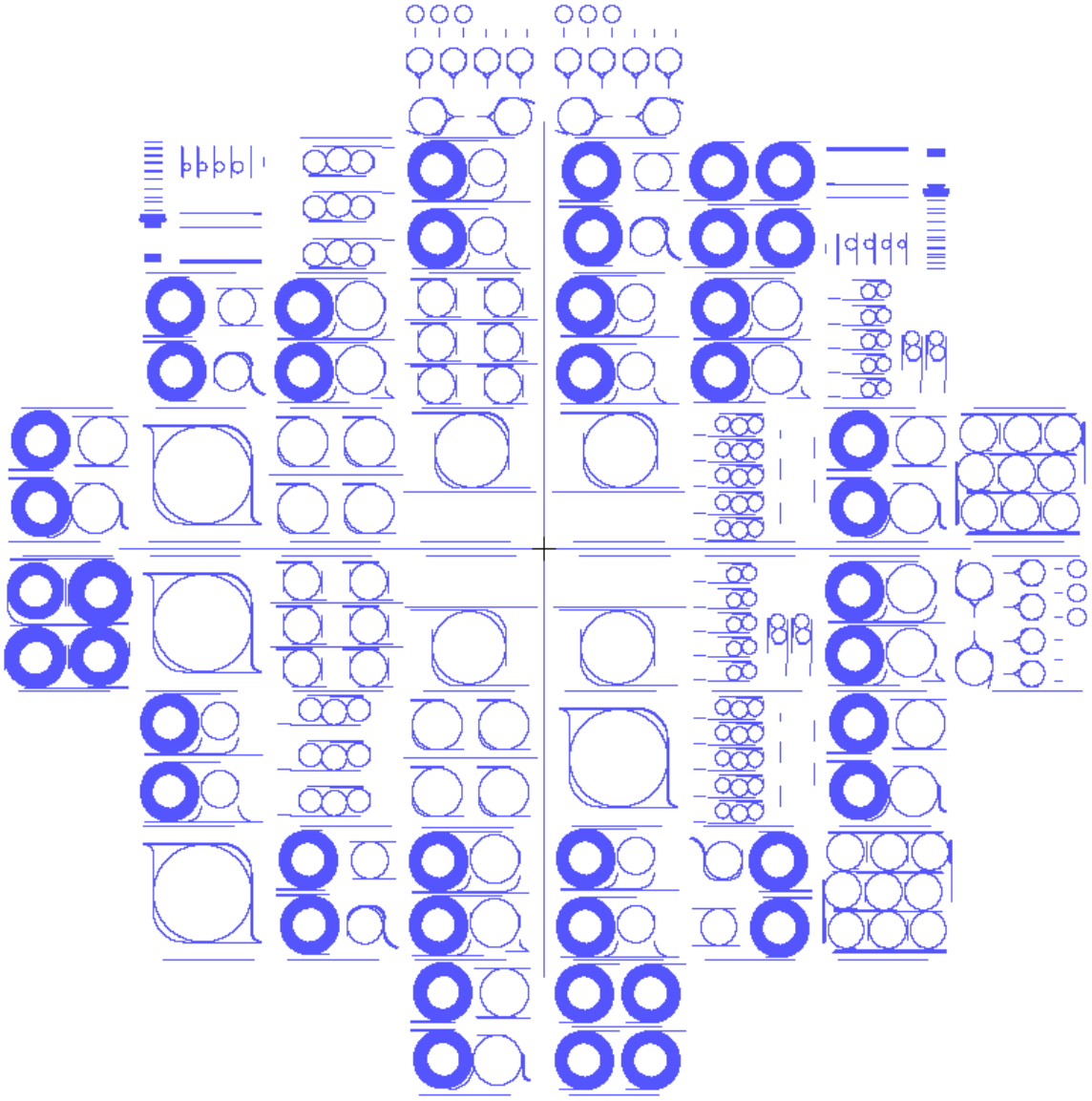

Figure 68. "OHY2" ebeam mask layout. The wafer contains several ring resonator structures with varying radius for OEO Hybrid PICs, test structures and delay lines, including the test cells produced with DUV lithography.

2.6.2 SECOND GENERATION

The results of the first generation of devices will be presented in 2.7. The first generation of devices were designed with basic building blocks and required polishing of the optical facets to be performed manually. This resulted in high propagation losses and unoptimized light coupling in and out the PICs.

The second generation of devices was fabricated with 90 nm thick waveguides, to further reduce the footprint, and integrated suspended heaters for phase shifting [59], shown in Figure 63. The design

was improved with respect to the first generation by using adiabatic couplers and bends, both for connecting waveguides and rings, as shown in 2.4.3.

OHY3 was focused on having low linewidth lasers. The layout is shown in Figure 69.

Two types of on-chip reflectors were studied:

- Bragg gratings, with different lengths and grating orders;
- Ring-based reflectors, with an integrated reflective directional coupler;
- Ring resonators coupled to Bragg gratings, for cavity length increase.

OHY4 (Figure 70) included a variety of structures to build an integrated OEO PIC, such as ring resonators and delay lines.

In terms of devices, OHY4 integrates many of the structures of OHY2, with the improved building block design.

Since the second generation wafers had very high losses (that will be presented in 2.7.1), a third generation wafer, OHY5, was fabricated after the thesis.

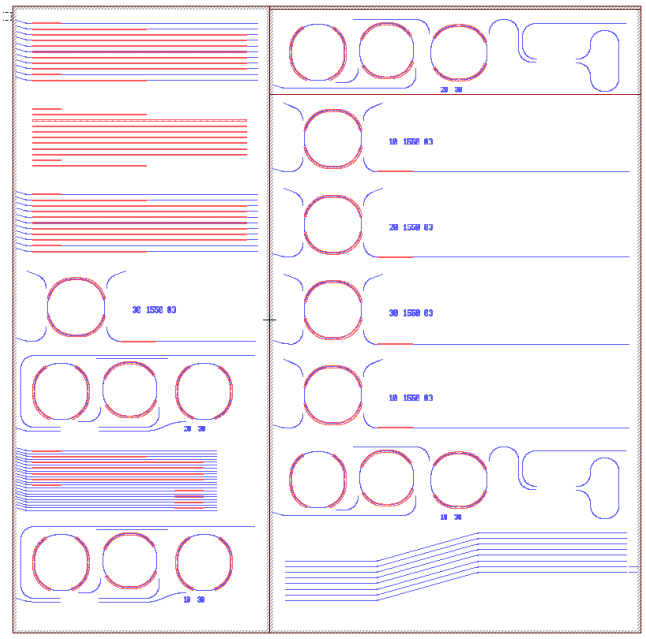

Figure 69. "OHY3" layout. An entire wafer was processed with DUV lithography. The blue mask layer is for waveguides, the red mask layer is for Ti/TiN heaters. Waveguide design includes the adiabatic bends and rings.

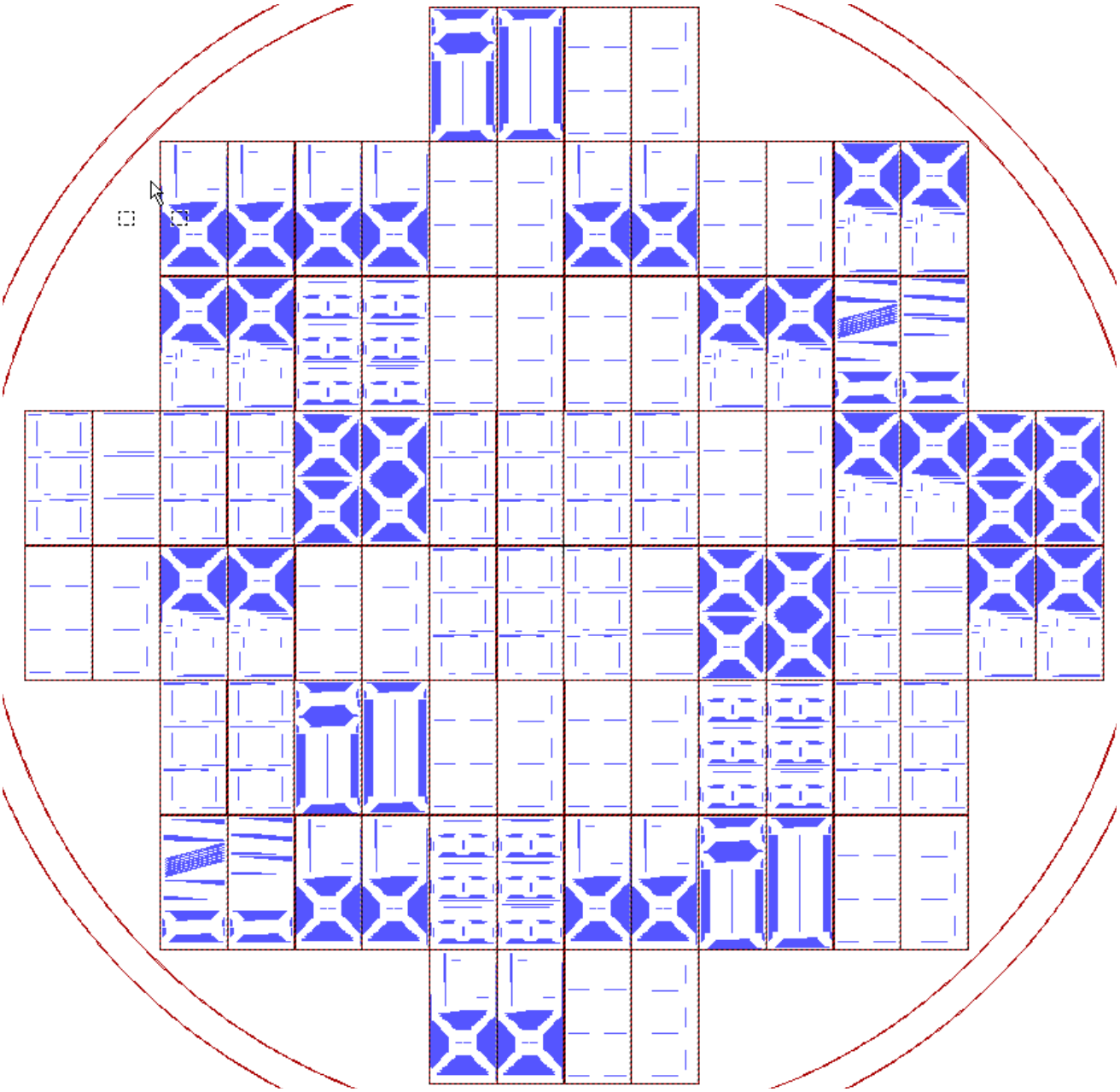

Figure 70. “OHY4” wafer mask layout with several cavity designs for integrated OEO applications, standalone ring resonators and test structures. A wafer was processed with ebeam lithography.

2.6.3 LIST OF PROCESSED WAFERS

Table 8 shows the list of fabricated wafers with the mask name reference, the generation they belong to, the corresponding waveguide thickness and the fabrication technology used.

Mask name	*Generation*	*Waveguide thickness*	*Lithography*
MMICOUP	1st	70 nm	DUV
LIGNPERT			DUV
ANN8			DUV
ANN4			DUV
OHY2			e-beam
OHY3	2nd	90 nm	DUV
OHY4			e-beam

Table 8. List of fabricated wafers during the thesis, divided by the generation of the integration platform.

2.7 DEVICES CHARACTERIZATION

In this section the measurements on the passive devices and some hybrid systems are presented.

2.7.1 PROPAGATION LOSSES

Two methods were used in order to calculate propagation losses. The first one consists in measuring the fiber-to-fiber losses of delay lines of different length. The second method extracts propagation losses starting from ring resonator measurements and is presented in 2.7.4.

The first method of measurement is straightforward. Delay lines with different lengths up to 75 cm are fabricated on test chips, as shown in Figure 65. Light is injected from a tunable laser at a wavelength of 1550 nm and collected to a photodetector through an optical fiber (Figure 71).

The equation linking the measured losses and the length of the delay line is:

$$a_{tot} = 2a_{coup} + a_{prop}L \quad [dB] \tag{51}$$

where $\boldsymbol{a_{tot}}$ is the total measured (fiber-to-fiber) losses, $\boldsymbol{a_{coup}}$ is the chip-to-fiber coupling losses (counted twice, and supposed to be equal), $\boldsymbol{a_{prop}}$ are the linear propagation losses to be found and $\boldsymbol{L}$ is

the length of the delay line. By using different delay line lengths, we can extract a linear interpolation for this equation and estimate propagation and coupling losses, as shown in Figure 72. The figure shows a measure of propagation losses of 57.7 dB/m, while coupling losses are estimated to 3.1 dB per facet with a lensed fiber.

Figure 73 shows a measurement on the second generation of wafers, where the measured propagation losses have increased to 234.6 dB/m. The reason was found to be an insufficient annealing temperature of the upper cladding oxide. An improved fabrication run of a third generation (OHY5), fabricated after this thesis, solved this issue and reduced overall propagation losses. The measured propagation losses values decreased to around 2 dB/m in this third generation.

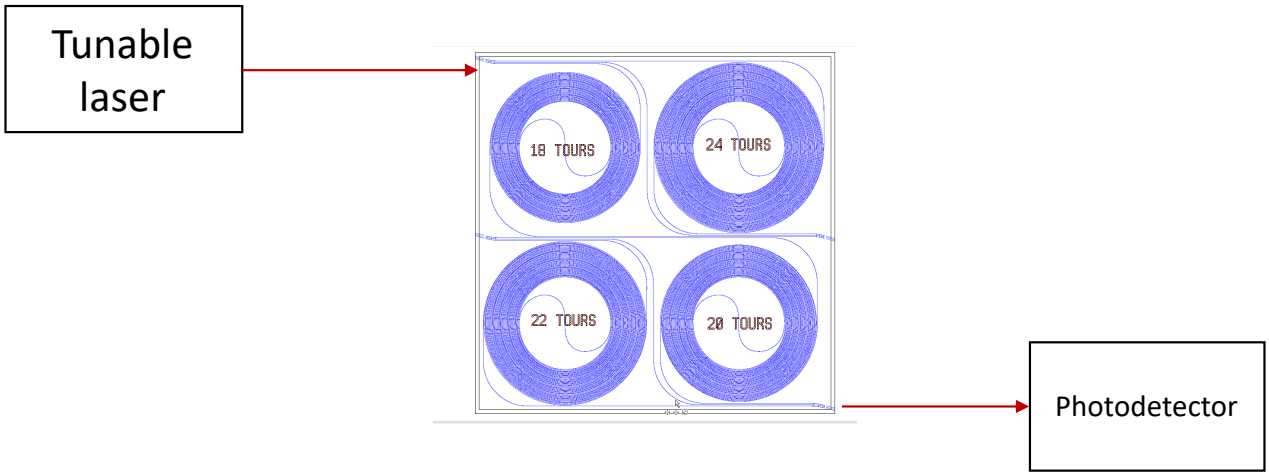

Figure 71. Measurement setup for propagation losses through delay lines. The coupling in and out the chip is performed with lensed fibers.

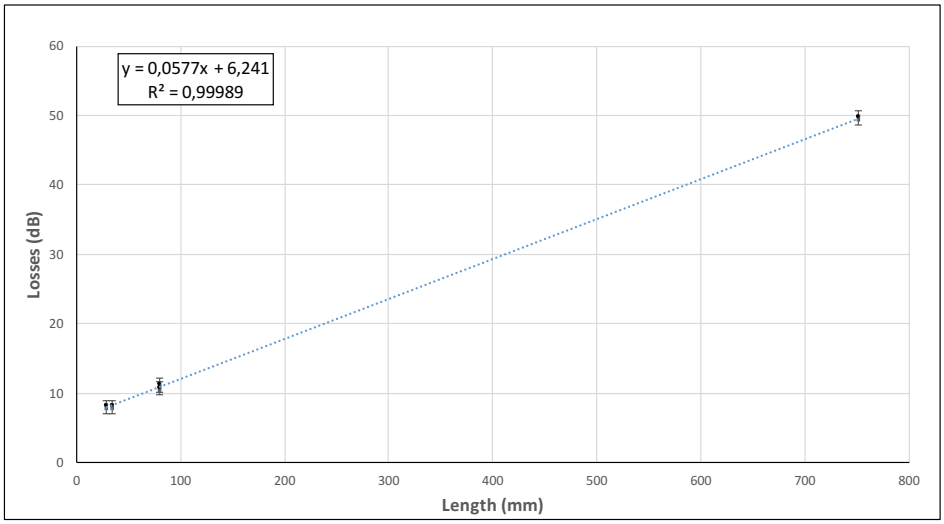

Figure 72. Data analysis of propagation losses (57.7 dB/m) and optical coupling losses (3.1 dB/facet) measured on a wafer of the first generation.

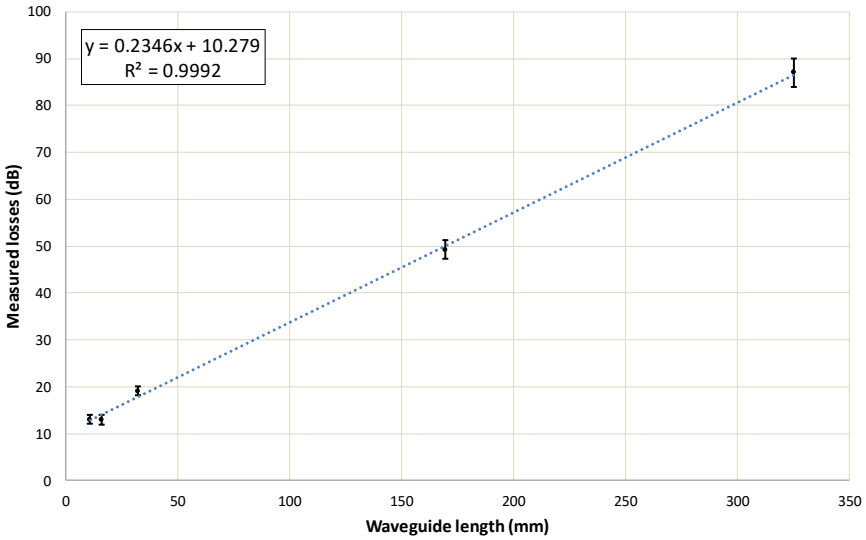

Figure 73. Data analysis of propagation losses (234,6 dB/m) and optical coupling losses (5.1 dB/facet) measured on a wafer of the second generation.

2.7.2 Mode adapter

The mode adapter was characterised to find the mode size and divergence with a far-field setup shown in Figure 74, comprising a tunable laser input and a rotating 1D detector array in order to image the beam in three directions.

The measurements are performed on 90 nm thick waveguides, on a PIC from OHY3 (second generation). Some test structures were placed on the lithography mask in order to check the variation of the mode divergence while changing the waveguide width, ranging from 500 to 1000 nm with a 100 nm step. Results are shown in Figure 75. The mode size is slightly narrower than the simulated result of 10 µm * 10 µm. This can be attributed to taper width uncertainty and from an incertitude of the refractive index of silica.

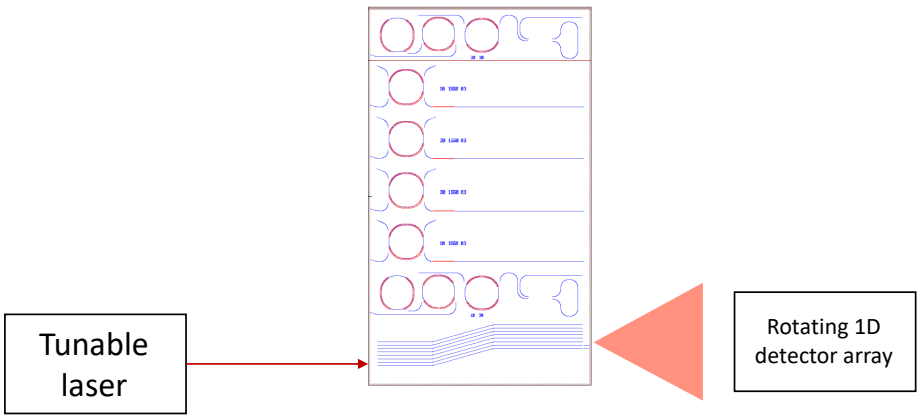

Figure 74. Far-field setup for the characterization of the mode adapter on a wafer of the second generation. Several sub-micron spot-size converters are defined with DUV lithography.

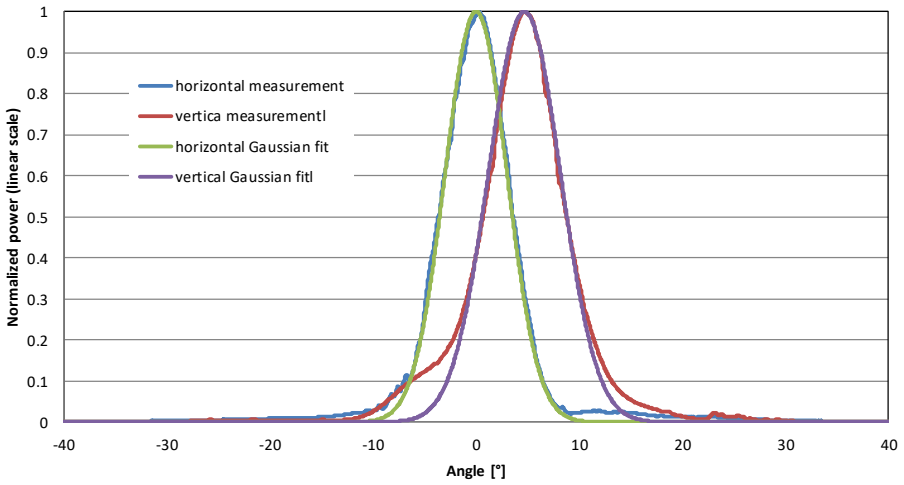

Figure 75. Far field divergence profile of a 800nm wide SSC for horizontal and vertical cut. The mode size extracted from the gaussian fit is 9.4 μm x 8 μm.

2.7.3 BRAGG GRATINGS

The measurement setup (Figure 76) mainly consists of high resolution optical spectra acquisition using APEX's Optical spectrum analyser and its built-in tunable laser, with the aid of a circulator. The reflection spectrum for different reflector parameters is acquired, with two objectives: first of all, one needs to check that the design parameters, such as the Bragg wavelength and the width of the reflection, correspond to the design; on the other hand, when resistive heaters were integrated on the wafer, we wanted to check the tunability of the wavelength with respect to the injection current.

The measurements in Figure 77 show the reflection from the first generation of wafers, where heaters were not present and such the reflection wavelength was fixed. A design wavelength of 1550 nm for the main reflection gave a peak around 1533.8 nm. This corresponds to an error in the Bragg grating dimensions of around 3 nm for a Bragg grating of 526 nm. Further designs and tunability through heaters have been demonstrated in [59].

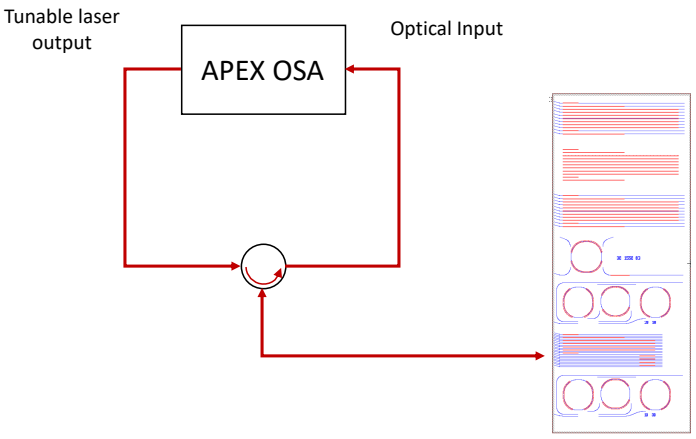

Figure 76. Optical reflectivity measurement setup for Bragg gratings characterization. The measurements are performed with a high resolution APEX OSA.

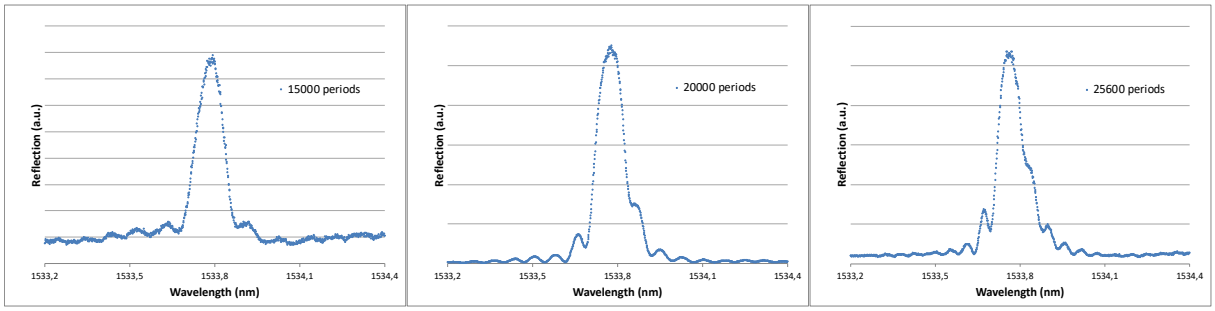

Figure 77. Measured reflection spectra of the 1st generation for 3 Bragg reflectors with different length, with a width difference in the waveguide of 30 nm. Vertical axis has a 10 dB/division scale.

2.7.4 RING RESONATORS

Ring resonators are the most important designed device for optoelectronic oscillator integration, for filtering and delay of the optical signal. The measurements carried out on those devices had two main purposes:

- The measurement of the transmission spectra;
- The evaluation of propagation losses.

The measurement of the transmission spectra is a meaningful way to understand the functioning of ring resonators. The theory of resonators was explained extensively in paragraph 2.4.3.

Four ports ring resonators were fabricated in a test structure with the layout shown in Figure 78. The idea is to extract all the parameters from identical ring resonators with different coupling strength.

Coupling distances were chosen between 2.4 and 3.2 µm, but only the first 6 rings (2.4 to 2.9 µm) could be measured due to a damage to the chip facet.

The measurement setup uses the APEX's optical spectrum analyser tunable laser output to scan in wavelength the response of the filters. The tunable laser spans from 1520 to 1626 nm. The light is coupled in and out the chip with lensed fibers.

The output signal is then coupled back to the OSA optical input. The APEX OSA is adapted to our measurements due to its high resolution (down to 5 MHz). Figure 79 presents a typical measurement result.

Several resonances are acquired around one wavelength every 5 nm from 1521 to 1626 nm, to get averaged results from scattered data.

The coupling with the drop port was not achieved due to the low power response and higher coupling losses with respect to the measurement in 2.7.1, as this measurement was performed with the first iteration of the optical coupling bench.

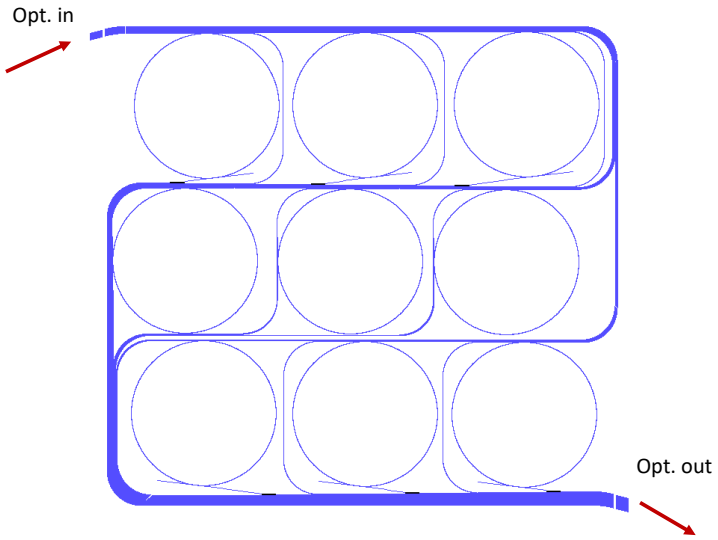

Figure 78. 9 Mask layout from OHY2 (1st gen.) for ring resonator characterization. The 9 rings have a radius of 3mm and coupler distance ranging from 2.4 to 3.2 µm.

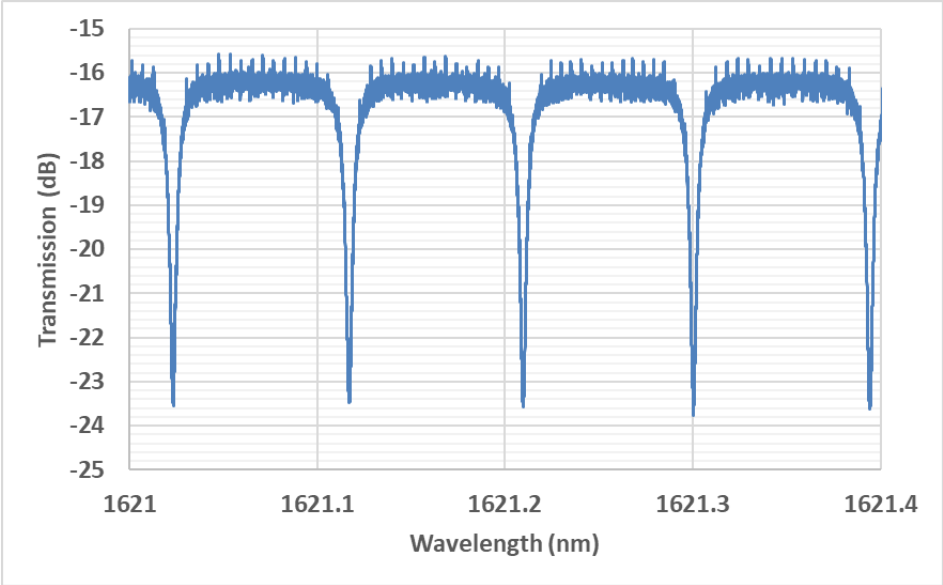

Figure 79. Characterization of the through port response of the first ring resonator. The measurement has been performed with a high resolution APEX OSA.

The mathematical treatment of the measurements raw data was performed with a MATLAB script. The script solves the following system of equations:

$$\begin{cases} E_t = \dfrac{t - t a_r e^{j\theta}}{1 - t^2 a_r e^{j\theta}} \\ \Delta\lambda = \dfrac{\lambda^2}{\pi L_{res} n_g} \dfrac{1 - a_r t^2}{\sqrt{a_r t^2}} \end{cases} \tag{52}$$

in order to extract the coupling strength t and the ring losses a_r. Since the signal from the drop port was not extracted, we don't have a third equation to distinguish between propagation losses and coupler excess losses. These two values are then treated like if losses were due to propagation losses only, and the two couplers are considered identical.

First of all, the group index is extracted. As expected, it decreases slightly with increasing the wavelength, as seen in Figure 80. There is a high dispersion of the extracted values due to the uncertainty of the wavelength response measurement of the ring. High resolution spectra require a long acquisition time in which the ring response can vary due to self-heating effects and other instabilities.

The finesse is the second parameter which is extracted. This parameter increases when the coupling strength is decreased, as shown in Figure 81 for two of the wavelengths in our measurement range. In the same figure the extinction ratio of the ring is plotted. This value is defined as the peak rejection of the filter, in dB, at resonant condition. Good resonator designs lead to high finesse thus high rejection values. The first generation of devices were limited to finesse around 20 and an filtering extinction ratio up to 7 dB.

The solution of the equation system in terms of evaluated coupler transmission coefficient and propagation losses is plotted in Figure 82.

The design value of transmission for a 2.9 μm coupler was 98.5% at 1550nm, while a value of 97% was measured. It must be reminded that the contributions of propagation losses and excess coupler losses cannot be distinguished.

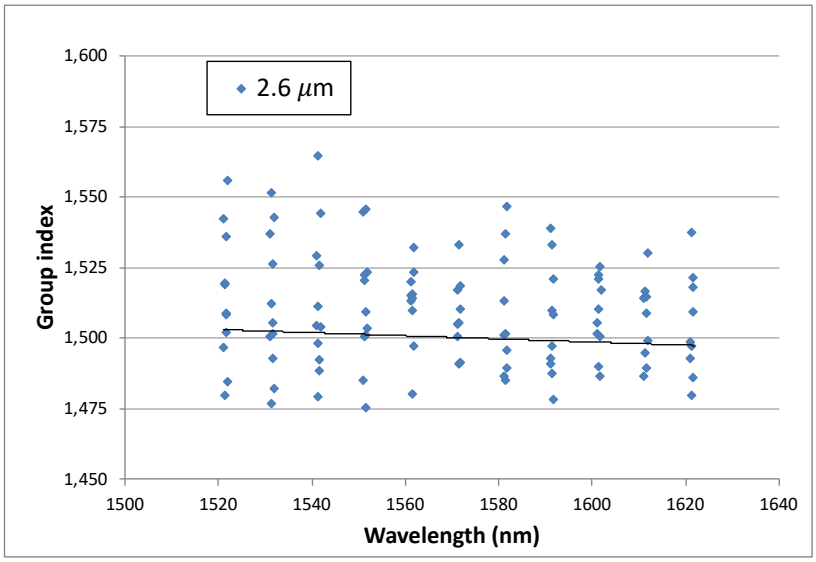

Figure 80. Group index extracted form ring resonator optical transmission spectra. The ring has a 2.6 μm gap coupler.

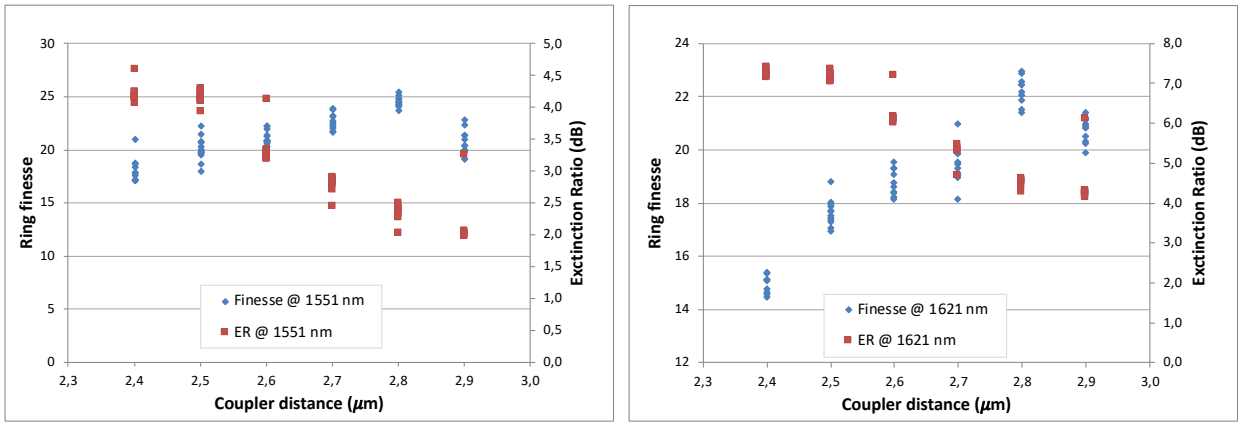

Figure 81. Extraction of Ring Finesse and Extinction Ratio from transmission spectra on the through port. Left: 1551 nm. Right: 1621 nm.

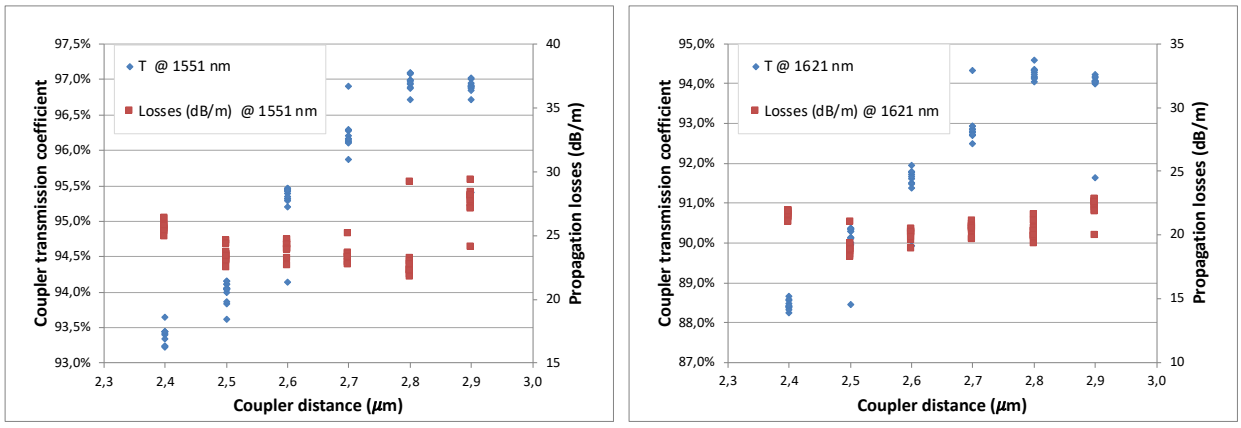

Figure 82. Extraction of coupler transmission coefficient and propagation losses from transmission spectra on the through port. Left: 1551 nm. Right: 1621 nm.

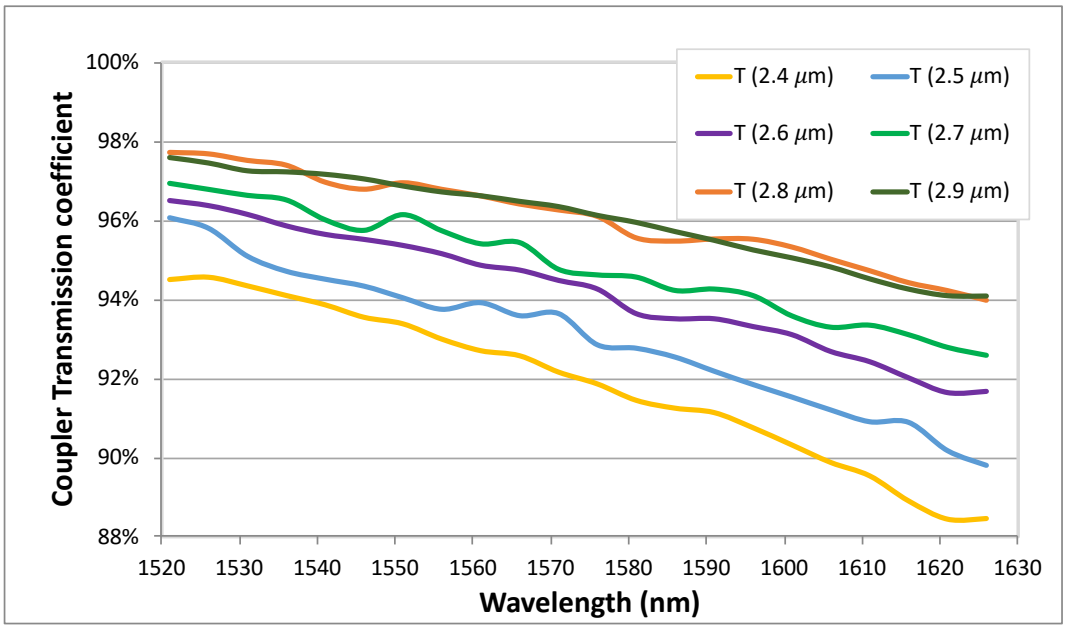

Figure 83. Average coupler transmission coefficient in function of wavelength for different coupler gap.

Figure 83 shows the extracted transmission value, in percentage, of the measured resonators. The design targeted low losses and coupling strengths between 1 and 5% at 1550 nm. While the coupling strength was reasonably well controlled, the resonators resulted strongly undercoupled due to propagation losses higher than expected.

For all measured values there is a gap with respect to the computed coupling values, and the transmission value is slightly overestimated. However, the transmission in function of wavelength corresponds to a weak coupler, as the cosinus-like dependence from the wavelength is very weak. The coupling of the 2.8 and 2.9 μm couplers are almost superimposed, showing a problem for these two values of coupling strength.

Propagation losses in function of the wavelength are shown in Figure 84. The extracted losses parameter, a_r, is measured in equivalent dB/m, as the coupler excess losses cannot be distinguished from propagation losses.

For the lowest losses case, broad peaks at wavelength which might be due to N-H bonds are observed. Longer wavelengths do not suffer this material-induced effect; thus, the propagation losses are lower.

It must be noticed that the losses measured with the ring resonator method does not correspond to the values of 57.7 dB/m measured with the delay lines. The reason could be an inhomogeneity on the wafer due to the very high strain-induced wafer bending, produced by the very thick (>13 μm) oxide layer.

The design of the ring couplers for OEO application targeted losses lower for an order of magnitude. After the end of the research activity covered by this dissertation, several improvements have been made in the fabrication process, strongly reducing the overall propagation losses, and in the design, introducing the adiabatic directional couplers for ring resonators. The new ring resonator design is shown in the mask layout in Figure 85. The response of a ring of the improved second run (OHY5) is shown in Figure 86. The propagation losses measured on the wafer were 2 dB/m. The extinction ratio is improved to more than 50 dB of rejection at 1630 nm, to be compared with Figure 79.

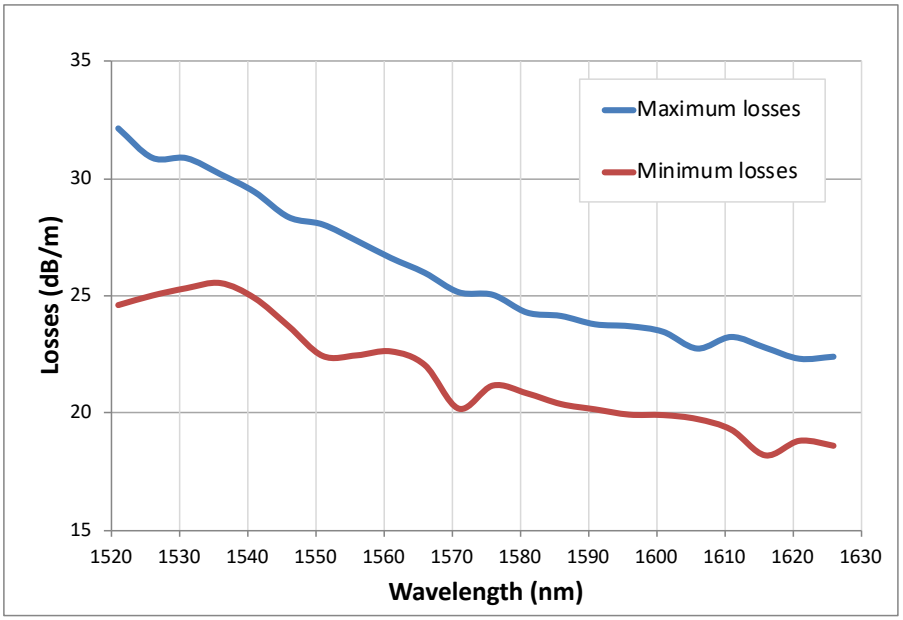

Figure 84. Best and worst extracted propagation losses from ring resonator optical spectra. In the lower curve, the broad absorption at 1535, 1560 and 1575 nm might be due to N-H bonds.

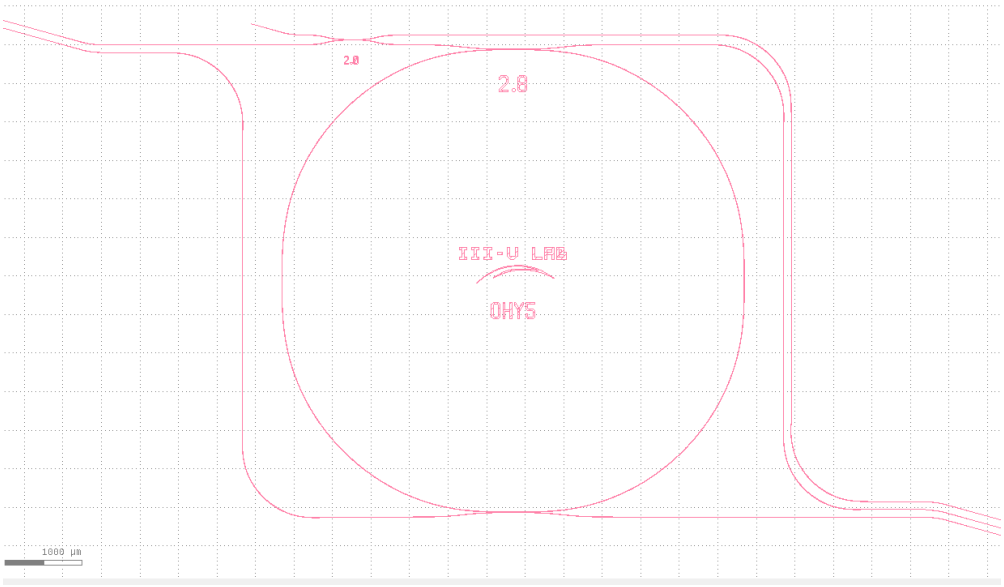

Figure 85. Improved ring layout for 10 GHz filtering. The wafer OHY5, from the third generation, implemented the soft bend ring design and adiabatic directional couplers.

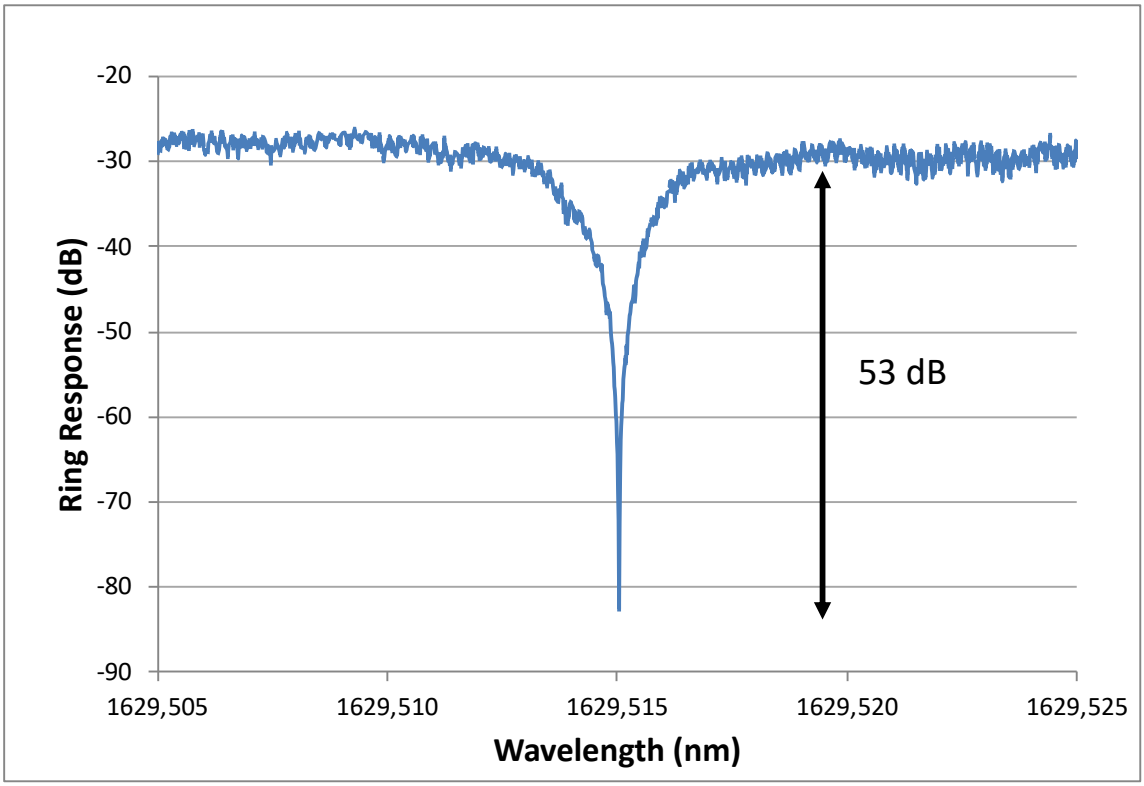

Figure 86. Ring resonator through port measurement from OHY5.

2.8 CONCLUSIONS AND PERSPECTIVES

This chapter presented the passive photonic integration platform that was chosen and developed during the thesis.

The choice of high aspect ratio waveguides fabricated in SiN on SiO_2 was motivated by the analysis of loss processes in rectangular waveguides and a review of the available platforms. The main parameters considered in the choice were the potential of very low propagation losses, in the class of 1 to 10 dB/m, the capability to integrate ring resonators and delay lines in a reasonable footprint and the availability of integration techniques with an active PIC made on InP.

The design of several building blocks and their relative measurements were shown throughout the chapter. At the end of the 3-year Ph.D. the SiN passive integration platform developed with CEA-LETI had the availability of building blocks such as input/output optical mode adapters, optimized bend sections, ring resonators, directional couplers, Bragg reflectors. These building blocks allow for the design of complex PICs for a variety of applications of hybrid III-V/SiN components like Integrated Opto-Electronic Oscillators, low linewidth lasers with different reflector architectures and mode-locked lasers for optical comb generators, to name a few.

Propagation losses were measured as well, but both generation of wafers resulted having very high losses, ranging between 20 and 200 dB/m depending on the generation of the wafer or the measurement method. These values are however inadequate for microwave photonic filtering applications.

The technological process and the design were improved throughout the generations of wafer, until the wafer OHY5 of the third generation, which gave the best results so far in terms of losses (2 dB/m) and filtering capabilities and opened up interesting perspectives for the later research at III-V Lab.

The improvements in the technological process came from different aspects of the design of the PIC. The first example is the difficulties found on the thin waveguides (70 nm) of the first generation: the thickness of cladding oxide needed to avoid coupling towards the Silicon substrate was around 26 μm (considering upper and lower cladding), which would cause a significant bow (around 500 μm) of the wafer and caused the break of the wafer itself on one occasion due to the accumulated strain. This event drove the design towards thicker waveguides (90 nm), which needed thinner oxide cladding but also had the advantage of reducing the minimum curvature radius resulting in reduced overall footprint of the PICs or a larger number of integrated functions.

A second improvement was the definition of etched facets within the fabrication process. In the first generation the wafer was cleaved in quarters, then diced to separate each cell. Despite using a relatively thin saw disk, the quality of the facet was still not good enough to allow efficient coupling in and out the passive PICs, thus a manual polishing of the facets with Al_2O_3 nanoparticles was needed; however, this process was expensive, time consuming and not reproductible. The definition of facets by etching and subsequent separation of the components by back-side dicing drastically improved the overall quality of the produced components.

3 ACTIVE CIRCUIT ON INDIUM PHOSPHIDE FOR OPTOELECTRONIC OSCILLATORS

Integrated microwave photonics is the key technology for compact generation, processing and transport of high speed analog signals. This chapter reviews and describes the InP integration platform used at III-V Lab for active devices. The description and design of building blocks is presented as well. The outcome of this chapter is the active PIC described in Chapter 1, in which a laser, a modulator, a photodiode and several optical amplifiers are monolithically integrated.

3.1 INTRODUCTION

Chapter 1 described the general hybrid PIC architecture, and Chapter 2 introduced the passive SiN/SiO_2 platform for delay and filtering functions.

This chapter describes the integration platform on Indium Phosphide (InP) substrate, where active components for light generation, modulation and detection are fabricated.

The first section of the chapter describes the InP material system, and how InP-related materials can be used for building block fabrication. A brief treatment of the physics of quantum wells is presented, in order to introduce the mechanisms behind light generation and absorption. All building blocks rely on a P-I-N diode structure, which is presented at the end of the section.

The second part describes the Semi-Insulating Buried Heterostructure (SI-BH) integration platform of III-V Lab. A strong emphasis is put on how to design and integrate two different active regions for light generation and absorption purposes.

The third section presents the several building blocks needed in the PIC and the integration within our SI-BH platform.

The fourth section is devoted to the description of the technological process flow for the fabrication of InP PICs in the SI-BH platform.

The fifth section describes the design of the Application- Specific Photonic Integrated Circuit (ASPIC), presented in Chapter 1, for integrated Opto-Electronic Oscillator applications. The PIC includes a CW DFB laser, an electro-absorption modulator (EAM), several optical amplifiers (SOA) and a photodiode. The target chip layout is shown in Figure 87. The PIC was fabricated in a Multi-Project Wafer fabrication run targeting high speed Externally Modulated Lasers (EML) and EML with booster SOAs. The building blocks of these configurations and the OEO PIC are the same, and the design of each building block is discussed throughout the chapter.

The last section presents the measurements performed on the building blocks of the PIC. Such measurements assess the design of each component and allows us to understand how they will behave at the system level.

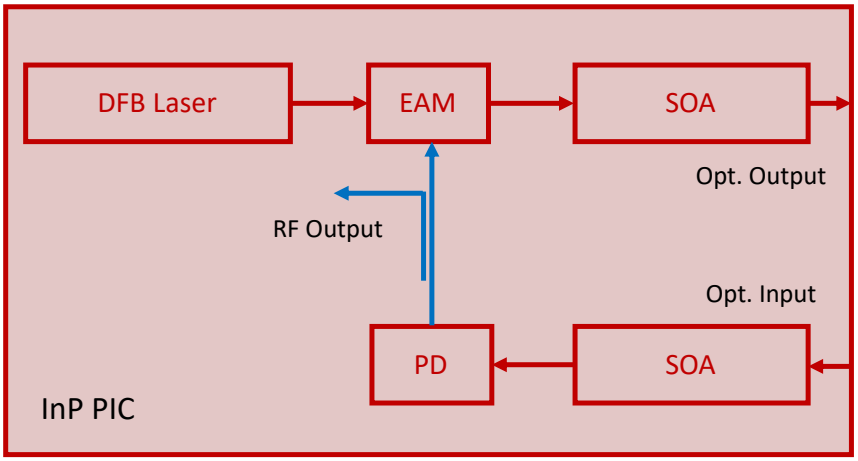

Figure 87. Active PIC architecture on Indium Phosphide photonic integration platform.

3.2 InP material system for active PIC integration

This section describes the Indium Phosphide material system and the physics behind multi quantum well structures.

3.2.1 Physical properties of InP-related materials

Indium Phosphide and related materials are the platform of choice for active components fabrication in the 1.5 μm wavelength region.

Indium Phosphide is a binary semiconductor made of Indium and Phosphorus, with a zinc-blende (face-centered cubic, FCC) lattice, like most of III-V semiconductor materials. It has a 5.8687 Å lattice constant. Indium Phosphide is used in combination with its related alloys in order to build opto-electronic devices. These materials are usually lattice-matched to InP, in order to have high quality material growth. Material strain (tensile or compressive) can be used to engineer the optical properties of such materials, especially when combined with quasi-2D structures like quantum wells.

The main ternary alloy used in opto-electronic devices fabrication is $In_{1-x}Ga_xAs$. One can change Indium and Gallium concentrations to change the parameters of the material, such as photoluminescence wavelength and refractive index. The lattice-matched ternary alloy, a special case of the generic material, is $In_{0.53}Ga_{0.47}As$. Its Photoluminescence wavelength lies at 1.67 μm. It is mostly used for photodiode absorption layers.

There are two families of quaternary alloys lattice matched to InP, namely InGaAsP and InAlGaAs. We concentrate here on InGaAsP materials, which is the one of choice in the majority of fabrication runs at III-V Lab.

InGaAsP belongs to a family of alloys of the kind $A_xB_{1-x}C_yD_{1-y}$. The properties of such semiconductor can be found by combining the properties of the basic binary semiconductors. Each property ***b*** of the material can be roughly estimated with the formula:

$$b(x,y) = (1-x)yb_{InAs} + (1-x)(1-y)b_{InP} + xyb_{GaAs} + x(1-y)b_{GaP} \qquad (53)$$

for a generic $In_{1-x}Ga_xAs_yP_{1-y}$ alloy. It must be noticed that the lattice matched InGaAs is a special case of the above formula. Relevant properties of InP, other binary III-V semiconductors and the related alloys are listed in Table 9.

In Figure 88 is shown the relationship between lattice constant and the bandgap energy of III-V semiconductor materials, reworked from [60]. Two additional materials are added in the figure as a reference, namely InGaAs and Q117. Q117 is one of many quaternary InGaAsP alloys grown at III-V Lab, having Photoluminescence (PL) wavelength around 1.17 μm, hence the name. It is the material of choice for quantum well barriers or waveguide slabs.

Layers of alloys and materials are grown on InP wafers by MOVPE (Metal-Organic Vapor Phase Epitaxy) or MBE (Molecular Beam Epitaxy). Both epitaxial techniques allow nm-scale control of the layer thickness.

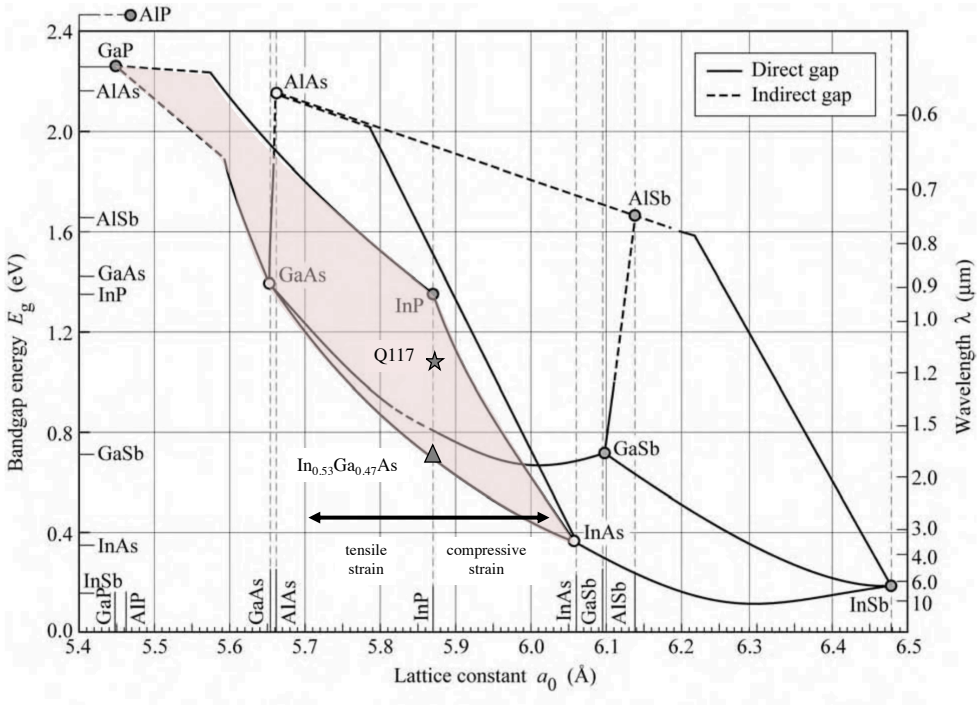

Figure 88. Bandgap and lattice constant of the main III-V semiconductor materials. The shaded red area is the InGaAsP design region. Lattice-matched InGaAs and the "Q117" InGaAsP grown at III-V Lab are shown. Reworked from [60].

Alloy	*Type*	*Bandgap (eV)*	*PL (μm)*	*Lattice constant (Å)*
InP	Binary	1.35		5.8687
GaAs	Binary	1.43		5.65325
InAs	Binary	0.36		6.0583
GaP	Binary	2.26		5.4505 A
InGaAs	Ternary		1.67	InP
InGaAsP	Quaternary		0.95 – 1.67	InP
Q117	Quaternary		1.17	InP

Table 9. Properties of III-V semiconductors and of the InGaAsP family of alloys. From [61].

3.2.2 PHYSICS OF QUANTUM WELLS

A quantum well is a stack of three materials in which the middle one has a lower bandgap than the surrounding ones. This configuration creates a finite potential barrier for electrons and holes as shown in Figure 89.

The following treatment only considers 3 bands of interest: the conduction band, the heavy holes and the light holes band.

We can solve the Schrodinger equation for the electrons:

$$\left(-\frac{\hbar^2}{2}\frac{\partial}{\partial z}\left(\frac{1}{m_e(z)}\frac{\partial}{\partial z}\right)+\Delta E_c(z)\right)\Psi(z)=E\,\Psi(z), \tag{54}$$

where $m_e(z)$ is the effective mass of electrons and $\Delta E_c(z)$ is the barrier height, with zero value in the well and ΔE_c on the barriers.

The previous equation represents the well-known quantum mechanics problem of a particle in a finite height potential well. The solutions of the equation are discrete (quantized) with energy eigenvalues [62]:

$$E_n=\frac{\hbar^2}{2m_e}\left(\frac{n}{\pi L_z}\right)^2, \tag{55}$$

where n is the quantum number, the mass of the electron is the mass in the well material, L_z is the well width.

The corresponding wave function is a cosine peaked at the centre of the well, for the first energy level. The particle is thus confined in the well.

As we solve the equation for the two relevant valence bands (Heavy Holes and Light Holes), we can calculate the transition energy between valence and conduction band states.

The band structure of a quantum well is shown in Figure 89, with the relevant transition energies.

While the energies are quantized in the ***z*** direction, they follow a parabolic curve in the other two directions, thus the energies allowed for electrons in the conduction band can be written as:

$$E_n(k) = E_n(0) + \frac{\hbar^2 k_\perp^2}{2m_{e\perp}}, \tag{56}$$

where the effective masses and the wavenumber are calculated in the two directions perpendicular to the ***z*** axis and $E_n(0)$ is the quantized energy found in Equation 55.

One important parameter that can be calculated from the previous relation is the (2D) Density of States $\rho_{2D}(E)$, counting how many electronic states are available in the band structure for a given energy. The 2D Density of states in a quantum well is shown in Figure 90. It can be seen that many electronic subbands contribute to the total density of electronic states, with one parabolic relation like the one in Equation (56) per each discrete eigenvalue of the quantum well itself. The Density of states of the first electronic subband (hence the superscript in the equation) is described by: 56

$$\rho_{2D}^{(1)}(E) = \frac{m_r}{\pi\,\hbar^2 L_z}, \tag{57}$$

where m_r is the reduced mass defined as $m_r = (1/m_e - 1/m_h)^{-1}$, taking into account electrons (m_e) and holes (m_h) contributions for the given electronic transition.

The density of states will strongly influence the rate of electronic transitions for a given photon energy, as we will see later on.

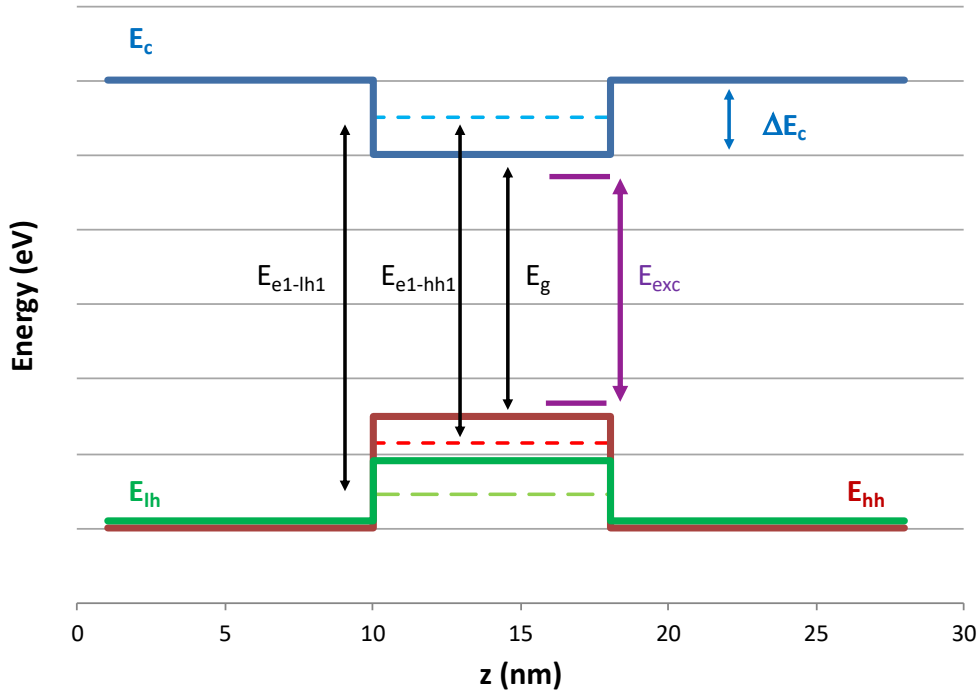

Figure 89. Quantum well energy band structure, with electron and hole energy levels. Several electronic transitions are .

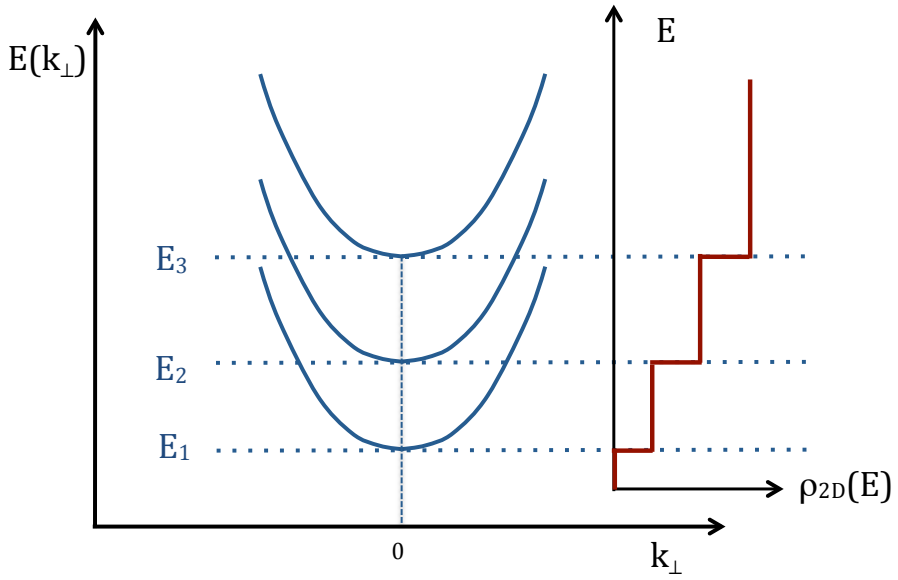

Figure 90. 2D Density of states for a quantum well structure.

3.2.3 PHOTON-ASSISTED ELECTRONIC TRANSITIONS

We already mentioned electronic interband transition processes in Chapter 2, as a loss mechanism in semiconductor materials: an electron is excited from the valence band to the conduction band with the absorption of a photon. But electronic transitions can happen in both directions, with an electron falling in the valence band with the emission of a photon.

Two emission mechanisms are possible. The first one is the spontaneous emission, in which an electron decays from the conduction to the valence band spontaneously, and the properties of the emitted photon (phase, polarization, wavelength) are governed by quantum mechanics and depend on the transition and its energy, but also on the starting and arriving electronic band (Pauli's exclusion principle).

The second mechanism is the stimulated emission, where an electronic decay with the emission of a photon is triggered by the interaction with an exciting photon. The emitted photon has the property to be identical to the exciting photon; in this case, the selection rules for energy and momentum conservation are automatically satisfied. This mechanism is the basis of optical gain in materials.

The three mechanisms of absorption, spontaneous emission and stimulated emission are shown in Figure 91.

Let us mention that the excitonic energy shown in Figure 89 comes from the Coulomb interaction of two charged particles [63]. In our case the particles are free electrons and holes in the conduction and valence bands, respectively, that can form a bound state quasi-particle, an exciton, with a binding energy lower than the bandgap. This can lead to an absorption peak at energies lower than the bandgap.

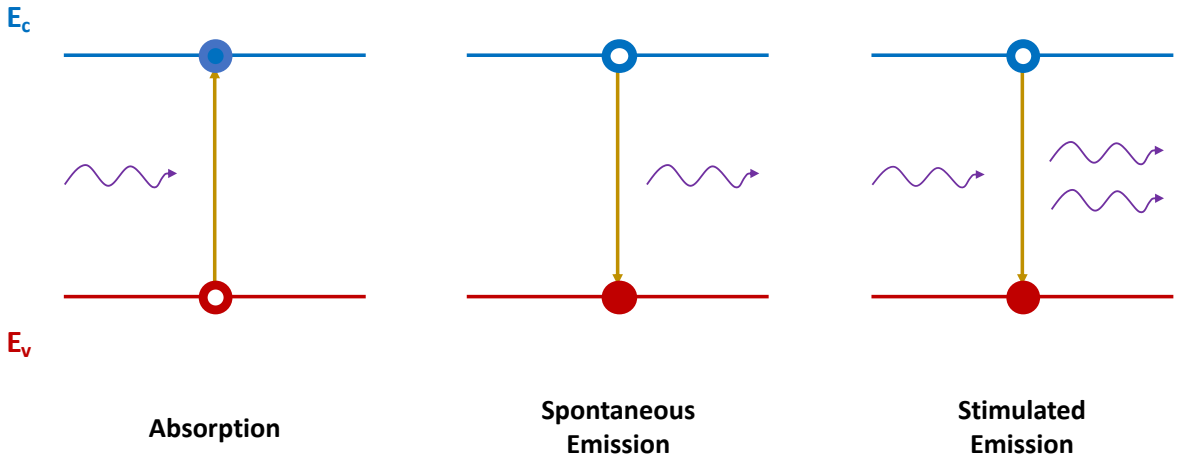

Figure 91. Photon-assisted electronic transitions between valence and conduction bands in a semiconductor material.

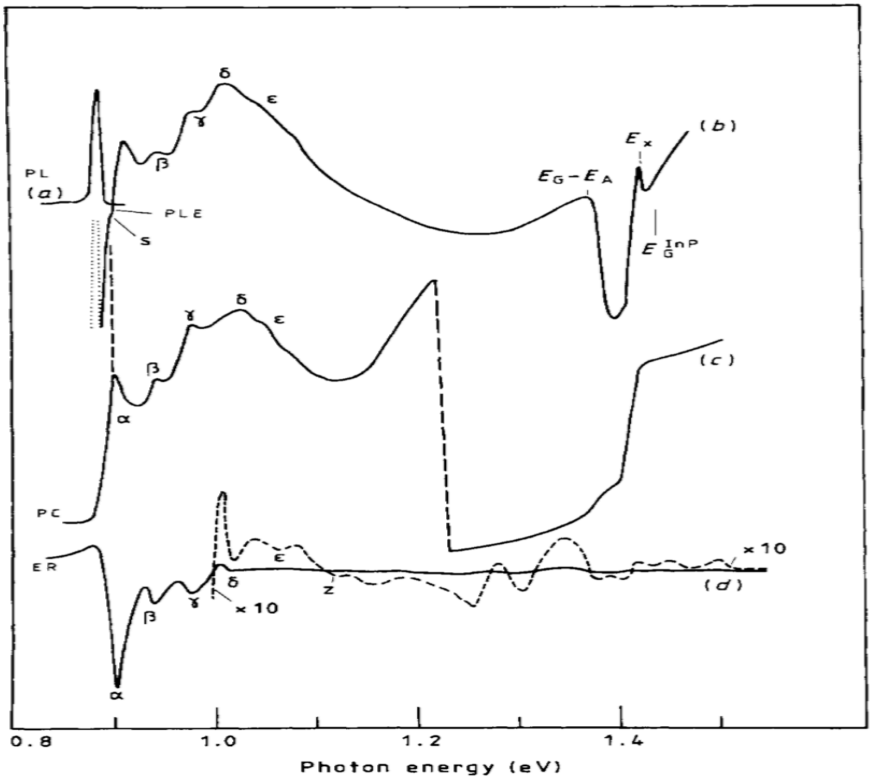

Figure 92. Figure reprinted from [63] showing the photoluminesce (a), PL excitation (b), photoconductivity (c) and electroreflectance (d) spectra for a 11 nm quantum well.

3.2.4 GAIN IN SEMICONDUCTOR MQW STRUCTURES

As seen in Figure 91, we can consider a semiconductor as a two-energy level system in which the excited level is the conduction band while the ground state is the valence band.

Absorption and stimulated emission are twin processes governed by the same equation, just with a reversed sign, and are the two processes governing the optical gain. The spontaneous emission phenomenon is still present, but in laser design is often considered as an optical noise floor.

We have seen in Paragraph 3.2.3 that selection rules must be applied in order to allow electronic transitions between electronic bands. Each of these transitions will have a specific strength, which can be identically zero for forbidden transition. The strength of the transition will then depend on the material itself and its energy band structure, which can be engineered with strain applied on the material, but also from the properties of the photon who participates to the light-matter interaction, influencing the selection rules for electronic transitions. All these contributions to the transition strengths are described with a transition matrix, describing the probability to have a transition from a given initial state of the particle to a given final state.

For these transitions to happen there must be some free carrier available in one of the bands and some free final state: each process' rate is thus directly proportional to the carrier densities of the particles.

In equilibrium, the valence band will be strongly populated by electrons, while the conduction band will have a very low number of electrons, due to the position of the Fermi level in a semiconductor material. The photons entering the structure will be absorbed if there is an electronic transition of the same energy.

Out of equilibrium, when a net amount of charge is injected in the quantum well, the quasi-Fermi levels of the particles will move to account for the net charge. The net recombination rate is directly proportional to the carrier density difference in the two levels: starting at low carrier injection and increasing the injection level, the losses will be proportionally reduced, until the point at which the processes of absorption and stimulated emission are in equilibrium and the material becomes transparent.

When the amount of free carriers in the excited state exceeds the amount of free carriers in the ground state, we observe a condition called population inversion. In this condition the stimulated emission rate increases, and the material is said to have optical gain, which is described by [64]:

$$g_{mat}(\hbar\omega) = \frac{\pi e^2 \hbar}{2m_e^2 \epsilon_0 n_r c} \frac{1}{\hbar\omega} |M|^2 \rho_{2D}(\hbar\omega)(f_c - f_v) \tag{58}$$

where $\boldsymbol{e}$ is the unit charge, $\boldsymbol{m_e}$ is the electron effective mass, $\boldsymbol{n_r}$ is the refractive index, $\hbar\omega$ is the photon energy, $\boldsymbol{M}$ is the transition matrix element, $\boldsymbol{f_c}$ and $\boldsymbol{f_v}$ are the conduction band and valence band Fermi functions, respectively.

Figure 93 shows the material gain for a typical design of quantum well gain at III-V Lab. The simulation was performed with BCBV, a MQW gain calculation software developed at III-V lab.

The well has compressive strain, with a lattice parameter higher than InP. As already mentioned, strain in semiconductor heterostructures drastically change the transition matrix element $\boldsymbol{M}$ and, due

to the modified selection rules, it might favour TE or TM-polarized light emission. Compressive strain in quantum well materials favors TE light gain, as shown in Figure 93.

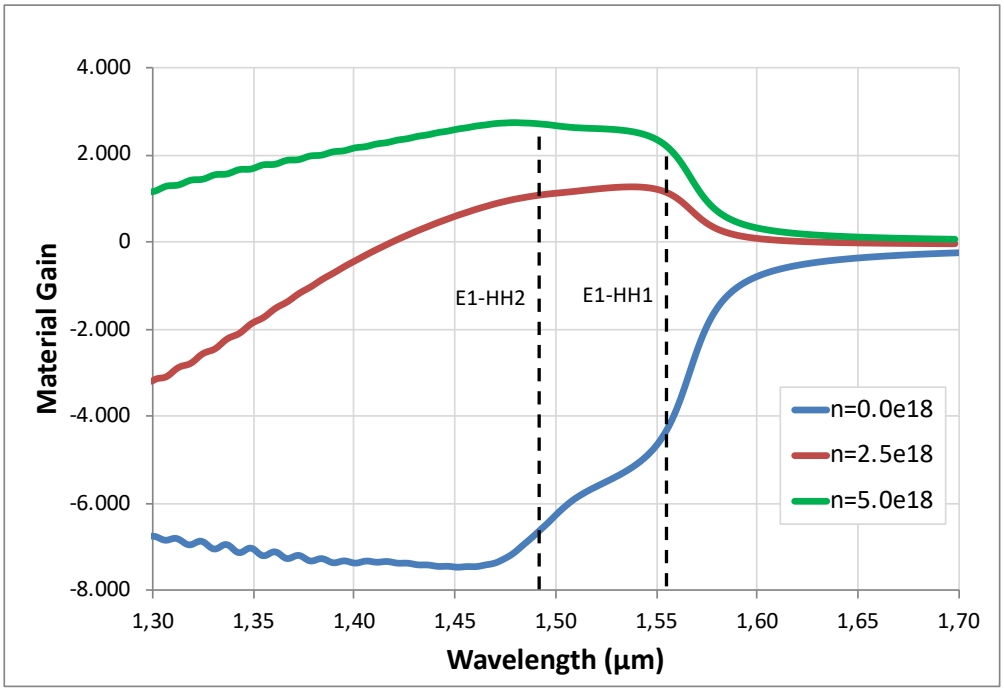

Figure 93. (TE) Material gain for typical quantum well design: 8 nm well with PL 1.57 µm and compressive strain, 10 nm barrier made of Q117. The parameter ***n*** is the injected carrier density (cm^{-3}).

3.2.5 Quantum-Confined Stark Effect

We have seen how radiative transition obey fundamental physical laws and can be described in terms of transition energy by a Hamiltonian corresponding to a finite potential well. This Hamiltonian is modified when an external voltage is applied to the structure.

The band structure is tilted linearly due to the corresponding electric field. The energy levels of electrons and holes are modified as well (Figure 94), thus the transition energies are different between the biased and unbiased states. From Figure 94 two effects are immediately visible.

The first effect is the reduction of the transition energies (***red shift***) when the electrical field is applied. The absorption spectrum is modified, thus, for a fixed laser wavelength, the effective transmission in the structure is changed, giving the possibility to use quantum well structures for light modulation.

The second effect is the reduced overlap of the electron and hole eigenfunctions. Since the transition probability depends on the overlap integral of these two eigenfunctions (***Fermi's golden rule***), the absorption is strongly reduced.

The consequences of these two physical effects on the absorption spectrum are shown in Figure 95, where the shape of the absorption spectrum drastically changes when the electric field is applied.

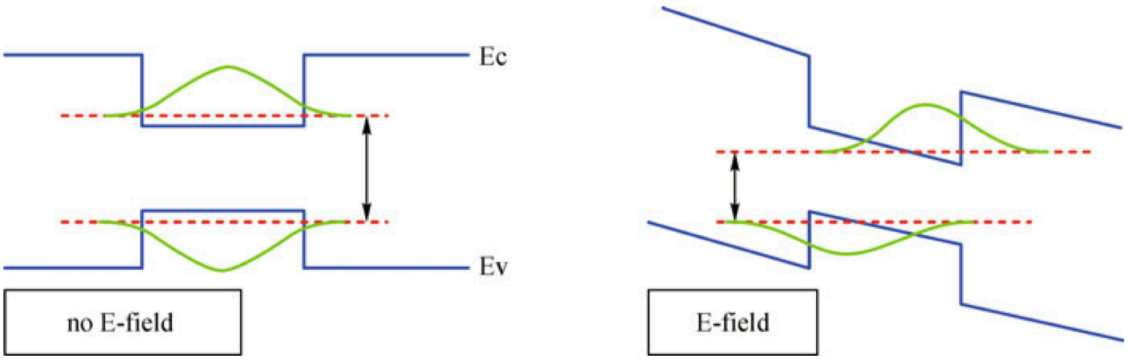

Figure 94. Quantum well energy states and eigenfunctions without and with an external electrical field. From [65].

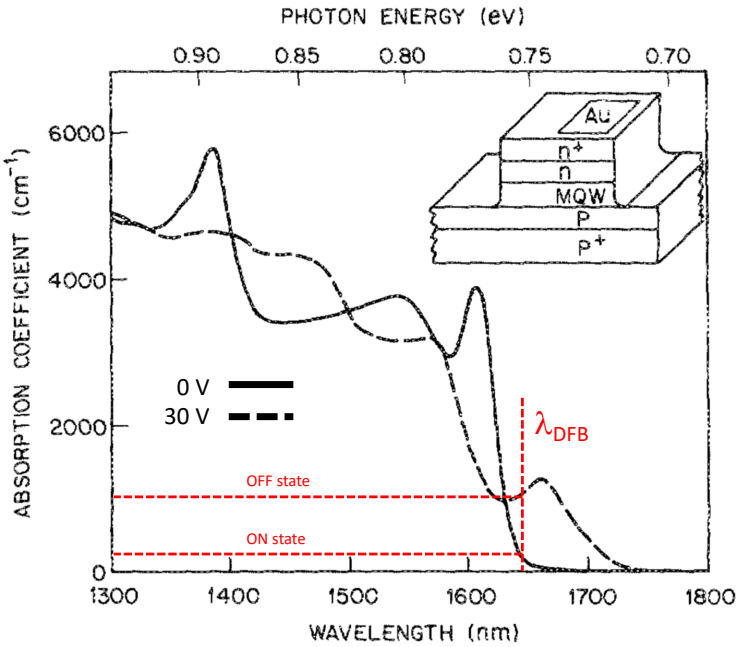

Figure 95. Absorption spectra in a multi-quantum well epitaxial structure with and without an external electric field. Reprinted from [66].

3.2.6 P-I-N Diode

Photon emission processes are enhanced when the system is out of equilibrium, as previously seen when gain in multi quantum well structures was discussed: optical gain depends on the difference in quasi-Fermi levels of electrons and holes.

Since an injection of carriers is needed, the multi quantum well active region must be surrounded by a suitable electrical structure allowing for easy carrier injection in the quantum well. The structure

used for the majority of opto-electronic devices is the P-I-N diode, whose band diagram is shown in Figure 96. The band diagram is extracted with BCBV.

The intrinsic region mainly consists of the active MQW region, while P and N doped semiconductor layers are integrated to allow the current flow: the electrical current is injected in the P side, while the N side acts as ground contact.

It must be noticed that this structure is also useful when reverse biased, since the electrical field is mainly acting on the intrinsic region. This allows the fabrication of modulators or photodiodes with the same fabrication process and possibly the same material stack of laser diodes.

P and N sides are made with InP in our case, and the doping can reach 10^{18} cm^{-3}. This is an important feature since P- and N- doped semiconductors have different material absorption at the wavelength of interest: N-doped InP has absorption around 2 cm^{-1} while P-doped InP has an absorption value higher by an order of magnitude.

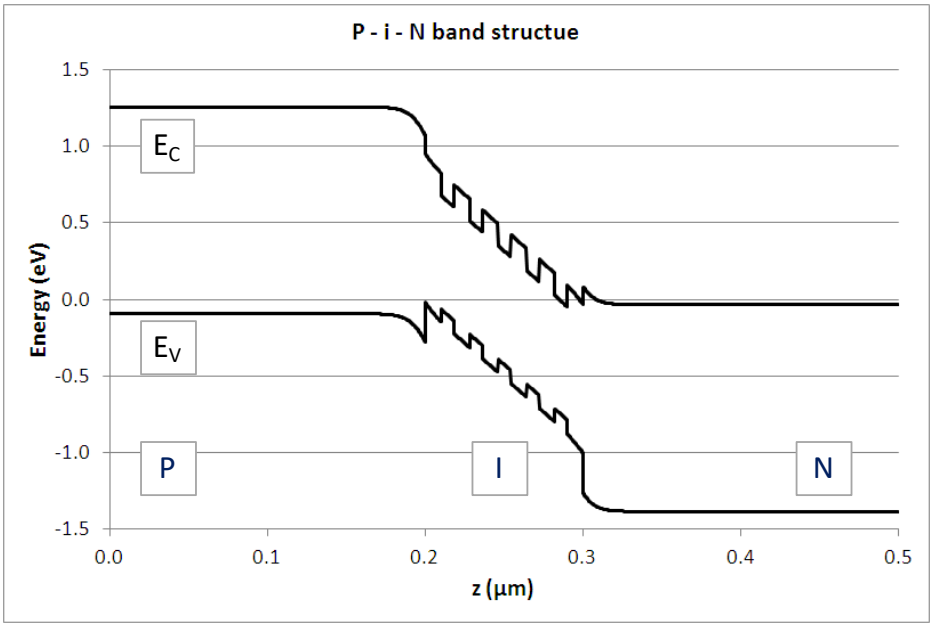

Figure 96. Quantum well P-I-N diode band diagram

3.3 Description of the InP Integration Platform

This paragraph describes the InP integration platform in terms of materials, waveguide design and physical structures for light generation and modulation.

3.3.1 SI-BH Integration platform

This section describes the Semi-Insulating Buried Heterostructure (SI-BH) waveguide process that was used for the devices developed in the frame of this work and how different MQW layer stacks are monolithically integrated.

SI-BH waveguide structures belong to the class of low refractive index difference waveguides. The semi-insulating material used at III-V Lab is based on a Fe-doped InP layer. The presence of semi-insulating lateral cladding reduces the leakage current in the lateral direction, improving current injection in quantum wells, as shown in

Figure 97. Additional Ruthenium-doped or Silicon-doped layers can be integrated to reduce p-dopant diffusion in the Fe:InP, especially for Zn atoms [67].

SI-BH confined active waveguides are capable of withstanding generation of high optical power, and thus high photocurrents, when used in absorption mode [67]. This is due to the high thermal conductivity of InP, which in turn translates to highly reliable devices.

The fabrication process of SI-BH waveguides is shown in Figure 98. A MQW layer stack is grown on the full wafer (a), where etching of the waveguides is performed (b). A thick layer of Fe:InP is grown to surround the MQW stack (c). A final regrowth of p-InP and contact layers is performed (d). A typical SEM image of a typical SIBH structure grown at III-V Lab [68] is shown in Figure 99.

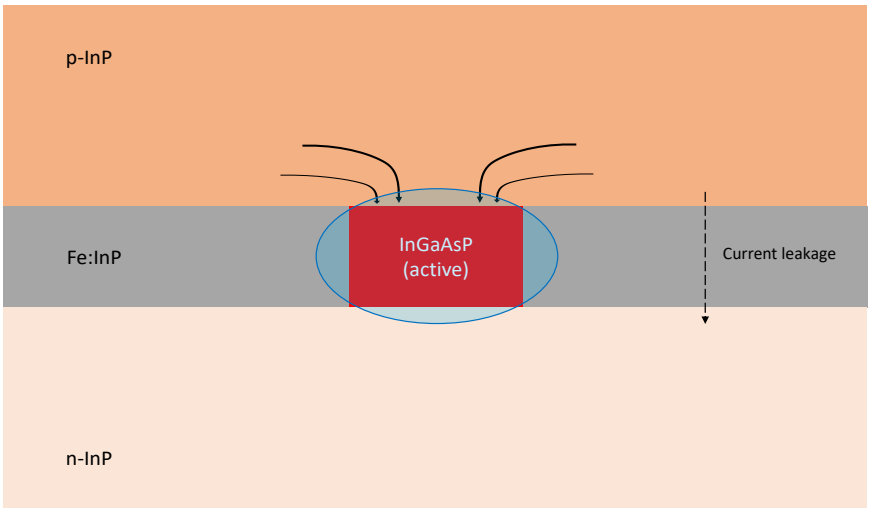

Figure 97. SI-BH waveguide structure with current flow and optical mode. The lateral current leakage can be negligible with careful material stack design.

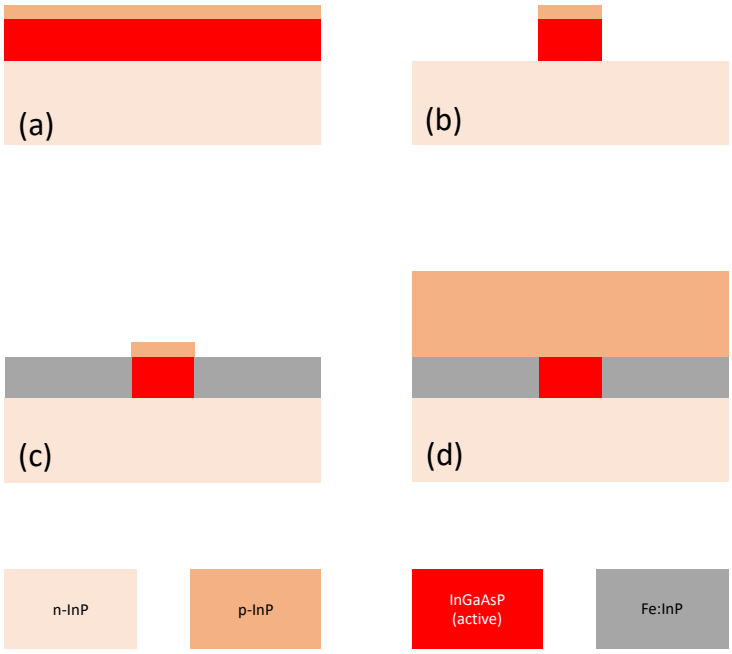

Figure 98.Schematic of SI-BH waveguide definition process with semi-insulating (Fe:InP) and p-InP regrowths.

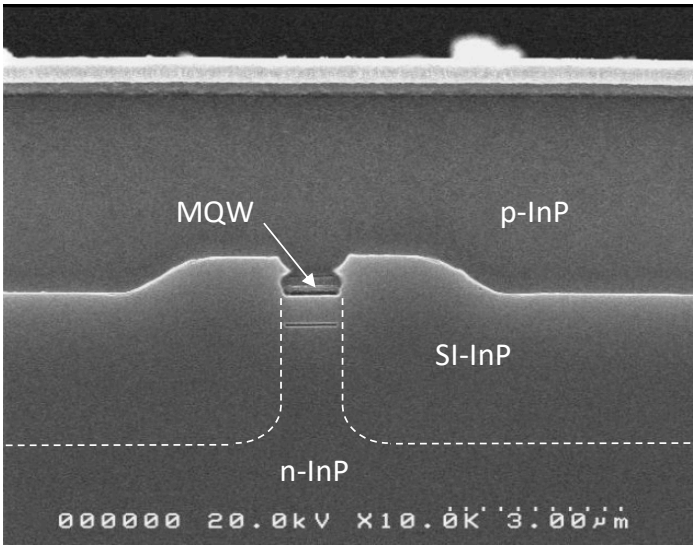

Figure 99. SEM image of the fabricated SI-BH active waveguide. Reprinted from [68].

Figure 100 shows the computed mode profile using Beamprop software for an SI-BH active waveguide, as designed for the fabricated devices. The waveguide is 2 µm wide. The MQW layer structure is composed of 8 quantum wells, of 8 nm width, separated by 10 nm wide barriers. The structure has 30 nm Separate Confinement Heterostructures. Barriers and SCH are made of Q117 InGaAsP, while the composition of quantum wells is adjusted to obtain the desired PL and strain values. Imaginary refractive index for gain and absorption is not considered in this mode computation. While the refractive index change is significant for p- and n- doped InP, where doping

values are above 10^{18} cm^{-3}, the Fe doping needed for electrical insulation is of the order of 10^{15} cm^{-3}, thus the refractive index is almost unaffected.

Refractive indices of materials used for the optical mode profile and wave propagation computation are summarized in Table 10.

Material	***Function***	***Refractive index***
InP	***Reference material***	3.16
p-InP	p-doped diode side	3.156
n-InP	n-doped diode side, substrate	3.155
Fe:InP	Semi-insulating layer	3.16
Q117	SCH, barriers	3.317
QQW	Quantum well	3.55

Table 10. Summary of refractive indices of materials grown on the InP platform

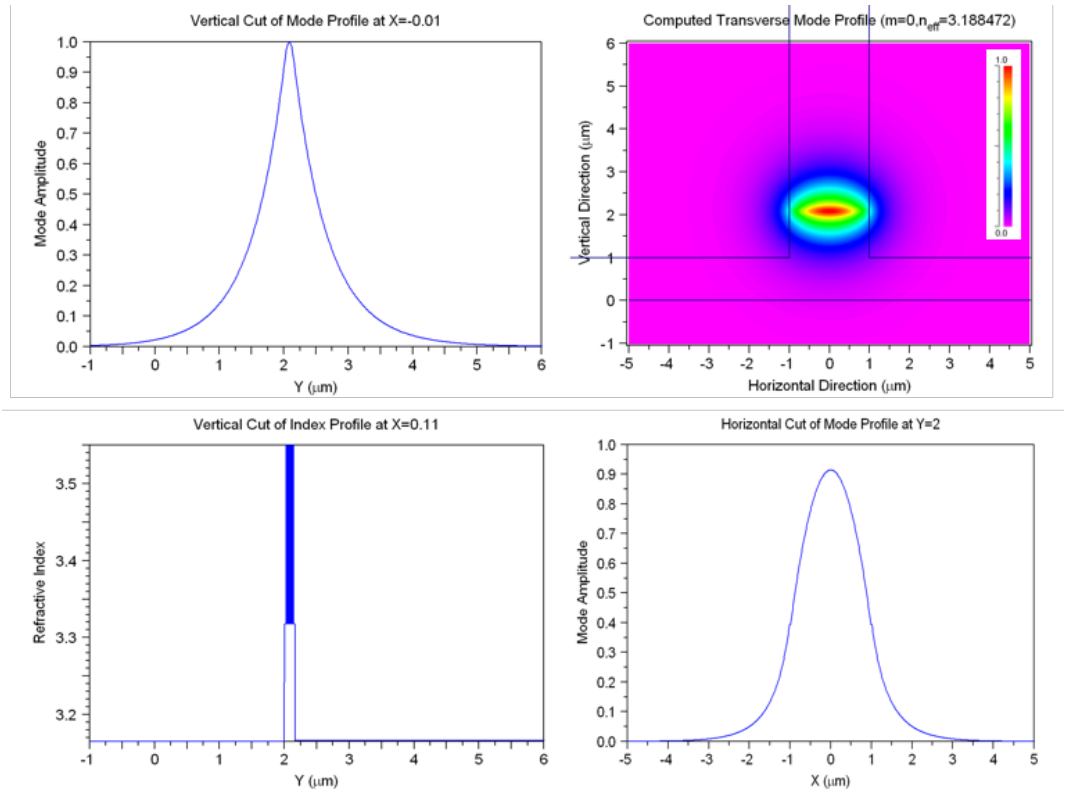

Figure 100. Simulation with BEAMPROP of the optical mode for an active SI-BH waveguide, with cut profiles and refractive index profiles.

3.3.2 Butt joint technology for EAM/DFB wavelength optimization

While it is possible to use the same MQW stack for laser and modulators [69], there is the possibility to differentiate the layer stacks for improved performances in terms, for example, of driving voltage and extinction ratio of the modulator [68].

The two different MQW stacks are integrated through a butt-joint process, described in Figure 101.

The starting point is the P-I-N MQW structure, before waveguide definition (a). A hard dielectric mask is used for etching the selected regions (b). A second MQW stack is grown on the wafer (c). The regrowth will be crystalline on the n-InP substrate, while on the hard mask a polycrystal is formed. The polycrystal is lifted with the hard mask (d). From this point onward, the fabrication continues with the definition of the waveguides as described in Figure 98.

In order to reduce unwanted reflections, the two optical modes should ideally be equal in size and effective refractive index. This mode adaptation can be done by changing the SCH layers thickness. Furthermore, the interface of the two layer stacks is tilted with respect to the waveguide direction, to redirect the back-reflections outside the input waveguide.

The joint optimization of the two MQW stacks MQW1 and MQW2 is also performed for gain and absorption curves. A sketch of this optimization process is shown in Figure 102.

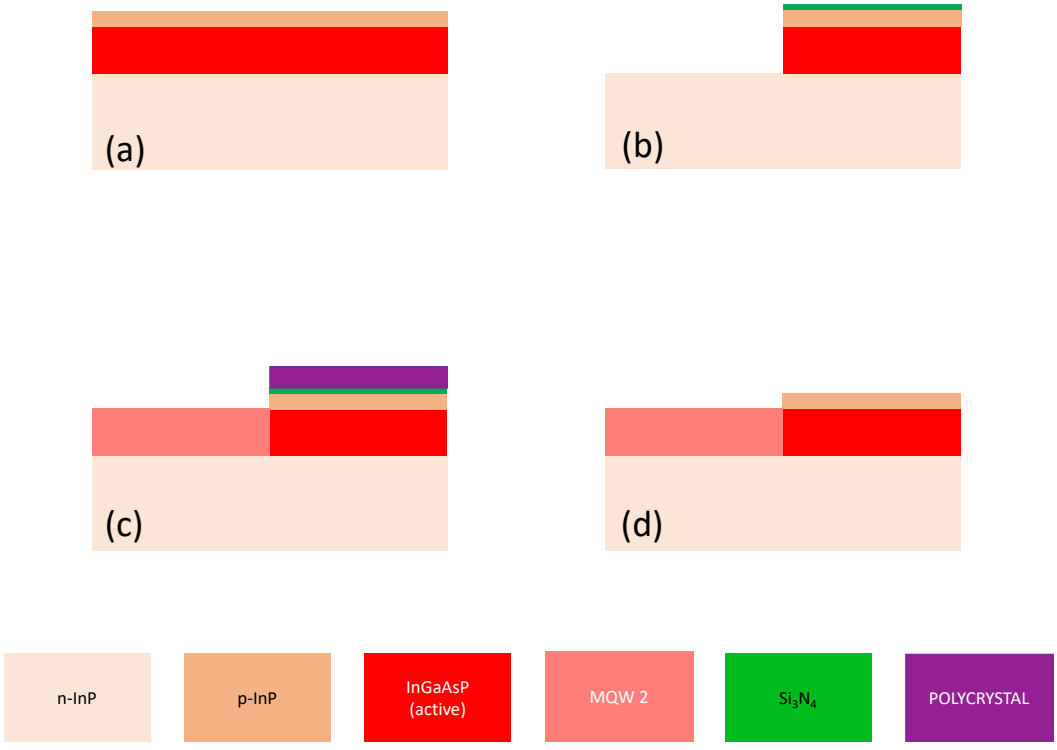

Figure 101. Butt-joint fabrication process for Laser-Modulator monolithic integration.

The desired DFB laser wavelength is the main reference. The MQW1 (laser) stack is fabricated to obtain desirable features such as high gain and low threshold current. The MQW2 stack has a gain curve which is shifted with respect to MQW1 towards lower wavelengths by an amount ***ΔPL***. The value range of ***ΔPL*** is found by imposing low absorption at 0 V in the modulator region, to obtain low insertion loss operation.

A trade-off between low insertion losses and low driving voltage operation of the modulator section is needed, as the two parameters are improved when shifting the PL wavelength in opposite directions. The extinction ratio of the modulator is also strongly influenced by the absorption difference between off (0 V) and on states. This parameter can be increased by increasing the length of the modulator, but a longer modulator has a reduced bandwidth due to intrinsic capacitance degradation.

The MQW1 stack will undergo the regrowth phase as a long high temperature annealing, leading to material diffusion between wells and barriers and subsequent quantum well intermixing. At the end of the regrowth the MQW1 stack will show a red shift in the PL wavelength that can be significant, up to 30 nm. This effect must be taken into account when designing Externally Modulated Laser (EML) with butt-joint fabrication process.

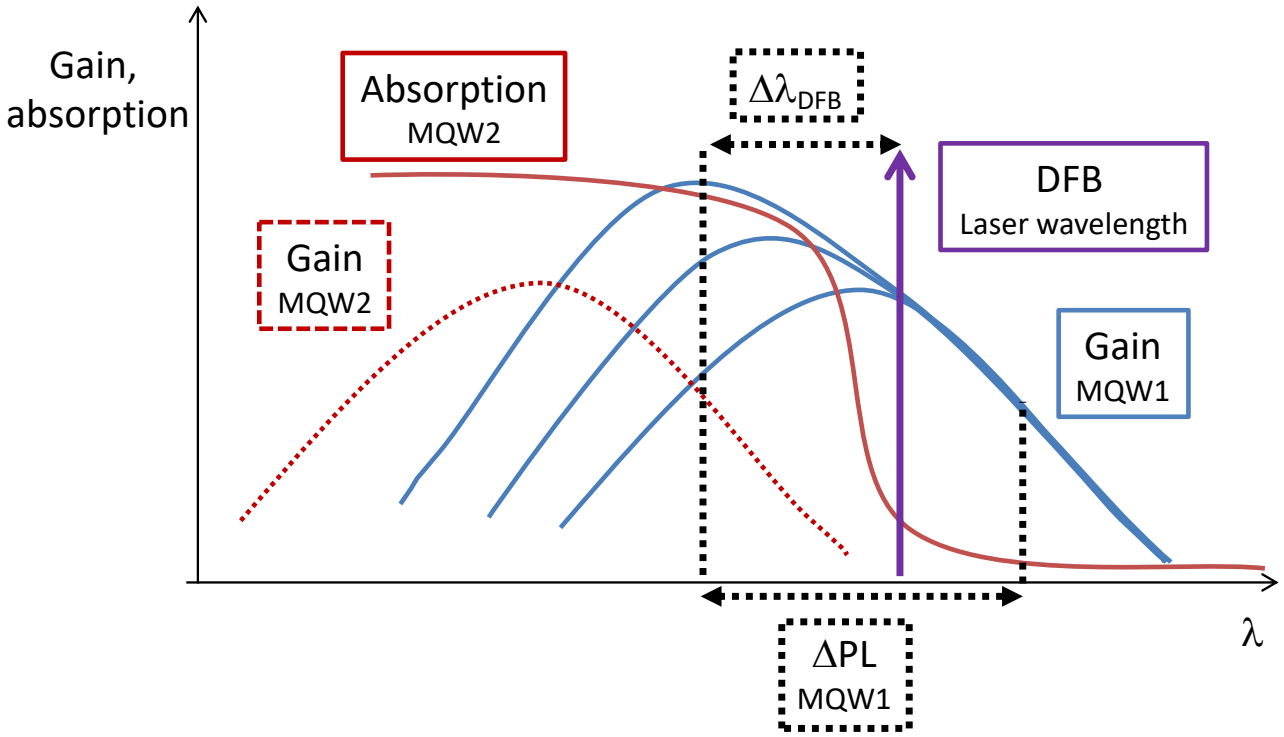

Figure 102. Optimization of the relative gain position of active regions of laser and modulator, in order to determine the optimal laser wavelength position.

3.4 SI-BH PLATFORM BUILDING BLOCKS DESCRIPTION

This section describes the building blocks for Photonic Integrated Circuits in the SI-BH integration platform.

3.4.1 SEMICONDUCTOR OPTICAL AMPLIFIER

Semiconductor Optical Amplifiers (SOAs) are used as on-chip amplifiers to compensate propagation losses inside the photonic integrated circuit.

The structure of an SOA is that of a P-I-N diode, where the injection of an electrical current allows the stimulated amplification of the incoming optical signal. The amplification of the optical signal should happen with a "single pass", avoiding back reflections and suppressing cavity effects.

The gain of an SOA is defined as the ratio between the output and input power in an active waveguide [70]:

$$G(\lambda) = \frac{P_{out}}{P_{in}} = \frac{(1-R_1)(1-R_2)G_0}{\left(1-G_0\sqrt{R_1R_2}\right)^2 + \left(4\sqrt{R_1R_2}G_0\sin^2\left(\frac{2\pi n_{eff}L}{\lambda}\right)\right)} \quad (59)$$

where $\boldsymbol{R_1}$ and $\boldsymbol{R_2}$ are the Fresnel reflectivities at the end facets, $\boldsymbol{L}$ is the length of the amplifier, λ is the wavelength and $\boldsymbol{n_{eff}}$ is the effective refractive index of the optical mode.

The reflectivities are low in the case of optical signal amplification inside the PIC, provided that mode adaptation is performed in case a butt-joint junction is used. When the signal is directed to or from outside the PIC, the waveguide is usually tilted with respect to the end facet; a tilt of 7° is used in our case, leading to a reflectivity of the order of 10^{-5}.

$\boldsymbol{G_0}$ is the single pass (net) gain of the amplifier, depending on the material stack and the geometry of the waveguide:

$$G_0 = \exp((\Gamma g - \alpha)L) \quad (60)$$

where Γ is the confinement factor in the active region, $\boldsymbol{g}$ is the material gain and α are the internal losses of the waveguide.

When the input power is increased above a certain amount, the gain starts decreasing, and the amplifier starts to lose efficiency. This phenomenon, which is called optical gain saturation, is described by the saturation output power ($\boldsymbol{P_{sat}}$). The expression of gain can thus include this saturation effect when the input power $\boldsymbol{P_{in}}$ becomes close to $\boldsymbol{P_{sat}/G_0}$:

$$G = G_0 \frac{1}{1 + {}^{P_{in}}/_{P_{sat}}} \quad (61)$$

The saturation power depends on the waveguide geometry, the confinement factor in the active region and material physical properties:

$$P_{sat} = \frac{dw}{\Gamma} \frac{h\nu}{\tau_c \frac{\partial g}{\partial N}} \tag{62}$$

where ***d***, ***w*** are the active region thickness and width, respectively, Γ is the confinement factor in the active region, $h\nu$ is the photon energy, τ_c is the mean carrier lifetime and $\partial g/\partial N$ is the differential gain.

Practical means to increase the optical saturation power are the gradual tapering of the SOA waveguide [70], or the decrease of the optical mode confinement on the active region [71].

The material gain depends on the injection level of the waveguide. A phenomenological expression for the material gain can be written as:

$$g = \frac{\partial g}{\partial N}(N - N_{tr}), \tag{63}$$

where ***N*** is the injected carrier density and N_{tr} is the transparence carrier density, defined as the current density for which the SOA gain is 1.

The gain of the SOA can also be saturated from the electrical point of view. High injection current levels saturate the electronic states in the E_1, HH_1 subbands, thus further current injection will only increase higher subband transitions.

3.4.2 DFB LASERS

Distributer Feedback (DFB) lasers are fabricated with the introduction of a periodical variation of refractive index in an active waveguide. This effective index variation causes a small, diffused light reflection throughout the waveguide.

As incident and reflected waves will interfere, we can write the phase condition for constructive interference:

$$k_I + k_R = \frac{2\pi m}{\Lambda} \tag{64}$$

where k_I and k_R are the incident and reflected waves wavevectors, ***m*** is the grating order (natural number) and Λ is the grating period.

At the resonant condition, we can write $k_I = k_R = 2\pi n_{eff}/\lambda_B$, thus the resonant (Bragg) wavelength λ_B can be written as

$$\lambda_B = \frac{2n_{eff}\Lambda}{m} \tag{65}$$

The fabrication of DFB lasers requires a good control of both material properties, through their refractive index and material composition, and of the technological process, since the grating periods required for a DFB on InP at 1.55 μm are of the order of 250 nm.

DFB lasers integrated in the SI-BH technology used in this work have a ***λ/4*** phase shift section at the center of the laser waveguide. This phase shift ensures the single-mode operation of the laser, when the two reflector sections are terminated with AR reflection coating on the two sides. The phase shift defines the laser cavity center. This structure is shown in Figure 103.

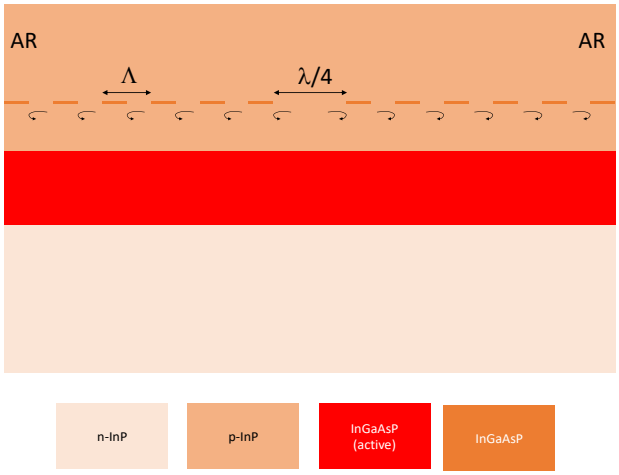

Figure 103. Cut view in the propagation direction of a DFB laser with l/4 phase shift. The Bragg grating is defined by etching in a dedicated quaternary layer, and the reflection is distributed throughout the structure.

3.4.3 Electro-Absorption Modulators

Electro-absorption modulators rely on the Quantum Confined Stark Effect described earlier in this chapter. The structure of the EAM is a reverse biased P-I-N diode, where an external electric field changes the absorption intensity. The multi quantum well structure can be chosen such that the absorption at zero field is low, to decrease insertion losses.

The modulator transmission with respect to the zero-field condition can be measured in function of the applied voltage, as shown in Figure 104. When the reverse bias is increased, the absorption increases, showing a plateau at the end of the bias region of interest.

We are interested in analog signals thus the linearity of electro-optical response is of great importance. One can define the differential transmission $\boldsymbol{dT/dV}$ as the first derivative of transmission with respect to voltage at the bias point $\boldsymbol{V_b}$, in small signal approximation. The requirement for highly linear modulator is that the second derivative $\boldsymbol{d^2T/dV^2}$ is as low as possible around the bias point to avoid signal distortion and harmonic generation.

The opto-electrical transfer function of the modulator is shown in Figure 104.

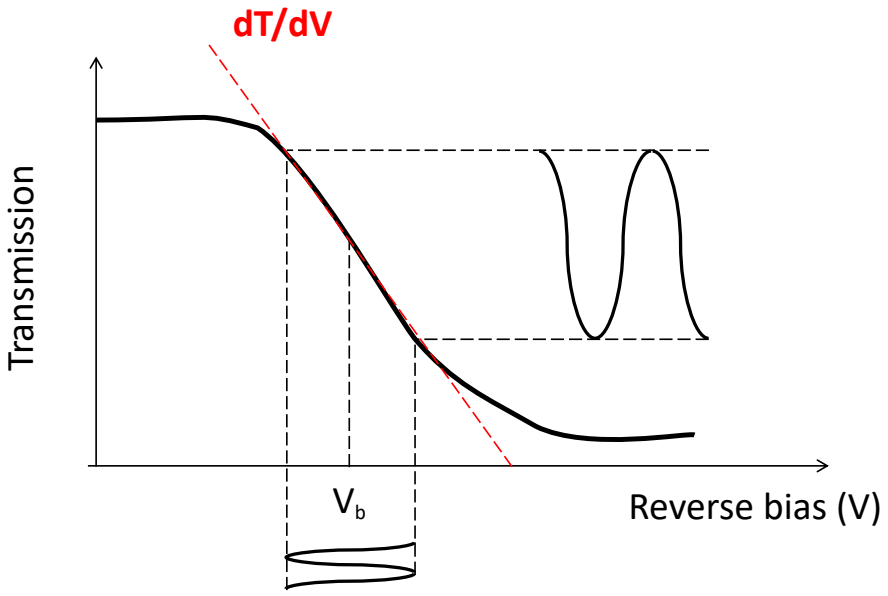

Figure 104. Electro-absorption Modulator opto-electrical transfer function with respect to the applied reverse bias. The modulation efficiency is represented by the slope of the transmission curve

In terms of electrical properties, the modulator behaves as a typical P-I-N diode in reverse bias. The electrical equivalent circuit is shown in Figure 105.

The parameters describing the EAM electrical circuit are the following:

- C_J is the junction capacitance, taking into account the charge accumulation at the edges of the active region, which can be modeled as a two-plates capacitor:

  $$C_J = \frac{\epsilon_J S}{t_J}$$

  Where ε_J is the dielectric constant of the active material, S is the active region surface and t_J is the active region thickness;
- R_J is the junction resistance, taking into account the current generation in the active region due to light absorption;
- R_S is the (differential) series resistance of the diode; in reverse bias conditions this resistance is high and can reach hundreds of kΩ;
- C_P is the parasitic capacitance due to the semi-insulating region below the contact area. The value of this capacitance can be found by considering the thickness of the semi-insulating region and the width of the contact area.
- R_G is the voltage generator series resistance; its value is usually 50 Ω to be adapted to standard RF circuitry;
- R_C is the charge resistance, added in parallel to the EAM in order to have impedance matching to the generator. As the series resistance is extremely high in reverse bias conditions, the value of the charge resistance is usually of 50 Ω.

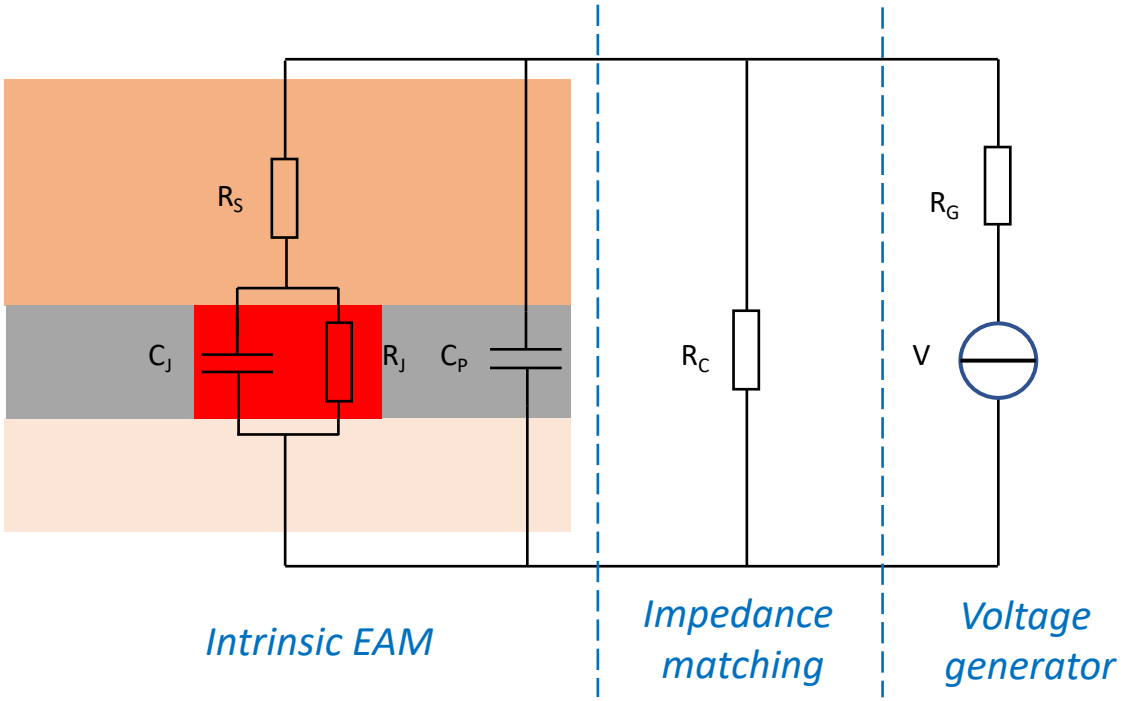

Figure 105. Electro-absorption Modulator equivalent electrical circuit with external impedance matching.

With the equivalent circuit above, and taking into account only the significant terms, the resulting RC cut-off frequency due to the RC constant can be calculated as:

$$f_{3dB} = \frac{1}{2\pi R_C (C_J + C_P)}. \tag{66}$$

The increase in modulation frequency can be obtained mainly by reducing the capacitance of the modulator: the junction capacitance is reduced with short, narrow waveguide modulators, of the order of 100 μm * 2 μm. The technological process can be optimized to reduce the parasitic capacitance, especially for what concerns the contact area and the material below the modulator contact, which is usually made of dielectric material (BCB + SiO_2).

Cut-off frequencies in excess of 20 GHz can be reached with a careful design of modulator structures.

3.4.4 PHOTODIODE

The vertical structure of the photodiode is a reverse-biased P-I-N diode structure. In this case, however, the generated photocurrent is modulated due to the periodic variation in the optical power received. There are two key parameters in the design of photodiodes: responsivity and cut-off frequency.

The design of high-speed waveguide photodiodes is very similar to the treatment of the electro-absorption modulator. Indeed, in the SI-BH integration platform the two devices have the same structure and the same absorption response as a function of the bias voltage.

The responsivity is the amount of current produced due to the absorption of the received optical power, measured in A/W:

$$\eta = \frac{I_{ph}}{P_{opt}}. \tag{67}$$

High responsivity is obtained with high absorption; thus, it is convenient to have large reverse bias voltages. With reference to Figure 106, the photodiode optimal bias region is well beyond the linear absorption region, where the transmission is minimized. Moreover, it is important that the extraction of the generated electron-hole pair is as efficient as possible. The transport of carrier from the active region to the contact layers is favored by a large reverse bias.

The optical power in the photodiode waveguide has an exponential decay:

$$P(z) = P_0 e^{-\alpha z} \tag{68}$$

so the length of the photodiode can be designed to obtain a sufficient ratio of absorbed power to injected power. Responsivity of the photodiode is a key parameter in analog optical link design, as will be seen later on in this chapter, and it shall be maximized.

The length of the photodiode and the increased absorption comes at expense of the junction and parasitic capacitances, and in turn of the opto-electrical bandwidth. The dimension of the photodiode shall be optimized to obtain the best compromise between the two parameters.

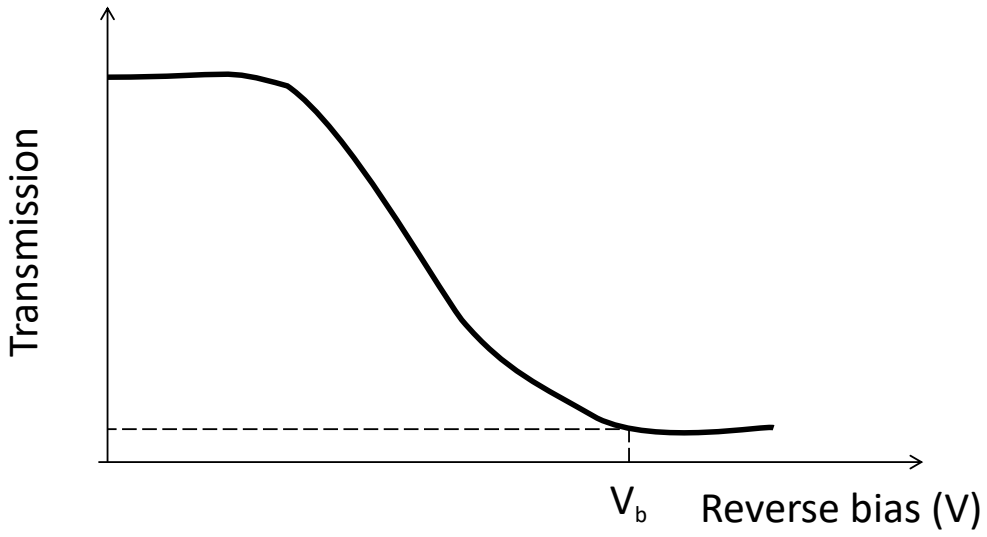

Figure 106. Bias condition of the EAM working as a photodiode.

3.4.5 Mode adapters

The efficiency of light coupling between two optical devices or fibers is defined as:

$$C \propto \frac{|\iint E_1 E_2 dxdy|^2}{\iint |E_1|^2 dxdy * \iint |E_2|^2 dxdy}. \tag{69}$$

That means that the coupling efficiency is proportional to the inner product of the electrical fields, $\boldsymbol{E_1}$ and $\boldsymbol{E_2}$, normalized to the intensity of the two optical modes.

Coupling efficiency is maximized when the two optical modes are similar in size and shape. The mismatch of optical modes can lead to coupling losses, defined as

$$\alpha_{coupling} = 10 \log C. \tag{70}$$

The principle of coupling and mode adaptation is independent on the two devices and only depends on the optical modes.

Various techniques are used to improve coupling efficiency from one component to the other:

- When the two devices are integrated, as in our case, a fine tuning of the optical mode can be performed by changing the thickness of layers such as the SCH layers, to improve mode coupling between the two MQW structures in the butt-joint integration technique; mode mismatch can lead to unwanted reflections and can degrade the PIC performances;
- When there is the need to couple light from the PIC to a passive circuit or an optical fiber, the waveguide is reduced with tapers. Waveguide width reduction causes a reduction of guiding strength of the waveguide, enlarging the optical mode to better match the optical mode of the optical fiber.

3.5 SIBH Platform Fabrication Process

This paragraph describes the technological process steps to fabricate the devices described earlier in our PIC integration platform.

The process for fabrication of Photonic Integrated Circuits is shown in Figure 107 and Figure 108.

It starts with an InP wafer, which will be our substrate. The substrate can be semi-insulating to allow high-speed operation, even if it is not the case for the devices used in this work. The first MQW layer stack is grown (a), along with a thin p-doped layer. In case DFB lasers will be integrated with this MQW stack, a 30 nm InGaAsP layer is grown as well for the bragg grating.

A hard mask is deposited on the wafer and patterned. A deep etch is performed (b) to define the butt-joint regrowth areas. The second MQW layer stack is grown, with a p-InP cap to cover it. It must be noticed that the first MQW stack sees this step as a high temperature annealing, and the PL wavelength will shift. This must be taken into account in the wavelength optimization of an EML. The mask is kept during the regrowth phase (c) and a polycrystal is deposited on its surface. This polycrystal will be lifted off.

An e-beam lithographic process is performed on the wafer. The mask is deposited and patterned with an electron beam (d). A shallow etching is performed until the thin quaternary layer is removed in the unprotected areas (e). E-beam lithography is a high-resolution technique needed to define and fabricate gratings in the order of 100 nanometers. The wafer is then covered with a p-doped InP layer to fill the etched gaps (f).

The wafer and the layer stacks are ready for waveguide definition. In Figure 108, a cut view of the waveguide fabrication process is shown. The wafer is patterned with a standard lithographic process with a hard mask (g). A 2 µm-deep etch is performed to remove the active region (h). Semi-insulating material (Fe:InP) is grown on the entire wafer (i). The polycrystal is again lifted off with the hard mask. A thick p-InP layer and the ternary InGaAs contact layers are grown (j). The wafer is patterned again to define the high-speed areas, then etched (k). A thick layer of SiO2 is grown, with a SiN thin top layer (l). Metal contacts are deposited on the semiconductor and the dielectric area (m).

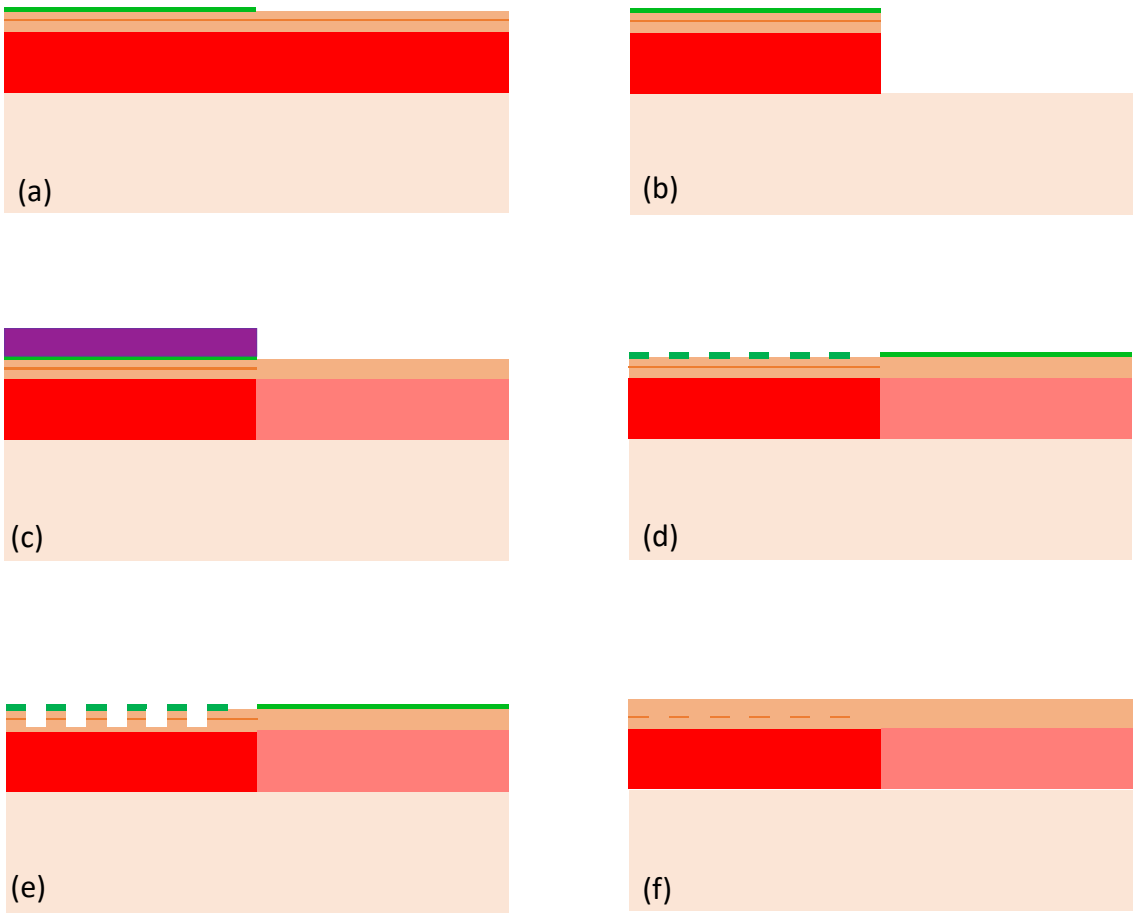

Figure 107. Fabrication process of InP PICs in the SIBH Integration Platform: epitaxial growth (a), butt-joint (b, c) and grating definition (d, e). Wafer ready for waveguide definition (f).

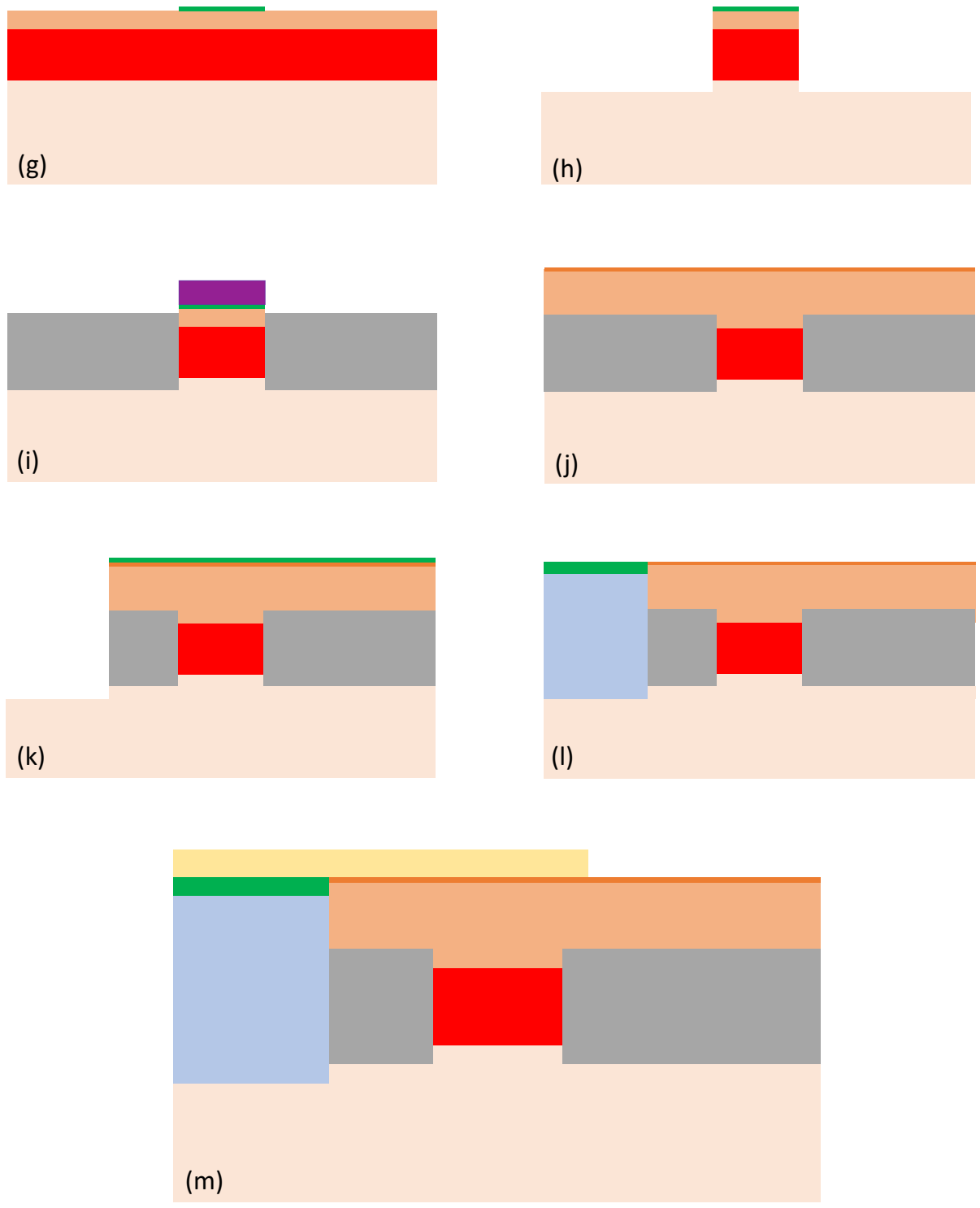

Figure 108. Fabrication process of InP PICs in the SIBH Integration Platform: waveguide definition (g, h), InP:Fe growth (i), p-InP growth (j), MESA etching (k) and SiO2 deposition (l), contact metal deposition (m).

3.6 PHOTONIC INTEGRATED CIRCUIT DESIGN

This section describes the impact of design parameters on the final system and how such parameters have been chosen for the PIC design itself.

The chip layout is presented in Figure 109. The design of this photonic integrated circuit was based on the specific requirement for the optoelectronic oscillators of this work. It was constrained by the design rules of the fabrication run in which it has been inserted. This device was fabricated in the frame of an internal multi-project wafer.

From the top left, a short SOA (SOA1), a high-speed photodiode (PD) and a second, long SOA (SOA2) can be seen. This section chip can be fiber-coupled through the input tapers from both sides, to allow testing with (Opt in2) or without (Opt in1) the passive SiN PIC, to allow standalone measurements of the InP PIC.

From the bottom left, we find a monitoring photodiode (MON), the DFB laser (DFB), the high-speed modulator (EAM) and a short SOA (SOA3). The light can be coupled out of the PIC from the right side (Opt out) with a lensed fiber or a passive PIC. On the left, the output is power and wavelength monitor output (Mon out) for testing the DFB laser standalone.

Both facets are anti-reflection coated, with less than 10^{-5} reflectivity.

The PIC is designed in a 1150 x 400 µm footprint.

The PL wavelength of the EAM MQW stack is 40 nm lower than the Laser/SOA stack.

The main fabrication steps are visible in the mask layout, namely butt joint regrowth regions (grey shaded areas), waveguides (blue lines), contact layer (light blue shaded areas), dielectric MESA (dark blue shaded areas) and metallization (golden pads areas).

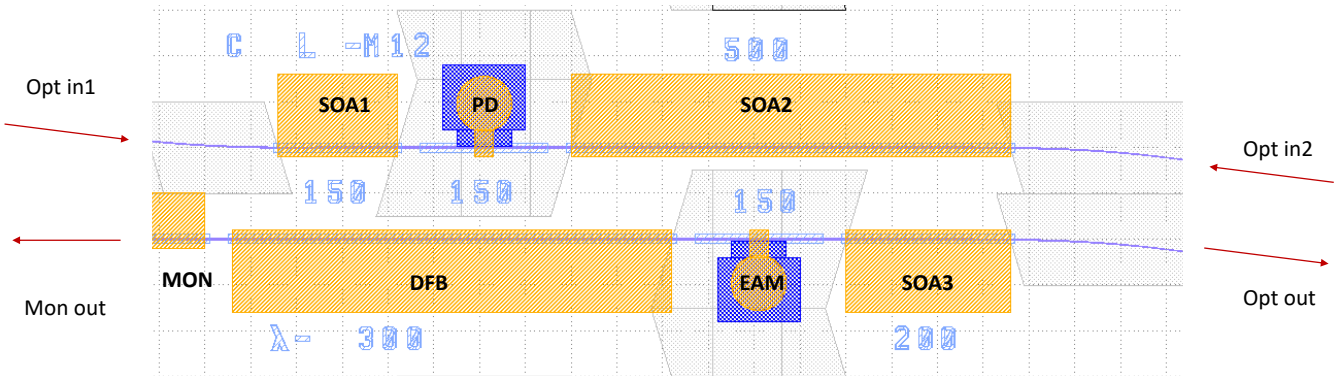

Figure 109. Mask layout of the fabricated OEO PIC in the SIBH InP integration platform.

3.6.1 DFB LASER AND MONITORING PHOTODIODE

The DFB laser is working as a CW source. Its length is 500 μm, a standard dimension for this platform.

The ideal source would be a low RIN laser, which will in turn reduce amplitude to phase noise conversion [72]. One way to reduce the RIN of a semiconductor laser diode is to use devices with high optical output power [73].

The Bragg grating has a λ/4 shift; such shift is slightly moved on the right-hand side to reduce the effective reflectivity of the grating resulting in an asymmetric optical power emission. As a consequence, the optical power hitting the modulator is increased. The design lasing wavelength is 1520 nm.

On the backside, a monitoring photodiode is built with the same MQW material. This has the purpose of monitoring the power of the laser by a simple photocurrent monitoring.

3.6.2 EAM

The EAM section is fabricated on the second MQW layer stack. The PL wavelength of this layer stack is at 1510 nm. This wavelength has been chosen to have a modulator with high efficiency at low bias points.

There is a trade-off to be made in the design of electro-absorption modulator between the absorption capabilities of the waveguide (extinction ratio) and the electro-optical bandwidth. Once the waveguide width and the fabrication process are chosen, we are able to calculate the junction and parasitic capacitances mentioned in equation 66, to find the total capacitance of the PIN diode per unit length. Long modulators favour high extinction ratio but have an increased total capacitance hence a lower electro-otpical bandwidth. A length of 150 μm is chosen for the modulator. The calculated 3 dB bandwidth is 14 GHz, while the extinction ratio should be between 15 and 20 dB, .

3.6.3 SOAS

There are 3 SOAs in the PIC design. All of them are used as boosters, to amplify light coming in or out the PIC.

Their lengths are determined by functions and layout constraints:

- SOA1 is a short amplifier at the input of the photodiode; this SOA is used in the system configuration where the passive PIC is absent, and an optical fiber is used. It is short since power being coupled back in the PIC can be amplified with external amplifiers, if needed.
- SOA2 is the counterpart of SOA1 for the system configuration where the light is coupled back from a passive PIC. It must be long to compensate coupling losses and propagation losses in the passive PIC.
- SOA1 is a short SOA at the output of the Laser/EAM chain; it is short due to the presence of the DFB and can be coupled out to fibers or the passive PIC.

3.6.4 PHOTODIODE

The photodiode is made with the same layer stack as that of the modulator. The chosen length was 150μm. This length is a good compromise between speed (14 GHz) and responsivity.

A reverse bias of 2V was chosen for the photodiode, to ensure high absorption.

3.7 EVALUATION OF DEVICES FROM THE FABRICATION RUN

3.7.1 DFB LASER

DFB lasers were characterized through the rear optical output to determine the basic parameters of the diode.

A pulsed measurement of the optical power was performed, to avoid heating-induced roll-off. The DFB was injected with 10% duty cycle, 1 ms current pulses, and the output power was collected in a broad-area detector. The voltage curve and the optical power response are shown in Figure 110. The optical power emitted was 3 mW with the monitoring photodiode unbiased. This power is relatively low, since lasers fabricated with a similar process surpassed 10 mW of optical power. These poor results are attributed to problems with epitaxial regrowth steps.

Power was collected with a lensed fiber to measure the optical spectrum of the DFB, shown in Figure 111. This corresponds to the designed laser wavelength.

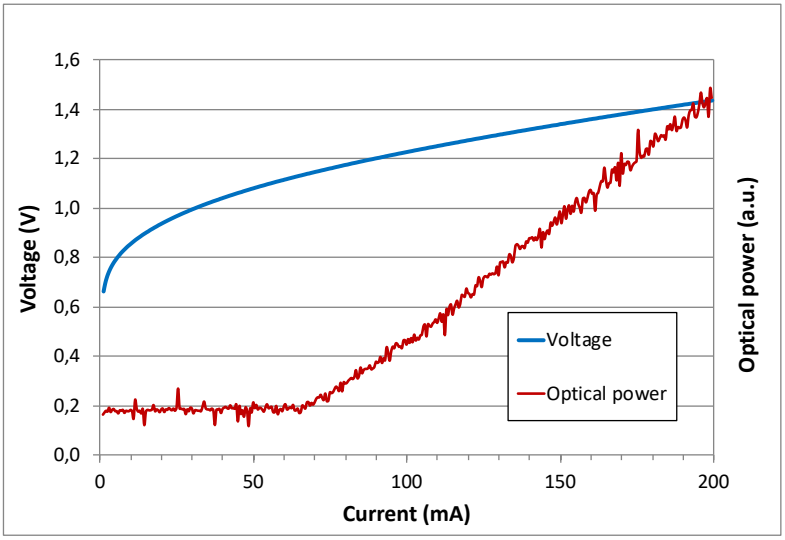

Figure 110. DFB laser elctrical and optical characterization. The optical power was collected from the monitor optical port.

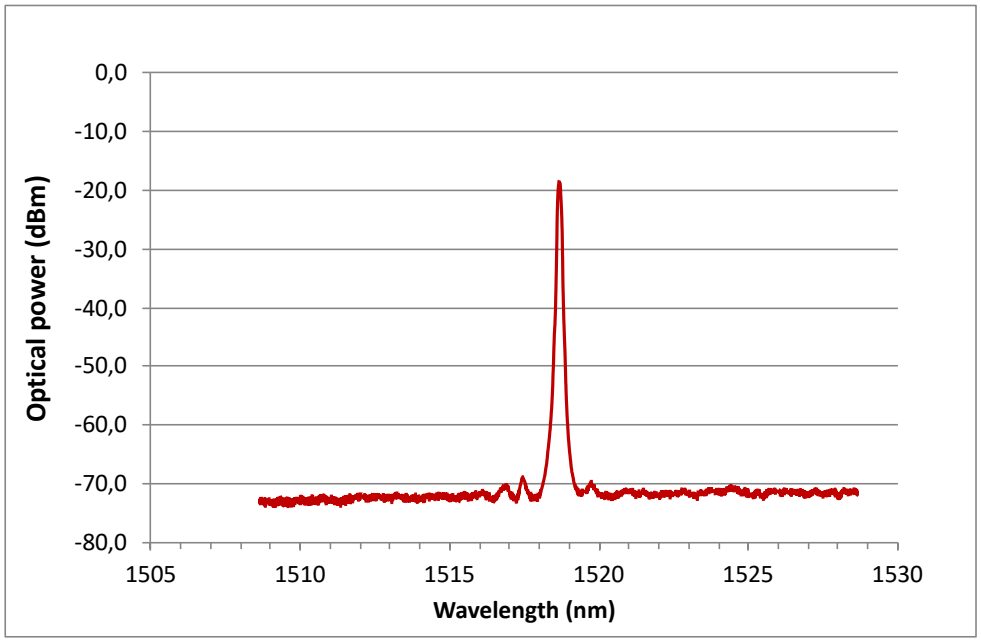

Figure 111. Measured DFB laser optical spectrum showing single-mode behaviour with 50 dB SMSR.

3.7.2 Electro-Absorption Modulator

The extinction ratio and differential transmission measurement can be performed at the same time. The DFB laser is biased at its own working point and the DC voltage on the modulator is swept from 0 to few Volts in reversed bias condition. The optical power emitted by the chip is detected on a broad area detector. The absolute value of the optical power is in this case not important, rather we measure the relative power with respect to 0 V bias. The normalized transmission of the modulator is defined as:

$$T(V) = \frac{P(V)}{P(0)}. \tag{71}$$

The slope efficiency is the derivative of the transmission with respect to the voltage. It measures how efficiently the modulator transforms the electrical signal into light modulation. It can be expressed as:

$$\frac{dT}{dV} = \frac{d}{dV}\left(\frac{P(V)}{P(0)}\right). \tag{72}$$

The results of transmission measurement and the corresponding ***dT/dV*** parameter are shown in Figure 112.

From the graph we notice that we can find a bias point where the efficiency is the greatest, corresponding to the region with the steepest derivative. This region is between 1.4 and 1.6 V in the case of the modulator presented in the figure. The bandwidth of the modulator is what will ultimately limit the frequency operation of the PIC.

The modulator is measured in an EML (Externally Modulated Laser) configuration, in which only the laser, the modulator and an output taper are integrated. A bias tee is used to feed the output RF signal from a Vectorial Network Analyzer.

The optical output power is collected into an optical fibre and detected with a calibrated 20 GHz photodiode, which feeds the input port of the VNA.

From Figure 113 we can see a bandwidth in excess of 14 GHz. The bandwidth increases with increasing reverse bias due to the reduction of parasitic capacitance.

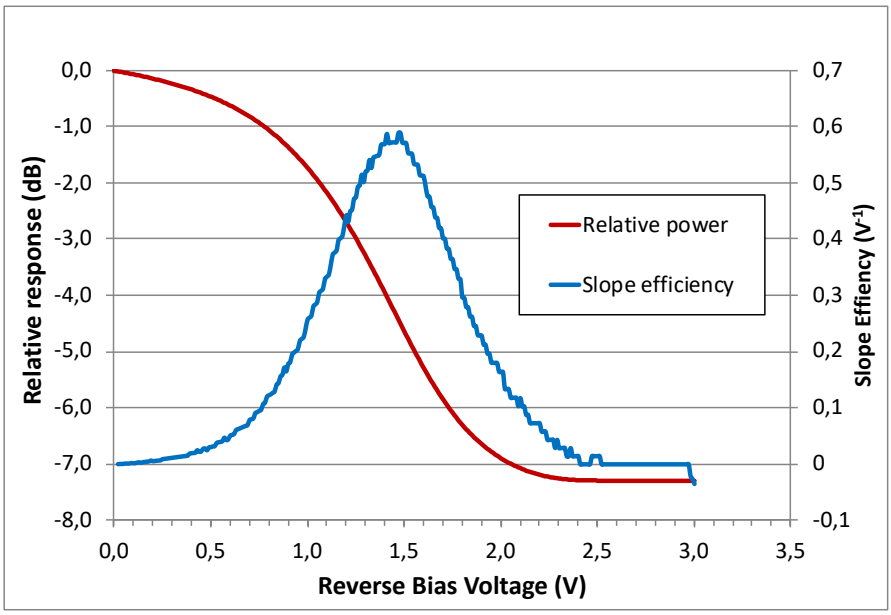

Figure 112. Measured relative power transmission and derived slope efficiency of the Electro-absorption Modulator

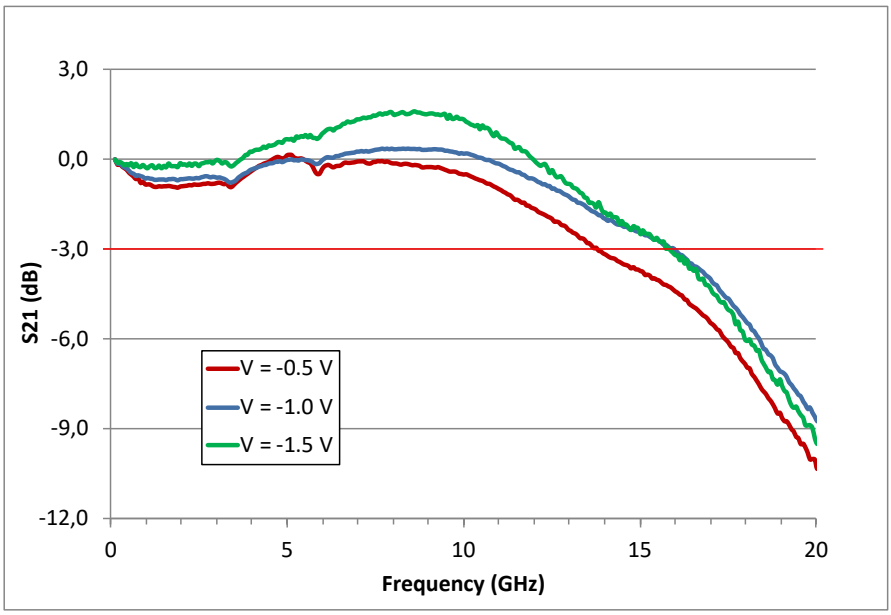

Figure 113. Measured modulator bandwidth at three different bias points, with bandwidth larger than 14 GHz

3.7.3 PHOTODIODES

Two parameters are needed for photodiode characterization, namely responsivity and bandwidth.

The photodiode responsivity is measured through the photocurrent and the optical input power. The setup is made with a DFB laser, a high power EDFA and an EML used as a receiver. The modulator is reverse biased to be used as a photodiode.

The optical output of the laser is fed into the EDFA. The 10% output of a 10dB coupler is used to monitor the power output of the fibre amplifier; the 90% port is injected into the EML. The optical power level is changed by changing the EDFA pump laser current. The test bench is shown in Figure 114. This setup is quite unusual for this specific measurement, but it allows us to characterize a modulator used as photodiode in the closest configuration to the final system.

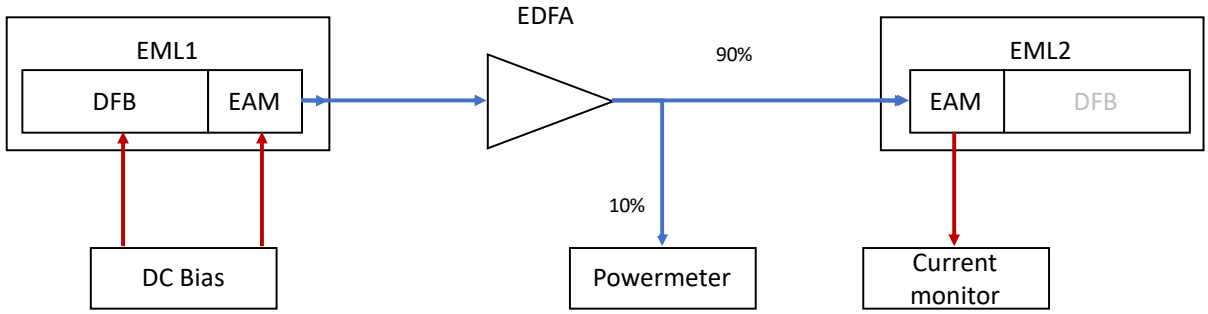

Figure 114. Test bench for the measurement of responsivity for and EAM used as a photodiode.

The current generated on the photodiode will be:

$$i_{ph} = P_L G_{opt} \alpha_c \eta_D \tag{73}$$

Where P_L is the laser power, G_{opt} is the optical gain, α_c are the coupling losses in the EML and η_D is the photodiode responsivity.

By calculating the ratio between the photodetector current and the injected optical power $P_L G_{opt}$ one can extract the parameter $\alpha_c \eta_D$, which is the photodiode responsivity times the coupling losses. The results are shown in Figure 115. The value of the slope is 0.14 A/W, which is low mainly due to the coupling losses.

The bandwidth of the photodiode was measured with a VNA-based setup, where a modulated signal is injected in the EAM. The device was a standalone EAM. The measurement is shown in Figure 116. A bandwidth of 9 GHz was obtained on this 150 μm long device. It must be noticed that this value is lower than the bandwidth of the device when used as a modulator, but the components are different.

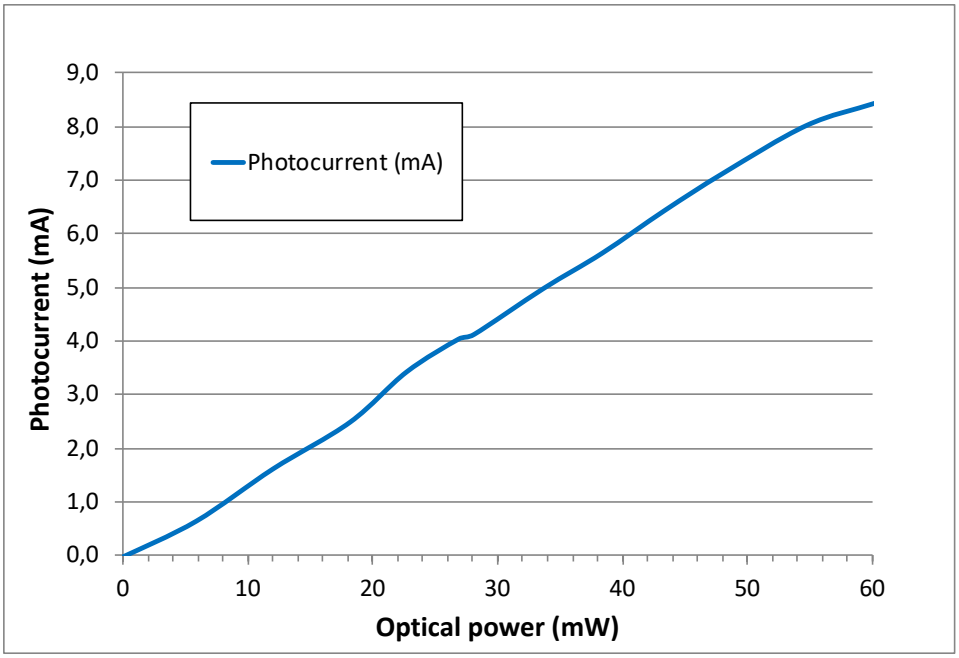

Figure 115. Measured fiber-coupled Photodiode responsivity.

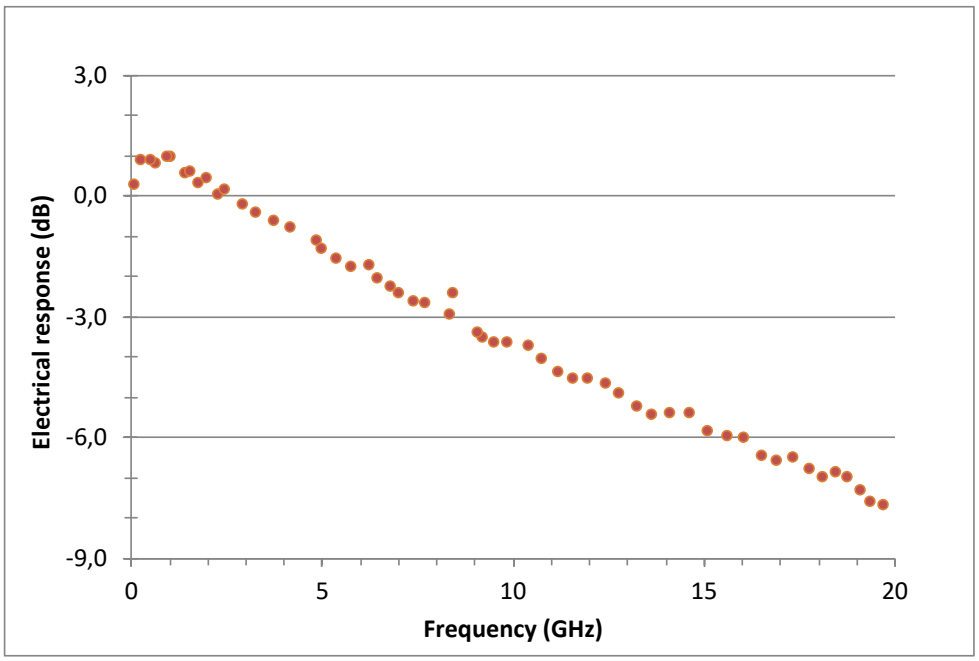

Figure 116. Measured Photodiode opto-electrical bandwidth.

3.8 CONCLUSIONS

This chapter presented the design and characterization of building blocks for the InP platform.

A brief explanation of the physics of quantum well and light generation and absorption was presented. The discussion of the relative position of the two active regions absorption and emission spectra was presented as well, as it is a key point for the EAM working point optimization.

The second section of this chapter presented the design of each building block of the SI-BH platform to achieve the OEO PIC integration.

The DFB laser has been designed to obtain moderate output power in order not to saturate the modulator. The Bragg grating design allows for asymmetrical power extraction towards the modulator, diminishing the power sent to the monitoring photodiode. The measurements show a good behavior of the laser output in terms of wavelength, but low output power.

The length of the modulator was designed to achieve a flat frequency response at 10 GHz, high extinction ratio and high slope efficiency. The design of an integrated electro-absorption modulator for analog applications is among the key novel features in this manuscript. A bandwidth of 14 GHz was measured, while the slope efficiency showed relatively low values with respect to previously obtained results.

A high-speed photodiode was integrated in the PIC, for optical-to-electrical conversion. The photodiode has been fabricated on the same layer stack of the modulator. This allows the fabrication of high-speed photodiodes within the SI-BH integration platform without need of further fabrication steps. The obtained bandwidth is less than 10 GHz, lower than the modulator bandwidth.

Several optical amplifiers were added to the design to allow on-chip optical power amplification to compensate for coupling losses towards the passive SiN/SiO_2 PIC.

The design of the PIC was made to be compatible with the current SI-BH integration platform, and to be integrated in an MWP fabrication run.

It was not possible, within the three years of research described in this manuscript, to optimize the PIC design and fabricate a second generation of devices. Indeed, from the discussion of system-level results that will be described in Chapter 4, meaningful modifications of the current SI-BH integration platform would be needed in order to address an optimized PIC design. One of the possible improvements of the SI-BH platform described in this Chapter would be to addition in the epitaxial structure of a slab waveguide under the active region, in order to increase the power handling capabilities of the fabricated waveguides. This modification would benefit the laser output power and its RIN [73], the power handling capabilities of the modulator [74] and photodiode, and the output saturation power of the SOAs, possibly leading to an all-optical gain integrated OEO. The impact of the design trade-offs made within the current SIBH integration platform will be explored throughout the fourth and last chapter, where the system-level measurements will be presented.

4 CHARACTERIZATION OF OPTICAL LINKS AND INTEGRATED OSCILLATORS

This chapter presents the measurements in which the components described in Chapters 2 and 3 are integrated in systems within different configurations or architectures.

4.1 INTRODUCTION

The objective of my Ph.D. research, as stated in the general introduction of this manuscript, is to build an integrated Opto-Electronic Oscillator with Photonic Integrated Circuits. In this final chapter I will describe the experiments for several PICs, in order to demonstrate the feasibility of an integrated OEO. This chapter is divided in four sections, each devoted to one experiment.

The first section describes an OEO based on electro-absorption modulators. In this experiment the emitter and the receiver are separated on two chips, fabricated at III-V Lab in in a MWP fabrication run we will call "EML Run". The objective of the section is to demonstrate the capability of EAMs to function as analog amplitude modulator. The EAM replaces the more commonly used Mach-Zehnder modulator, which is difficult to integrate on Indium Phosphide due to size constrains and performance trade-offs. The receiver chip is another in which only the EAM is used, to function as a photodiode, to demonstrate the need of only two active regions for a fully integrated OEO, as described in chapter 3 for the full PIC design. Oscillations at 10 GHz are obtained thanks to an EDFA, arising the need of optical amplification for positive gain.

The second section describes the PIC designed and described throughout Chapter 3, in a MWP fabrication run we will call "OEO Run". Even though it was not possible to obtain oscillations, the section gives good hints on how to improve the design, such as having higher power and avoiding RF crosstalk on the chip. Moreover, thermal crosstalk between components is investigates, especially for what concerns the interaction of the SOA and the EAM, the latter being the most sensitive component in the design.

The third section presents measurements performed on an integrated electrical frequency generator fabricated at III-V Lab within the IPHOS project, before my thesis. The PIC contains 2 DFB lasers, optical amplifiers, modulators and high speed photodiodes, in order to generate high frequency electrical signals through optical signal beating on the UTC photodiode. The PIC is used in an OEO configuration through a combination of optical and electrical injection locking. The advantage of heterodyne RF generation is the tunability of this OEO, by tuning the DFB laser currents. Tuning from 15 to 20 GHz is obtained with a simple change of the DFB laser current.

The last section presents the measurements performed on ring resonators used as microwave filters, the last building block to be demonstrated with respect to the PIC architecture shown in Chapter 1. The measurements on the ring resonators are performed on its two output ports with two modulation

schemes, amplitude and phase modulation. The ring shows a bandpass filter behavior at 10 GHz when injected with an amplitude modulated optical signal.

4.2 EAM-BASED OEO

In this experiment we test the idea of optoelectronic oscillator integration by photonic integrated circuits. We use an external modulation configuration for the link, consisting in a laser, a modulator and a photodiode [75].

Two devices from the "EML Run" are used for the measurements, one EML in transmission mode and a second one in reception mode, where only the EAM is used as a photodiode. The setup is show in Figure 117.

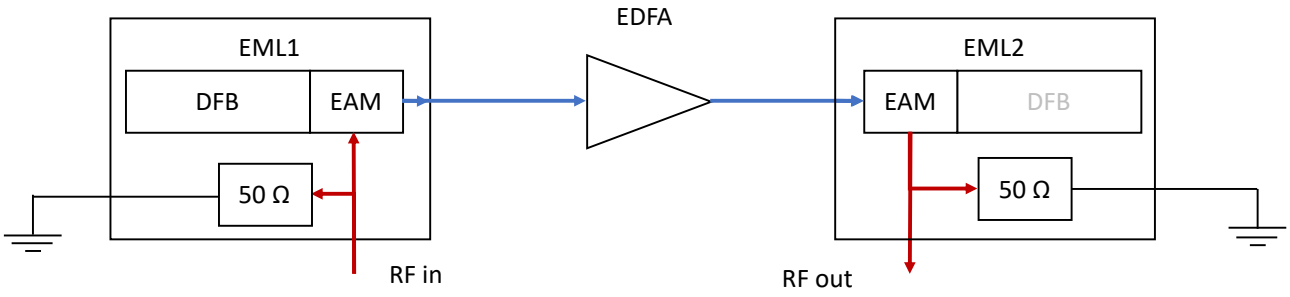

Figure 117. Open-loop measurement setup of the EAM-based OptoElectronic Oscillator

The experiment will allow us to evaluate three main points:

- The integration of laser and modulation structures by use of two semiconductor active region stacks, one for lasers and amplifiers and the second for the "absorption" functions, both modulation and detection;
- The feasibility of an all-optical gain analog link, and the extraction of the optical gain and power needed to do so;
- A wavelength detuning between those two active regions that favors a high extinction ratio for the modulator, to achieve high link gain despite the low optical power delivered by this first generation of devices;

The use of only two layer stacks for the production of all the functions needed in the PIC is driven by the need of simplicity in the fabrication phase. These devices are fabricated within the "EML Run", and the fabrication of the building blocks of such Photonic Integrated Circuits has been described in Chapter 3.

In order to prove the feasibility of an integrated OEO with such integration technique two Externally modulated laser (EML) devices are used. The first one is used as the emitter, with a laser and the modulation section working at the same time, while in the second chip the modulation section is continuously biased to act as a photodiode while the laser is left switched off.

For what concerns the second point on the list, the rationale of an all-optical gain OEO is that the monolithic integration of required optical and electrical component, to our knowledge, is not achieved yet on InP platforms, thus one cannot build an electrical amplifier between the photodetector and the modulator monolithically. The use of an external electrical amplifier is a backup solution that is not the preferred one as it will increase the dimensions of the system and electrical amplifiers are known to add phase noise to the system, especially close to the carrier.

The third point is about one of the original features of this kind of oscillators, the electro-absorption modulator. The choice of the amplitude modulator comes from consideration on the size and performances of the devices. Mach-Zehnder modulators have been for years the standalone device of choice for a number of analog photonic applications. The most prominent technology is the LiNbO (lithium niobate) platform, which allows relatively low insertion losses when connected optical fibers, good modulation efficiency and large modulation bandwidths. Mach-Zehnder modulators in InP technology are produced as well and may be integrated with laser diodes. However, both platforms deliver devices with lengths of at least few millimeters, which is the target size of the whole oscillator PIC. The candidate for the replacement of the MZM is the electro-absorption modulator, which uses the quantum confined stark effect to change the absorption of quantum well structures when an electric field is applied. The main difference with respect to the Mach-Zehnder modulator is the strong wavelength-dependent behaviour of the structure, in which the parameters to optimize are the respective positions of the gain curve of the first layer stack, the absorption curve of the second stack and the DFB emission wavelength, as described in Chapter 3.

The importance of the high-efficiency modulator is easily seen in the expression of the link gain of an EAM-based analog link [74]:

$$g = \left(\alpha P_L G_{opt} \eta_D \frac{dT}{dV}\right)^2 R_M R_D |H_M(f)|^2 |H_D(f)|^2 \tag{74}$$

where α are the optical losses factor, comprising all coupling and transmission losses, P_L is the laser power, G_{opt} is the optical amplifier gain, , η_D is the detector responsivity (in A/W), dT/dV is the modulator slope efficiency, , R_M and , R_D are the modulator and detector load resistances, $H_M(f)$ and $H_D(f)$ are the frequency responses of the modulator and detector, respectively, in the voltage domain. The H parameters describe the electro-optical bandwidth of the devices. However, they have a small influence at low frequencies where those two factors will be considered equal to 1.

The rest of the equation can be seen then as the expression for the DC gain, which will be the departure point of any consideration about the link gain. As we can see, two more factors are the modulator and detector load resistances. In order to perform impedance matching with external sources these loads are set to 50 Ω.

The term in parentheses can be divided into two factors. The first factor is the photodetector current, defined as

$$i_{ph} = \alpha P_L G_{opt} \eta_D \tag{75}$$

in which the loss factor α also takes into account the bias-dependent transmission losses of the modulator. The contribution of modulator losses can go up to 10 dB, depending on the bias point.

The second factor in parentheses is modulator's small signal differential transmission ***dT/dV***, also called slope efficiency. This factor impacts the modulation depth of the optical signal, or, equivalently,

sets the extinction ratio obtained from an AC signal of fixed amplitude when the DC bias is set at a certain point.

This parameter is measured indirectly by measuring the optical attenuation with respect to the bias point, as shown in Chapter 3. For these EML devices the measurement is shown in Figure 118.

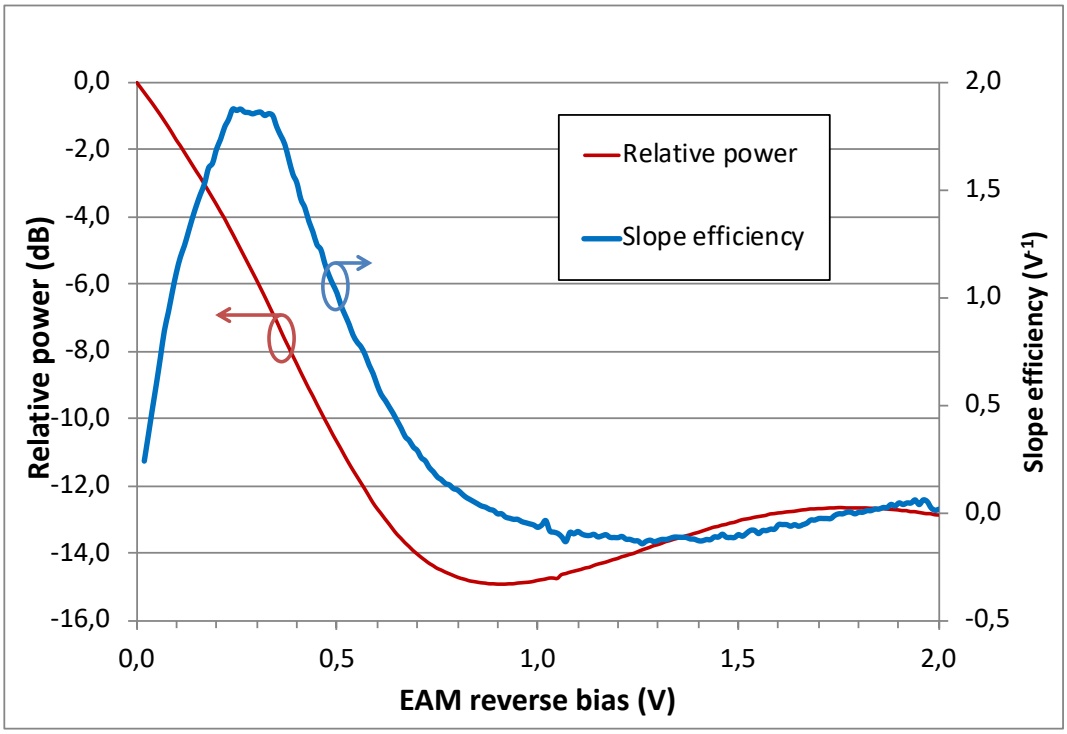

Figure 118. Measured relative power and slope efficiency of the devices produced with this fabrication run.

4.2.1 THEORETICAL LINK GAIN AND MEASUREMENT

The theoretical calculation for the open-loop link gain starts from the expression of what can be called "DC gain", that is, when we exclude from the gain link calculation all the (electrical) frequency-dependent terms:

$$g_{DC} = \left(\alpha P_L G_{opt} \eta_D \frac{dT}{dV}\right)^2 R_M R_D = \left(i_{ph} \frac{dT}{dV}\right)^2 R_M R_D \qquad (76)$$

where α is the total optical losses (including all losses), $\boldsymbol{P_L}$ is the laser power, $\boldsymbol{G_{opt}}$ is the optical gain in the link, η_D is the photodiode responsivity; all these terms can be regrouped in the photodiode current $\boldsymbol{i_{ph}}$. $\boldsymbol{dT/dV}$ is the modulator efficiency, $\boldsymbol{R_M}$ and $\boldsymbol{R_D}$ are the resistances of the modulator and detector, respectively. As the responsivity of the integrated photodiode can only be coarsely estimated and coupling losses can vary from one measurement to another, using the photodiode current $\boldsymbol{i_{ph}}$ is much more convenient to calculate the link gain since it can be directly measured. As both devices are terminated with a parallel 50 Ω resistor, the values of $\boldsymbol{R_M}$, $\boldsymbol{R_D}$ are set to 50 Ω.

The parameter that may vary in this kind of measurement is the efficiency of the modulator when the bias voltage is swept, and the steepness of the absorption curve changes accordingly. The measurements are performed as a function of the frequency with a VNA, but due to the large electro-optical bandwidth of the components, the low frequency response will correspond to the DC gain, on which a certain number of considerations can be made for the behavior of the system.

An example of link gain measurement from the "EML Run" components in the configuration of Figure 117 is shown in Figure 119, with a modulator voltage of -0.3 V. The dip at 12 GHz was observed throughout the whole measurement session so we suspected an issue with the EML assembly.

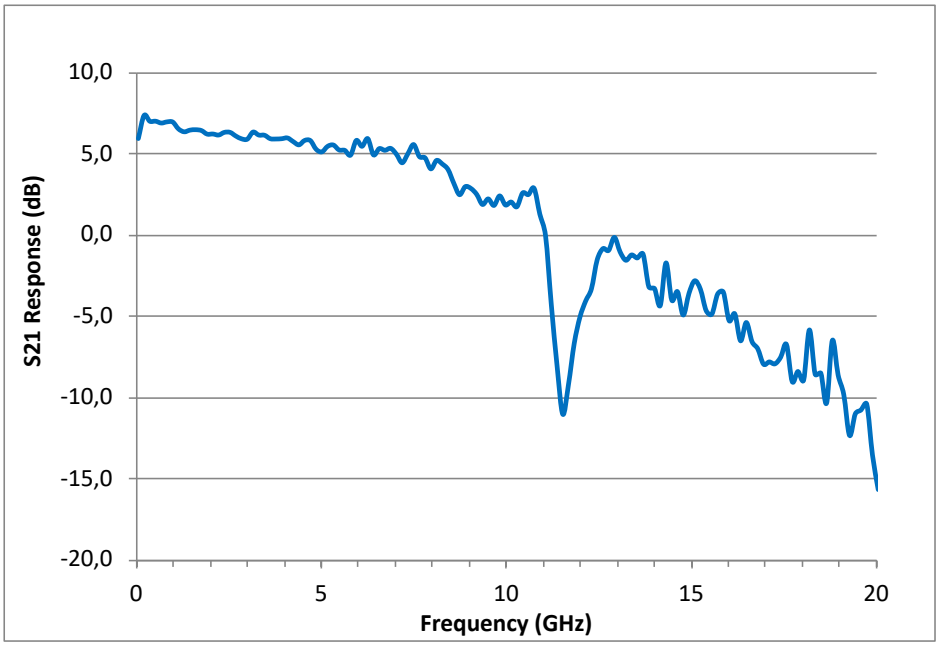

Figure 119. Open-loop gain measurement with modulator bias condition V_{EAM}= -0.3 V.

Figure 120 shows the comparison between the measured and the calculated link gain. The receiving MEA was biased at -1.5 V, and the voltage on the emitting MEA was swept from 0.1 to 0.5 V.

The theoretical calculation is the expected value of the DC gain from the measured photocurrent, and the extracted modulator efficiency from Figure 118. The average value of the link gain at the lowest frequency (40 MHz) is considered.

We can see a good correspondence between the model and the experimental values between 0.1 and 0.4 V. The model starts to fall off at 0.5 V, but it must be noticed that the effect of the modulation depth was not considered so far, and it could explain the loss of RF power at large absolute values of the bias point.

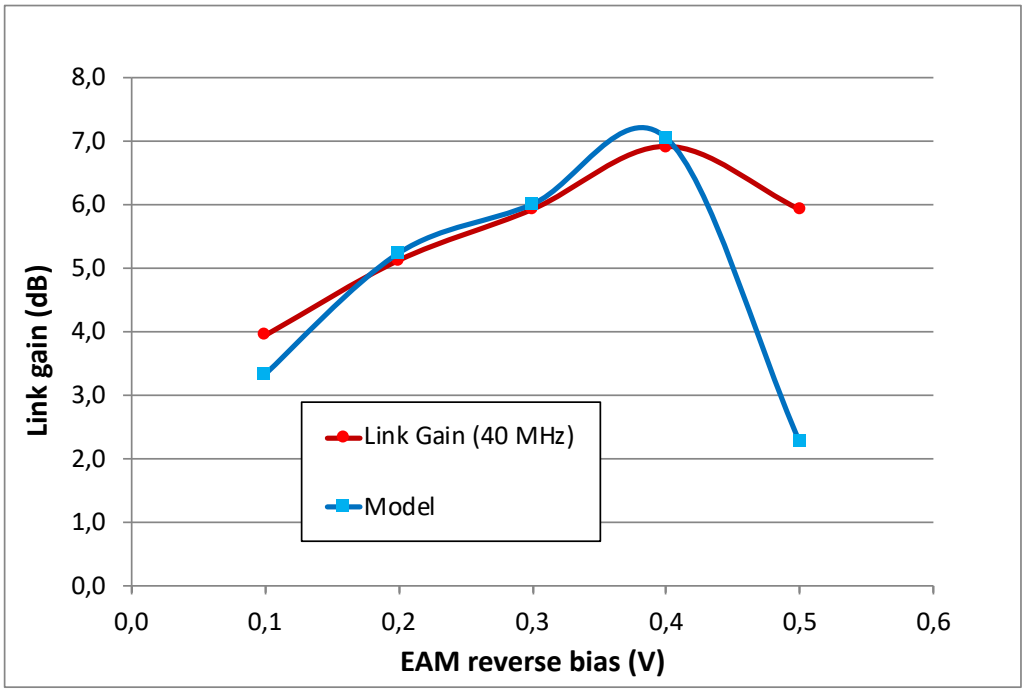

Figure 120. Comparison between measured and calculated optical link gain.

It must be noticed that these devices were optimised for very low bias operation. However, the operation point does not allow efficient junction depletion and thus low parasitic capacitance. The effect of carrier-induced capacitance is seen when measuring the EAM bandwidth at different bias points, as shown in Figure 121. The noise on the curve at the -1V bias point is due to the high absorption losses inside the modulator, thus the received optical power on the photodiode in the measurement setup is very low. This measurement shows how the frequency response of the link is affected by the components' frequency performances.

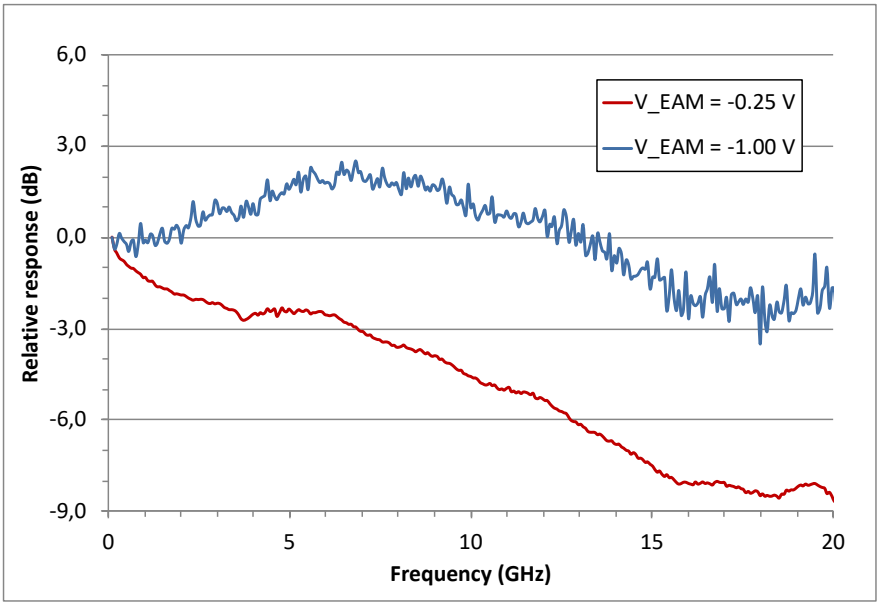

Figure 121. Measured modulator electro-optical bandwidth at different bias points

4.2.2 CLOSED LOOP EXPERIMENT

The two EML were measured in closed loop configuration. A 10 GHz electrical filter was added between the photodetector output and the modulator RF input. The output electrical signal was measured on an electrical spectrum analyser. Two snapshots of the electrical signal are shown, in Figure 122 and Figure 123.

Figure 122 shows the electrical signal with a large frequency span of 20 MHz. Two cavity modes can be seen 8 MHz apart from the main signal. The cavity mode spacing depends on the fiber delay used for the oscillator. In our case, a total fiber delay of around 25 m was used, mainly included within the EDFA and the short fiber interconnections from the PICs.

Figure 123 shows a narrower span of 2.5 MHz, to point out the noise seen around the signal. This noise is mainly attributed to the acoustic noise surrounding the setup and electrical noise from the electrical power supplies and environment, as well as fiber coupling instability, which was performed in a lab environment with micropositioners.

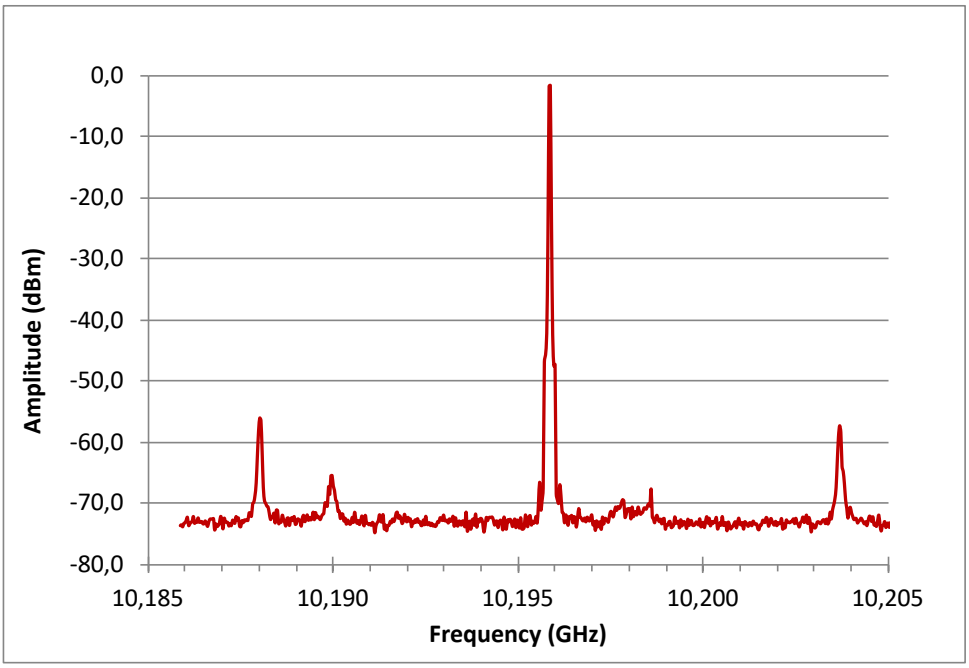

Figure 122. Plot of the generated 10 GHz microwave signal in the closed-loop experiment. Span of 200 MHz.

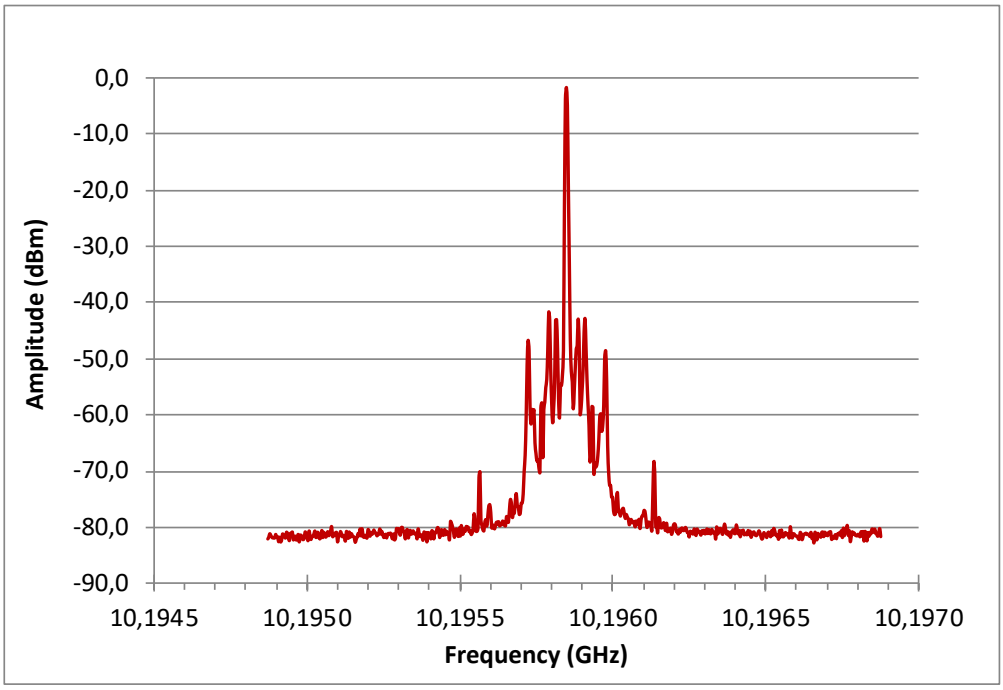

Figure 123. Close-to-carrier plot of the generated 10 GHz microwave signal in the closed-loop experiment. Span of 2.5 MHz.

4.2.3 Discussion of results

This experiment aimed to demonstrate the capability of electro-absorption modulators to work as analog amplitude modulators and replace the Mach-Zehnder modulator in an integrated Optoelectronic Oscillator.

The main parameters governing the low frequency open-loop link gain of the OEO are the generated photocurrent on the photodiode, i_{ph}, and the modulator efficiency dT/dV. In order to obtain positive all-optical gain both of these parameters must be maximized. The photodiode current is increase when the received optical power is increased; in our case, we used an EDFA to boost the optical power from the emitter EML, but the full on-chip integration of the OEO would require high power lasers and SOAs to obtain a positive loop gain. The slope efficiency parameter is optimised through the codesign of the laser and modulator gain and absorption curves; the modulators presented in this section had good peak slope efficiency of 1.8 V^{-1}, which resulted in good electrical-to-optical conversion of the microwave signal.

A 10 GHz signal was generated with an all-optical gain approach, with the addition of a 10 GHz bandpass filter. The signal showed noise close to the carrier due to the mechanical instabilities of the optical coupling to lensed fibers. Due to these instabilities it was not possible to faithfully extract the phase noise of this signal.

4.3 INTEGRATED OEO PIC

A Photonic Integrated Circuit designed to implement an Optoelectronic Oscillator was fabricated and tested at III-V Lab. It comprises: a DFB laser, an electroabsorption modulator (EAM), semiconductor optical amplifiers (SOAs) and a photodiode. The optical coupling in and out the chip was performed via mode adapter in order to expand the optical mode and ease coupling to optical fibers or passive PICs, such the ones described in chapter 2. The fabricated PIC is shown in Figure 124.

It can be noticed from the photo that this MWP run encountered fabrication issues, especially for what concerns the defect concentration on the chip. These defects have a strong impact on the performances of the whole PIC.

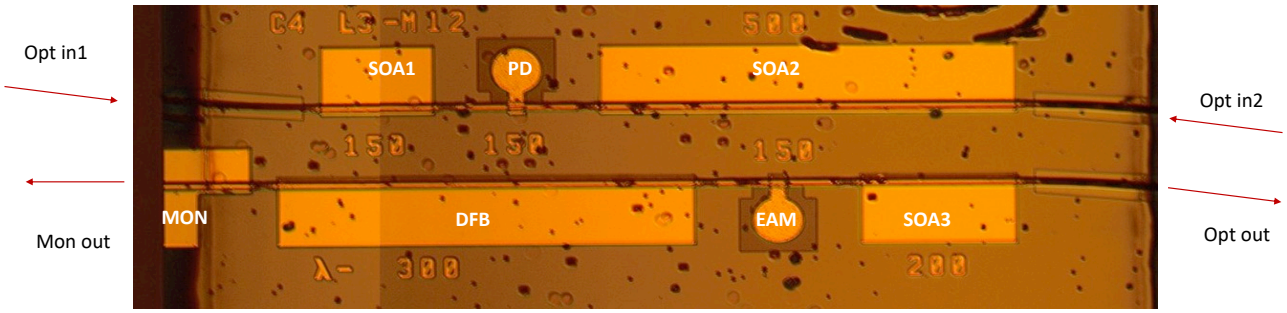

Figure 124. Photo of the fabricated OEO PIC on the SIBH integration platform.

Two epitaxial structures have been used for the fabrication of the PIC. The first layer stack is used to define the DFB laser and the optical amplifiers, where the only difference is the periodic or complete etching of the Bragg grating layer. The second layer stack is used for the modulation and detection functions.

Standalone components and mutual thermal coupling effects of multi-section biasing will be described in the next paragraphs, also including gain measurements with the PIC used as transmitter and receiver sections for an optical microwave link.

4.3.1 DFB LASER

P(I) characterization of the laser is shown in Figure 125. The closest measurement to the standalone behavior of the laser is the red curve, where both the EAM and the SOA sections are left unbiased. The measurement is performed with the SOA3 biased at 50 and 100 mA, which enables a rough estimation of the the gain of the SOA itself. The power measurement is performed with an integrating sphere, taking into account the optical losses caused by the spot-size converter.

As can be seen from the figure the optical power coming from the laser itself is low, and the optical amplifier can only partially increase the optical power value to around 19 mW, with a bias current of 100 mA. The lack of optical power will be one of the issues affecting the link gain, as will be seen in 4.3.4.

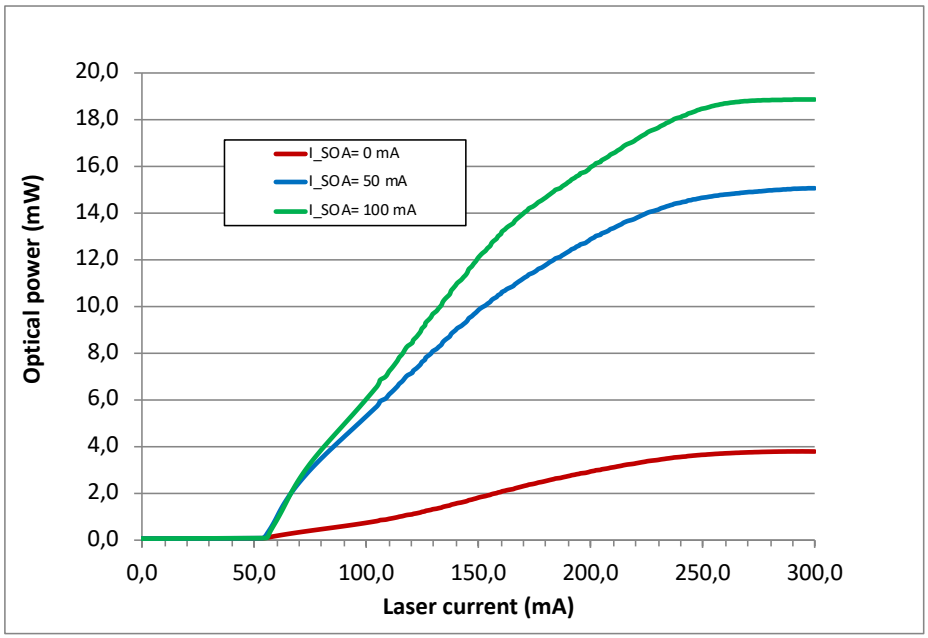

Figure 125. PIC output optical power with unbiased EAM and different SOA bias condition

4.3.2 Electro-absorption Modulator

The behavior of the modulator is similar to what has been shown in 3.7.2. In order to measure the extinction ratio and the modulation efficiency in operating conditions, the measurements were performed with different SOA3 bias currents.

The measurement of the extinction ratio (the normalized transmission values) as a function of the bias voltage are shown in Figure 126 for three SOA current values. It is unclear why the modulator changes its behavior when the amplifier is turned on. One hypothesis is that the amplifier is an absorbing section, thus when it is left unbiased the optical waveguide may be saturated. A second hypothesis is the thermal crosstalk between the SOA and EAM sections. The thermal crosstalk induces a shift in the modulator response as the temperature locally increases. Both mechanisms are possible and may concur to the change of response of the modulator.

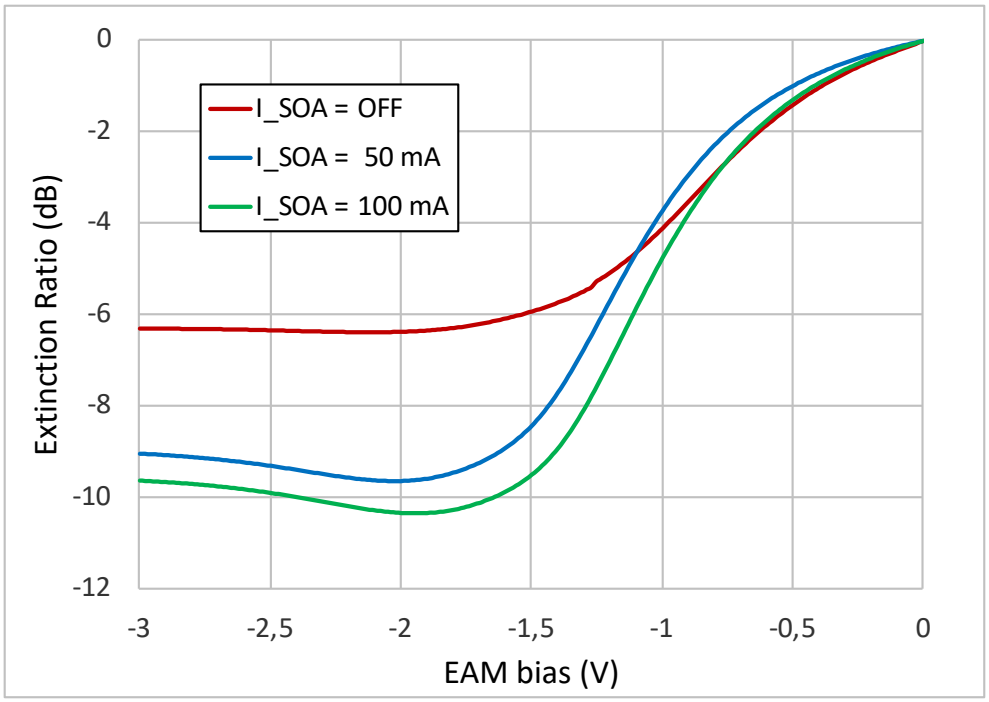

Figure 126. Measured extinction ratio of the Electro-absorption Modulator at different SOA bias point. The laser current is 200 mA.

The modulator efficiency was calculated through its response as it was done in Chapter 3. As the extinction ratio curve changes when the SOA is turned on, it was of interest to measure the change in slope efficiency with respect to the SOA bias current. The DFB laser bias current was kept at 200 mA. Results are shown in Figure 126.

It is worth remembering that the slope efficiency is related to the numerical derivative of the extinction ratio with respect to the applied voltage. Results calculated in Figure 127 show how the modulator efficiency is slightly increased, going from 0.71 V^{-1} at 0.8 V when the SOA has no bias current applied to 0.82 V^{-1} at 0.9 V with 100 mA of SOA bias current. The effect of the amplifier bias current must be taken into account in order to properly set the working point of the PIC.

4.3.3 Semiconductor amplifier

The semiconductor optical amplifier is used to increase the link gain and possibly reach oscillation condition with all-optical gain [76]. The SOA3 gain was extracted from measurements of optical output power similarly to Figure 125. The gain is referred to the 0 mA SOA current bias condition.

It can be seen that the gain is 7 dB at 100 mA and gain saturation onsets quite early with the bias current. It must be remembered that the devices performances are worse than expected due to the issues in the fabrication process.

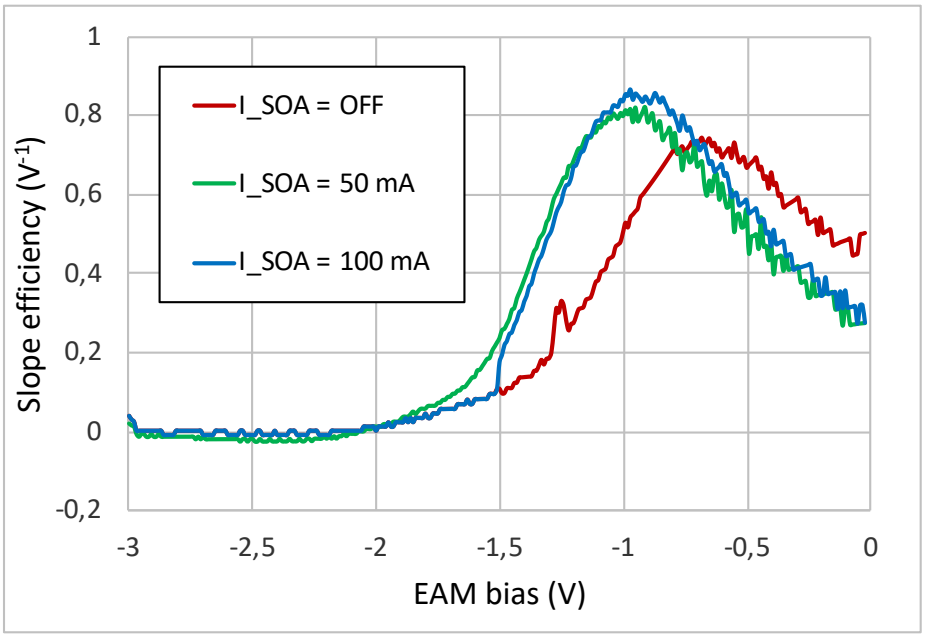

Figure 127. Extracted slope efficiency of the Electro-absorption Modulator at different SOA bias point. Laser current is 200 mA

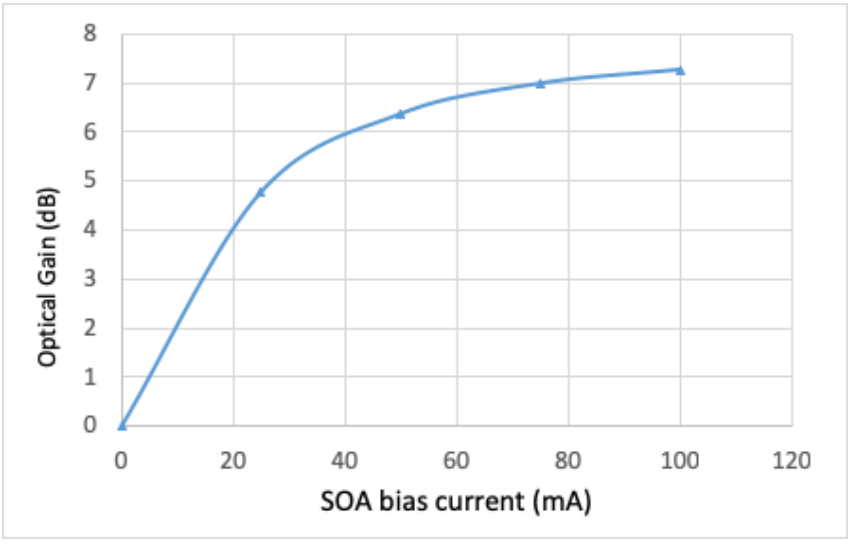

Figure 128. Extracted on-chip gain of SOA3 from PIC output power measurements.

4.3.4 Open-loop link gain

The open-loop link gain for an EAM-based photonic link reads:

$$g = \left(\alpha P_L G_{opt} \eta_D \frac{dT}{dV}\right)^2 R_M R_D |H_M(f)|^2 |H_D(f)|^2 |H_{SOA}(f)|^2 , \quad (77)$$

where α is the total optical losses, P_L is the laser power, G_{opt} is the optical gain of the amplifiers, η_D is the photodiode responsivity, dT/dV is the slope efficiency of the modulator, R_M and R_D are the modulator and photodiode series resistances, respectively, H_M, H_D and H_{SOA} are the frequency

responses (S_{21} parameter) of the modulator, photodiode and SOA, respectively. The term $H_{SOA}(f)$ was added since the SOA has a frequency response corresponding to a microwave high pass filter [77].

The method for measuring and evaluating the link gain at low and high frequency is the following: the low frequency gain is evaluated through the DC photocurrent and the frequency behavior through S parameters measurements with a Vectorial Network Analyzer (VNA).The optical power is collected from Opt. Out port and reinjected in the Opt. In 1 port, with reference to Figure 124.

The difference with the previous experiments is that we are now dealing with a Photonic Integrated Circuit, thus biasing more than one section of the circuit has an impact on the behavior of all devices.

Several open-loop gain measurements were performed with a VNA setup in order to validate the presented model. Low frequency values (40 MHz) of the measured S parameters are presented in Figure 129, with the corresponding theoretical gain. The modulator bias condition gives dT/dV = 0.8 V^{-1}, from the previous measurements.

The results show a good correspondence between the measured values and the model, but a very low open loop gain, lower than -20 dB.

The first reason is the low optical power at the input of the receiver section. The needed photocurrent for positive gain would be around 25 mA, which is an order of magnitude higher than what was obtained in the experiment. Higher optical power can be obtained using high power optical amplifiers, changing the layer stack of the "emission" devices (laser and SOAs) and adapting the optical mode to the modulator and photodiode.

A second reason for the low DC gain is the low slope efficiency of the modulator in this run, with values of dT/dV = 0.8 V^{-1}, far from the 1.8 V^{-1} of the standalone EML of paragraph 4.1.

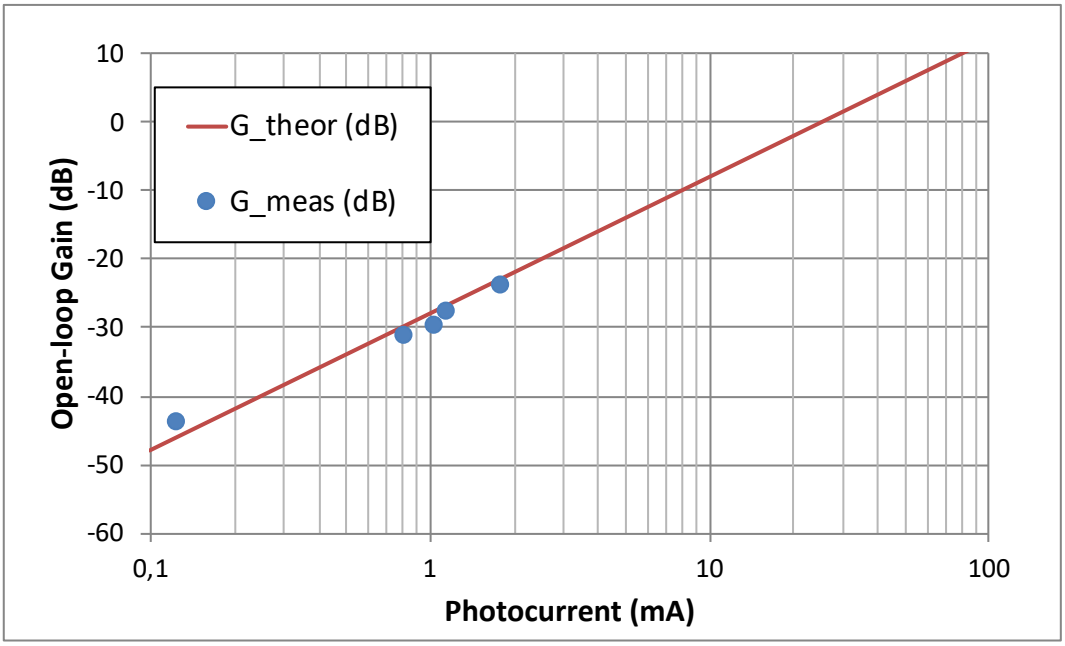

Figure 129. Integrated Opto-Electronic Oscillator open-loop gain model. Red curve: gain simulation with the parameters extracted from the standalone devices. Blue dots: measured values at different photocurrent levels.

4.3.5 CROSSTALK MEASUREMENT

Another issue raised within this experiment is the electrical crosstalk between the input (modulator) RF port and the output (photodiode) RF port.

The fabricated PIC was mounted on an alumina carrier and wire bonding was used to interconnect modulator and photodiode to the RF waveguides on the alumina (Figure 130). The two waveguides were placed on the same side of the alumina, and long bonding caused parasitic effects that in the end affected the electrical performances of the PIC. It is also worth mentioning that both the EAM and the photodetector are on the same chip with a common n-side contact that increases the risk for crosstalk on the chip.

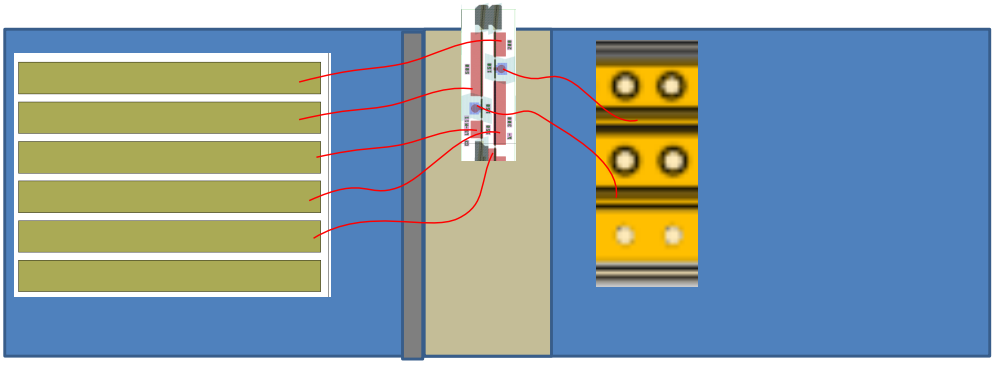

Figure 130. Carrier and PIC interconnection design for the OEO PIC characterization.

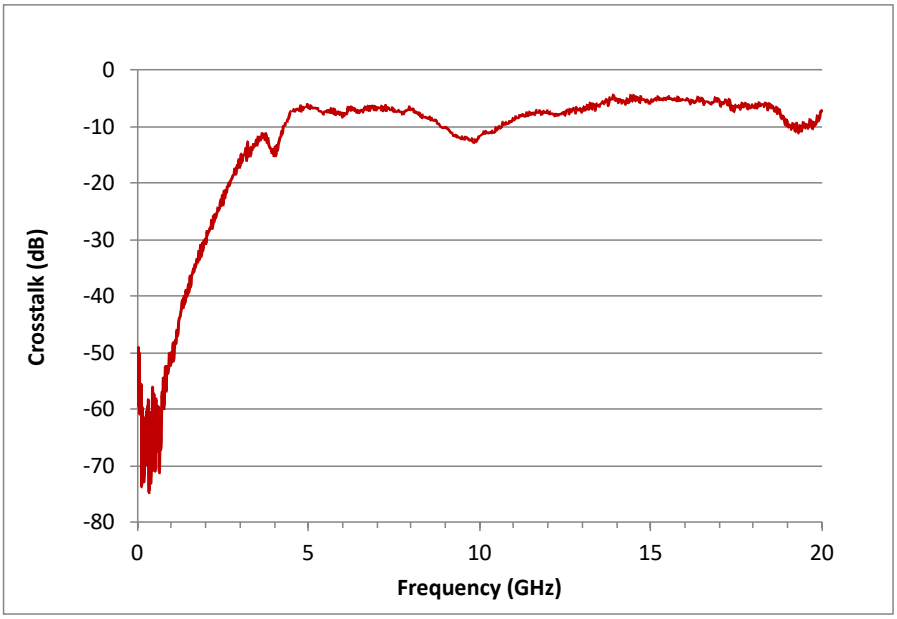

Figure 131. RF cross-talk measurement of the two RF waveguides on the alumina carrier.

The RF alumina was designed for higher frequencies and we observed a field leakage in the adjacent waveguide as shown in Figure 131.

The intrinsic RF waveguide coupling goes up to -4 dB, while this parameter should be minimized: a careful electrical design and alumina design is needed in order to avoid degradation of the integrated PIC performances.

4.3.6 Discussion of the results

The integrated OEO InP PIC designed in Chapter 3 was presented at the subsystem level. Due to the presence of several active components, the changes in behavior of standalone components was assessed; the characterization was concentrated on understanding how the presence of the SOA would affect the behavior of laser and modulator, to take it into account when setting the working point of the PIC. The thermal crosstalk between different active devices is mainly due to the local heat generation of the biased SOA.

The open-loop gain of the fiber-coupled PIC was measured as well, but the maximum obtained link gain was -20 dB. This underperforming value was partially due to the issues encountered in the fabrication and p-contact epitaxial growth processes, as already previously discussed, but also from the intrinsic lack of optical power generated from the PIC. Around 10 dB of optical power would be needed to reach positive gain; in addition, one must also consider that the total losses (coupling and propagation) of the SiN passive PIC could be higher than the fiber coupling losses obtained in this experiment. For this reason, an active InP platform integrating high power devices should be envisioned.

4.4 Tunable Optoelectronic oscillator

One of the desirable features of an oscillator is the capability to change its output frequency, ideally leaving all other properties unaffected, such as the phase noise of the generated signal.

The objective of this experiment is to demonstrate a tunable optoelectronic oscillator starting from an integrated heterodyne source [14] and aims to validate a different integrated OEO architecture with respect to the one presented so far. The PIC that was used has been fabricated within the IPHOS project long before the beginning of the thesis. Nevertheless, this PIC can be used in an OEO configuration and can give us useful data on how to possibly integrate such architecture with specific passive circuits in a future dedicated tunable OEO PIC design, which can be considered a natural evolution of the architecture presented in 4.3.

The PIC is shown in Figure 132. It contains:

- two DFB lasers, with 120 GHz spacing between the lasing wavelengths (DFB1 and DFB2);
- a passive 2x2 MMI coupler;

- several optical amplifiers (SOAs);
- electro-absorption modulators (EAM);
- high speed UTC photodiodes (UTC).

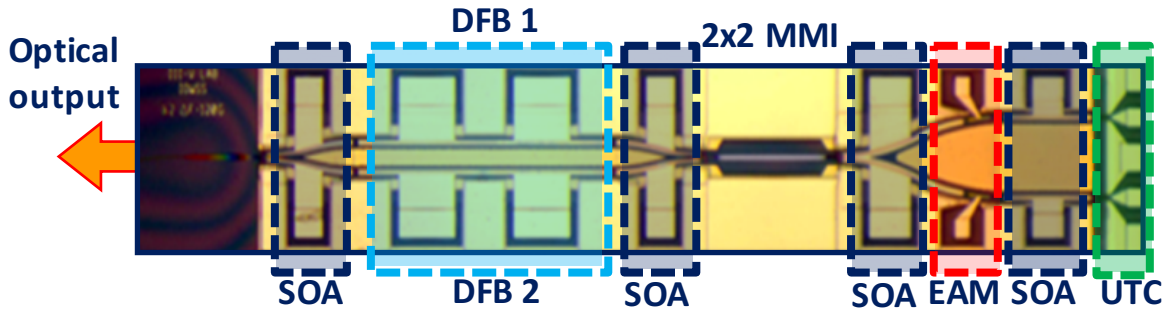

Figure 132. Picture of the IPHOS PIC with the different monolithically integrated devices

The generation of electrical frequencies is achieved in this case by mixing the two DFB tones on the UTC photodiodes. Each DFB wavelength can be tuned by current injection; in this way, electrical frequencies from 5 to 120 GHz can be generated with continuous tuning. The purpose of the electro-absorption modulator is to allow the digital modulation of the optical signals, translating into a modulation of the electrical carrier. The PIC is a fully integrated, frequency agile optoelectronic millimeter wave transceiver, when paired with an external antenna [78].

The optical linewidth of the two DFB lasers is quite high (~5 MHz), generating an electrical beatnote which has poor spectral quality, which limits in turn the transmission distance and reliability. In order to overcome this limitation a reinjection experiment was performed, in which the optical signals are modulated by an external phase modulator and re-injected in the chip from the rear optical output. The optical injection locking technique correlates the phase noises of the two optical tones so the electrical linewidth is greatly reduced [79]. In order to build an optoelectronic oscillator from the above pic we proceed in a similar way, but an on-chip reinjection path is used. In order to explain how the experiments were conducted the experiment is described as a sequence of three steps: 1-free running operation of the dual wavelength laser source, 2-mutual optical injection, 3-mutual optical injection combined with delayed electrical injection.

4.4.1 Electrical frequency selection: free running condition

The DFB lasers have a λ/4 phase shift in the middle of the cavity. The optical power is emitted on both sides, and this allows us to extract light on the rear optical coupler, which has a 7° tilt with respect to the facet to avoid backward reflections.

The two laser tones are set such that their optical frequency difference is the desired electrical frequency for the oscillation. The signal is detected on a fast (20 GHz) photodiode and the generated

electrical frequency is monitored on the electrical spectrum analyser (ESA). DFB currents are adjusted accordingly to set or change the desired beat frequency.

In this phase of the experiment (Figure 133) only the DFB lasers (and the rear SOAs) are turned on; the reinjection SOAs, shaded in blue, are turned off. Light goes out from the rear output coupler following the blue path shown on the chip. The corresponding optical spectrum (Figure 134) shows the two DFB tones with around 17 GHz spacing.

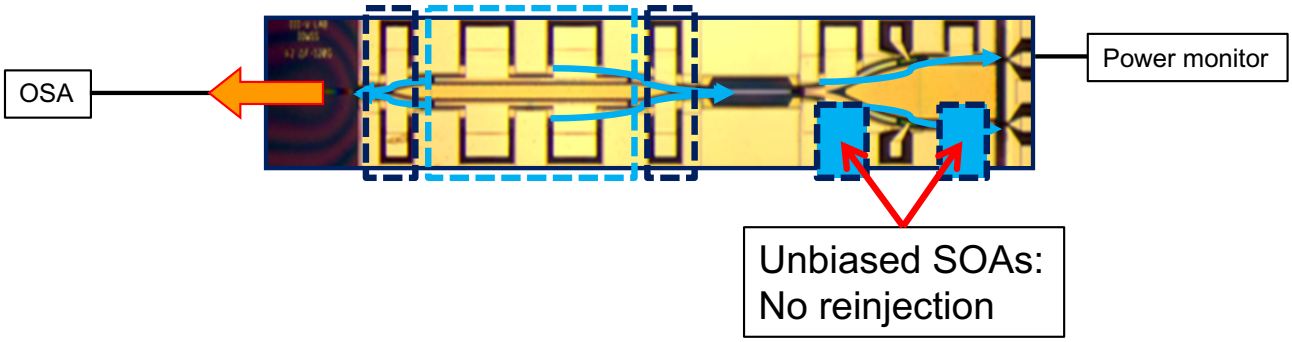

Figure 133. Free running condition: the optical output is collected on the OSA from the rear optical port. The SOAs are unbiased and there is no reinjection.

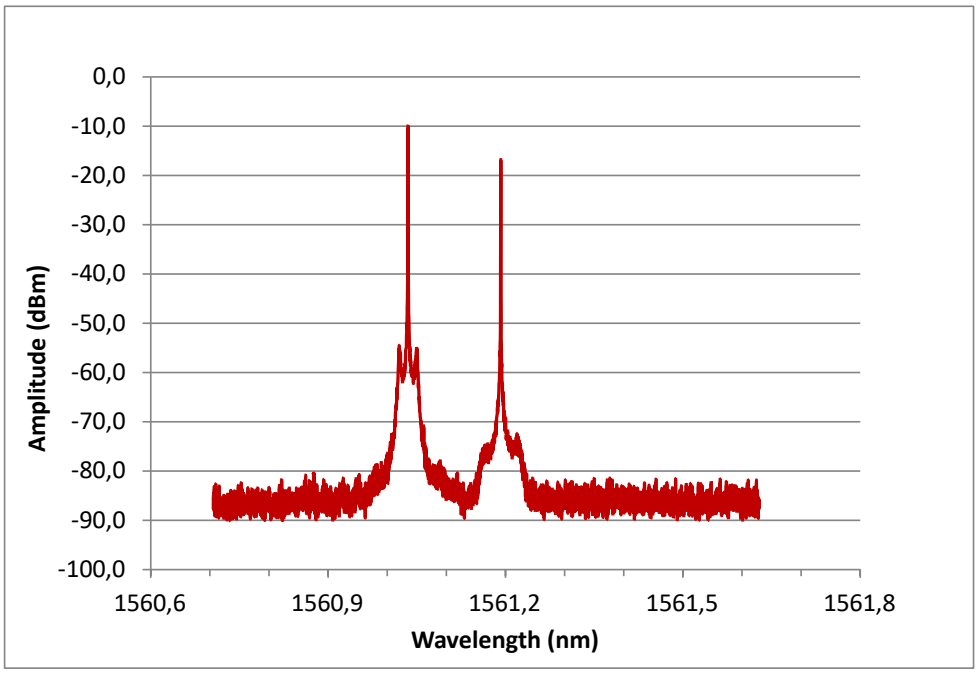

Figure 134. Free running condition: optical spectrum

4.4.2 MUTUAL OPTICAL INJECTION LOCKING

The reinjection SOAs are turned on during the second part of the experiment (Figure 135). The optical signal is also travelling towards the rest of the PIC, in this second case. The two DFB tones are amplified, combined and amplified again until they reach the integrated UTC photodiode. Since the photodiode is left unbiased, the signal travels through and gets reflected on the cleaved facet of the chip, then travels back towards the lasers. The injection ratio is controlled through properly biasing the optical amplifiers.

Both wavelengths are injected in both lasers, so each DFB acts as a master and slave laser at the same time, if this is seen as a "classical" injection locking scheme. The main signature of the mutual optical injection locking is seen on the optical spectrum as sidebands with the same frequency spacing of the two original DFB tones (Figure 136). These sidebands are generated by non-linear processes induced in the gain medium by the presence of two wavelengths at the same time. The electrical spectrum is also measured (Figure 137), giving a beat signal at the DFB wavelength difference, in this case around 17.4 GHz.

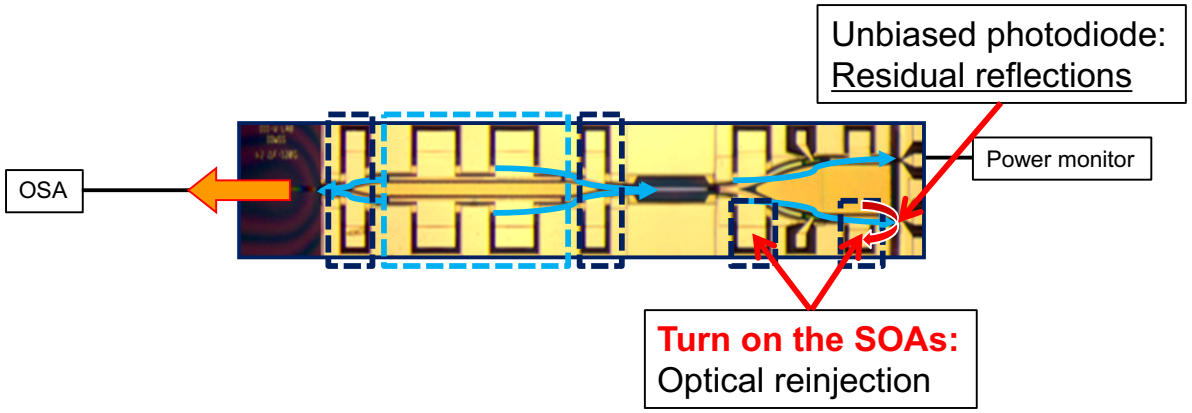

Figure 135. Mutual optical injection locking: the SOAs are biased and the reflection from the photodiode allows for mutual optical reinjection of the two lasers.

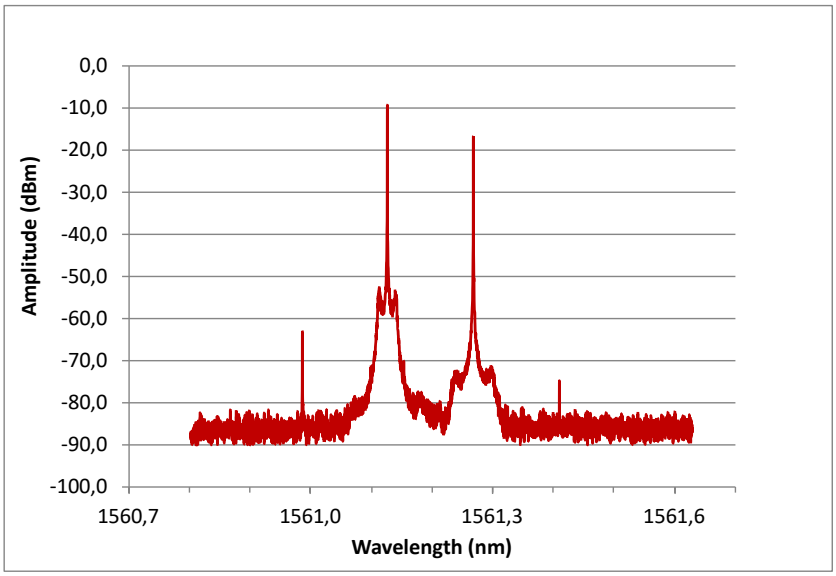

Figure 136. Mutual optical injection locking: optical spectrum

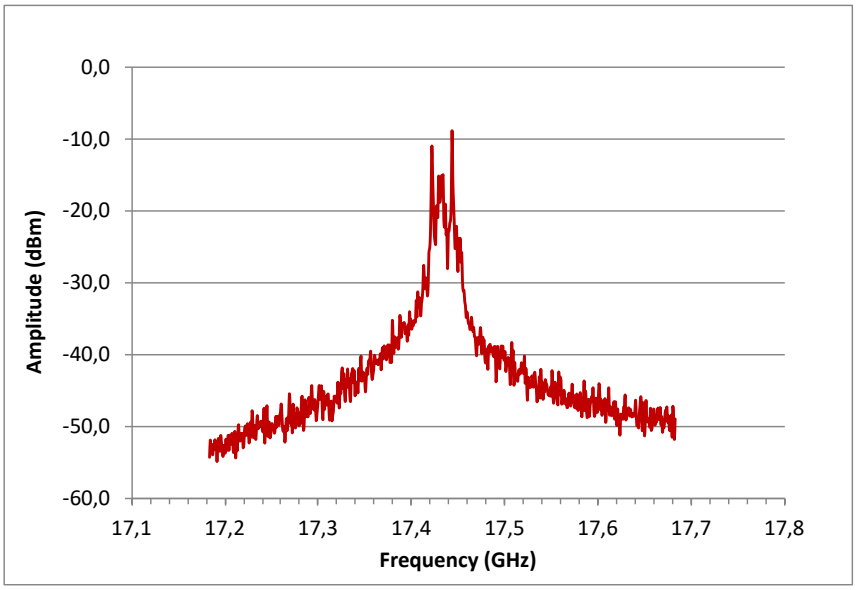

Figure 137. Mutual optical injection locking: electrical spectrum with 700 MHz span

4.4.3 CLOSED LOOP

As third and last phase of the experiment the O/E loop is closed on the integrated modulator (Figure 138). Two stages of electrical amplification are needed to reach the oscillation condition; the first amplifier is a 20 GHz bandwidth low noise amplifier, while the second one is a 40 GHz high saturation power amplifier. Both stages were needed since the optical signal was very weak, of the order of a hundred microwatts.

A high pass filter was added between the first and second electrical amplifiers. The use of this kind of electrical filter is a unique approach in this OEO demonstrator: usually, the filter is needed to select one of the many cavity modes created by the electro-optical cavity; the filter is required to be narrowband around the desired oscillation frequency. Narrow bandpass filters, however, have very limited tunability, and would nullify the advantages of heterodyne electrical frequency generation. On the other hand, one must be careful on the adjustment of the gain level in the loop, since the (electrical) single mode behaviour of the cavity is not assured any more.

One way to limit the mode hopping and the instability of the cavity is to use a short fibre delay to have a large mode spacing. The length used in this experiment is 7m, corresponding to an FSR of around 18 MHz. It has to be noticed that this is an extremely short optical delay length with respect to classical OEO systems, which use fibre lengths of the order of 1km, but meter-class optical delays can be integrated on out passive platform PIC as shown in 2.7.1, with a delay of 75 cm on 1 cm^2 footprint.

When the loop is closed on the integrated modulator the two laser tones and the lateral peaks undergo amplitude modulation, which in turn will create lateral modulation peaks to reinforce the existing ones. The effect of the electrical modulation is clearly seen on the optical spectrum (Figure 139), as the magnitude of the modulation peaks increases of 8 dB for the left peak and 17 dB for the right one. This asymmetry can be explained by the fact that the modulation efficiency of the electro absorption modulator is wavelength dependent.

The effect of the closed loop on the electrical spectrum is a redistribution of the energy from a broad electrical spectrum to distinct modes created by the resonant cavity, as expected. The comparison of electrical signals in open loop (optical injection) and closed loop configurations are shown in Figure 140. The linewidth of the signal is strongly improved and a Side-Mode Suppression Ratio (SMSR) of more than 25 dB is reached between the resonant signal and its adjacent cavity modes. This SMSR can be further improved with electrical or optical filtering techniques.

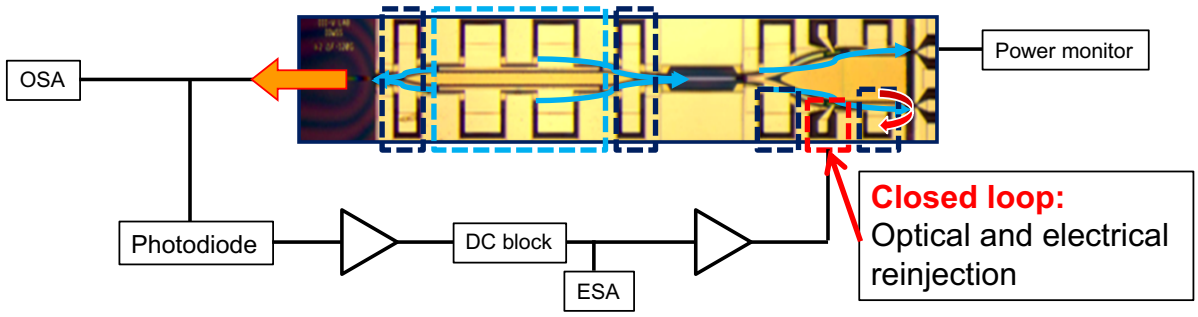

Figure 138. Closed loop condition: the generated electrical signal is amplified and applied to the modulator in the reinjection path.

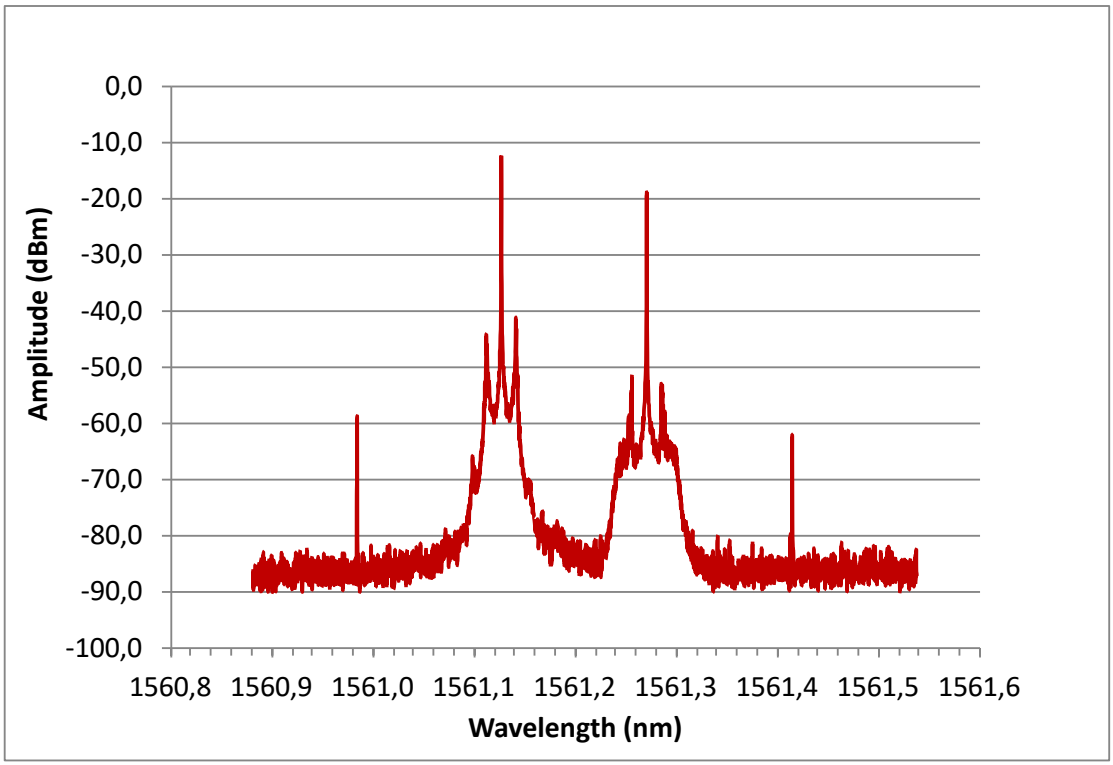

Figure 139. Closed loop condition: optical spectrum with clearly visible modulation sidebands.

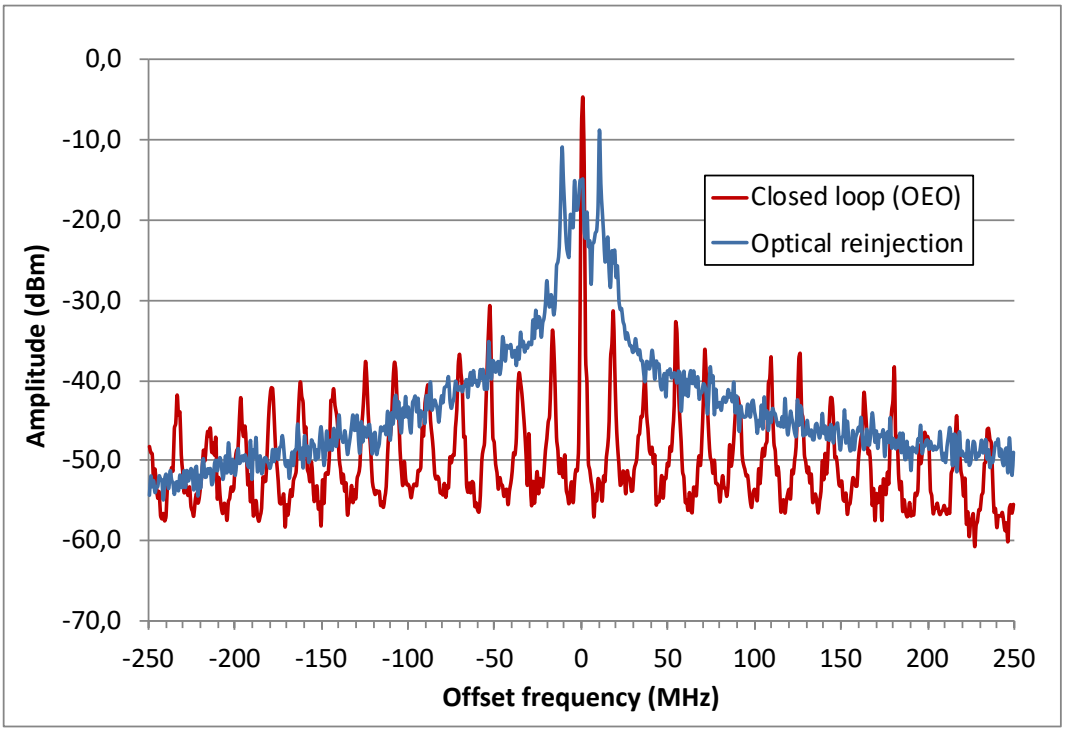

Figure 140. Comparison of electrical spectra between the optical reinjection condition (Blue curve) and the closed-loop condition (Red curve), with 500 MHz span. The electrical linewidth of the signal is greatly reduced.

4.4.4 Tuning of the electrical frequency

The advantage of the heterodyne technique for electrical frequency generation comes from the fact that frequency differences in the microwave or millimetre range can be produced by lasers with a slight variation of the DC bias current.

During the experiment one laser bias current was kept fixed at a value of 49.6 mA. The current of the other DFB laser is swept from 155 to 160.7 mA to achieve tuning of the electrical frequency from 20.1 to 15.3 GHz (Figure 141). The tuning factor of the electrical frequency with respect to the DFB bias current is roughly -1 GHz/mA.

The tunability of the oscillator is limited by the nominal frequency (or wavelength) offset of DFB lasers, which was set at 120 GHz since this PIC was designed to generate wavelengths from DC up to 120 GHz. In order to obtain the frequencies from 15 to 20 GHz the PIC needs to work in extreme conditions: the DFB with the lower wavelength is biased with high current to bring it close to the second DFB, which is biased not far above threshold.

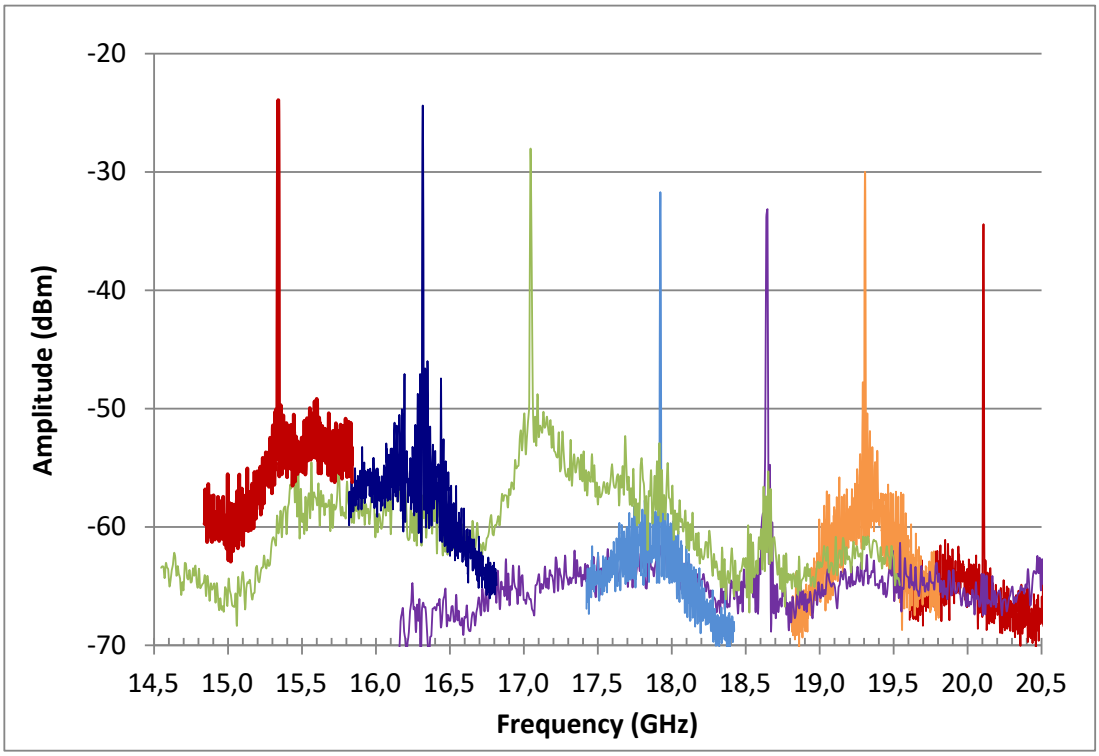

Figure 141. Electrical frequency tuning: the change in the electrical frequency is obtained by changing one of the DFB bias current.

4.4.5 Discussion and limitations

Heterodyne technique allows for wide tunability of the generated electrical frequency. In this experiment, however, the electrical spectrum showed instability over time. As previously mentioned, one way to stabilize the oscillation is to control the loop gain by adjusting the gain of the second electrical amplifier.

When the second amplification stage was set at moderate gain the system experienced mode hopping only between the adjacent modes 18 MHz apart from each other. This kind of behavior comes from the fact that slow variations of temperature of the fibre, or rather phase changes in the OEO or reinjection paths due to temperature, current injection noise, and other undesirable effects, can modify the position of the cavity modes. The gain is almost constant and slightly above 0 dB, so the mode hopping happens only if the oscillating mode is moved too far away in a lower gain region, so the adjacent mode starts oscillating.

When the same amplifier is set at high gain several modes are in competition, even hundreds of MHz away from each other. This happens because the open loop gain becomes positive in a large frequency region and there is not a narrowband electrical filter in the loop. This behavior also shows that the reinjection mechanism is overrun by the large positive gain region, since the self-stabilization mechanism of injection locking is not able to keep the oscillation at a fixed frequency.

Two reinjection experiments were previously performed on the same chip, in our lab. In the first one [79], the reinjection path was an external fibre loop in which light was phase modulated by a

frequency synthesizer. The mutual injection locking was performed on the 5th optical harmonic generated by the phase modulator, to achieve a 90 GHz stabilized electrical frequency with an 18 GHz signal on the phase modulator. This experiment showed a drastic decrease in linewidth of the generated electrical frequency, reaching 30 Hz (limited by the resolution of the electrical spectrum analyzer).

The second reinjection experiment [80] used the same on-chip reinjection path as this experiment, in order to lock the lasers to the 7th optical harmonic at a frequency of 33.5 GHz, with a driving signal of 4.8 GHz.

One can extract two fundamental limitations of the system we used for the oscillator in the above configuration, when watching the previous experiments from a critical point of view. First of all, the on-chip reinjection path has a very low quality factor, due to the propagation losses in the InP-related materials, compared with the fibre-based re-injection loop. The second important (hidden) parameter is the bandwidth of the integrated modulator, which has a 3dB electro-optical bandwidth of few GHz. This low modulator bandwidth allows injection locking on harmonics (since the modulation frequency is low) but has an extremely low efficiency at the frequencies of the experiment.A similar approach of heterodyne injection locking is used in the photonic oscillator described in [81].

4.5 RING RESONATOR AS MICROWAVE PHOTONIC FILTERS

The objective of this paragraph is to show how ring resonators can be used as microwave photonics filters, as introduced in Chapter 1.

The ring resonator has been introduced in Chapter 1 as the element performing the microwave filtering in the optical domain.

The principle is shown in Figure 142. An integrated ring filter in an add-drop configuration has a response of evenly spaced peaks like the blue curve on the left, acting as a periodic electrical band pass filter, as shown in the right. The electrical signal is generated by the optical sidebands reaching the photodiode. Thus, using different modulation formats and filtering configurations on the optical signals, it is possible to build tunable and reconfigurable filters in the microwave domain.

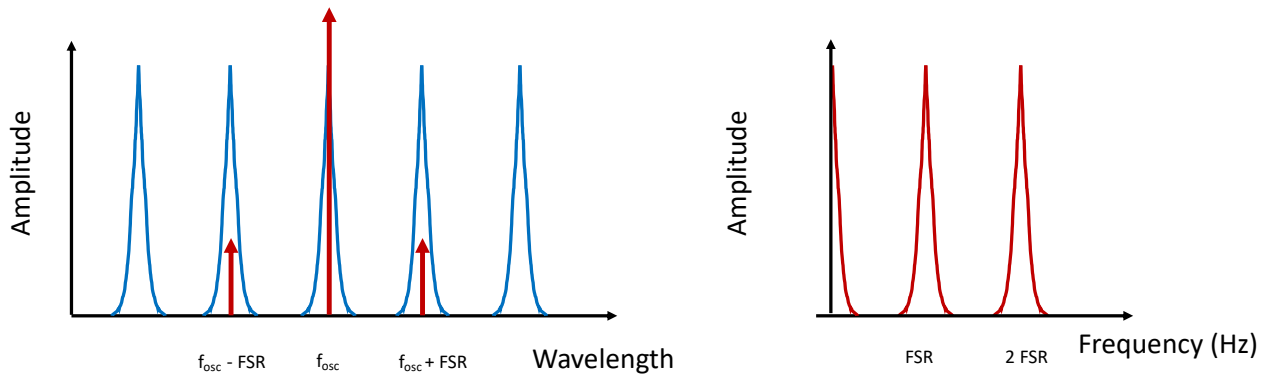

Figure 142. Optical filtering principle of a ring resonator. Left: ring filter response of the drop port and optically modulated signal. Right: ring filter response of the drop port in the electrical domain.

The configuration chosen at the system level was shown in Chapter 1 in the OEO PIC design. The integrated EAM applied an amplitude modulation to the signal, that was then collected to the photodiode from the drop port of the resonator. This is the configuration shown in Figure 142.

The advantage of amplitude modulation is that since the peaks of the ring are evenly spaced, both carrier and sidebands will be within the filter passband in a configuration in which optical power is monitored and maximised, like the one we designed. Since the two modulation sidebands are in phase, the two RF signals generated from their beating with the carrier on the photodiode will sum up. We will also verify that the optical lineshape seen in Chapter 2 is reproduced in the electrical domain.

We used four configurations for testing the ring resonator: a combination of phase or amplitude modulation with through or drop port measurement. The chip used for the measurement was presented in Chapter 2. The PIC has 9 ring resonators with 10.5 GHz FSR, and both notch and drop ports available. The first ring was used for the functional demonstration, and it had a finesse of around 17 for a 10.4 GHz ring.

All setups have the main elements in common, namely the external laser, the polarization controls (PC) before and after the modulator, the modulator itself (phase modulation, PM, or amplitude modulation, AM), the optical amplifier (EDFA), the device under test (DUT), the photodiode and the RF amplifier. The RF response is measured using a VNA.

4.5.1 THROUGH PORT MEASUREMENT WITH PHASE MODULATION

The first setup is used to measure the ring through port with phase modulation, and it is shown in Figure 143.

In Figure 144 one can see the optical and electrical spectra of the different measurements.

In (1), (2) and (3), the laser wavelength is between two optical notches. The corresponding electrical spectrum gives peaks corresponding to the differences of the CW signal and the sidebands.

Phase modulation creates sidebands with opposite phase, thus the RF signal is enhanced when one of the two sidebands is attenuated by the ring resonators.

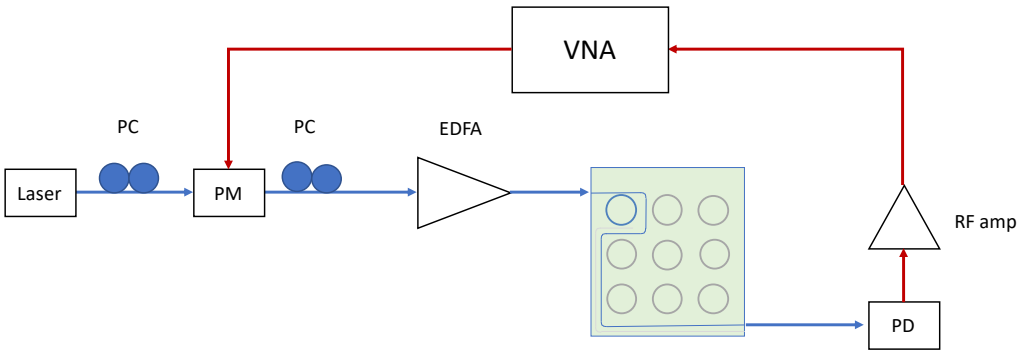

Figure 143. Measurement setup for phase modulation measurement on the through

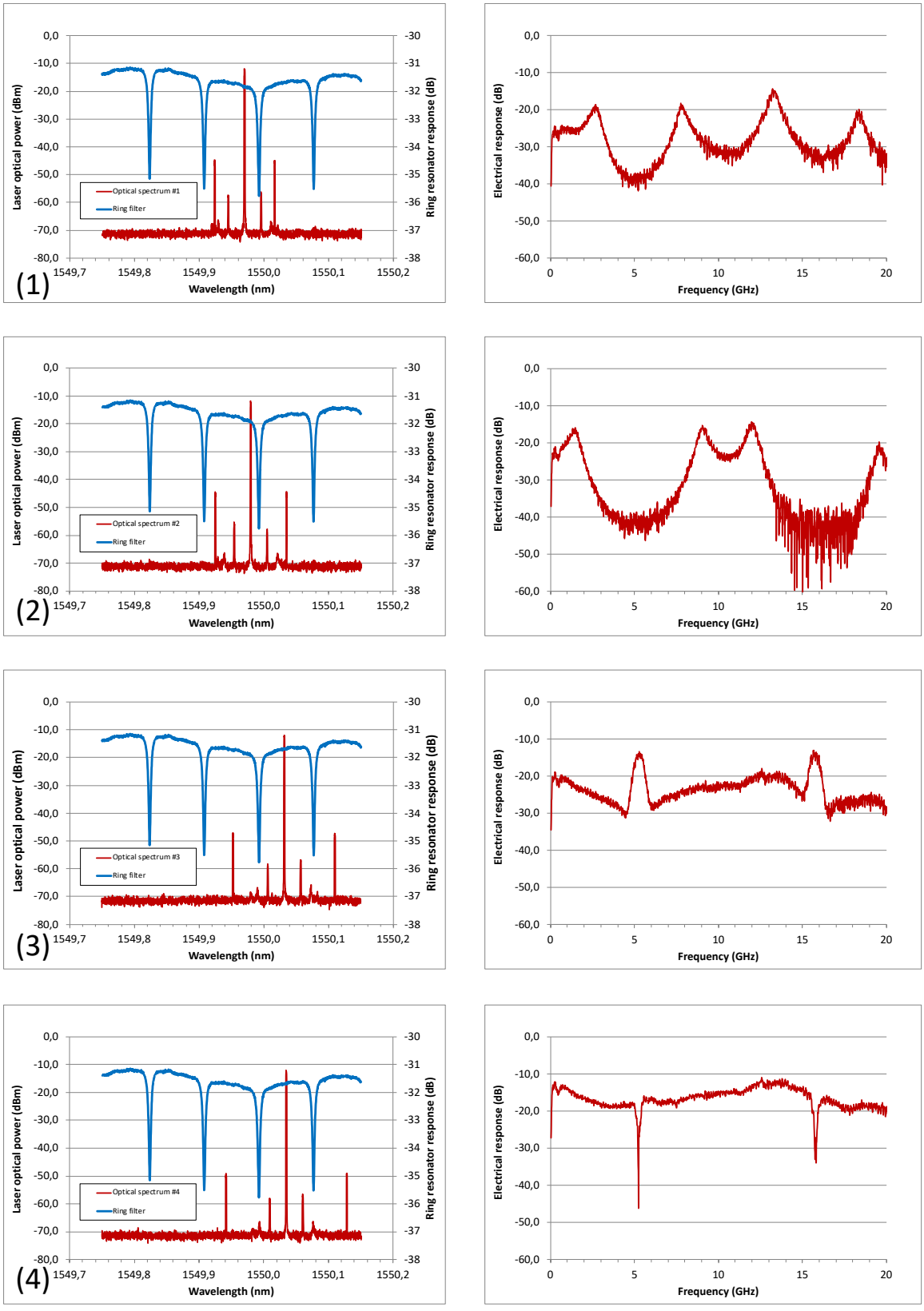

Figure 144. Through port response of the ring resonator with phase modulation

In (4), the CW laser has the same distance from the two notches. In this case, a very sharp decrease in power is observed due to the mutual attenuation of both sidebands.

4.5.2 DROP PORT MEASUREMENT WITH PHASE MODULATION

A similar setup is used to test the drop port of the resonator with phase modulation, as shown in Figure 145.

Two cases of DFB position with respect to the filter response were studied, as shown in Figure 146.

In case (5) the optical signal is slightly not centered on the ring resonance. The phase modulated signal is cancelled when the two optical sidebands are both transmitted, giving a sharp notch around 10 GHz.

In case (6) the DFB is exactly on the ring resonance. In this case, the signal is always cancelled, since the two sidebands always have the same magnitude.

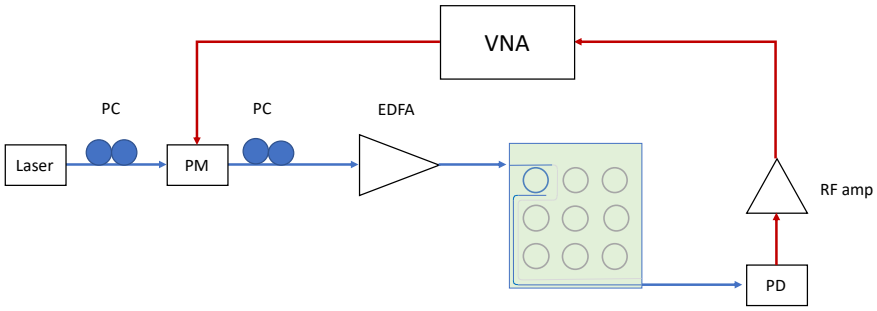

Figure 145. Measurement setup for phase modulation measurement on the drop port

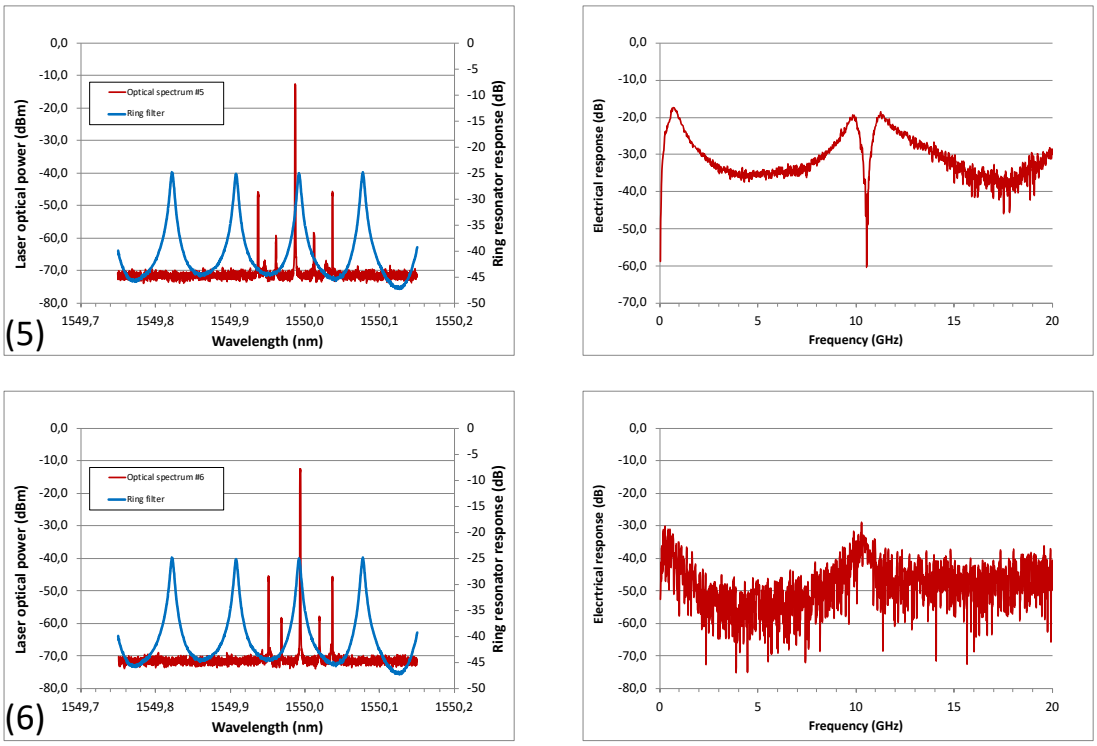

Figure 146. Drop port response of the ring resonator with phase modulation

4.5.3 THROUGH PORT MEASUREMENT WITH AMPLITUDE MODULATION

The second modulation technique is amplitude modulation. Unlike phase modulation, in this case the two sidebands are in phase and thus sum up when both reach the photodetector.

Figure 147 shows the setup of amplitude modulation measurement on the through port.

In both cases studied, the DFB signal was between two notch dips of the ring resonator. The electrical response shows no effect of the filter except for small dips at 5 GHz for case (7).

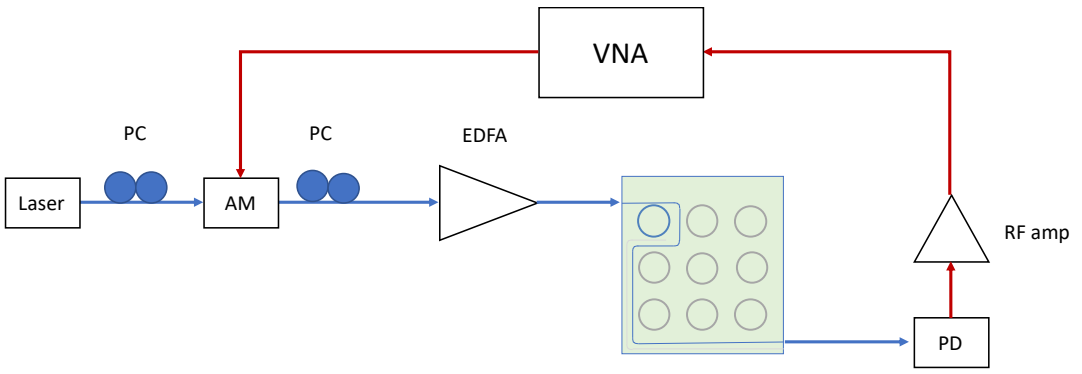

Figure 147. Measurement setup for amplitude modulation measurement on the through port

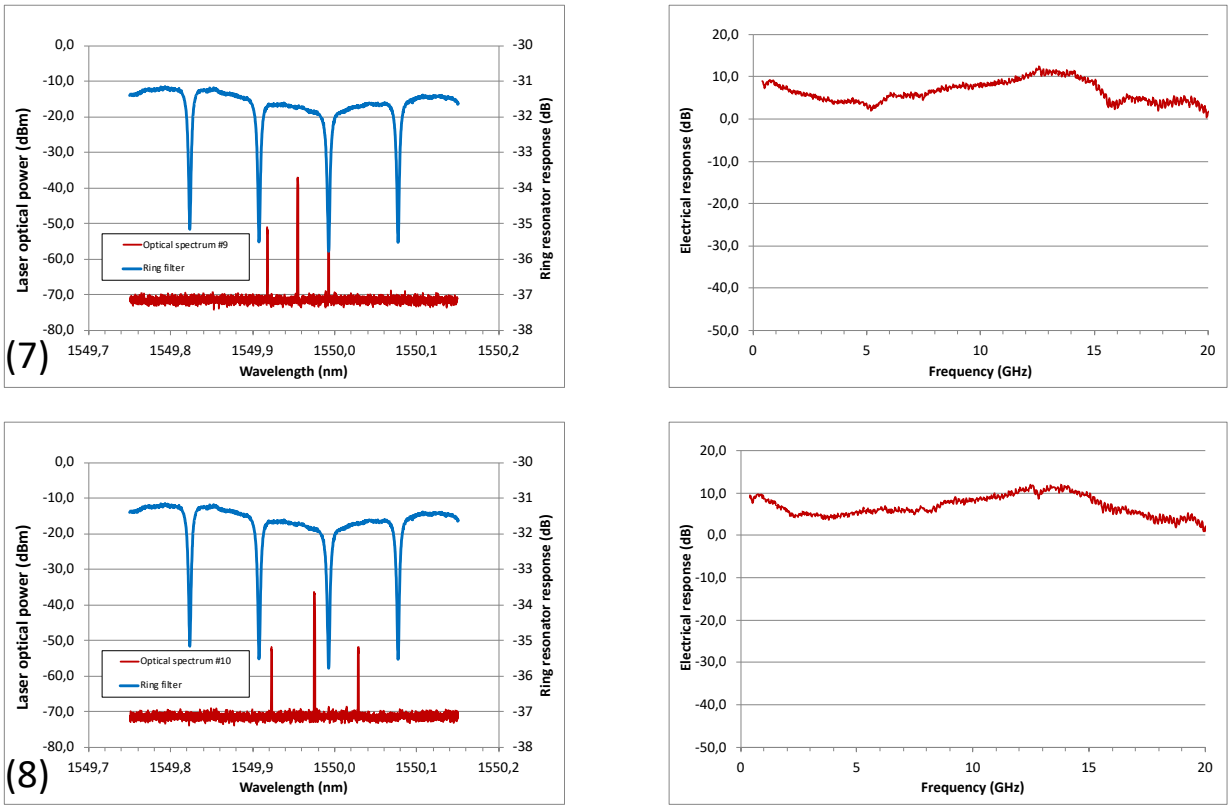

Figure 148. Through port response of the ring resonator with amplitude modulation

4.5.4 DROP PORT MEASUREMENT WITH AMPLITUDE MODULATION

The last configuration of the measurement is with amplitude modulation on the drop port of the ring resonator, as shown in the setup of Figure 149. This is the chosen configuration at system level.

Three cases have been studied, shown in Figure 150. Case (9) is the most important one, in which the DFB laser wavelength corresponds to a resonance of the ring filter. In this case, a strong resonance is seen in the electrical spectrum, corresponding to the free spectral range of the resonator.

Case (10) shows the DFB signal displaced with respect to the filter response, but still inside its bandwidth. Two peaks appear below and above 10 GHz, corresponding to the difference in frequency of the DFB signal with the ring response adjacent peaks.
Case (11) shows the DFB signal out of the filter pass bandwidth, in between two resonances, with peaks at 5 and 15 GHz. It must be noticed that in this case the carrier is strongly suppressed.
The working point of this configuration must be carefully controlled as the optical carrier must be kept as close as possible to the top shape of the filter. This requires specific control loops that can range from Pound-Drever-Hall (PDH) techniques to optical injection locking of the laser diode on the resonator itself [82].

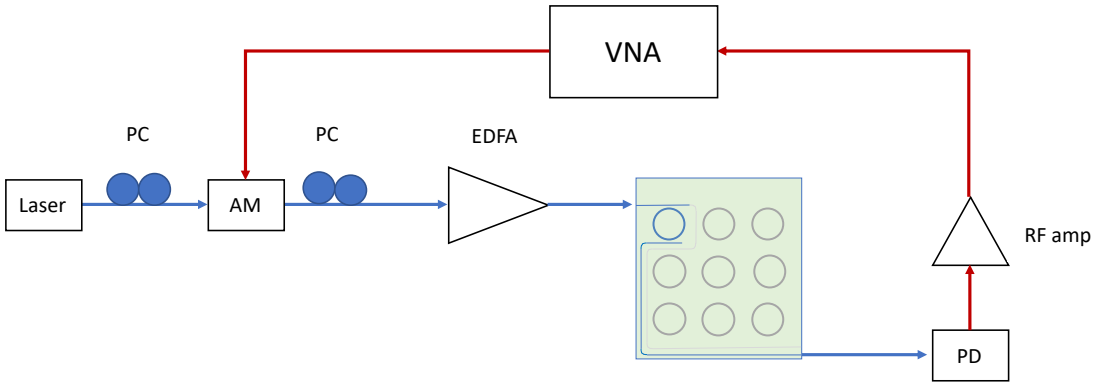

Figure 149. Measurement setup for amplitude modulation measurement on the drop port

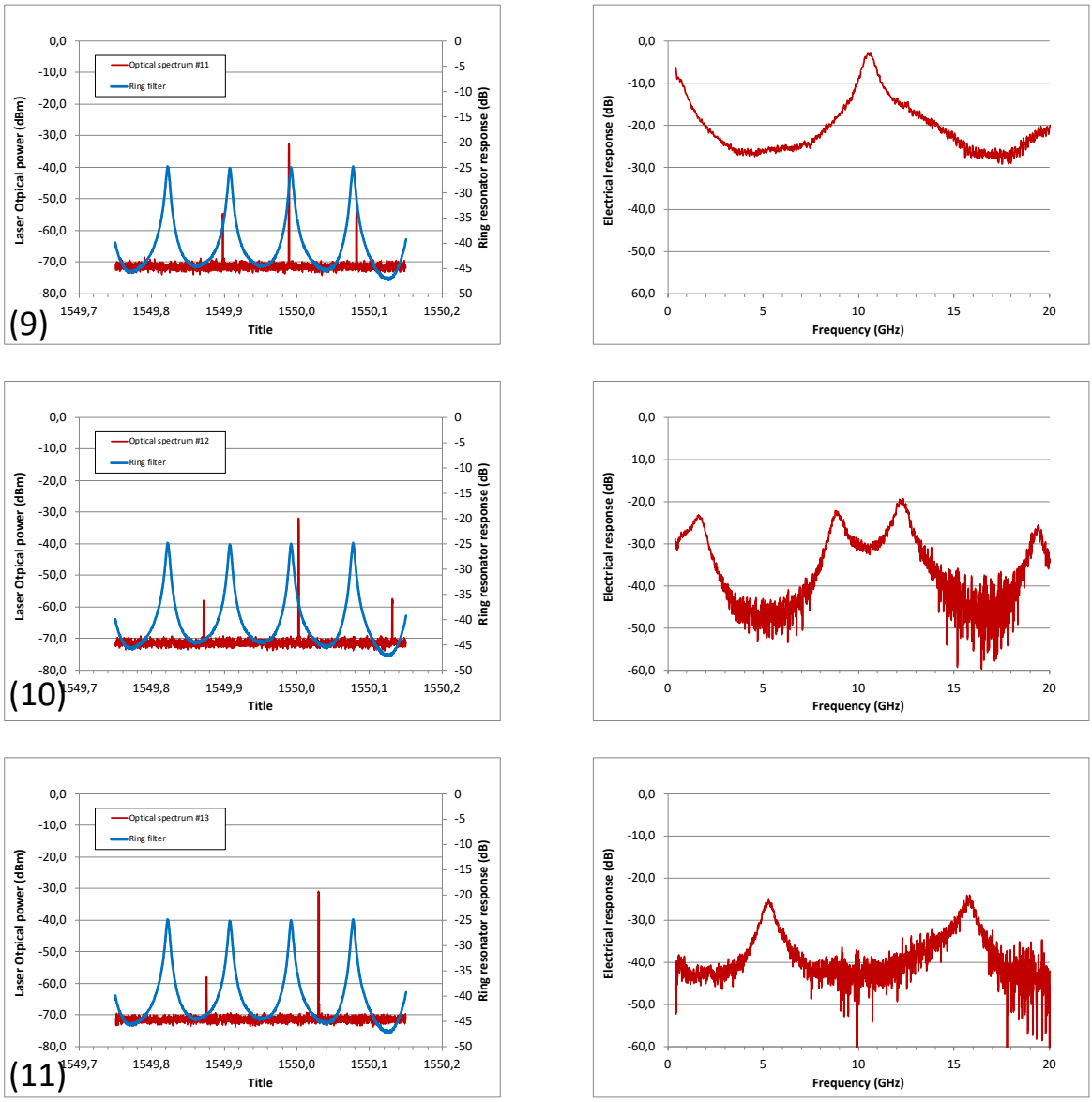

Figure 150. Drop port response of the ring resonator with amplitude modulation

4.5.5 Discussion of the results

The measurements in Figure 150 demonstrate the capability of the ring resonator to act as an electrical passband filter.

A better view of the peak of Figure 150 is shown in Figure 151. The optical lineshape of the filter response is faithfully reproduced in the electrical domain, with a finesse of 17.5, which is really close to what was measured in the optical domain. This implies that the improved technological process shown at the end of Chapter 2 could strongly reduce the electrical bandwidth of the ring filter, leading to high quality factor ring resonators for microwave filtering in the optical domain.

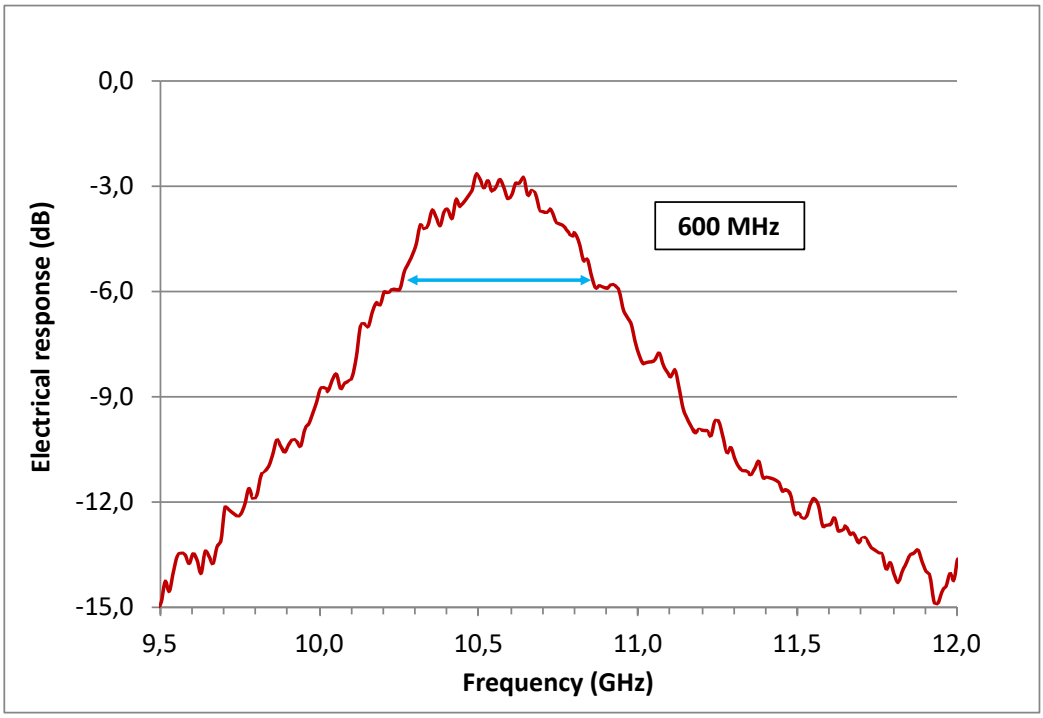

Figure 151. Ring resonator filter response around the 10.5 GHz peak and measured FWHM

4.6 Conclusions

This chapter showed characterizations of several PICs in OEO configuration.

The first section presented the validation of Externally Modulated Laser (EML) and the electro-absorption modulator as building blocks for integrated OEO PICs.

Oscillations at 10 GHz were obtained in a setup comprising two EMLs and an EDFA. The lab setup suffered from the surrounding mechanical noise, clearly seen in the electrical spectra.

The second section presented the results of the PIC designed in chapter 3. The PIC integrated a DFB laser, an electro-absorption modulator, several SOAs and a photodiode.

The open loop link gain was measured up to -24 dB and was not able to sustain oscillations. The main causes for the low link gain might be a low slope efficiency of the modulator and a lack of optical power in the optical loop. A further optimization step is needed in order to obtain the full active optical functionalities needed for integration.

The third paragraph showed measurements performed on a PIC in an OEO configuration. The PIC was a tunable electrical frequency generator fabricated during the IPHOS project. The PIC integrated 2 DFB lasers, several SOAs, electro-absorption modulators and high-speed UTC photodiodes.

The PIC was used in an OEO configuration with optical and electrical injection feedback in order to stabilize the tunable beatnote of the 2 DFB lasers. Oscillations from 15 to 20 GHz were obtained.

The last paragraph demonstrated the function of RF filtering through the optical domain, performed with a ring resonator.

The chosen architecture with a ring resonator in drop configuration, with a modulation amplitude scheme has been proven, with RF filtering properties in agreement with the optical properties observed.

This demonstration completes the main function of the passive PIC, the RF filtering, but the passive cavity design can still be enriched with more complex architectures.

5 CONCLUSIONS AND PERSPECTIVES

This manuscript is an overview of the research carried out at III-V Lab on Hybrid OptoElectronic Oscillators and the tools and methods implemented to reach such goal.

Chapter 1 presents the proposed configuration of an application-specific Photonic Integrated Circuit (PIC) Optoelectronic Oscillator, working as a microwave signal generator for a variety of applications, namely electronic warfare and RADAR systems. A state of the art of photonic integration for electrical signal generation is presented, along with some elements of noise in oscillators and its origins. The noise performances of an integrated solution will strongly impact its fields of application; the chapter presented the case study of a RADAR system and the impact of close-to-carrier noise for the detection of airborne targets.

In order to fabricate the proposed integrated OEO architecture, two photonic integration platforms were used: an Indium Phosphide (InP) PIC for the fabrication of active components, and Silicon Nitride (SiN) waveguides on Silica on Silicon for the fabrication of on-chip delay lines and optical filters. The latter is the topic of Chapter 2, where this integration platform is described.

The passive integration platform with Silicon Nitride waveguides was developed from scratch with the CEA-LETI in Grenoble. CEA-LETI was already fabricating thick SiN waveguides (800 nm), thus the specific fabrication technology for thin, low propagation losses waveguides was developed.

The platform was chosen among others for its superior potential for integrated microwave photonic applications: very low propagation losses coupled with reasonable bending radiuses for chip compacity, as shown throughout the chapter.

The design of the building blocks is presented, from the waveguide itself to ring resonators and Bragg gratings. The coupling with optical fibers and the InP PIC was ensured by tapered spot-size converters.

Three generations of wafers were designed in the time frame of this thesis, and two of them were fabricated and characterized. The fabrication process evolved as well throughout the generation, increasing performances and stability, thanks to the improvements in the fabrication process flow and a co-design of devices, fabrication and back-end processes.

With an eye to the final application, the design of the third generation of wafers (OHY5) yielded good enough results for a design freeze, standardization of the fabrication process and possible industrialisation of the low losses SiN platform. The later work at III-V lab using the SiN platform demonstrated its flexibility and the potential to become a reference platform in the European microwave photonic ecosystem: we mention the examples of a low-linewidth laser and a mode-locked laser built with this same photonic integration platform.

The InP SI-BH integration platform used throughout this manuscript is a standard at III-V Lab and is described in Chapter 3. Such platform has shown in the past good potential in terms of lasers and modulators for integrated transmitters for telecom applications. The design of the building blocks up to the complete InP PIC is described: a laser, an electro-absorption modulator, a semiconductor optical amplifier and a photodiode were integrated with a butt-joint technique.

Unfortunately, several issues during the fabrication and epitaxy process led to underwhelming performances with respect to past PIC fabrication runs. Nevertheless, it was possible to extract useful data on the needs of an integrated OEO in terms of standalone components and at the whole PIC level, paving the road for the design of a new InP integration platform. One of the fundamental limitations found during the measurements of the InP PIC was the lack of available optical power to ensure all-optical gain operation, that would benefit the noise performances of an integrated solution.

The ideas for a new photonic integration platform were still at a rudimental stage at the end of this thesis, but the integration of slab-coupled high-power devices was its main foundation. This would lead to a new waveguide design for electro-absorption modulators and photodiodes based on the design of high-power slab-coupled DFB lasers and SOAs already fabricated at III-V Lab at that time. The biggest effort in the design would be the mutual optimisation of at least two waveguides epitaxial structures and the interconnection and mode adaptation between them. Such an integration platform that could allow the fabrication of complex active PICs for Integrated Microwave Photonics applications, which are so far limited in performance by the unavailability of a specific active integration technology.

Given the availability of such integration platform, the PICs and configurations described in Chapter 4 could be readily integrated, since both elements composing the hybrid III-V/SiN PIC were demonstrated. This last Chapter is divided in 4 sections, each discussing a challenge faced during the integration of an OEO.

The Electro-Absorption Modulator (EAM) is discussed in the first section as an alternative for integrated microwave photonics to bulkier Mach-Zehnder modulators. It is also shown that the same structure of electro-absorption modulators can also be used as a photodiode. Oscillations at 10 GHz were obtained in a lab demonstrator also discussed in a paper at MWP 2017 conference. The setup also involved an EDFA, which guaranteed sufficient power levels for all-optical gain operation. This was the first clue leading to the idea of a high-power photonic integration technology.

The second section presented the results obtained on the InP PIC in the configuration presented in Chapter 1. A gain of -24 dB, measured in a closed-loop configuration, was insufficient to obtain self-sustaining oscillation. The next generation of these PICs should have increased optical power handling capabilities and a strongly optimized optical coupling to further reduce losses in the cavity and allow a demonstration of the proposed architecture.

The third section demonstrates the tunability of an OEO with an on-chip optical reinjection path. The technique of optical injection locking was used on a PIC to stabilize the beatnote that two DFB lasers generated on an UTC photodiode; the OEO loop was closed on an EAM, generating sidelobes that triggered the injection locking mechanism. A tunability between 15 and 20 GHz was demonstrated, limited by the EAM bandwidth and the DFB central wavelength design. This demonstrator was discussed in MWP 2016 conference paper and opens new perspectives for integrated OEOs in high frequency applications up to the K-band and even 5G communication systems.

The last section is devoted to the ring resonator, which is a basic yet very powerful building block for photonic filtering and signal processing. The filtering properties were extracted from electro-optical measurements and a bandpass filtering at 10 GHz was shown.

The general outcome of this manuscript, although not being a fully integrated OEO, is the demonstration of its building block functionalities on the two integration platforms of choice, InP and SiN, and how to improve them to reach the full integration. In its current state, this hybrid integration technology already demonstrated applications in integrated microwave photonics that go beyond the topic of this dissertation. With the current rate of improvement of photonic integration technologies, it is not impossible that such an architecture could become feasible in a matter of years.

6 BIBLIOGRAPHY

[1] X. S. Yao and L. Maleki, "Optoelectronic microwave oscillator," ***J. Opt. Soc. Am. B,*** vol. 13, pp. 1725-1735, 8 1996.

[2] M. Lewis, "Novel RF oscillator using optical components," ***Electronics Letters,*** vol. 28, no. 1, pp. 31-32, 1992.

[3] O. Lelièvre, V. Crozatier, P. Berger, G. Baili, O. Llopis, D. Dolfi, P. Nouchi, F. Goldfarb, F. Bretenaker, L. Morvan and G. Pillet, "A model for designing ultralow noise single- and dual-loop 10-ghz optoelectronic oscillators," ***Journal of Lightwave Tehcnology,*** vol. 35, pp. 4366-4374, 2017.

[4] MicroSemi Corporation, "Vectron product line page," [Online]. Available: https://www.vectron.com/products/crystals/phase_noise_crystals.htm.

[5] E. Rubiola, Phase Noise and Frequency Stability in Oscillators, Cambridge University Press, 2010.

[6] A. D. Martino, Introduction to Modern EW systems, Second Edition, Artech House electronic warfare lybrary, 2018.

[7] S. Romisch, J. Kitching, E. Ferre-Pikal, L. Hollberg and F. Walls, "Performance evaluation of an optoelectronic oscillator," ***IEEE Transactions on Ultrasonics, Ferroelectrics, and Frequency Control,*** vol. 47, p. 1159–1165, 2000.

[8] W. Loh, J. Klamkin, S. M. Madison, F. J. O'Donnell, J. J. Plant, S. Yegnanarayanan, R. J. Ram and P. W. Juodawlkis, "Slab-coupled optical waveguide (SCOW) based optoelectronic oscillator (OEO)," ***43rd Annual Precise Time and Time Interval Systems and Application Meeting,*** 2011.

[9] X. Yao and L. Maleki, "Multiloop optoelectronic oscillator," ***IEEE Journal of Quantum Electronics,*** vol. 36, p. 79–84, 2000.

[10] O. Lelièvre, V. Crozatier, G. Baili, P. Berger, G. Pillet, D. Dolfi, L. Morvan, F. Goldfarb, F. Bretenaker and O. Llopis, "Ultra-low phase noise 10 ghz dual loop optoelectronic oscillator,"," ***2016 IEEE International Topical Meeting on Microwave Photonics (MWP),*** pp. 106-109, 2016.

[11] F. VanDijk, A. Enard, X. Buet, F. Lelarge and G. Duan, "Phase noise reduction of a quantum dash mode-locked laser in a millimeter- wave coupled opto-electronic oscillator,"," ***Journal of Lightwave Technology,*** vol. 26, pp. 2789–2794,, 2008.

[12] M. Vallet, M. Romanelli, G. Loas, F. v. Dijk and M. Alouini, "Self- stabilized optoelectronic oscillator using frequency-shifted feedback and a delay line," ***IEEE Photonics Technology Letters,*** vol. 28, p. 1088– 1091, 2016.

[13] G. Pillet, L. Morvan, M. Brunel, F. Bretenaker, D. Dolfi, M. Vallet, J. Huignard and A. L. Floch, "Dual-frequency laser at 1.5 um for optical distribution and generation of high-purity microwave signals," ***Journal of Lightwave Technology,*** vol. 26.

[14] P. Primiani, F. vanDijk, M. Lamponi, M. Chtioui, M. Vallet, M. Romanelli and M. Alouini, " Tunable optoelectronic oscillator based on an integrated heterodyne source," ***2016 IEEE International Topical Meeting on Microwave Photonics (MWP),*** p. 251–254, 2016.

[15] S. Srinivasan, D. T. Spencer, M. Heck, E. Norberg, G. Fish, L. Theogarajan and J. E. Bowers, "Microwave generation using an integrated hybrid silicon mode-locked laser in a coupled optoelectronic oscillator configuration," ***CLEO: 2013.***

[16] C. Gunn, D. Guckenberger, T. Pinguet, D. Gunn, D. Eliyahu, B. Mansoorian, D. V. Blerkom and O. Salminen, "A low phase noise 10ghz optoelectronic rf oscillator implemented using cmos photonics," ***Digest of Technical Papers: IEEE International Solid-State Circuits Conference,*** p. 570–622, 2007.

[17] W. Zhang and J. Yao, " A silicon photonic integrated frequency-tunable optoelectronic oscillator," ***International Topical Meeting on Microwave Photonics (MWP),*** p. 1–4, 2017.

[18] D. Spencer, T. Briles, T. Drake, J. Stone, R. Ilic, Q. Li, L. Sinclair, W. D., Newbury, K. N. Srinivasan, S. Papp, D. S., A. Bluestone, T. Komljenovic, N. Volet, L. Theogarajan, J. Bowers, M. Suh, K. Yang and S. Lee, "Full stabilization and control of an integrated photonics optical frequency synthesizer," ***IEEE Photonics Conference (IPC),*** pp. 341-342, 2017.

[19] V. Ilchenko, J. Byrd, A. Savchenkov, A. Matsko, D. Seidel and L. Maleki, "Miniature oscillators based on optical whispering gallery mode resonators," ***IEEE International Frequency Control Symposium,*** p. 305–308, 2008.

[20] OEwaves, "Nano OEO Product page," [Online]. Available: https://oewaves.com/hi-q-nano-oeo-1.

[21] D. Marpaung, J. Yao and J. Capmany, "Integrated microwave photonics," ***Nature Photonics,*** vol. 13, no. 2, pp. 80-90, 2019.

[22] D. Rabus, Integrated Ring Resonators: The Compendium, Springer Berlin Heidelberg, 2007.

[23] R. Olshansky, "Propagation in glass optical waveguides," ***Review of Modern Physics,*** vol. 51, no. 2, pp. 341-367, 1979.

[24] V. S. Ilchenko, X. S. Yao and L. Maleki, "Microsphere integration in active and passive photonics devices," vol. 3930, pp. 154 -- 162, 2000.

[25] J. Taylor and V. Tolstikhin, "Intervalence band absorption in InP and related materials for optoelectronic device modeling," ***Journal of Applied Physics,*** vol. 87, no. 3, p. 1054, 2000.

[26] E. Haga and H. Kimura, "Free-Carrier Infrared Absorption in III-V Semiconductors. GaAs, InP, GaP and GaSb," ***Journal of the Physical Society of Japan,*** vol. 19, no. 5, pp. 658-669, 1964.

[27] J. F. Bauters, M. J. R. Heck, D. D. John, J. S. Barton, D. J. Blumenthal, J. E. Bowers, C. M. Bruinink, A. Leinse and R. G. Heideman, "A comparison of approaches for ultra-low-loss waveguides," in ***OFC/NFOEC***, 2012.

[28] T. Barwicz and H. A. Haus, "Three-dimensional analysis of scattering losses due to sidewall roughness in microphotonic waveguides," ***Journal of Lightwave Technology,*** vol. 23, pp. 2719-2732, 2005.

[29] F. VanDijk, G. Kervella, M. Lamponi, M. Chtioui, F. Lelarge, E. Vinet, Y. Robert, M. J. Fice, C. C. Renaud, A. Jimenez and G. Carpintero, "Integrated InP Heterodyne Millimeter Wave Transmitter," ***IEEE Photonics Technology Letters,*** vol. 26, no. 10, pp. 965-968, 2014.

[30] V. Moskalenko, S. Latkowski, S. Tahvili, T. de Vries, M. Smit and E. Bente, "Record bandwidth and sub-picosecond pulses from a monolithically integrated mode-locked quantum well ring laser," ***Optics Express,*** vol. 22, 2014.

[31] D. D'Agostino, G. Carnicella, C. Ciminelli, P. Thijs, P. J. Veldhoven, H. Ambrosius and M. Smit, "Low-loss passive waveguides in a generic InP foundry process via local diffusion of zinc," ***Opt. Express,*** vol. 23, pp. 25143-25157, 2015.

[32] M. Lysevych, H. Tan, F. Karouta and C. Jagadish, "Single-Step RIE Fabrication Process of Low Loss InP Waveguide Using CH4/H2 Chemistry," ***Journal of The Electrochemical Society,*** vol. 158, p. 281, 2011.

[33] J. H. Angenent, M. Erman, J. M. Auger, R. Gamonal and P. J. A. Thijs, "Extremely low loss InP/GaInAsP rib waveguides," ***Electronics Letters,*** vol. 25, pp. 628-629, 1989.

[34] M. Razeghi, M. Defour, F. Omnes, P. Maurel, J. Chazelas and F. Brillouet, "First GaInAsP-InP double-heterostructure laser emitting at 1.27 um on a silicon substrate," ***Applied Physics Letters,*** vol. 53, 1988.

[35] H.-H. Chang, A. W. Fang, M. N. Sysak, H. Park, R. Jones, O. Cohen, O. Raday, M. J. Paniccia and J. E. Bowers, "1310nm silicon evanescent laser," ***Opt. Express,*** vol. 15, pp. 11466-11471, 2007.

[36] J.-M. Fedeli, F. Schrank, E. Augendre, S. Bernabe, J. Kraft, P. Grosse and T. Enot, "Photonic-Electronic Integration With Bonding," ***IEEE Journal of Selected Topics in Quantum Electronics,*** vol. 20, pp. 350-358, 2014.

[37] A. Biberman, M. J. Shaw, E. Timurdogan, J. B. Wright and M. R. Watts, "Ultralow-loss silicon ring resonators," ***Opt. Lett.,*** vol. 37, pp. 4236-4238, 2012.

[38] K. K. Lee, D. R. Lim, L. C. Kimerling, J. Shin and F. Cerrina, "Fabrication of ultralow-loss Si/SiO2 waveguides by roughness reduction," ***Opt. Lett.,*** vol. 26, pp. 1888-1890, 2001.

[39] M. Borselli, T. J. Johnson and O. Painter, "Beyond the Rayleigh scattering limit in high-Q silicon microdisks: theory and experiment," ***Opt. Express,*** vol. 13, pp. 1515-1530, 2005.

[40] F. Y. Gardes, J. A. Kubby, G. T. Reed, G. T. Reed, A. P. Knights, G. Mashanovich, P. E. Jessop, L. Rowe, S. McFaul, D. Bruce and N. G. Tarr, "Sub-micron optical waveguides for silicon

photonics formed via the local oxidation of silicon (LOCOS)," ***SPIE Integrated Optoelectronic Devices,*** 2008.

[41] Y. A. Vlasov and S. J. McNab, "Losses in single-mode silicon-on-insulator strip waveguides and bends," ***Opt. Express,*** vol. 12, pp. 1622-1631, 2004.

[42] R. Adar, Y. Shani, C. H. Henry, R. C. Kistler, G. E. Blonder and N. A. Olsson, "Measurement of very low-loss silica on silicon waveguides with a ring resonator," ***Applied Physics Letters,*** 1991.

[43] H. Lee, T. Chen, J. Li, O. Painter and K. J. Vahala, "Ultra-low-loss optical delay line on a silicon chip," ***Nature Communications,*** vol. 3, 2012.

[44] M. L. Gorodetsky, A. A. Savchenkov and V. S. Ilchenko, "Ultimate Q of optical microsphere resonators," ***Opt. Lett.,*** vol. 21, pp. 453-455, 1996.

[45] F. Sedlmeir, R. Zeltner, G. Leuchs and H. G. Schwefel, "High-Q MgF2 whispering gallery mode resonators for refractometric sensing in aqueous environment," ***Opt. Express,*** vol. 22, pp. 30934-30942, 2014.

[46] J. Kischkat, S. Peters, B. Gruska, M. Semtsiv, M. Chashnikova, M. Klinkmüller, O. Fedosenko, S. Machulik, A. Aleksandrova, G. Monastyrskyi, Y. Flores and W. T. Masselink, "Mid-infrared optical properties of thin films of aluminum oxide, titanium dioxide, silicon dioxide, aluminum nitride, and silicon nitride," ***Applied Optics,*** vol. 51, p. 6789, 2012.

[47] H. El Dirani, L. Youssef, C. Petit-Etienne, S. Kerdiles, P. Grosse, C. Monat, E. Pargon and C. Sciancalepore, "Ultralow-loss tightly confining Si3N4 waveguides and high-Q microresonators," ***Opt. Express,*** vol. 27, pp. 30726-30740, 2019.

[48] S. C. Mao, S. H. Tao, Y. L. Xu, X. W. Sun, M. B. Yu, G. Q. Lo and D. L. Kwong, "Low propagation loss SiN optical waveguide prepared by optimal low-hydrogen module," ***Opt. Express,*** vol. 16, pp. 20809-20816, 2008.

[49] J. F. Bauters, M. J. R. Heck, D. D. John, J. S. Barton, C. M. Bruinink, A. Leinse, R. G. Heideman, D. J. Blumenthal and J. E. Bowers, "Planar waveguides with less than 0.1 dB/m propagation loss fabricated with wafer bonding," ***Opt. Express,*** vol. 19, pp. 24090-24101, 2011.

[50] K. Luke, A. Dutt, C. B. Poitras and M. Lipson, "Overcoming Si3N4 film stress limitations for high quality factor ring resonators," ***Optics Express,*** vol. 21, 2013.

[51] R. G. Hunsperger, Integrated optics: theory and technology, Springer-Verlag, 2009.

[52] Jared F. Bauters and Martijn J. R. Heck and Demis John and Daoxin Dai and Ming-Chun Tien and Jonathon S. Barton and Arne Leinse and Ren\'{e} G. Heideman and Daniel J. Blumenthal and John E.Bowers, "Ultra-low-loss high-aspect-ratio Si3N4 waveguides," ***Opt. Express,*** vol. 19, pp. 3163-3174, 2011.

[53] F. Ladouceur and P. Labeye, "A new general approach to optical waveguide path design," ***Journal of Lightwave Technology,*** vol. 13, pp. 481-492, 1995.

[54] D. T. Spencer, Y. Tang, J. F. Bauters, M. J. R. Heck and J. E. Bowers, "Integrated Si3N4/SiO2 ultra high Q ring resonators," in ***IEEE Photonics Conference***, 2012.

[55] W. Huang and S. Lessard, "Wavefront-tilt effect in nonparallel optical waveguides," ***Journal of Lightwave Technology,*** vol. 10, pp. 316-322, 1992.

[56] K. S. Chiang, "Effective-index method for the analysis of optical waveguide couplers and arrays: an asymptotic theory," ***Journal of Lightwave Technology,*** vol. 9, pp. 62-72, 1991.

[57] H. Debregeas, C. Ferrari, M. A. Cappuzzo, F. Klemens, R. Keller, F. Pardo, C. Bolle, C. Xie and M. P. Earnshaw, "2kHz Linewidth C-Band Tunable Laser by Hybrid Integration of Reflective SOA and SiO2 PLC External Cavity," in ***2014 International Semiconductor Laser Conference***, 2014.

[58] W. R. McKinnon, D.-X. Xu, C. Storey, E. Post, A. Densmore, A. Delage, Waldron.P., J. H. Schmid and S. Janz, "Extracting coupling and loss coefficients from a ring resonator," ***Opt. Express,*** vol. 17, pp. 18971-18982, 2009.

[59] P. Primiani, S. Boust, J. Fedeli, F. Duport, C. Gomez, J. Paret, A. Garreau, K. Mekhazni, C. Fortin and F. Van Dijk, "Silicon Nitride Bragg Grating With Joule Thermal Tuning for External Cavity Lasers," ***IEEE Photonics Technology Letters,*** vol. 31, pp. 983-986, 2019.

[60] E. F. Schubert, Light-Emitting Diodes, Cambridge University Press, 2006.

[61] "Ioffe Institute semiconductor material properties," [Online]. Available: http://www.ioffe.ru/SVA/NSM/Semicond/.

[62] F. Schwabl, Quantum Mechanics, Springer, 2002.

[63] M. S. Skolnick, P. R. Tapster, S. J. Bass, A. D. Pitt, N. Apsley and S. P. Aldred, "Investigation of InGaAs-InP quantum wells by optical spectroscopy," ***Semiconductor Science and Technology,*** vol. 1, pp. 29-40, 1986.

[64] R. H. Yan, S. W. Corzine, L. A. Coldren and I. Suemune, "Corrections to the expression for gain in GaAs," ***IEEE Journal of Quantum Electronics,*** vol. 26, p. 213–216, 1990.

[65] Y. Rong, Y. Huo, E. T. Fei, M. Fiorentino, M. R. T. Tan, T. Ochalski, G. Huyet, L. Thylen, M. Chacinski, T. I. Kamins and J. S. Harris, "High speed optical modulation in Ge quantum wells using quantum confined stark effect," ***Frontiers of Optoelectronics,*** vol. 5, pp. 82-89, 2012.

[66] I. Bar-Joseph, C. Klingshirn, D. A. B. Miller, D. S. Chemla, U. Koren and B. I. Miller, "Quantum-confined Stark effect in InGaAs/InP quantum wells grown by organometallic vapor phase epitaxy," ***Applied Physics Letters,*** vol. 50, pp. 1010-1012, 1987.

[67] N. Dagli, High-Speed Photonic Devices, CRC Press, 2006.

[68] H. Debrégeas, F. Lelarge, R. Brenot, C. Caillaud, J. Provost, F. Pommereau, T. D. H. Nguyen, D. Lanteri, K. Mekhazni, S. Barbet, A. Garreau, J. Paret, G. Glastre, C. Fortin and E. .. Derouin, "Record 6dBm electroabsorption modulated laser for 10Gb/s and 25Gb/s high power budget

access networks," in ***2017 Optical Fiber Communications Conference and Exhibition (OFC)***, 2017.

[69] A. Garreau, M. Cuisin, J. Provost, F. Jorge, A. Konczykowska, C. Jany, J. Decobert, O. Drisse, F. Blache, D. Carpentier, E. Derouin, F. Martin, N. Lagay, J. Landreau and C. Kazmierski, "Wide Temperature Range Operation at 43Gbit/s of 1.55µm InGaAlAs Electroabsorption Modulated Laser with Single Active Layer," in ***2007 IEEE 19th International Conference on Indium Phosphide Related Materials***, 2007.

[70] M. J. Connelly, Semiconductor optical amplifiers, Springer, 2002.

[71] P. W. Juodawlkis, J. J. Plant, W. Loh, L. J. Missaggia, F. J. O'Donnell, D. C. Oakley, A. Napoleone, J. Klamkin, J. T. Gopinath, D. J. Ripin, S. Gee, P. J. Delfyett and J. P. Donnelly, "High-Power, Low-Noise 1.5-µm Slab-Coupled Optical Waveguide (SCOW) Emitters: Physics, Devices, and Applications," ***IEEE Journal of Selected Topics in Quantum Electronics,*** vol. 17, pp. 1698-1714, 2011.

[72] G. Baili, M. Alouini, T. Malherbe, D. Dolfi, J. Huignard, T. Merlet, J. Chazelas, I. Sagnes and F. Bretenaker, "Evidence of ultra low microwave additive phase noise for an optical RF link based on a class-A semiconductor laser," ***Opt. Express,*** vol. 16, pp. 10091-10097 , 2008.

[73] M. Faugeron, M. Tran, F. Lelarge, M. Chtioui, Y. Robert, E. Vinet, A. Enard, J. Jacquet and F. VanDijk, "High-Power, Low RIN 1.55 µm Directly Modulated DFB Lasers for Analog Signal Transmission," ***IEEE Photonics Technology Letters,*** vol. 24, pp. 116-118, 2012.

[74] G. Betts, X. Xie, I. Shubin, W. Chang and P. Yu, "Gain limit in analog links using electroabsorption modulators," ***IEEE Photonics Technology Letters,*** vol. 18, p. 2065–2067, 2006.

[75] P. Primiani, H. Débrégéas, D. A. M. Lanteri and F. vanDijk, "Electro-absorption modulator-based optoelectronic oscillator," in ***2017 International Topical Meeting on Microwave Photonics (MWP)***, 2017.

[76] O. Lelièvre, V. Crozatier, G. Baili, P. Berger, P. Nouchi, D. Dolfi, L. Morvan, O. Llopis, K. Mezkhani, R. Brenot, J. Paret, A. Garreau, P. Charbonnier, F. Duport, F. VanDijk, F. Goldfarb and F. Bretenaker, "All photonic-gain optoelectronic oscillator at 10 GHz," in ***2018 International Topical Meeting on Microwave Photonics (MWP)***, 2018.

[77] R. Boula-Picard, M. Alouini, J. Lopez, N. Vodjdani and J.-C. Simon, "Impact of the gain saturation dynamics in semiconductor optical am- plifiers on the characteristics of an analog optical link," ***Journal of Lightwave Technology,,*** vol. 23, p. 2420 – 2426, 2005.

[78] F. VanDijk, G. Kervella, M. Lamponi, M. Chtioui, F. Lelarge, E. Vinet, Y. Robert, M. J. Fice, C. C. Renaud, A. Jimenez and G. Carpintero, "Integrated inp heterodyne millimeter wave transmitter," ***IEEE Photonics Technology Letters,*** vol. 26, p. 965–968, 2014.

[79] G. Kervella, F. VanDijk, M. Alouini, M. Chtioui and M. Lamponi, "Low phase noise fully integrated millimeter-wave photonic source using cross injection locking,," in ***2015 40th***

International Conference on Infrared, Millimeter, and Terahertz waves (IRMMW-THz), 2015.

[80] A. Jankowski, G. Kervella, M. Chtioui, M. Lamponi and F. VanDijk, "Optoelectronic comb generation and cross-injection locking of photonic integrated circuit for millimetre-wave generation„" in ***42nd European Conference on Optical Communication (ECOC)***, 2016.

[81] A. Thorette, P. Primiani, M. Romanelli, M. Alouini, F. VanDijk and M. Vallet, "Self-stabilized optoelectronic oscillator using optical feed- back on integrated heterodyne source," in ***Conference on Lasers and Electro-Optics Europe European Quantum Electronics Conference (CLEO/Europe-EQEC)***, 2017.

[82] S. Boust, H. E. Dirani, F. Duport, L. Youssef, Y. Robert, A. Larrue, C. Petit-Etienne, E. Vinet, S. Kerdiles, E. Parfon, M. Faugeron, M. Vallet, C. Sciancalepore and F. VanDijk, "Compact optical frequency comb source based on a DFB butt-coupled to a silicon nitride microring," in ***International Topical Meeting on Microwave Photonics (MWP)***, 2019.

[83] J. Piprek, Semiconductor Optoelectronic Devices: Introduction to Physics and Simulation, Elsevier Science, 2013.

RESUMÉ

Les Oscillateurs Opto-Electroniques (OEO) permettent la génération par voie optique de signaux ultra-pures dans le domaine des micro-ondes, et commencent à être déployés dans différents systèmes, y compris les systèmes de guerre électronique (RADAR, échantillonnage optique).
Toutefois la taille des OEOs empêche leur intégration dans des systèmes exigeants en termes de SWaP (size, weight and power consumption).

Le but de cette thèse est l'étude de l'Oscillateur Opto-électronique et des technologies d'intégration photoniques qui pourraient permettre la réduction en taille de ce système.
La thèse se déroule en quatre chapitres, chacun dédié à un des thèmes fondamentaux de cette étude.

Dans le premier chapitre je présents l'Oscillateur Opto-électronique en tant que système. Les premiers OEO ont été fabriqués au JPL (Jet Propulsion Laboratory) par Yao et Maleki en 1996, démontrant excellentes performances en termes de bruit de phase. Le bruit de phase est une mesure de la précision instantanée d'un oscillateur, et il est fondamentale pour les applications de mesure de vitesse et direction dans les systèmes RADAR. Le principe de fonctionnement d'un système RADAR est basé sur l'effet Doppler, ou l'on envoie une porteuse électrique par biais d'une antenne et l'on détecte un faible signal réfléchi par la cible. Ce signal est décalé en fréquence proportionnellement à la vitesse relative de la cible ; le bruit de phase de l'oscillateur à cette fréquence décalée est le principal facteur limitant de détection du système RADAR.
Également, le décalage Doppler est aussi proportionnel à la fréquence de la porteuse. A cause des contributions des différents bruits additifs, le bruit de phase est assez élevé proche de la porteuse. A ce propos, il est avantageux de travailler avec des fréquences de porteuse de l'ordre de plusieurs GHz.
La génération de signaux micro-ondes par voie optique a l'avantage d'avoir un bruit de phase quasi-indépendant de la fréquence générée, alors que les technologies électroniques s'appuient sur la multiplication d'oscillateurs en quartz à basse fréquence (10-100 MHz). La multiplication de fréquence par un facteur N entraine une augmentation du bruit de phase de 20*log(N), ce qui réduit la plage d'application des systèmes RADAR.

La caractéristique principale d'un Oscillateur Opto-électronique est la propagation du signal micro-onde dans une cavité mixte, optique et électrique. La Figure 152 montre l'architecture classique d'un OEO : une porteuse optique est générée dans un laser à faisceau continu (CW Laser) et passe par un modulateur d'amplitude (très souvent un modulateur Mach-Zehnder), où la conversion électro-optique aura lieu. Le signal est donc propagé dans une boucle de fibre dont la longueur peut atteindre plusieurs kilomètres, grâce aux très faibles pertes de propagation (0.2 dB/km). Le signal optique est converti dans le domaine électrique par une photodiode rapide, et ensuite filtré et amplifié.

L'architecture proposée dans cette thèse pour l'intégration d'un OEO est montrée en Figure 153.
Le système intégré est composé par deux Circuits Photoniques Intégrés (PICs) sur substrats différents, avec une intégration hybride. Les éléments actifs sont fabriqués sur un substrat de Phosphure d'Indium (InP) grâce à la plateforme d'intégration du III-V Lab. Le laser continu un laser DFB mono-longueur d'onde, le modulateur fonctionne par le principe d'électro-absorption (détaillé en Chapitre 3); ces composants sont intégrés avec des amplificateurs optiques, qui remplacent les amplificateurs électriques, et une photodiode rapide. Le PIC actif a une entrée et une sortie optique pour l'interface avec un PIC passif fait sur substrat Silicium, avec des guides d'ondes en Nitrure de Silicium (SiN) pour

atteindre des très faibles pertes de propagation. Le but du PIC passif est de remplacer le délai en fibre optique et le filtrage du signal micro-onde, fait dans le domaine optique à travers un résonateur en anneau.

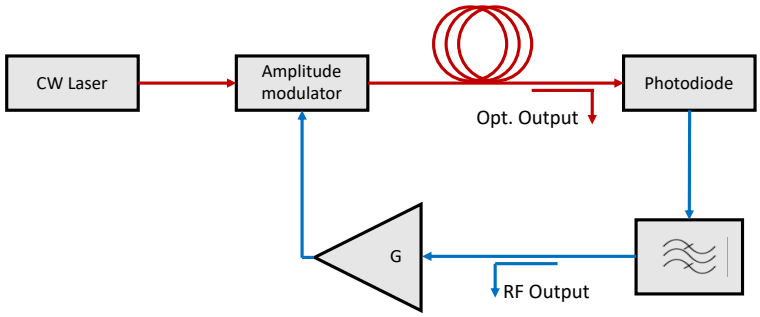

Figure 152. Architecture classique d'un OEO.

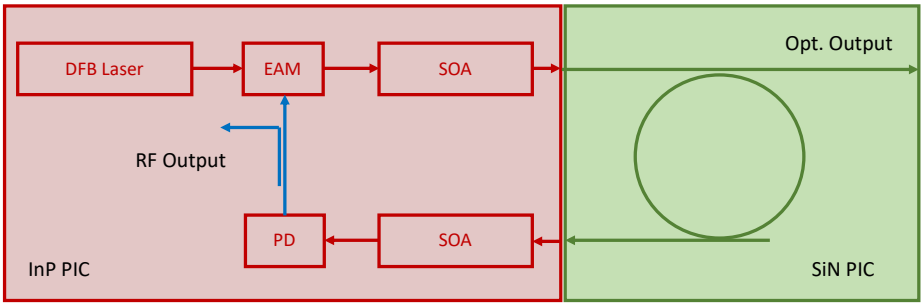

Figure 153. Architecture d'oscillateur intégré proposée dans la thèse.

Dans le chapitre 2 différentes plateformes d'intégration sont comparées en termes de pertes de propagation, paramètre fondamental pour le bon fonctionnement de délais très longs et du résonateur en anneau, compacité et capacité d'intégration avec le PIC actif en InP.
Évidemment, le InP est un candidat très intéressant pour l'intégration de l'entièreté du système sur la même puce, mais les guides en InP souffrent de pertes de propagation trop importantes par rapport à celles visées dans la thèse. La deuxième plateforme considérée est le Silicium, dont l'utilisation a fortement augmenté dans le passé récent grâce à la forte compacité et la possibilité d'utiliser des procédés de fabrication bien établis dans l'industrie électronique, qui a énormément baissé les coûts de production.
La plateforme choisie pour la fabrication du PIC passif est celle avec des guides d'onde en SiN sur substrat Silicium, qui permet une fabrication en grande échelle, mais aussi des très faibles pertes de propagations. Des pertes de l'ordre de 1 dB/m ont été démontrés sur des guides avec une structure à haut facteur de forme (Figure 154), avec un cœur de 40 nm d'épaisseur.
La raison derrière le choix de guides à haut facteur de forme est la possibilité de réduire les pertes dues à la rugosité latérale des guides. Des guides à cœur très fin permettent d'un côté de minimiser le recouvrement latéral entre le mode optique et le flanc rugueux du guide, mais de l'autre côté augmentent les pertes quand l'on cherche à réduire le rayon de courbure dans le circuit.
Le besoin d'une certaine compacité, pour permettre des configurations complexes sur des tailles de PIC raisonnable, nous porte à choisir des guides d'épaisseur plus importants, entre 70 et 90 nm, visant des pertes de propagation de l'ordre de 10 dB/m et avec des rayons de courbure critiques en dessous du millimètre.

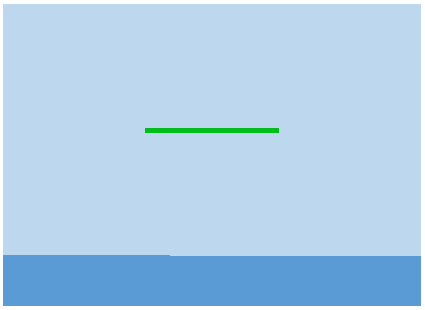

Figure 154. Guide d'onde en SiN (vert) interré dans de la silice (blue ciel) sur substrat Si (blue)

Le chapitre 2 montre le travail de design des guides, prenant en compte les différents paramètres du guide même pour un fonctionnement monomode, et les briques de base qui composeront les PICs :

- un adaptateur de mode en entrée/sortie de la puce, pour couplage sur une fibre optique ou le PIC actif ;
- des guides courbés;
- des coupleurs directionnels;
- les résonateurs en anneaux.

La deuxième partie du chapitre discute les résultats expérimentaux obtenus. Une des puces de test est composé par 9 anneaux avec force de couplage différente, pour en extraire les paramètres fondamentaux : indice effectif, pertes de propagation, force de couplage. Les pertes de propagation sont estimées avec cette méthode entre 20 et 30 dB/m. Néanmoins, il est évident que les pertes en excès causées par le coupler directionnel.
Une stratégie pour réduire ces pertes en excès est celle de dessiner des courbures adiabatiques pour réduire la différence de vitesse de phase entre le guide de couplage e celle du résonateur.
Les résultats expérimentaux des anneaux fabriqués avec cette technique ont donné des très bons résultats en termes de filtrage, avec une très bonne rejection de 53 dB (Figure 155).

Le chapitre 3 décrit le fonctionnement du PIC actif fabriqué sur plateforme InP, à partir des phénomènes physiques de gain et absorption dans les matériaux semi-conducteurs à puits quantiques. La fabrication des composants actifs a bénéficié de la plateforme d'intégration du III-V Lab, qui donne la possibilité d'intégrer des lasers DFB et des modulateurs à électro-absorption par moyen d'un recroissance épitaxiale dite butt-joint.
L'élément innovant de cette thèse est l'utilisation de la structure épitaxiale du modulateur en tant que photodiode, ce qui simplifie le procédé de fabrication. Les guides d'ondes utilisées sont des guides interrés avec de l'InP dopé Fe semi-isolant (SI-BH), montrés en Figure 156.
Le chapitre détaille le design, la fabrication et la caractérisation des briques de base et de leurs performances pour atteindre un gain de boucle positif, condition nécessaire pour obtenir une oscillation et donc un OEO.

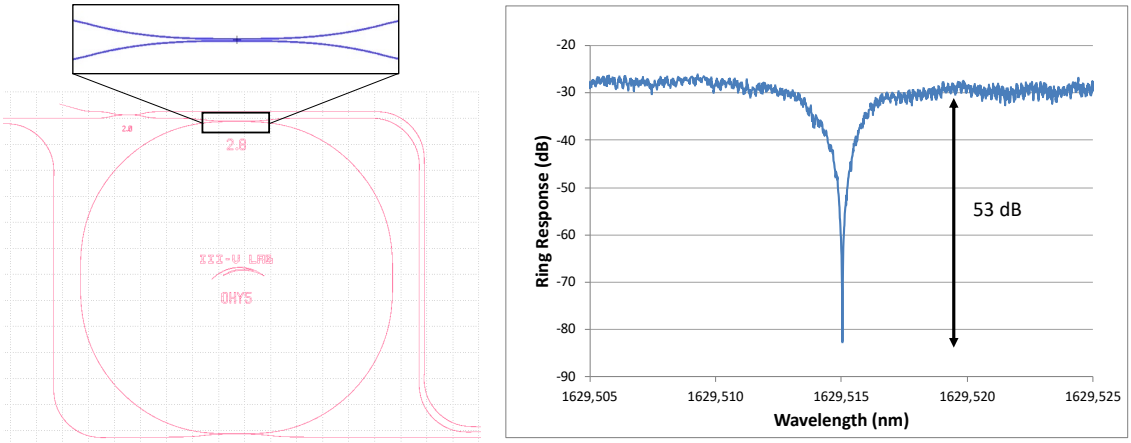

Figure 155. Gauche : résonateur en anneau fabriqué avec coupleur directionnel adiabatique. Droite : réponse optique de l'anneau en configuration de filtre en rejection.

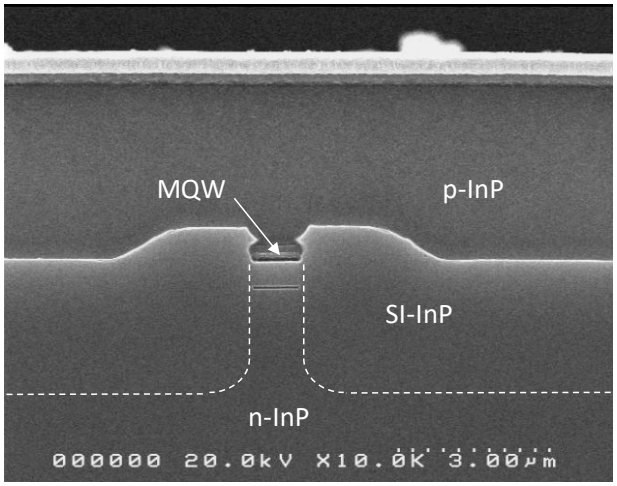

Figure 156. Image SEM d'un guide d'onde SI-BH fabriqué sur InP au III-V Lab.

Le quatrième et dernier chapitre montre les caractérisations au niveau de système de plusieurs combinaisons de briques de base, qui mènent au fur et à mesure à un meilleure compréhension des besoins, des contraintes, et du potentiel d'un oscillateur intégré.
La première expérience vise à démontrer la possibilité d'utiliser des modulateurs à électro-absorption dans un OEO, en tant que partie de modulation et de réception (photodiode).
Cette expérience a quantifié l'influence des paramètres du modulateur sur le gain de liaison, notamment l'efficacité différentielle dT/dV. Un oscillateur a été obtenu, malgré les instabilités mécaniques du couplage puce-fibre, fait en environnement laboratoire.
Le PIC actif montré en Figure 157, a été caractérisé dans une deuxième expérience, pour démontrer la capacité de fabriquer tous les composants sur la même puce, notamment utilisant deux sections égales en tant que modulateur et photodiode. En plus, cette puce donne la possibilité d'investiguer l'interaction (surtout thermique) des différent composants lors que plusieurs fonctionnent au même temps L'étude a aussi permis de comprendre les limitations en terme de puissance de la plateforme, et de prévoir des amélioration pour obtenir une plateforme d'intégration à haute puissance.

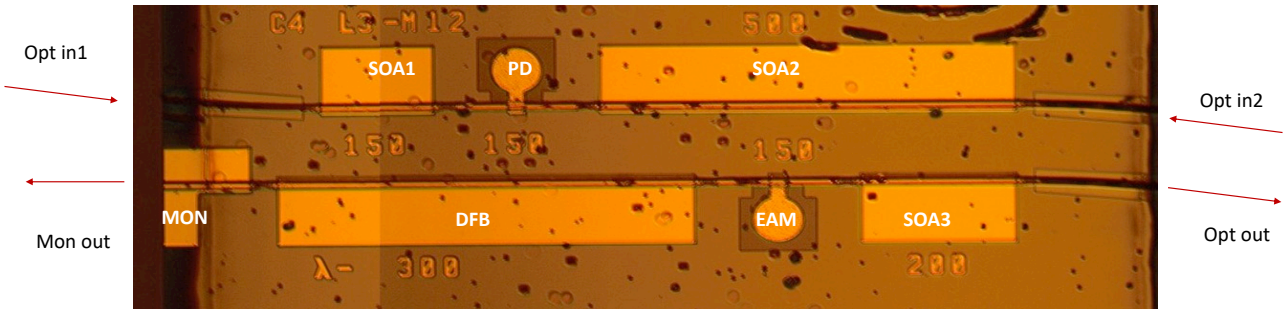

Figure 157. Photo su PIC OEO fabriqué sur la plateforme SI-BH.

Une étude sur l'accordabilité des oscillateurs a été mené sur une puce fabriquée dans le cadre du projet IPHOS ; cette puce comprends deux lasers, qui peuvent être utilisé pour la génération de micro-onde par battement hétérodyne sur une photodiode. Une configuration avec réinjection mutuelle électrique et optique permet un verrouillage des deux laser et ainsi une raie plus fine et accordable entre 15 et 20 GHz (Figure 158), tout en changeant le courant des deux lasers.

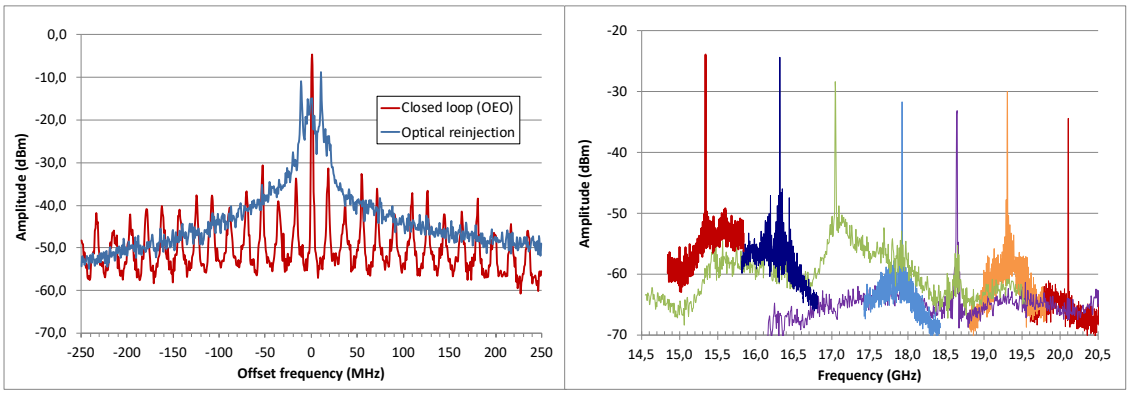

Figure 158. Gauche: spectre électrique en boucle fermée de l'OEO obtenu de la puce IPHOS. Droite: spectres électriques de l'OEO accordés entre 15 et 20 GHz.

Enfin, la dernière expérience concerne la capacité de filtrage du résonateur en anneau. Dans cette expérience, la raie d'un laser accordable est faite correspondre à une des résonances de l'anneau, puis modulée en amplitude.
La Figure 159 montre les spectres optique et électrique de cette expérience, et du fonctionnement de l'anneau autant que filtre électrique à 10 GHz.

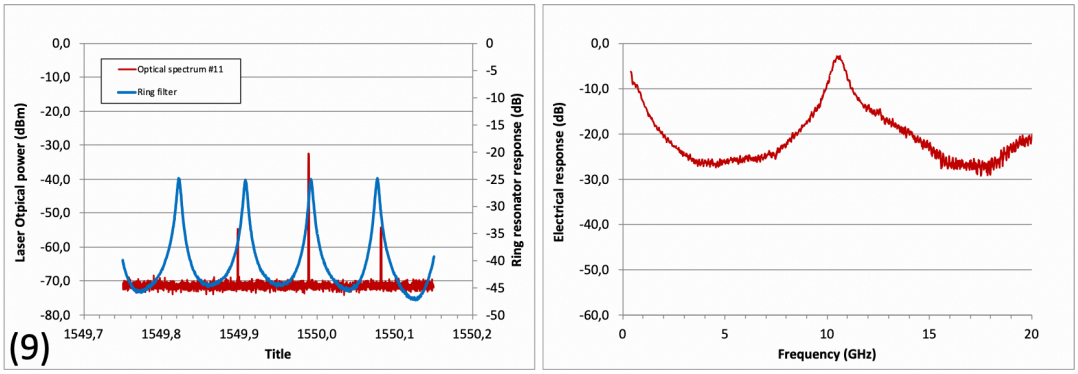

Figure 159. Spectres optique et électrique de la réponse du résonateurs en anneau

Malgré l'impossibilité de démontrer un OEO complètement intégré, ce manuscrit a guidé le lecteur sur la démonstration des briques de base de l'architecture proposée, sur les deux plateformes d'intégration InP et SiN.